Antennas for CubeSat Communication

Miroslav VELJOVIC

Two antennas got married on a roof.
The ceremony wasn't much,
but the reception was excellent!

(unknown author)

Abstract

CubeSats are a type of small satellites ($<500\,\mathrm{kg}$) that weigh several kilograms and consist of multiple Units (U) measuring $100 \times 100 \times 113.5\,\mathrm{mm}^3$. CubeSats emerged as a low-cost alternative to conventional large satellites, and have since demonstrated capabilities for communication, Earth observation, technology demonstration and many other. Following their success in the research and education domains, for which they were developed, CubeSats have attracted the attention of industry thanks to their cost-efficient, yet promising, features.

The primary goal of CubeSats, as it is the case with any miniaturized satellite, is to reduce the cost of orbital deployment. CubeSats are commonly launched as a secondary payload on large launch vehicles. One or several satellites are placed in a dedicated deployment system, which typically accommodates three CubeSat Units, and deployed with a loaded spring when the satellite is in orbit. The deployment system strictly limits the dimensions of any features on the CubeSat surface.

CubeSat antennas perform the same functions as antennas on conventional satellites, such as telemetry and command, communication, navigation or inter-satellite links (ISL). However, most traditional antennas for small satellites are not suitable for CubeSats due to the profile constraints of the deployment system. Two approaches for antenna design are generally adopted. In the first, one or several low-profile antennas are placed on the CubeSat exterior. In the second, deployable antenna structures are used if the CubeSat platform does not offer sufficient dimensions. At low frequencies, the additional space is required to achieve a good radiation efficiency, whereas at high frequencies an increased antenna aperture provides a high gain. In any case, the stowed volume of the antenna may not violate the profile limitation specified by the standard.

This thesis describes different antenna geometries, both low-profile and deployable, which enable several communication aspects of an Internet-of-Things (IoT) constellation of 3U CubeSats in the Low Earth Orbit (LEO). Wideband aperture-coupled patch antennas for TT&C and data downlink in S and X bands are presented in the beginning. A thoroughly investigated shielded-stripline feeding structure enables a wideband circular polarization (CP) with a unidirectional radiation, and demonstrates capabilities such as interference suppression at adjacent frequencies and efficient CubeSat integration. Patch-antenna arrays in L band are then presented, which radiate several independent beams for the capacity increase of an IoT machine-to-machine (M2M) communication system. The high permittivity of the antenna substrates lead to a strong coupling to the 3U CubeSat structure, emphasizing the importance of the antenna placement. Finally, different configurations of high-gain fixed-beam reflectarrays (RA) and

transmitarrays (TA) are for the first time proposed for CubeSat ISL LEO communications in K band. Two novel unit cells are presented for RA and TA antennas, based on coupled loops and aperture-coupled patches, respectively. An axially corrugated CP horn antenna is designed as the feeding element for the arrays. A prototype of this antenna is fabricated using additive manufacturing in aluminum.

The main novelty of the proposed solutions is in their electromagnetic performance, as opposed to most CubeSat antenna designs where the mechanical design is the main achievement. The presented antennas succeed to exhibit a wide bandwidth or a specified radiation under strict size constraints. The performance of all antennas, presented in this thesis, is validated by agreements between the calculation and 3D-simulation results and the VNA and anechoic-chamber measurements of several prototypes.

Résume

Le CubeSat est une catégorie de petits satellites (< 500 kg) qui pèsent quelques kilogrammes et se compose d'une ou plusieurs unités (U) mesurant $100 \times 100 \times 113,5$ mm³. Le CubeSat est apparu comme une alternative à faible coût aux satellites conventionnels et a depuis démontré ses capacités de communication, d'observation de la Terre, de démonstration technologique etc. Suite à son succès dans les domaines de la recherche et de l'éducation pour lesquels il a été développé, le CubeSat a attiré l'attention de l'industrie grâce à ses capacités prometteuses et peu coûteuses.

L'objectif principal du CubeSat, comme pour tous les satellites miniatures, est de réduire le coût du déploiement orbital. Les CubeSats sont généralement lancés en tant que charge utile secondaire sur les grandes fusées. Un ou plusieurs satellites sont placés dans un système de déploiement dédié, qui accueille généralement trois unités de CubeSat. Ils sont déployés avec un ressort lorsque l'orbite visée est atteinte. Le système de déploiement limite strictement les dimensions de tous les dispositifs placés sur le châssis d'un CubeSat.

Les antennes pour CubeSats fonctionnent de la même manière que les celles des satellites conventionnels : elles assurent la télémétrie et la commande, la communication, la navigation ou les liaisons inter-satellites (ISL). Cependant, la plupart des antennes traditionnelles pour petits satellites ne conviennent pas aux CubeSats à cause des contraintes de taille du système de déploiement. Deux approches pour la conception d'antennes sont généralement adoptées. Dans la première, une ou plusieurs antennes à bas profil sont placées sur la surface externe du CubeSat. Dans la seconde, quand la plateforme CubeSat n'offre pas les dimensions suffisantes pour un bon rendement à basses fréquences, ou pour un gain élevé à hautes fréquences, des antennes déployables sont utilisées. Dans les deux cas, les dimensions de l'antenne non déployée ne doivent pas dépasser les limitations de volume.

Cette thèse adresse les géométries d'antennes minces et/ou déployables qui couvrent plusieurs aspects de communication d'une constellation « Internet of Things » (IoT) de CubeSats 3U sur orbite terrestre basse (LEO). La thèse présente plusieurs antennes patch à large bande excitées au travers d'une fente dans le plan de masse pour la télémétrie et la commande (TT&C) ainsi que pour la liaison descendante de données dans les bandes S et X. Une structure d'alimentation triplaque blindée assure une performance à polarisation circulaire dans une large bande avec un rayonnement unidirectionnel. Cette structure permet aussi la suppression des interférences dans les fréquences voisines et l'intégration efficace dans un CubeSat. Des réseaux d'antennes patch en bande L sont ensuite présentés, qui permettent de rayonner plusieurs faisceaux indépendants

pour l'augmentation de capacité d'un système de communication IoT. La permittivité élevée des substrats d'antennes conduit à un fort couplage avec le châssis du CubeSat 3U, mettant en évidence l'importance du placement de l'antenne. Enfin, différentes configurations d'antennes type « reflectarray » (RA) et « transmitarray » (TA) à gain élevé sont proposées pour la première fois pour la communication ISL en bande K pour les CubeSats. Deux nouveaux éléments unitaires sont présentés pour les antennes RA et TA respectivement, basées soit sur des boucles couplées soit sur des patchs couplés par une fente dans le plan de masse. Une antenne cornet corrugué à polarisation circulaire est conçue pour alimenter les réseaux. Un prototype de cette antenne est réalisé en utilisant la fabrication additive en aluminium.

La principale originalité des résultats obtenus est dans la qualité des performances électromagnétiques, contrairement à la plupart des études où l'innovation se trouve dans la conception mécanique des antennes. Les antennes développées possèdent une large bande passante pour une performance de rayonnement améliorée par rapport à l'état de l'art. De plus, ces caractéristiques sont obtenues sous des contraintes géométriques strictes. Les performances de toutes les antennes présentées dans cette thèse sont validées par la comparaison entre les résultats numériques et les mesures de plusieurs prototypes.

Сажетак

CubeSat је тип наносателита који се састоји из запреминских јединица (*U*) димензија 100 × 100 × 113.5 mm³. Сателити типа *CubeSat* представљају економичну алтернативу великих сателита и од свог настанка су демонстрирали функције као што су радио-комуникације, фотографисање Земље, итд. На основу успеха у областима образовања и истраживања, за које су првенствено намењени, *CubeSat* сателити су привукли пажњу индустријског сектора захваљујући својим економичним, али обећавајућим особинама.

Главни разлог за развој наносателита је смањење трошкова њиховог лансирања у орбиту. *CubeSat* сателити се најчешће лансирају као секундарни товар на великим ракетама. Један или неколико сателита, укупне запремине до 3*U*, се постављају у специјалан одељак који избацује сателите помоћу опруге када достигну одговарајућу орбиту. Овакви системи за лансирање строго ограничавају максималне дозвољене димензије *CubeSat* сателита.

Антене на *CubeSat* сателитима врше исте функције као и антене на конвенционалним сателитима. Међутим, већина антена за друге врсте малих сателита нису одговарајуће за *CubeSat* сателите због физичких ограничења система за лансирање. Антене за *CubeSat* сателите се могу поделити у две групе. У прву групу спадају антене ниског профила које се налазе на површини сателита. Антене друге групе користе различите врсте механизама за повећање укупних димензија антене. Такво повећање је неопходно како би се остварио задовољавајућ степен корисног дејства или добитак антене на ниским или високим фреквенцијама, респективно.

Ова дисертација описује неколико антена које омогућавају различите радио-комуникационе функције унутар мреже 3*U-CubeSat* сателита у ниској Земљиној орбити. Неколико широкопојасних микротракастих антена у *S* и *X* фреквенцијским опсезима, спрегнутих са водом за напајање путем прореза, су представљене на почетку. Оклопљена структура за напајање у техници асиметричних тракастих водова омогућава код антена овог типа широкопојасну кружну поларизацију израчених таласа, потискивање интерференције из суседних фреквенцијских опсега и ефикасну интеграцију са металном *CubeSat* структуром. Затим су представљени низови микротракастих антена у *L* опсегу који зраче неколико независних снопова у циљу повећања капацитета радио-комуникационог система. Висока пермитивност супстрата изазива јаку спрегу антена са структуром сателита, због чега се положај антене на *CubeSat* структури мора узети у обзир.

Последњи део ове дисертације предлаже нове конфигурације антенских низова великог добитка у *K* опсегу за радио-комуникацију између *CubeSat* сателита, типа *reflectarray* и *transmitarray*. По један елемент је дизајниран за сваки од ових низова, на бази спрегнутих микротракастих петљи и микротракастих антена спрегнутих помоћу прореза. Кружно поларисана левак антена је дизајнирана специфично за напајање датих низова. Прототип левак антене је направљен помоћу технике 3*D* штампе алуминијумског прашка.

Електромагнетске карактеристике антена описаних у оквиру ове дисертације представљају њихов главни новитет, насупрот већини досадашњих *CubeSat* антена, чији допринос лежи у механичком дизајну. Описане антене испољавају широкопојасне карактеристике упркос строгим ограничењима укупних димензија. Поклапање резултата нумеричких прорачуна и симулација са једне стране, те мерења у анехоичној комори путем векторског анализатора мрежа са друге стране, потврђује рад свих антена представљених у оквиру ове дисертације.

Кључне речи: 3*D* штампа, *CubeSat*, антена, антенски низ, међу-сателитска веза, микротракаста антена, мрежа за напајање, наносателит, сателитске радио-комуникације, спрега путем прореза, тракасти вод, широкопојасни

Acknowledgment

I would like to thank the members of the jury, Prof. Jose Encinar, Prof. Cyril Luxey, Prof. Romain Fleury, and the jury president, Dr. Sidi-Rachid Cherkaoui, for their participation in the oral exam of this thesis. Their useful comments and suggestions have improved the quality of the final manuscript and have sparked new ideas for the future work on this topic. I am thankful to Astrocast for supporting the work on this thesis, and I especially enjoyed working with Mehrdad, Ester and Kevin during this time. The friendly ACI team at EPFL, notably José, Jean-Marie, Jean-Marc, performed the fabrication of many prototypes, and their work is greatly appreciated. I wish to express my gratitude to Tomislav and Antoine of SwissTo12, and Frank, Przemyslaw and Alberto of Viasat, for their help and advice during prototype measurements.

Working on a PhD thesis is a stressful task, unless your thesis advisor is Anja Skrivervik. Her scientific and diplomatic skills, devotion to PhD students and a warm personality have allowed me to be optimistic and productive, while enjoying my work in the previous years. Together with Prof. Juan Mosig, she created a friendly, supportive atmosphere in LEMA, and afterwards MAG, which I will always remember for the scientific and inter-cultural exchanges during many social events. A big thank you goes to all MAG, LEMA and LWE members, with whom I had a big pleasure working and interacting over the past four years. For the most of this period, my office mates were two wonderful people, Danelys and Anton. Known as 'The Skriverviks', the three of us had many jokes and interesting talks, and they were the main people responsible for my good mood. I also wish to thank Santiago for his unconditional assistance and scientific discussions we had in the early years of my PhD.

The most valuable aspect of the PhD at EPFL is the chance to meet people from all around the world and learn about new cultures, while challenging your views at the same time. Among many others, I mostly wish to thank my Greek friends and the Satellite team, for many inspiring discussions and relaxing events. Over the years, however, I have received the largest support in every aspect from the Serbian community in Lausanne, especially the notorious group 'Kafana na Balkanu'. They played a big role in this thesis, and for that, they have my sincere gratitude.

During the PhD, one person went alongside me through every achievement and obstacle we encountered together. For the love you have given me every single day, Katarina, you deserve to share this success as your own.

My family was and continues to be my biggest support. In spite of having spent over two decades in education, my family has taught me the most valuable lessons in life. Mama, Tata, Milena, Jovana, Luka, to you I dedicate this thesis.

Acronyms and Abbreviations

ADCS	Attitude Determination and Control System
AR	Axial ratio
COTS	Commercial off-the-shelf
CP	Circular polarization
DMLS	Direct laser metal sintering
EM	Electromagnetic
FEM	Finite-element method
FN	Feeding network
FSS	Frequency-selective surface
FTBR	Front-to-back ratio
GNSS	Global navigation satellite system
IoT	Internet of Things
ISL	Inter-satellite link
LEO	Low Earth orbit
LP	Linear polarization
M2M	Machine to machine
MoM	Method of moments
PEC	Perfect electric conductor
P-POD	Poly-picosatellite deployer
RA	Reflectarray
RHCP/LHCP	Right/left-hand circular polarization
SO	Space operations
SLL	Sidelobe level
TA	Transmitarray
TT&C	Telemetry, tracking & command
U	Unit
WG	Waveguide

Contents

1. General Introduction

1.1. The CubeSat Standard

CubeSat is a standard for modular nanosatellites, defined by the CubeSat Design Specification (CDS), also known as the CubeSat standard [1]. A CubeSat is composed of multiple volume units (U) of 100 x 100 x 113.5 mm^3. The CubeSat size varies from 0.25U to 27U, and some common form factors are shown in Figure 1.1 [2]. Strictly speaking, a nanosatellite is defined in terms of mass (not volume) and implies any spacecraft with mass between 1 kg and 10 kg [3]. The two definitions are sometimes misleading since CubeSats in general can have a mass from less than 1 kg to 30 kg, but a majority falls within the nanosatellite mass range. The two terms are even sometimes mistakenly used as synonyms, due to the popularity of the CubeSats in the recent years.

The CubeSat was invented in 1999, by Professor Jordi Puig-Suari of California Polytechnic State University and Professor Bob Twiggs of Stanford University, as an academic project that allowed graduate students to design and operate a small spacecraft [4]. The 100-mm cube was deemed sufficient to accommodate basic satellite components – a communication payload, solar panels and a battery. The first CubeSat was launched in 2003, and over 1000 CubeSats are deployed to orbit to date, with over 80 destroyed in failures of launch vehicles [2]. The majority of CubeSats were developed for academic and educational purposes until 2013, when the CubeSat number starts growing rapidly, a majority being for commercial applications. The development cost of early CubeSats was reduced by using commercial off-the-shelf (COTS) components for onboard systems, and conducting only the most important space-eligibility tests. New CubeSats increasingly use high-performance custom-made modules, which include communication, propulsion, antennas, etc., specifically developed for certain missions [2].

CubeSats typically serve purposes such as Earth observation, IoT communication, amateur radio, etc [3], [5]. They present a cost-efficient opportunity to validate a new technology or even perform biological experiments in space [6]. Several countries used CubeSats as their first national satellite. Two 6U CubeSats were successfully used in 2018 during a mission to Mars, with more interplanetary CubeSats planned [7].
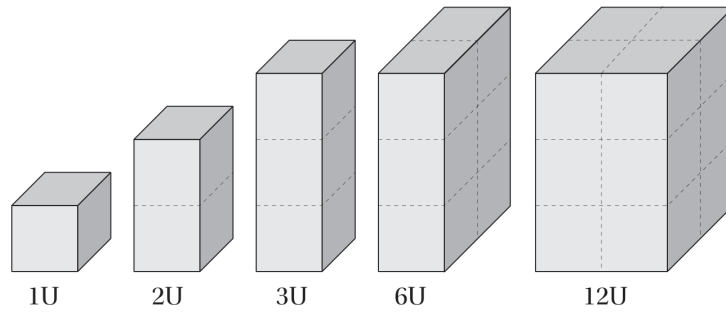
Figure 1.1. CubeSat models with different common form factors.

The main motivation for the development of any nanosatellite is the cost reduction of the orbital deployment. CubeSats are typically launched to Low Earth Orbit (LEO) as a secondary payload of larger missions or from the International Space Station [3]. A CubeSat dispenser (or deployer) system, called the Poly-PicoSatellite Orbital Deployer (P-POD), was developed simultaneously with the CubeSat standard [1]. The system is an aluminum compartment that accommodates a 3U CubeSat (or multiple smaller form-factor satellites) with a hatch and a spring mechanism. Following the hatch opening, the system deploys nanosatellites by simply ejecting them into orbit using a loaded spring, located at the bottom of the compartment. Most modern dispensers operate with a similar principle. The dispenser strictly limits the maximum feature dimension on the spacecraft surface. Therefore, any deployable components (solar panels, antennas, magnetometers) must be stowed within this volume during launch, with a typical profile margin from 6.5 mm to 9 mm.

The total number of launched and announced CubeSats is presented in Figure 1.2, versus their form factor. The first CubeSats were typically 1U. It was shown over time that a 3U CubeSat offers a good compromise between the cost and the available volume for onboard components, making it the most popular form factor to date. As the CubeSats in the recent years start to perform functions that are more complex, the 6U size is also gaining in popularity.

1.2. CubeSat Antennas

Early CubeSats typically communicated in VHF, UHF and S bands due to good propagation characteristics at those frequencies and the availability of COTS components and modules. Since then, the CubeSat communication and other RF functions (e.g. RADAR) are increasingly performed at higher frequencies reaching Ka band, with some demonstration missions for optical communications [8]. The number of reported CubeSat communication modules versus the operating frequency is shown in Figure 1.3.
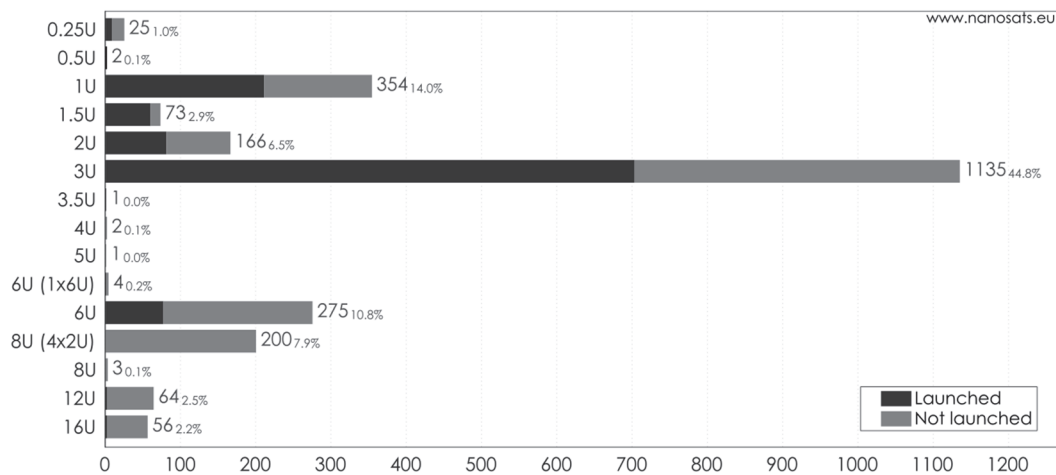
Figure 1.2. Launched and announced CubeSats versus the form factor [2].
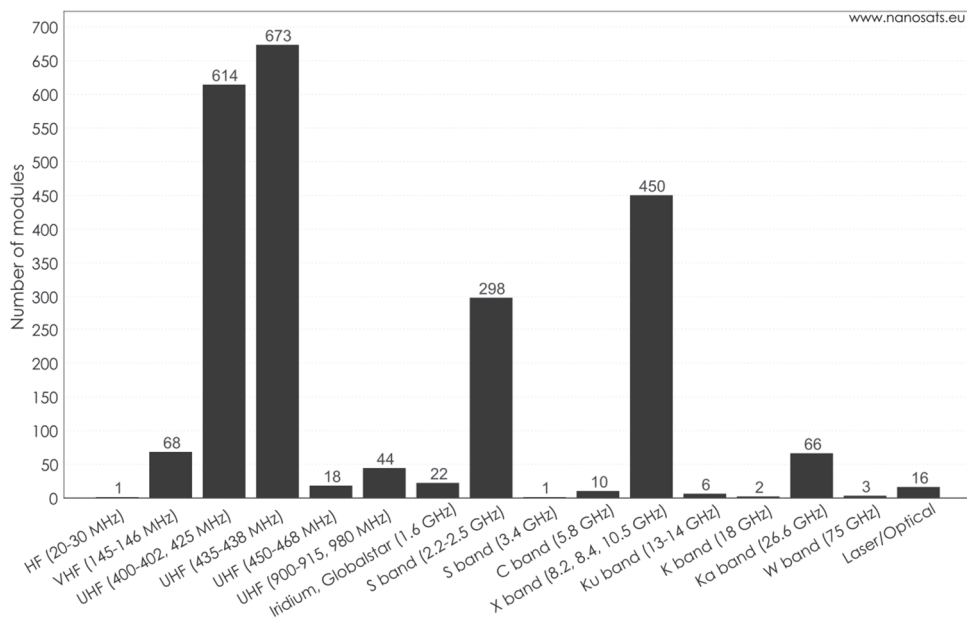
Figure 1.3. Number of reported CubeSat communication modules versus the operating frequency band [2].

A known tradeoff is considered when selecting the communication frequency of a CubeSat mission – lower frequencies generally offer a narrow bandwidth/low data rate and low path losses, and vice versa. The CubeSat antenna dimensions, complexity and the achievable performance also greatly depend on the frequency choice. Thus, the antenna type is a very important factor to be taken into account during the mission design. Antenna dimensions are proportional to the wavelength at the operating frequency. The antenna size normalized to the free-space wavelength, also known as the electrical size, often determines what kind of radiation can be

expected. Typically, electrically smaller antennas ($< \lambda_0$) exhibit a wide beamwidth and low gain values, whereas electrically large antennas ($> 5\lambda_0$) radiate high-gain narrow or shaped beams.

The electrical size of an entire 1U CubeSat platform is approximately $0.05\lambda_0$ to $12\lambda_0$ from VHF to Ka band, where CubeSats communication is performed. This suggests that the antennas, used across this vast spectrum, will have very different geometries to conform to the CubeSat chassis and achieve the specified performance. Typical antenna geometries, along with several exotic examples, are presented in Figure 1.4 versus the operating frequency. The 1U, 2U and 3U CubeSat dimensions are denoted in the figure for comparison.
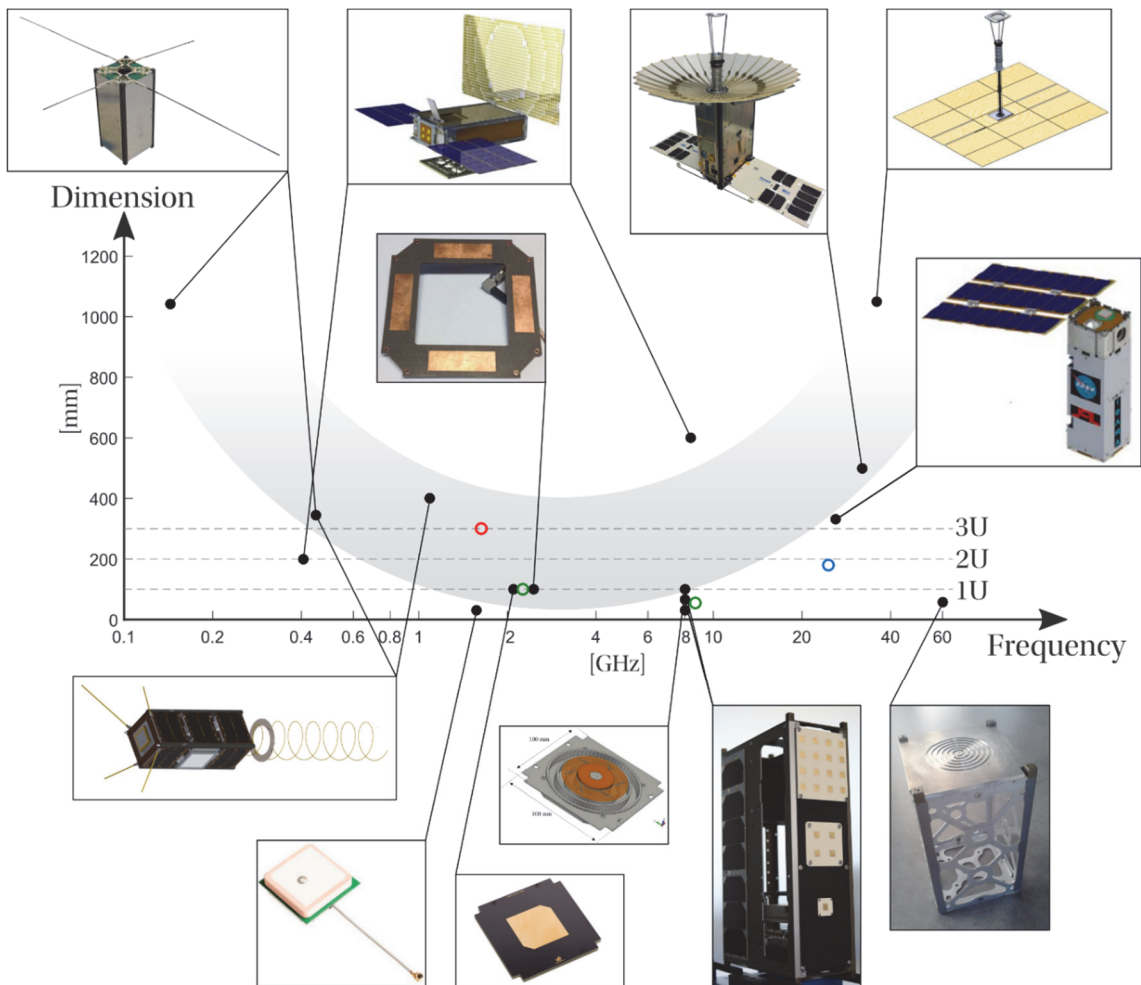
Figure 1.4. Examples of CubeSat antennas throughout the frequency spectrum. (Top, left to right) Deployable dipoles [9], MarCO reflectarray and planar UHF antenna [7], patch-antenna array [10], mesh reflector [11], one-meter reflectarray [12], ISARA [13]. (Bottom, left to right) GOMX-3 turnstile and helix [14], COTS GNSS patch, CP patch [15], isoflux patch with chokes and parasitic dipoles [16], patch-antenna arrays [17], bull's eye antenna [18].

The figure should be considered in combination with the number of communication modules in Figure 1.3 to get an insight into the representation of certain antenna geometries. It is by no means exhaustive, and more examples from the literature are presented throughout this thesis and discussed in detail at the beginning of every chapter. Colored markers in the figure represent the antennas developed in the scope of the thesis, where the colors correspond to the labels in Figure 1.7.

A general trend is evident in Figure 1.4, with relatively small antennas in L and S bands, and an increase in antenna size at the lower and higher frequencies. However, the size increase is driven by different mechanisms at the two frequency extremes. Low-frequency antennas (dipole, monopole, turnstile) require large dimensions simply to achieve a resonance with a good radiation efficiency. On the other hand, the large antenna apertures for the high-frequency antennas (array, reflector, reflectarray, etc.) compensate large path losses with a high gain or provide narrow beams for applications like RADAR [11], [12].

The CubeSat in-orbit orientation with respect to Earth (attitude) is determined and maintained by the attitude determination and control system (ADCS) [19]. The ADCS relies on sensors such as sun sensors, star trackers, gyroscopes, etc., and actuators such as thrusters, momentum wheels, moment gyros, etc. The process can be assisted by a purely passive attitude control using the gravity gradient or the Earth's magnetic field, depending on the specific CubeSat shape [20]. Early 1U CubeSats did not include an ADCS and they required near-omnidirectional antennas to sustain the communication link, regardless of the orbital attitude. Modern, miniature types of ADCS that are suitable for CubeSats achieve three-axis stabilization up to within 1°. Accurately maintaining the CubeSat orientation is crucial for the utilization of directive antennas or arrays. A comparison between the two antenna-ADCS scenarios is illustrated in Figure 1.5.
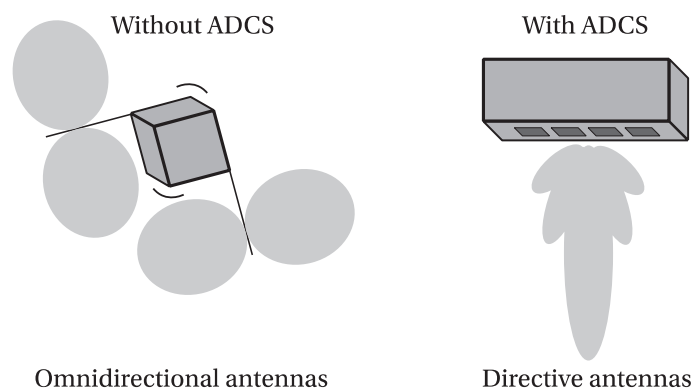
Figure 1.5. A comparison of two CubeSat communication scenarios – with or without ADCS – and examples of associated antenna geometries.

1.3. Objectives and Thesis Organization

1.3.1. Motivation and Objectives

The research in this thesis was done in collaboration with Astrocast – a Swiss start-up company that builds and operates an IoT CubeSat constellation in LEO [21]. The company was founded in 2014 by the team that successfully developed and launched the SwissCube, EPFL's 1U research CubeSat, which holds the world record for the longest continuous operation of a CubeSat (over 10 years at the writing time of this thesis) [22].

The aim of the Astrocast network of CubeSats is to provide bidirectional, cost-efficient communication to remote Earth areas in L band. The network nodes are 3U CubeSats, having their long axis aligned with the orbital velocity vector, with a large face oriented towards Earth at all times. Although this attitude is less advantageous in terms of passive stabilization with the gravity gradient, it allows more planar antennas to be placed on the CubeSat surface facing Earth. Each satellite is equipped with an accurate ADCS and a small propulsion module for maintaining the attitude and the orbital velocity over time. The CubeSats inside the network are uniformly distributed over several polar orbital planes. An inter-satellite link (ISL) is established by each satellite with two adjacent satellites in the same orbital plane [23]. More details about the configuration of the constellation can be found in Chapter 4.

The data is sent through the network using different frequencies, protocols and data rates [24]. The system is organized as shown in Figure 1.6. The CubeSats provide low-data-rate bidirectional M2M L-band links to a large number of user terminals within their coverage area. Each CubeSat radiates several independent beams through dedicated M2M transceivers, to increase the total system capacity. The aggregated user data is then sent through a high-data-rate K-band ISL among CubeSats within the same orbital plane. Once the data reaches the satellite, which has a connection established with the ground station, the data is downlinked to the Earth using a high-capacity X-band channel.

A separate Telemetry, Tracking and Command (TT&C) system, operating in S band, constantly monitors and performs orbital station-keeping of the CubeSat constellation. The satellites are also equipped with GNSS receivers, for accurate positioning.

Each of the described functions requires specialized antennas onboard every CubeSat platform. The design specifications for individual antennas are drastically different, based on the requirements of the corresponding functions. Circular polarization (CP) is used in all the mentioned links. Other RF specifications include the operating frequency, radiation beamwidth, maximum gain, impedance matching, and frequency bandwidths in terms of the return loss, gain and axial ratio (AR).
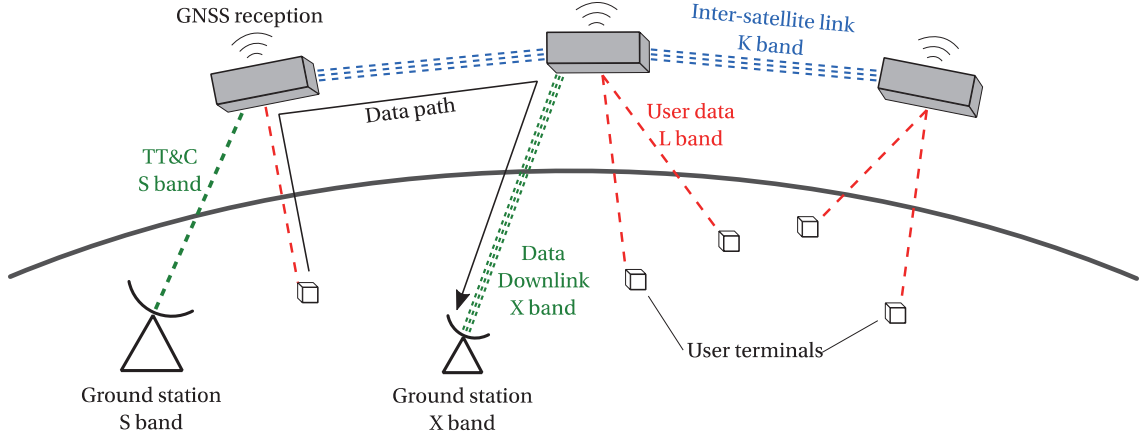
Figure 1.6. The overview of the CubeSat network (constellation).
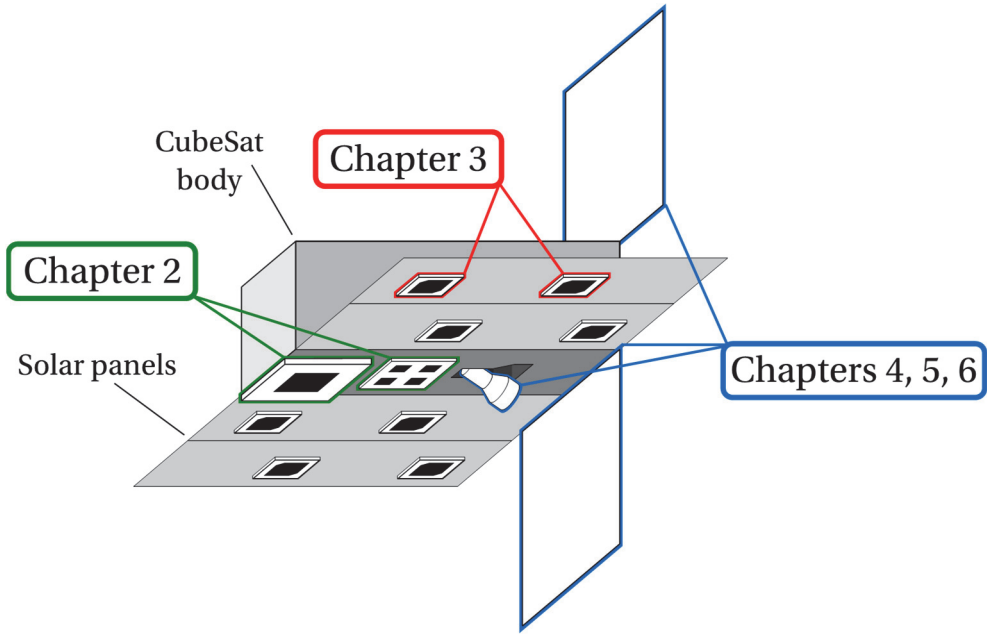
Figure 1.7. A sketch of the antennas presented in this thesis, placed on a 3U CubeSat.

The goal of this thesis is to propose novel antenna geometries, which satisfy the mentioned RF specifications under the strict volume constraints of the CubeSat standard, primarily the thickness limitation. Depending on the operating frequency, the size constraints have a different impact on the antenna design in terms of the electrical size. The antenna placement on the exterior of the satellite may in no case violate the thickness specified by the used dispenser system. Two types of designs are considered, depending on the function – reliable and robust low-profile antennas on the CubeSat surface for the critical functions such as TT&C, and deployable antenna arrays in cases where additional gain is required.

1.3.2. Thesis Outline

Each chapter of this thesis opens with a short literature review of the CubeSat antennas having the same, or closely related, function and geometry as the designs presented in the chapter itself. The 3U CubeSat platform, considered for all the antenna designs in this thesis, is shown in Figure 1.7. The figure indicates the locations of the antenna design within the thesis. The operating frequency and the size of the antennas is also indicated in Figure 1.4 with the same colors as in Figure 1.7. The thesis is organized as follows:

Chapter 2 presents several low-profile wideband CP stripline-fed aperture-coupled patch antennas in S and X bands. A shielded asymmetric-stripline structure enables a wideband element matching in spite of the CubeSat profile limitations at S-band frequencies [C1]. A detailed study of the electric field inside the shielded-stripline cavity helped to explain the underlying mechanisms for wideband operation, outlining a set of design rules for this type of antennas [J1]. The same approach is demonstrated on X-band aperture-coupled patch antennas and arrays, having simpler feeding networks. It is further shown how the cavity resonances can be used to suppress interference in an adjacent frequency band. The chapter proposes a novel integration method of the aperture-coupled patch antennas into the CubeSat metallic structure.

Chapter 3 describes a patch-antenna system for CubeSat duplex IoT communication in L band and proposes two- and four-element array configurations, where the elements are placed on the metallic backside of deployed solar panels. The antenna system radiates several independent beams to increase the IoT system capacity. The high-permittivity substrate, used for antenna miniaturization, causes a strong coupling with the asymmetric 3U ground plane. The resulting distortion of the radiation pattern demonstrated the influence of the antenna placement on the CubeSat [C2]. The chapter finally presents a dual-band dual-fed stacked-patch antenna in L and S bands, as means of optimizing the limited area on the CubeSat surface [C3]. Several feeding networks are compared, showing that the choice of the feeding method does not significantly affect the CP-gain bandwidth of the stacked-patch antenna.

Chapter 4 illustrates how a specific flying formation of the CubeSat network can be used to simplify the conventional complex high-gain ISL antennas. Design requirements are discussed for the considered CubeSat LEO constellation, in terms of the beam-scanning angle and the gain, versus the total number of CubeSats and the antenna aperture efficiency. The chapter for the first time proposes deployable fixed-beam reflectarray (RA) and transmitarray (TA) antennas for ISL applications in K band. Several RA and TA configurations are presented for 3U CubeSats.

Chapter 5 presents the elements of the RA and TA antennas from Chapter 4 – two novel RA and TA element geometries and a 3D-printed CP axially corrugated feed horn antenna. The foundations of the element-rotation technique and the unit-cell simulation environment are presented first. The coupled-loops RA element is then designed starting from the conventional split loop, significantly improving the CP reflection bandwidth while not compromising the

complexity [J2]. Furthermore, the slot shape of the previously reported aperture-coupled stacked-patches TA element is modified, which allowed reducing the number of metallic layers from five to three [J3]. Both proposed elements exhibit an excellent CP bandwidth with a very low profile, which is one of the main prerequisites for CubeSat ISL applications. A CP feed chain is designed as the feeding element of the RA and TA antennas, in which the axial corrugations improve the off-axis cross-polarization, and a septum polarizer enables a dual-CP operation. The measurement results of the horn prototype, fabricated using additive manufacturing in aluminum, confirm the predicted performance [C5].

Chapter 6 opens with a description of the array synthesis and analysis procedures, based on the simulation results of RA and TA elements and the feed horn presented in Chapter 5. Both antennas exhibit a wideband high-purity CP radiation due to the element-rotation technique used to achieve the phase shifting over the array surface. Instead of a known analytical formula, a simple technique is used for the generation of the array geometry, eliminating the phase errors for larger elevation incidence angles. The feed's incident radiation on the array is combined with the response of every unit cell to obtain the scattered fields on the array, which are then used to obtain the far fields of the full array. The calculation results of the two 900-element RA and TA antennas show 1-dB CP-gain bandwidths of ~6% with total antenna efficiency values exceeding 60%. The antenna prototypes will be evaluated in January 2020. The measurement results of two smaller-scale prototypes confirm the wideband CP performance of the RA and TA elements, in spite of the sub-optimal aperture efficiency.

Chapter 7 concludes the thesis, outlines the main results and discusses the future trends and challenges of CubeSat antenna design.

1.3.3. Research Projects

The work performed in the scope of this thesis was mainly funded by two Swiss Innovation Agency (Innosuisse, former CTI) projects, with Microwave and Antenna Group (MAG) as the research partner and Astrocast as the implementation partner. The aim of the first project, titled CubeSatCom, was the development of low-profile wideband patch antennas in S and X bands for TT&C and potentially for data downlink. The results produced during this project are presented in Chapter 2.

The second, more encompassing project was organized in the same manner and resulted in the development of the M2M antennas in L band and a case study on the K-band high-gain ISL antennas. Chapters 3 through 6 present the main results of this work. Additional work was performed in the scope of this project to help design several L- and S-band antennas for the first two precursor missions and the first orbital plane of CubeSats developed by Astrocast. This work is considered less interesting from a research point of view and it is therefore not included in this thesis.

The author of this thesis, together with the thesis supervisor, co-supervised several semester and bachelor student projects listed below. The work for most projects was performed in coordination with Astrocast and tackled several issues related to different parts of the CubeSat constellation. The results of the student projects were not directly included in this thesis, although they often helped the author of this thesis to get a better understanding of the problematics or served as the starting point for future work. The students' devoted work is greatly appreciated and it resulted in a successful project in all cases. The project reports can be found in the corresponding references. The student projects are:

[SP1] **X-band Antenna for CubeSat Satellite** – Joana Maria Llull Coll – 2016.

[SP2] **L-band Antenna for CubeSats** – Manuel Vonlanthen – 2017.

[SP3] **Terminal Antenna for Space Applications in L band** – Marina Ramos Cuevas – 2018.

[SP4] **Isoflux Patch Antenna in X band** – Carlos Megías Núñez – 2019.

[SP5] **Patch Antenna Design for the EPFL Rocket Team** – Alexandre Devienne – 2019.

For the duration of the doctoral studies, the author of the thesis was involved with several other research projects, not directly related to the thesis topic. The results of the work are not included here, since they are out of the scope of this thesis. Nevertheless, they served the author to get an insight into each of the corresponding domains of antenna research. The topics include:

- **SATCOM arrays** – a project to design mechanically steered high-gain waveguide arrays in Ku and Ka bands, to be fabricated using additive manufacturing techniques
- **Implantable antennas** – an initial study and a design of a cranial implantable antenna, to be used as a part of a potential system for wireless extraction of brain signals [C6], [C7]
- **THz sensors** – design of dipole antennas and coplanar-waveguide baluns for VO2 sensors at THz frequencies [C4]

2. Low-Profile Wideband CubeSat Antennas

CubeSats require telemetry, tracking and control (TT&C) antennas to receive telecommand signals from the ground stations and to downlink telemetry signals. As these signals are crucial for the satellite operation, the TT&C antennas need to be reliable. In addition, the antennas need to achieve a full spherical coverage to provide a link with ground stations regardless of the CubeSat's orientation, especially in the early stages following deployment.

A thorough review of existing designs and technologies is performed in the first part of this chapter, showing a variety of different and innovative designs, for the frequency range spanning from VHF to X band. A general trend is observed, where the antenna solutions exhibit an increase in performance and complexity with the increase in frequency: from simple deployable monopoles in UHF band to isoflux patch antennas in X band. The S-band frequencies seem to show a large potential for compact and at the same time performant designs, suitable for CubeSats. A number of solutions was proposed in the literature to tackle this trade-off for conventional small satellites, usually lacking one or several aspects required for CubeSat applications.

The goal of this chapter is to present a systematic design process and a detailed analysis of several low-profile wideband antennas for CubeSats in S and X bands. An aperture-coupled patch antenna is selected for this application, due to its wideband performance. The disadvantages of an initial microstrip-fed antenna are addressed and the design is modified for the CubeSat environment by introducing an asymmetric-stripline feeding network. After carefully investigating the effects of the field distribution inside the stripline, a significant performance improvement is obtained by a metallic enclosure of the stripline feed. The conditions and limitations under which this improvement is possible are studied in detail. The resulting cavity resonances can be harmful if they appear within the operating bandwidth. It is shown how the same resonances can be used to suppress the radiation in an arbitrary adjacent frequency band. The chapter further proposes an elegant method of integrating this type of antennas into the

CubeSat chassis, reducing the antenna profile on the exterior of the spacecraft. The efficient technique for performance improvement is finally implemented on patch elements and arrays in X band, demonstrating its potential for antennas having simple feeding networks.

2.1. Review of CubeSat TT&C Antennas

The most commonly used orbital deployment system for CubeSats is the Poly-PicoSatellite Orbital Deployer (P-POD), initially developed for the first CubeSats at Cal Poly [25]. The system is essentially an aluminum compartment that fits a 3U CubeSat (or multiple smaller form-factor satellites) with a hatch and a spring mechanism. Following the hatch opening, the system deploys nanosatellites by simply ejecting them into orbit using a loaded spring, located at the bottom of the compartment. The satellite orientation with respect to the Earth (i.e. satellite attitude) is undefined immediately after the ejection and ADCS is activated at this stage. The purpose of the ADCS system is to determine the current satellite attitude and rotate the spacecraft to a favorable orientation using a set of sensors and a, respectively [26].

The TT&C systems are the first to establish the communication with the ground stations after the orbital deployment. It is crucial for this link to be reliable, as it supports the attitude control system, and therefore, all subsequent satellite operations depend on the success of this stage [26]. As it is also the case with many other satellite systems, the key system component is the antenna. The fundamental goal of any TT&C antenna, or an antenna system, is to be able to communicate with the ground stations, regardless of the satellite attitude. This is typically achieved through one of the two approaches:

- Omnidirectional coverage by a single low-directivity antenna, or
- Sectorial coverage by a set of multiple, more directive, antennas placed on several spacecraft faces [8].

The choice of a suitable antenna configuration depends mostly on the TT&C operating frequency. As a rule of thumb, the lower-frequency systems use a single antenna, whereas several antennas are used at higher frequencies, as their reduced size allows for multiple antennas onboard a CubeSat. The antenna designs are compared in the following sections and sorted with respect to the operating frequency. The designs include standard geometries, as well as several exotic, specialized solutions. It should be noted that not all presented antenna solutions perform exclusively TT&C functions, but are mentioned here since they accurately represent their respective antenna classes, very often seen on CubeSats. Other than the examples presented in this thesis, there exists a large and continuously growing number of publications which introduce innovative solutions for modern CubeSat missions.

2.1.1. VHF/UHF Bands

The frequencies of VHF and UHF bands have been the most popular choice for CubeSat communication since the standard's development [2]. For most early CubeSats, it was also the only means of communication with the ground, and therefore included the telemetry and telecommand signals. The CubeSat mission designers have traditionally selected these bands for practical reasons: the good characteristics of the propagation channel and the availability of COTS components operating at these frequencies. However, the free-space wavelengths at the VHF and UHF radio bands, as defined by the IEEE [27], fall in the range from 300 mm to several meters. This makes the design of an efficient radiator a challenging task, having in mind the 1U-CubeSat size constraint of 100 mm.

To overcome this challenge, the deployable wire-based antenna structure is usually chosen [3]. Namely, the wire antenna is wrapped around the CubeSat or wound inside the spacecraft chassis during the launch, conforming to the standard maximal dimensions. After the placement in orbit, the antenna structure is deployed using a release mechanism, into its final, functional form. The antenna geometries are typically in the form of monopole, dipole, turnstile, and helix antennas.

Among the first batch of CubeSats, launched in 2003, was the *XI-IV* satellite from the University of Tokyo [28]. The CubeSat demonstrated the space use of a COTS camera and sent the data at 437 MHz (UHF). A linearly polarized dipole antenna is seen in Figure 2.1(a), as a wound wire at the exterior of the CubeSat. To further simplify the design and reduce the cost, many early CubeSats use an actual metallic tape measure as the antenna, due to its flexibility. One example is the *PhoneSat* built by NASA Ames Research Center, shown in Figure 2.1(b) [29]. *PhoneSat* uses the unmodified COTS smartphone and Arduino platforms, and communicates at 437 MHz (UHF). The tape-measure monopole antenna is stowed inside the chassis and automatically deploys after the CubeSat ejection. Two circularly polarized deployable antenna solutions are shown in Figure 2.1(c) – a high-gain helix antenna and a turnstile antenna, mounted on a *GOMX-3* CubeSat from GOMSpace [14].

VHF/UHF-dual-band antennas have also been investigated. In [30], the first and third harmonics of a monopole antenna were excited at 130 and 390 MHz to obtain saddle-shaped and hemispherical patterns, respectively. The physical structure of a passive attitude-stabilization system of a 3U CubeSat was used as an antenna in [20]. A single-port dual-band performance was enabled by physical band-stop filters positioned on the metallic strips. A highly-miniaturized planar UHF antenna is presented in [31].

2.1.2. S Band

The S-band frequencies include the Space Operation (SO) bands (2.025 – 2.11 GHz uplink, 2.22 – 2.29 GHz downlink), and the Amateur-Satellite Service band (2.4 – 2.45 GHz, the so-called

(a)

(b)

(c)
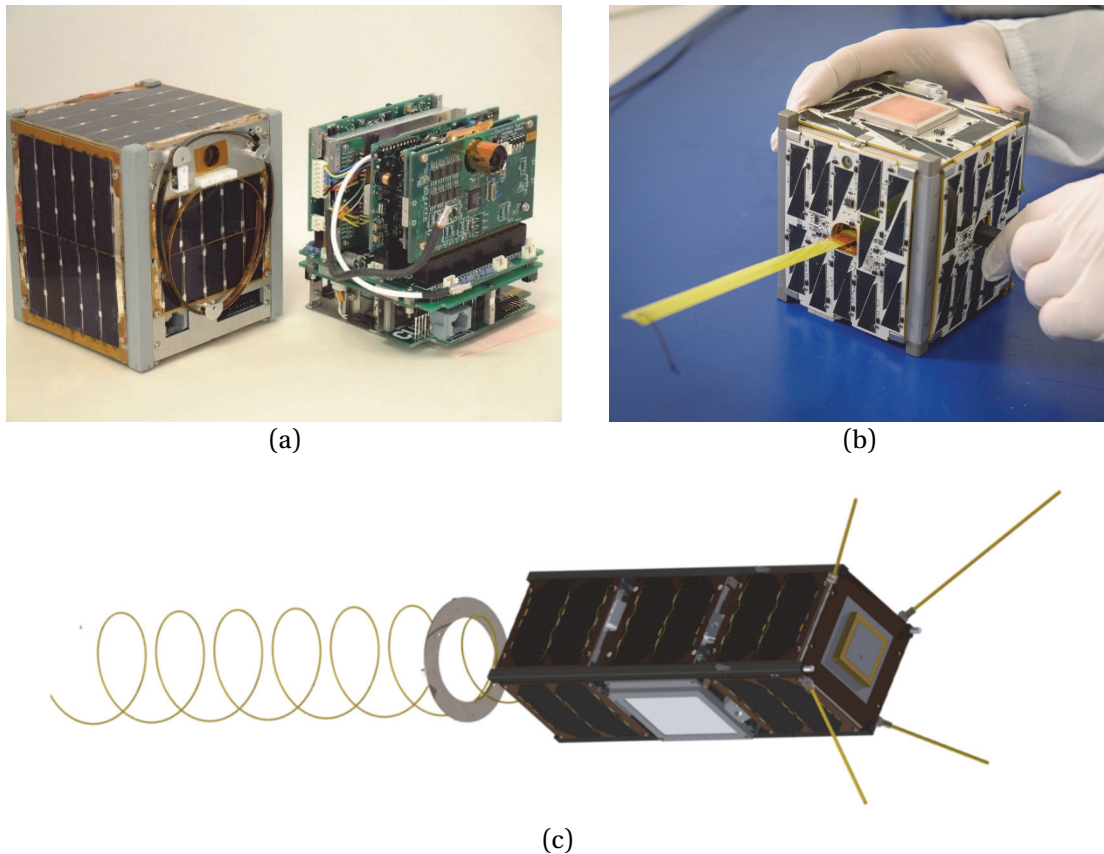
Figure 2.1. Deployable VHF antennas for CubeSats. (a) Stowed dipole antenna (left) and the interior of the 1U *XI-IV* CubeSat (right) [28]. (b) Monopole tape-measure antenna on the 1U *PhoneSat*, with a GPS patch antenna visible [29]. (c) High-gain helix antenna (left) and a turnstile antenna (right) on a 3U *GOMX-3* CubeSat [14].

13-cm band), allocated by the International Telecommunication Union (ITU) [24]. The SO bands are widely used for TT&C purposes and the amateur band serves for the CubeSat data downlink.

Various types of planar antennas are popular in this frequency range due to their low profile and reliability, as they require no deployment [3], [32], [33]. An inherent property of conventional patch antennas is their narrow bandwidth, and a majority of CubeSat patch antennas operates at a single frequency. Having a multiband or a wideband single-port antenna is an advantage, as the total number of antennas required for duplex communication is reduced. If a wide impedance bandwidth is achieved, it is another challenge to obtain good polarization properties across the same bandwidth, typically in terms of AR for CP antennas. Other common antenna types for small satellites include helix antennas and patch-excited-cup antennas [5]. These antenna geometries are not appropriate for CubeSats in S band without significant modifications, as their profile is significant compared to the CubeSat body.

Due to their low profile, traditional patch antennas are inherently suitable for any CubeSat operating in S-band. Very often, however, the conventional designs must be adapted for the particular needs of a specific CubeSat mission. An example is the patch antenna system in [34], where four LP patch antennas are sequentially excited to achieve CP. The antenna system is built with a gap at its center to accommodate a camera lens, as seen in Figure 2.2(a). A dual-CP S-band patch antenna, fed by a branchline coupler, is designed for CubeSats and presented in [35]. Capacitive coupling and a matching network based on chip inductors provide a dual-band performance, both in impedance and AR.

A variety of other, low-profile antenna geometries are proposed for CubeSats in S band. A CP crossed-dipole antenna for CubeSats, operating in the SO bands, is presented in [36]. This antenna type normally requires a metallic reflector at a distance of $\lambda_0/4$ to achieve a unidirectional radiation pattern. In this case, an artificial magnetic conductor is placed close to the dipole elements resulting in a significant profile reduction, while preserving a wideband performance. The antenna prototype is presented in Figure 2.2(b). A miniaturized slot antenna system for micro/nano-satellites in S band, shown in Figure 2.2(c), is introduced in [37]. The radiating slots are highly integrated with the metallic surface and backed by a cavity inside the satellite.

2.1.3. X Band

The TT&C communication in X band is interleaved with the payload data in the Space Research and Earth Exploration Services bands (7.145 – 7.235 GHz uplink, 8.025 – 8.5 GHz downlink), as allocated by the European Cooperation for Space Standardization (ECSS) [38]. The increase in frequency simultaneously allows a larger data rate and a greater freedom in antenna design, as the wavelengths in this band are in the order of 40 mm. Two examples that demonstrate how this freedom can be used are isoflux patch antennas shown in Figure 2.3 [16].

<div style="text-align:center">(a)   (b)   (c)</div>
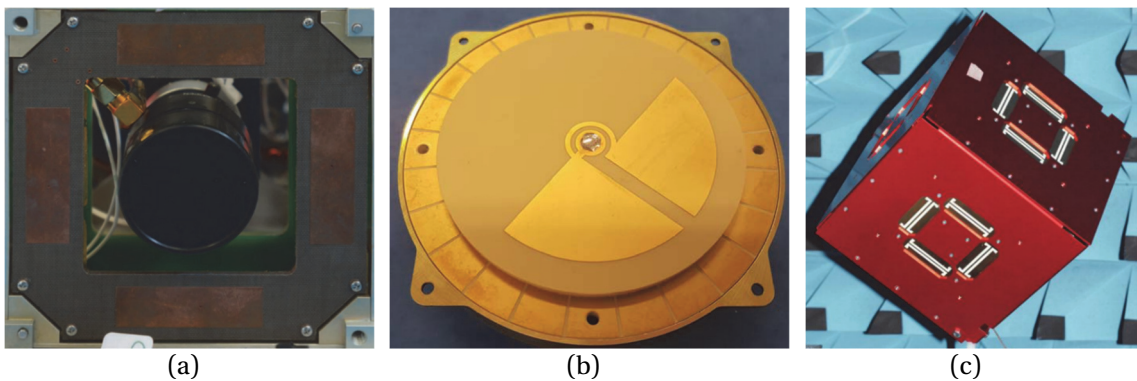
Figure 2.2. S-band CubeSat antennas. (a) Patch antenna array around a central camera lens [34]. (b) Crossed-dipole antenna over an artificial magnetic conductor [36]. (c) Miniaturized slot antenna system [37].
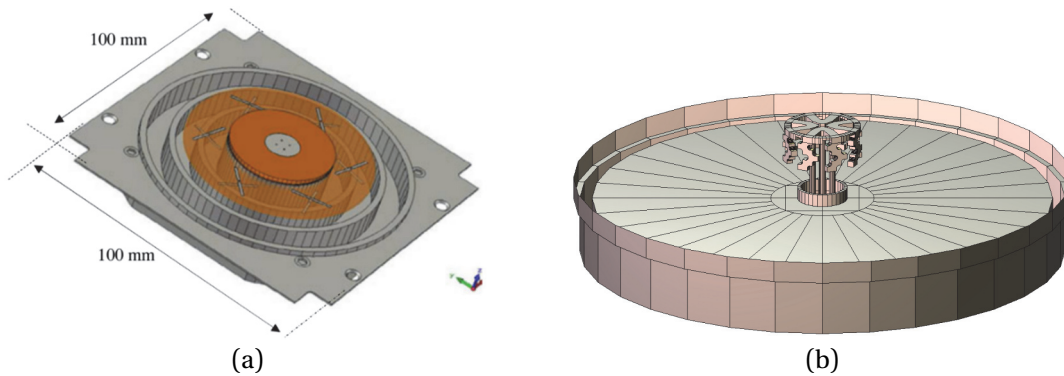
Figure 2.3. X-band isoflux CubeSat antennas. (a) Patch antenna with 12 parasitic dipoles over a corrugated ground plane [16]. (b) A miniaturized helix antenna [39].

Multiple crossed-dipole elements and deep concentric corrugations yield low AR values and an isoflux pattern suitable for LEO satellites. Other designs include the miniaturized helix antenna over a corrugated ground plane [39], various 2 x 2 sequentially-fed patch-antenna arrays [40], [41], and other [42].

2.2. Antenna Design Requirements

The following sections describe the design procedure for a low-profile wideband antenna in S band for 3U CubeSat applications. The initial design requirements are summarized in Table 2.1. The specified frequencies cover the SO and amateur bands, previously mentioned in Section 2.1.2. The designed antenna should simultaneously provide TT&C links at the SO frequencies, and data downlink in the amateur band.

A sketch of a 3U CubeSat is shown in Figure 2.4, where the space allocated for the antenna is indicated in gray. Throughout this thesis, the CubeSat body was modeled as a PEC box for simplicity. The antenna surface of 100 x 100 mm² corresponds to a 1U-CubeSat face, making it also suitable for CubeSats with a smaller form factor, such as 1U or 2U. Considering the low profile requirement of 0.08 λ0 at the lowest frequency, it is a challenging task to provide AR values smaller than 3 dB over a 20 %.

It can be argued that the profile requirement does not comply with the CubeSat standard, which defines the maximum feature thickness on the satellite surface to be 6.5 mm [1]. Considering the large required bandwidth in this specific scenario, the implementation partner of this project was prepared to back off the part of the chassis under the antenna until the standard is satisfied. Furthermore, a novel method of antenna integration was described in detail in Section 2.6.1, which reduces the antenna profile on the satellite surface.

Table 2.1. S-band CubeSat antenna design specifications.

Property	Value
Frequency [GHz]	2 – 2.45 (~20 %)
Gain [dBi]	> 5
Beamwidth [°]	> 50
S_{11} [dB]	< -10
AR @ BW [dB]	< 3
Dimensions [mm3]	100 x 100 x 12
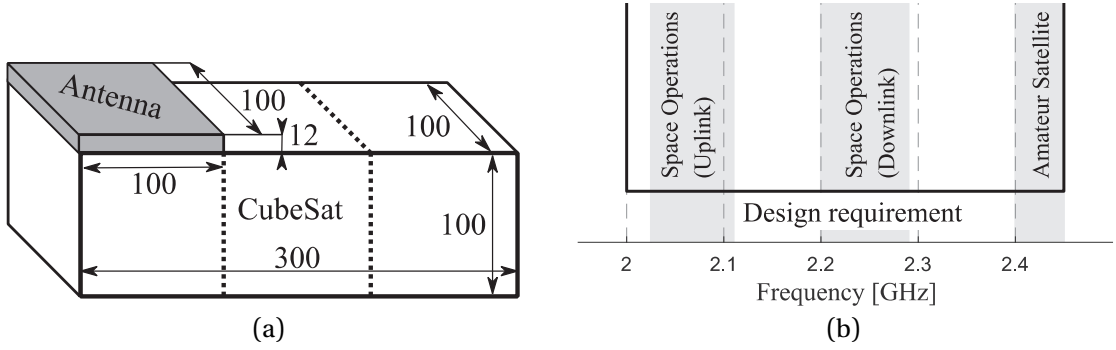
Figure 2.4. CubeSat antenna specifications. (a) Volume allocated for the S-band antenna on a 3U CubeSat. (b) Frequency requirements.

2.3. Microstrip-Fed Aperture-Coupled Patch Antenna

The low profile requirement naturally led to the choice of a patch antenna for this application. The aperture-coupling feeding method was selected, due to the superior bandwidth performance of that geometry, compared to other methods of patch-antenna excitation [43], [29], [30]. A microstrip-fed aperture-coupled patch antenna was initially designed in order to test the feasibility of covering the required bandwidth [C1]. A conventional LP microstrip-fed element was first tuned for the desired frequency band. A square metallic patch was suspended above the thin rectangular slot, under which a microstrip feeding line was placed perpendicularly. The circular polarization is then achieved using a crossed slot and a feeding network based on T-junction power dividers, quarter-wavelength transformers and phase-delay lines [C1]. The final antenna geometry is shown in Figure 2.6(a). The design was carefully analyzed in several intermediate models, presented in Figure 2.5, gradually increasing the feeding network complexity.

The thickness of a microstrip patch antenna and the dielectric permittivity of the substrate are key factors that influence the antenna bandwidth. A low-permittivity Rohacell foam (ε_r=1.08, tan δ=0.0002) is used as the patch support, as a means of maximizing the bandwidth. For support thicknesses roughly 0.1 λ_0 and larger, it is not difficult to obtain a wideband performance of this
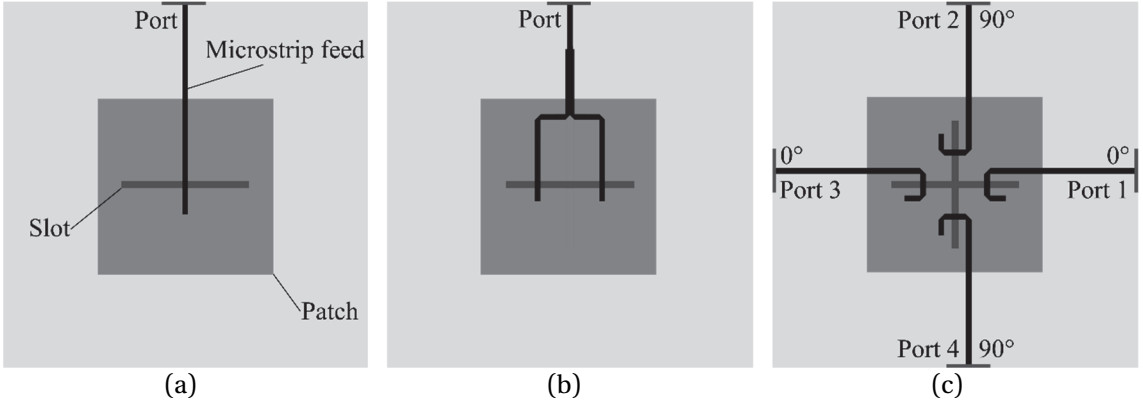
Figure 2.5. Evolution of the microstrip-fed aperture-coupled patch antenna. (a) – (b) LP models. (c) 4-port CP model.
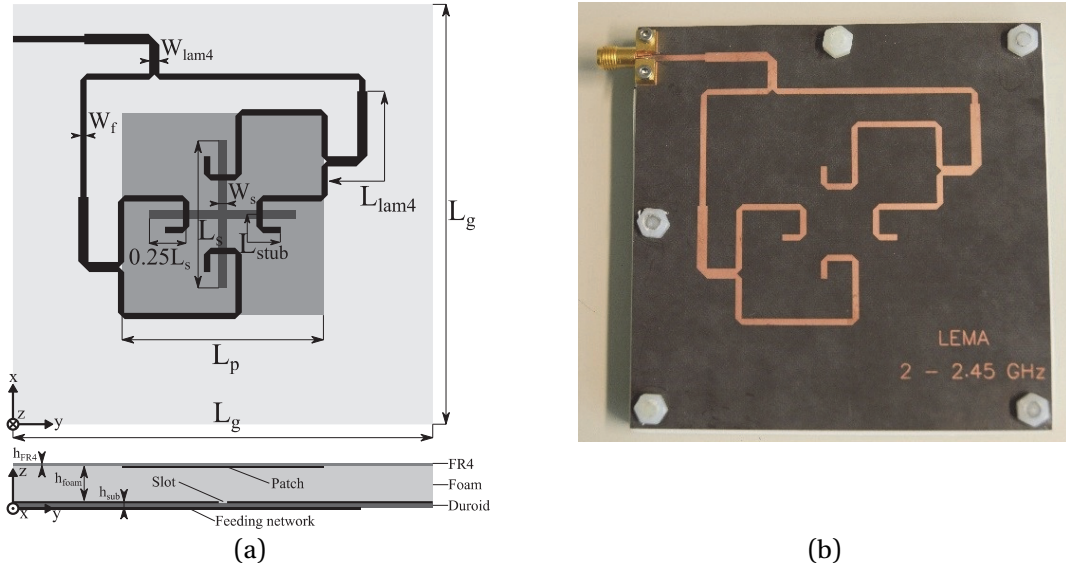
Figure 2.6. Microstrip-fed CP patch antenna. (a) Final antenna geometry. (b) Antenna prototype. Antenna dimensions (in mm): L_g=100, L_p=48, L_s=35, W_s=2, L_{lam4}=23.64, W_{lam4}=2.44, W_f=1.5, stub=9.5, h_{FR4}=0.2, h_{foam}=10, h_{sub}=0.508.

geometry. The support was then made as thin as possible, while preserving the wideband matching. The radiating patch was printed on a thin layer of FR4 (ε_r=4.5, tan δ=0.02) and Rogers RT Duroid 5870 (ε_r=2.33, tan δ=0.0012) was used for the feeding network and the ground-plane slots.

It is important to distinguish the return loss of the radiating element from the return loss of the entire antenna, including the feeding network. An example is a 4-element patch antenna array from [34] and [10], where the same radiating elements were used with two different feeding networks. This resulted in drastically different S_{11} parameters, seen from the antenna port, while

the element return loss remained unchanged. The matter should be investigated properly to avoid attributing some aspects of the full-antenna S_{11} response to the radiating element.

Therefore, it was necessary to evaluate the return loss of the radiating patch itself for the given CP excitation scheme. An intermediate 4-port model, seen in Figure 2.5(c), was created for that purpose. The port excitation mimics the feeding network performance, and the active S-parameters are calculated using:

$$active\ S_m = \sum_{n=1}^{4} S_{mn} \frac{a_n}{a_m}, \qquad m = 1..4 \tag{2.1}$$

where S_{mn} are the conventional S-parameters, and a_n is the incident power wave at port n. The active-S parameters give the power reflected at each port, with all ports excited in a desired way. Only active-S_1 parameter is presented in the simulated results, since the remaining ones show a similar trend.

The simulated and measured performance of different antenna models from Figure 2.5 and Figure 2.6 is presented in Figure 2.7. The full antenna satisfies the impedance matching requirement across the entire specified bandwidth. The low S_{11} values at the antenna port are a consequence of multiple reflections inside the feeding network. The effect is illustrated in Figure 2.8. Due to the specific feeding-network topology, the signals reflected at the patch arrive with a relative phase delay of 180° at the T-junction. This corresponds to an odd mode at the output ports of the divider and it is not supported due to symmetricity. Therefore, the signals suffer full reflection and ultimately arrive to the antenna input with an undesired phase, degrading the cross-polarization. This effect is mostly pronounced at frequencies of poor antenna matching, which is evident from the similarity of the active-S_1 and AR curves. The AR deterioration is not seen in other similar publications, since the available thickness in those cases is much larger, improving the element matching [C1]. In our scenario, the poor antenna matching at the band edges stems from the limited patch-support thickness.

The overall results show that this type of antenna geometry is an eligible candidate for CubeSat wideband applications. However, the design must be further modified to address its drawbacks and adjust it for our application, primarily improving the polarization characteristics over a wide bandwidth.

2.4. Stripline-Fed Aperture-Coupled Patch Antenna

Beside the AR, another disadvantage of the microstrip-fed antenna described in the previous section is a poor front-to-back ratio (FTBR) seen in Figure 2.7(d). The back lobe is caused by the spurious back-radiation of the slot, and it prevents a simple antenna placement onto a CubeSat surface. Furthermore, the microstrip-fed antenna is very sensitive to a proximity of a metallic surface below the feeding network [C1].
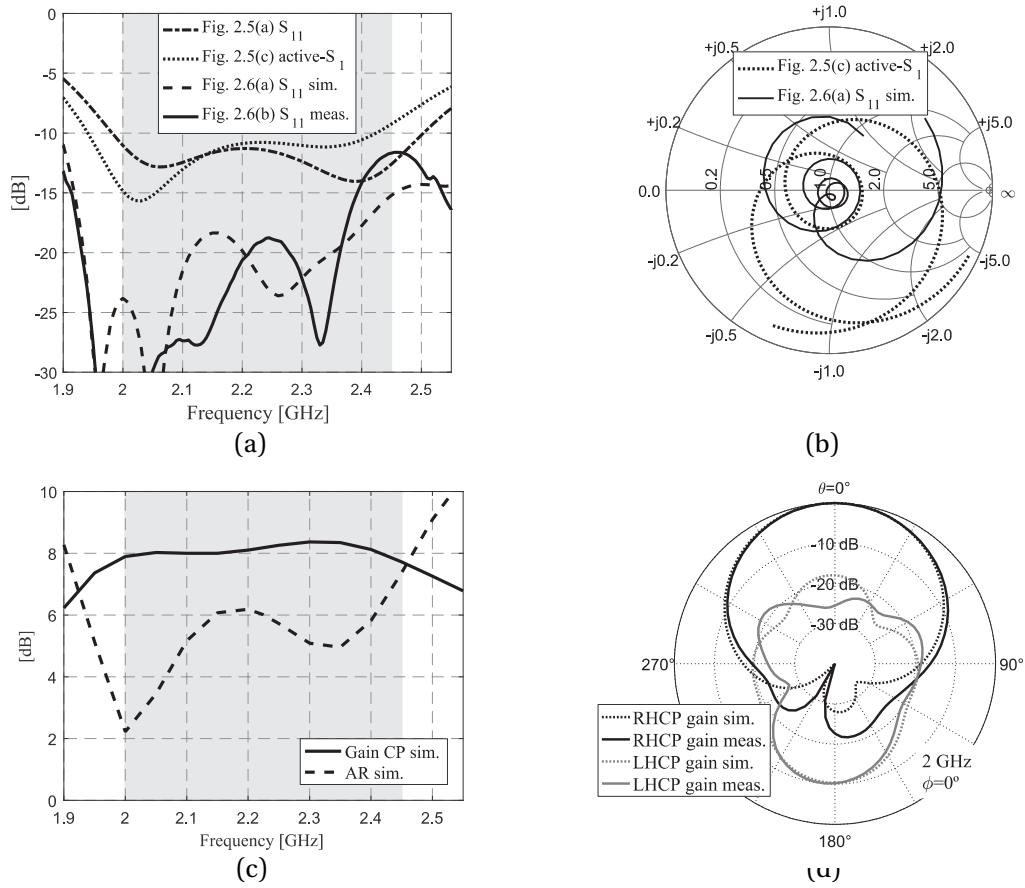
(a)

(b)

(c)

(d)

Figure 2.7. Simulation and measurement results of the microstrip-fed patch antenna [C1]. (a) S parameters corresponding to structures from figures 2.5 and 2.6. (b) Broadside gain and AR. (c) Radiation patterns.
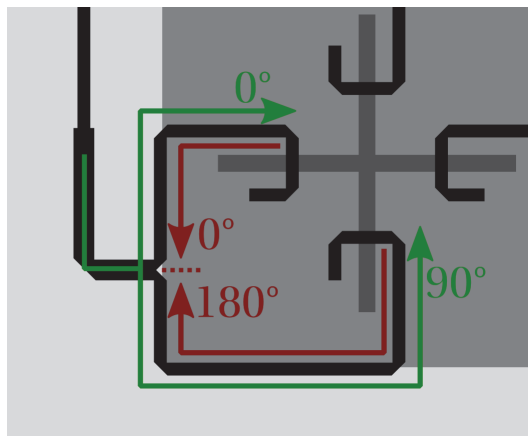

Figure 2.8. Incident and reflected signal paths and their relative phase values.

Starting from the initial geometry, the feeding network was realized in stripline technology to ensure a unidirectional pattern and isolate the feeding network from the satellite structure. The spurious back-radiated power in the microstrip-fed model manifests here as a strong electric field in the stripline. This effect greatly deteriorates the antenna performance, due to the reduction of the power accepted and radiated by the patch, predominantly at the edges of the band. Under the thickness constraints, a combination of methods is required to achieve a sufficiently high coupling from the feed lines to the radiating element, which will provide acceptable return losses. In scenarios where a larger antenna thickness is available, only a subset of these modifications would be sufficient for a satisfactory performance [C1].

2.4.1. Enclosed-Stripline Feeding Network

As a first step, an asymmetric-stripline feeding network is designed. In this structure, the electromagnetic fields are concentrated in the thinner, higher-permittivity dielectric, increasing the power delivered to the patch [46]. A second radiating patch is added to improve the coupling at the higher frequencies, without increasing the total antenna thickness.

Mode suppression techniques [47]–[49], e.g. shorting pins, were applied and studied in a large number of cases to understand their influence the antenna operation. The electric field is calculated inside the stripline of a 4-port antenna model, for different pin configurations. Considering the strong electric field in the stripline, none of the configurations was beneficial for the antenna operation in the required band. As seen, for instance, in Figure 2.9(a), where the pins are placed close to the coupling slots, the electric field values drop rapidly towards the slot edges. This non-uniform illumination of the slots reduces the coupling to the patches and consequently yields poor active-S-parameter values in the band of interest. In general, any shorting configuration that perturbs the electric field in the stripline, directly below the slot, also deteriorates the S-parameters. This effect is evident in Figure 2.9(d). The stripline is shorted at the corners, leading to a characteristic field pattern with a minimum at the center – below the slot.

Instead of suppressing the electric field in the feeding stripline, it is possible to utilize an advantageous field distribution to boost the coupling. It was observed that the electric field distribution directly below the slot determines the amount of coupling to the patch. The stripline structure is then enclosed with metallic walls on all sides. The electric field inside a fully shielded stripline, as shown in Figure 2.9(e), is favorable, since the large field strength under the slot boosts the coupling to the patch above. This was a key modification that significantly improved the wideband antenna performance.

2.4.2. Antenna Geometry and Performance

The antenna geometry is shown in Figure 2.10(a). The feeding network is modified by replacing the simple T-junction dividers and quarter-wavelength transformers with Wilkinson power

dividers. Unlike the T-junction dividers, Wilkinson dividers possess a high isolation of the output ports, which prevents the signals reflected from the patch to travel to the opposite slot and pollute the cross-polarization.

A prototype of the aperture-coupled stripline-fed stacked-patch antenna is shown in Figure 2.11. The asymmetric stripline is composed of a Rogers RT/Duroid 5870 (ε_r=2.33, tanδ=0.0012, h=0.508 mm), on which the lines and coupling slots are etched, and a low-permittivity Rohacell foam (ε_r=1.08, tanδ=0.0002, h=2 mm). The same foam material is used as the patch support, similarly as in the microstrip-fed antenna. The radiating patches are printed on a thin layer of FR4 (ε_r=4.4, tanδ=0.02, h=0.1 mm). In the first approximation, the metallic wall surrounding the stripline is modelled as a metallic pin wall, with pin separation of 15.6 mm (0.11 λg, where λg is the wavelength inside the stripline at 2 GHz). As the metallization is not feasible on the foam material, shorting pins are soldered manually to the two ground planes. After the first S_{11} measurements were done, the stripline with pins was additionally enclosed with a copper tape on all sides. The individual antenna layers are attached with nylon screws.
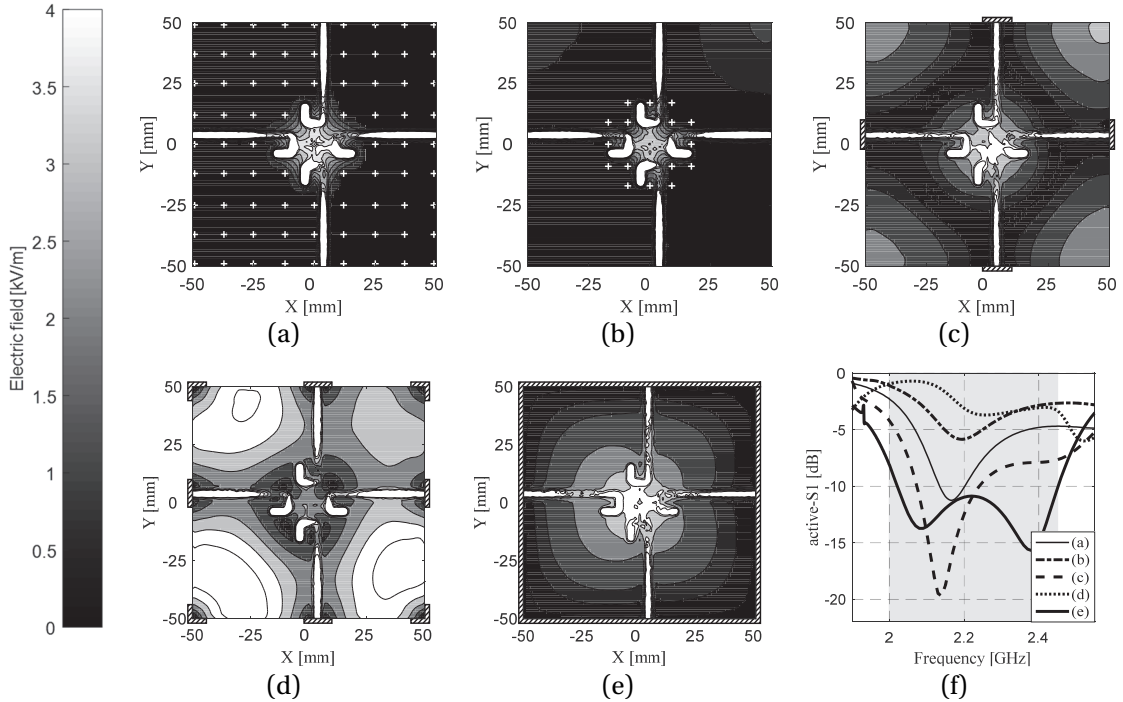
Figure 2.9. The complex magnitude of the electric field inside the feeding stripline for different pin and shielding configurations at 2.225 GHz, and the corresponding active-S1 parameters. (a) Densely placed shorting pins, spaced by 12.5 mm. (b) Shorting pins placed around the coupling slots, spaced by 8 mm. (c) Open stripline. (d) Stripline plates shorted on the corners. (e) Fully shielded stripline. (f) Corresponding active-S_1 parameters vs. frequency. The white plusses and the hatched regions mark the pin and shielding locations, respectively.
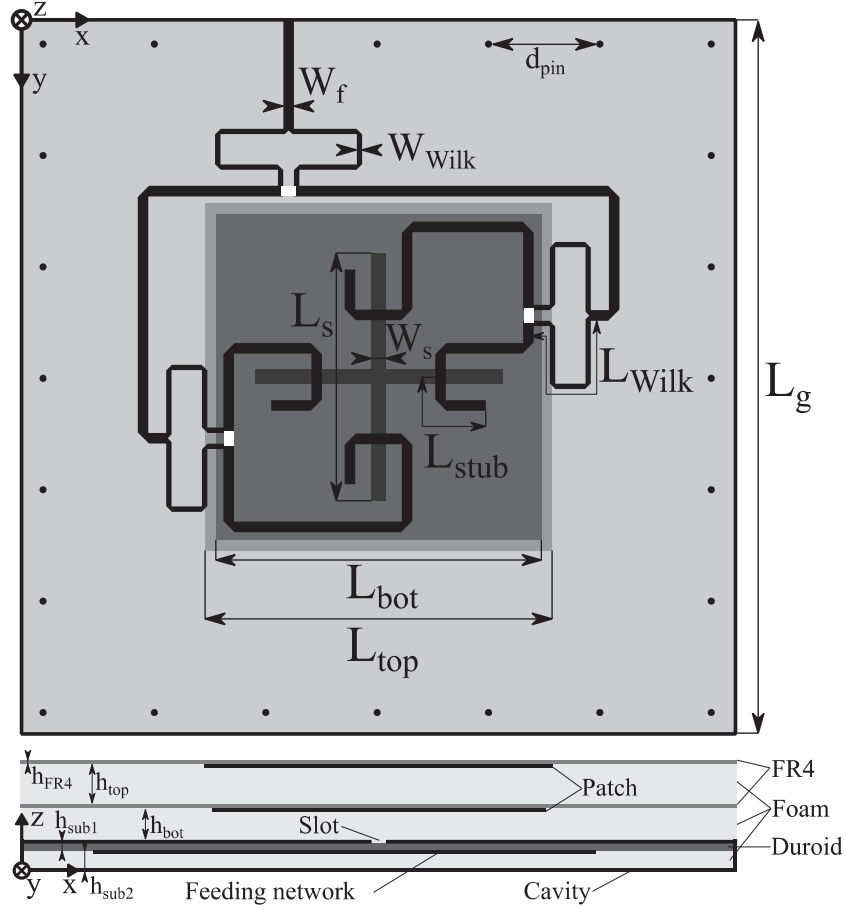
Figure 2.10. Stripline-fed stacked-patch antenna geometry. Antenna dimensions (in mm): L_g=100, L_{top}=49, L_{bot}=45.6, L_s=34.7, W_s=2, L_{Wilk}=24.75, W_{Wilk}=0.75, W_f=1.49, stub=11.8, d_{pin}=15.6, h_{FR4}=0.1, h_{top}=5, h_{bot}=4, h_{sub1}=0.508, h_{sub2}=2.

The simulation and measurement results of the antenna are shown in Figure 2.12. Simulated radiation efficiency of the antenna is from 76% to 90.5% in the frequency band 2 – 2.45 GHz. The highest efficiency values correspond to 2.1 and 2.4 GHz, which is coherent with the antenna active-S_1 parameter. The antenna back lobe is effectively removed, as the measured FTBR is higher than 30 dB. It would not be adequate to specify a total impedance bandwidth of the antenna, as the measured S_{11} is mainly produced by the feeding network. Instead, it can be stated that the antenna gain is larger than 5.9 dBi (3 dB less than the maximum gain) over a 27% bandwidth, and the AR bandwidth of the antenna (AR<3 dB) is 32%.

The simulated performance of the feeding network itself is shown in Figure 2.13. By comparing the return loss at the input port (S_{55}) with the return loss in Figure 2.12(a), it can be concluded that the antenna input matching is mostly determined by the feeding network. The phase difference between signals incident on any two adjacent ports is in the range from 82° to 99° along the whole band.
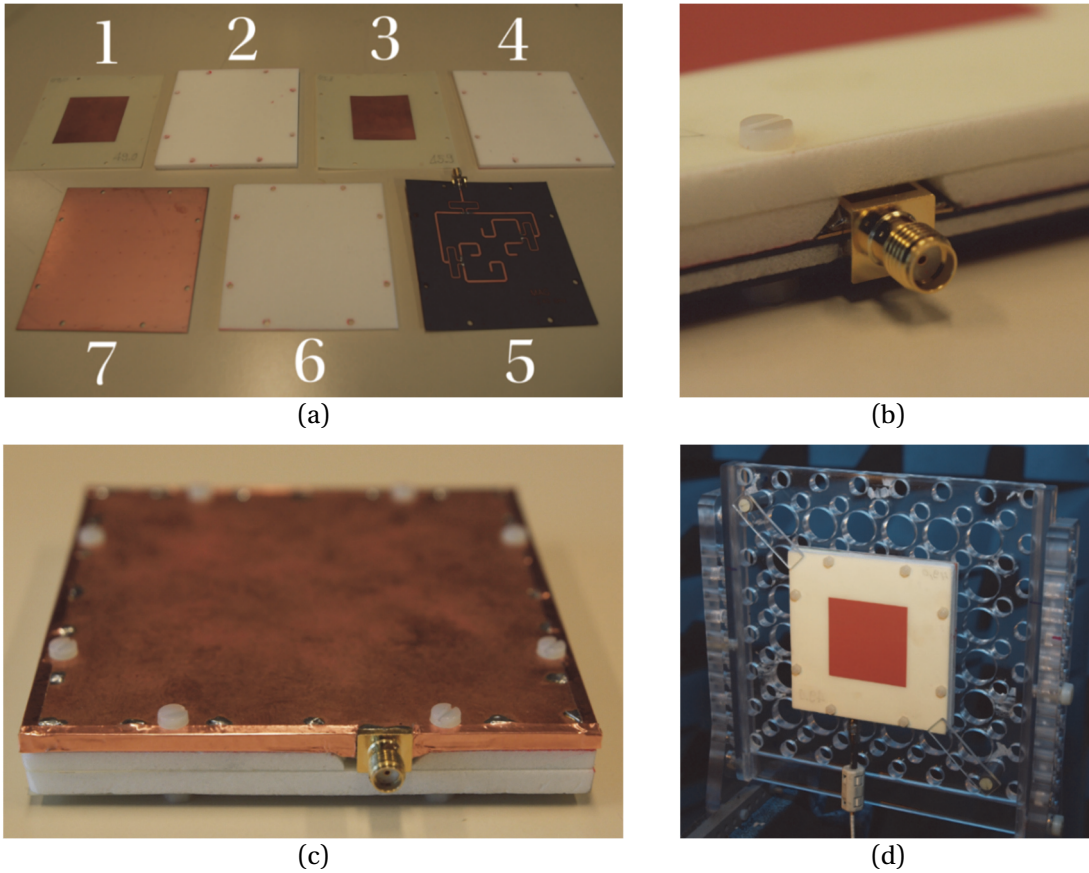
Figure 2.11. Stripline-fed stacked-patch antenna prototype. (a) Individual layers – the numbers denote the order of assembly. (b) A detail of the SMA connector before enclosing the stripline with a copper tape. (c) Antenna prototype (back view) with the soldered shorting pins and copper tape visible. (d) Antenna prototype (front view) inside the anechoic chamber.

2.5. Stripline-Cavity Resonance Analysis

A rectangular cavity is formed by enclosing the stripline feeding structure, which exhibits cavity resonances at certain frequencies. The resonances have a narrowband character, but are harmful for the antenna operation and it is crucial that they do not appear within the operating bandwidth [J1]. To illustrate this effect, the instantaneous electric field is simulated in the enclosed-stripline cavity, at the resonance frequency and away from it, and shown in Figure 2.15. Away from the resonance, the electric-field vector has an opposite direction at the opposite sides of the slots. This difference creates an electric field along the slot itself, which strengthens the coupling. The particular field distribution shown in the figure is a consequence of the feeding required for a CP radiation. On the contrary, the electric-field vector at the resonant frequency has a uniform direction across the entire cavity.
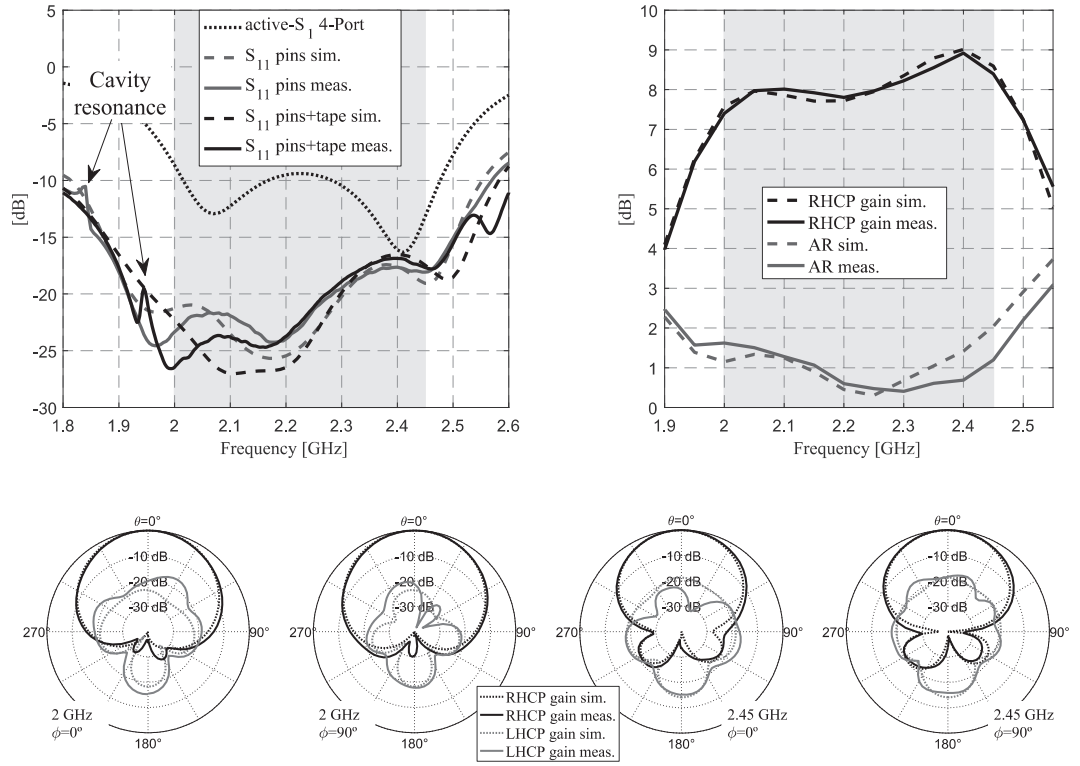
Figure 2.12. Simulation and measurement results of the stripline-fed stacked-patch antenna. (a) S parameters. (b) Broadside gain and AR versus frequency. (c) Radiation patterns.
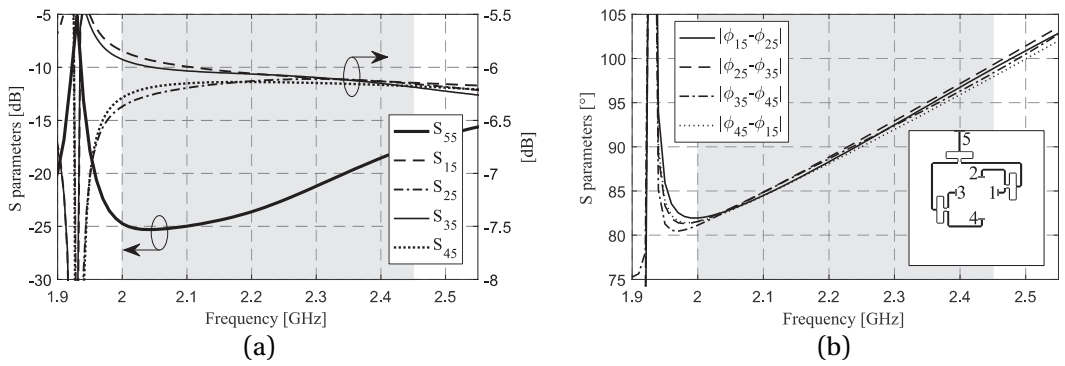
Figure 2.13. Simulated S parameters of the feeding network. (a) Magnitude. (b) Phase. Inset: Port numbering of the feeding-network.

25

The presented antenna has cavity resonances seen at the measured S_{11} curves of Figure 2.12(a). The model with the pins has a lower resonance (1.84 GHz) compared to the model with both pins and the copper tape (1.94 GHz), as the fringing fields increase the effective cavity size in the former case.

A good practice is to allow a safety margin between the operating band and the cavity resonance. If the cavity size is preserved, a higher permittivity substrate can be used for the feeding network. This will increase the electrical size of the cavity, further reducing the resonant frequencies. These resonances are not always visible in the simulation results due to the selection of the interpolating frequency-sweep technique used in the EM software.

The electric field in the stripline cavity preserves the same distribution at frequencies above and below the first resonance. This feature enables an equally good antenna operation on either side of the resonant frequency. Therefore, the cavity size can be reduced, which will shift the resonant frequency above the operating band. However, the cavity dimensions can be changed to a certain extent. Figure 2.14(c) shows the active-S parameters for different cavity sizes. A cavity too large will have a field distribution with low values at the slot location, as seen in Figure 2.14(a).

The consequence is a poor antenna matching at the higher edge of the frequency band, where this effect initially appears. On the other side, the proximity of the walls to the coupling slot limits the minimal cavity size. The electric field magnitude at the locations of slot edges is reduced in that case, as seen in Figure 2.14(b). This effect is dominantly present at lower frequencies, where the coupling to the patch is consequently deteriorated.

2.5.1. Interference Suppression in an Adjacent Frequency Band

A cavity size of 80 mm exhibits a resonance at 2.42 GHz, which can be seen Figure 2.14(c). At the resonant frequency, the electric field distribution in the feeding stripline is dominated by the cavity resonance. The electric field vector has the same direction at all locations in the stripline, as seen in Figure 2.15. This electric field polarity is analogous to the non-radiating cavity resonances in cavity-backed slot antennas, which is thoroughly studied in [50]. In our case, since the slots are used for coupling to the patches, the field polarity at the resonance inhibits this coupling. The energy is partly dissipated through dielectric and conductive losses in the cavity, and partly reflected in the feeding network and dissipated in the resistors. All the combined effects lead to a reduction of the antenna gain at the cavity resonance.

If the cavity size is properly selected, the resonance can be placed at an arbitrary adjacent frequency, leading to a reduced amount of received interference from that frequency band. The effect of gain reduction is narrowband and does not affect the antenna performance in the operating band. This feature is demonstrated in the design presented in the next section.
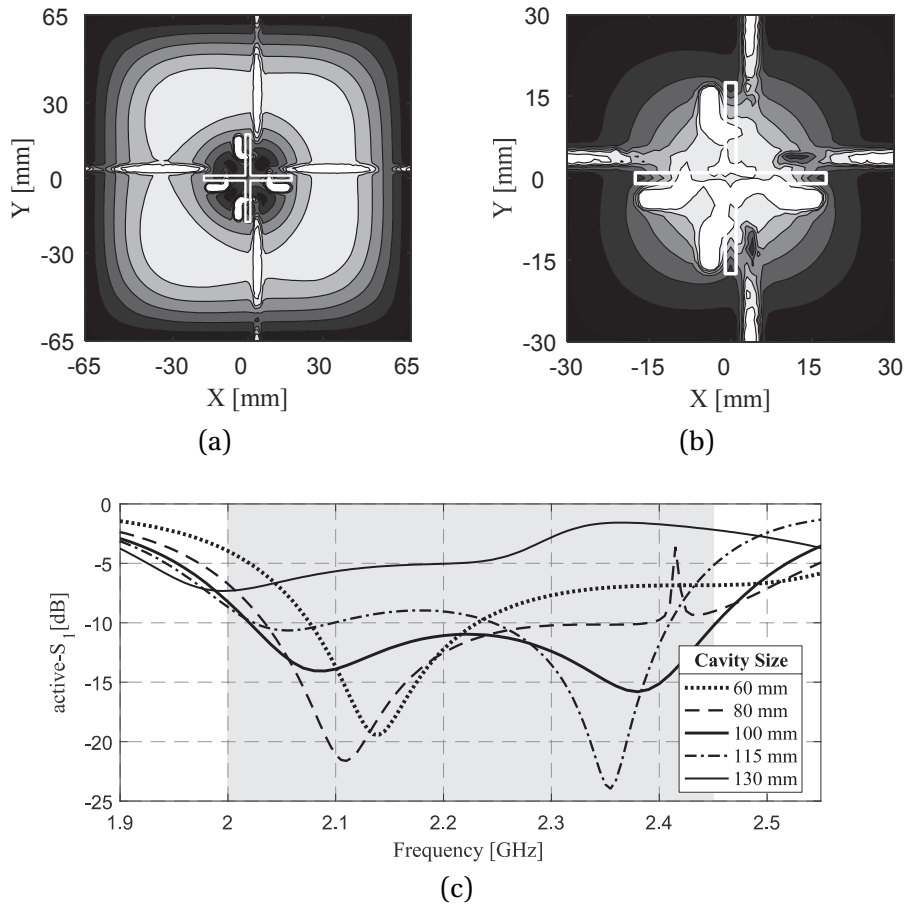
Figure 2.14. The magnitude of the complex electric field vector in the shielded stripline at 2.225 GHz, for the cavity size of (a) 130 mm and (b) 60 mm, and (c) the corresponding active-S_1 parameters. Slot locations are marked with solid white lines.
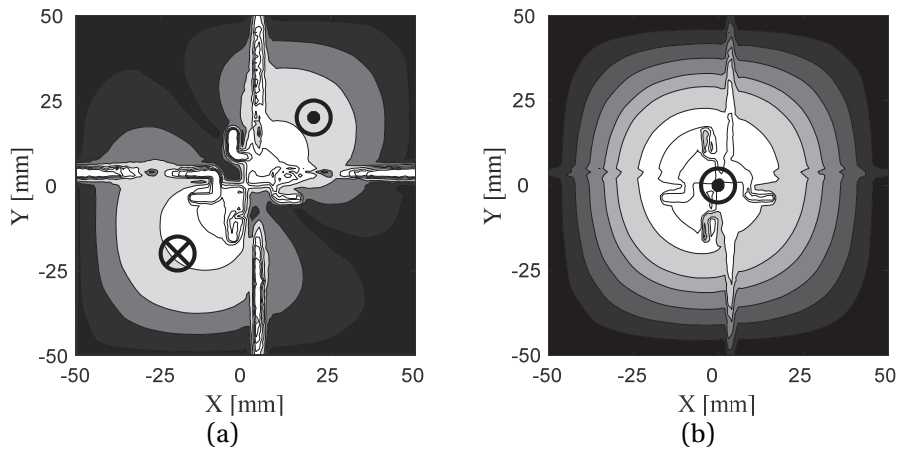

Figure 2.15. Instantaneous electric field magnitude inside the stripline. (a) 2.225 GHz (center frequency). (b) 1.94 GHz (cavity resonance). Dominant electric-field vector directions are marked in black.

Both the field distribution and the resonances of the cavity must be taken into account when selecting the cavity dimension. The range of viable dimensions depends mainly on the operating bandwidth of the antenna – the larger the bandwidth, the less frequencies are available for the suppressed band. This range can be modified by selecting a different combination of stripline dielectrics. However, it is recommended that the ratio of their dielectric permittivities (2.15) and the ratio of thicknesses (4) remain the same or larger. Otherwise, it will be difficult to achieve a sufficient coupling from the feed lines to the patch. If both criteria are fulfilled, the antenna will benefit from the field-distribution effects, without suffering from adverse resonances.

2.6. TT&C Antenna

The stripline-fed wideband antenna was modified to work as a TT&C antenna, at the ECSS frequencies in S-band [J1]. The frequency band of interest for this design is from 2 to 2.3 GHz, while the other design requirements remain unchanged. A small stripline cavity is selected and the resonance frequency is shifted above the operating band. The total antenna dimensions are then also reduced, which allows a greater flexibility of the antenna placement on the CubeSat. It was seen that a satisfactory performance could be achieved with one radiating patch only. In addition, the total thickness of the antenna is slightly reduced. The thickness can be reduced further if necessary, while accepting a lower radiation efficiency, and thus, a lower antenna gain at extreme frequencies.

The selected design has a cavity dimension of 78 mm, yielding a resonant frequency of approximately 2.45 GHz. That frequency corresponds to the amateur-satellite service band, which is very popular for CubeSat communications. If the antenna were to operate at the ECSS frequencies only, the signals in the amateur band would present a significant interference and the suppression of the received signal from that band would be an advantage.

The following sections present the antenna geometry, prototype construction, as well as simulation and measurement results. Section 2.6.1 proposes an elegant method of integrating this type of antennas into the CubeSat metallic chassis, which reduces the antenna extrusion on the satellite surface.

2.6.1. CubeSat Integration

As it was discussed in Section 2.2, the antenna would significantly violate the total dimension requirements, if it were to be simply placed on the CubeSat face. A very practical approach is to integrate the antenna into the CubeSat by placing the feeding stripline inside the satellite chassis, while keeping the patches on the exterior. The concept is illustrated in Figure 2.16. As a first approximation, it is assumed that the CubeSat chassis is a hollow metallic box with a thickness of 1.2 mm. In this configuration, the satellite face on which the antenna is mounted acts as a ground

plane with the coupling slots, and the adjacent faces are used as vertical cavity walls. The second stripline ground completely isolates the feeding network from the satellite interior. As the coupling slots are cut in the metallic face of the satellite, they now have a substantial thickness (1.2 mm) compared to the PCB metallization in the previous prototype (17 μm). The influence of the increased slot thickness can be partially neutralized by enlarging the slot width, or modifying the slot shape. If the desired cavity size does not match the dimensions of the satellite face, such as the TT&C antenna presented here, the antenna structure can be shifted towards one corner of the CubeSat and the remaining cavity walls can be modeled as pin walls. This halves the required number of pins, compared to the case where the antenna is positioned on the center of the face. The cavity's resonant frequency is then a function of pin-cage dimensions and can be altered, while keeping in mind the potential problems outlined in Section 2.5.1. Furthermore, the remaining part of the face remains available for other features on the satellite's surface, or antenna filters, diplexer, etc.

2.6.2. Antenna Prototype Construction

The TT&C antenna prototype was built using the same materials as in the previous model, and integrated in a 3U CubeSat mock-up during the S_{11} and radiation measurements. The geometry of the TT&C antenna, mounted on a CubeSat, is shown in Figure 2.17. The antenna was not significantly modified compared to the previous design, safe for the fact that the power dividers are tuned to the frequency of 2.15 GHz. A low-cost CubeSat mock-up was built using 1.2-mm-thick metallized panels of FR4 epoxy. The panel edges are ridged and interlocked for a better structural stability. The crossed-slot was cut in one of the long faces, where the antenna was to be mounted. The individual antenna layers, before assembly, are shown in Figure 2.18(a). After the structure was assembled, the edges and the slot were covered with a copper tape to electrically connect the individual panels and provide conductivity on the slot's vertical walls. The feeding
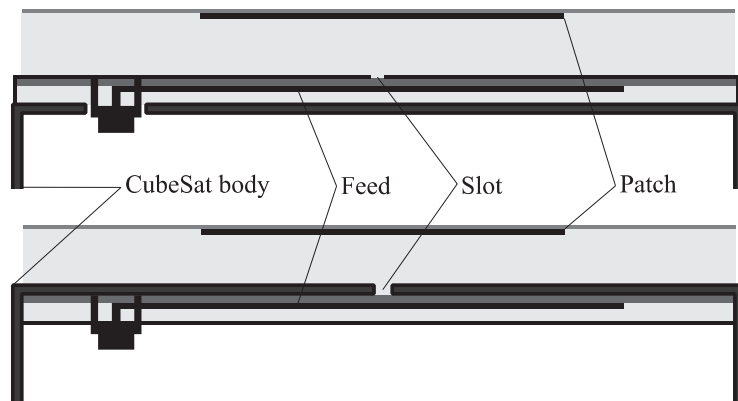
Figure 2.16. Aperture-coupled patch antenna on the CubeSat surface (top) and the same antenna integrated into the CubeSat chassis (bottom).

network was placed inside the CubeSat, against one of the corners. It was then attached to the structure with ten metallic screws that formed the remaining two vertical walls of the stripline cavity. The screws connect the two ground planes electrically, but also provide a mechanically rigid structure. The foam and the patch were placed above the slot and fixed to the structure with nylon screws.

The CubeSat mock-up was designed in such a way that the antenna can be placed on both the large and the small CubeSat face. This is simply done by exchanging the two panels seen on the left side of Figure 2.18(c), marked with letters 'L' and 'S'. Figure 2.18(d) and (e) show the assembly of the entire structure, with the antenna mounted on a large and small CubeSat face, respectively. The SMA connector is placed vertically in both cases, at the inside of the CubeSat. In this configuration, the measured return losses of this coaxial-to-stripline transition are smaller than -22 dB in the frequency range of interest.
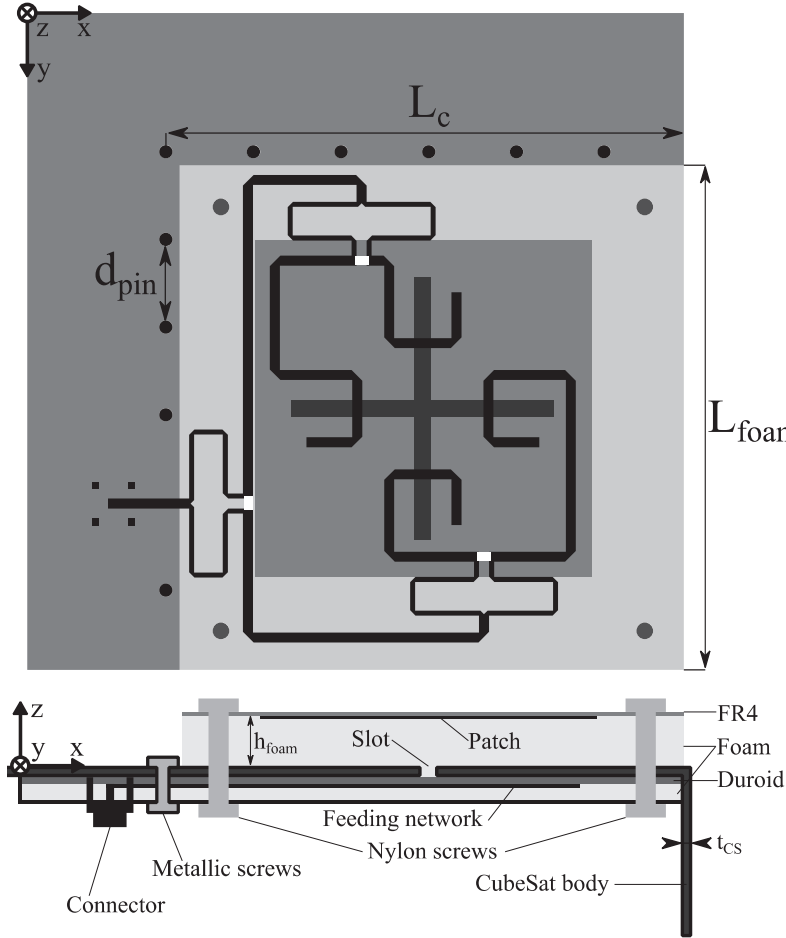
Figure 2.17. TT&C patch antenna integrated into a 1U CubeSat chassis. Antenna dimensions (in mm): L_c=78, Lf_{foam}=75, L_p=50, L_s=39, W_s=3, d_{pin}=13.2, h_{foam}=8, t_{CS}=1.2. The remaining parameters have the same values as in Figure 2.10.
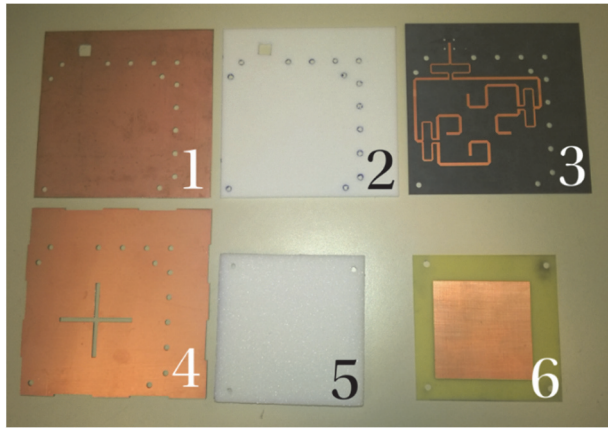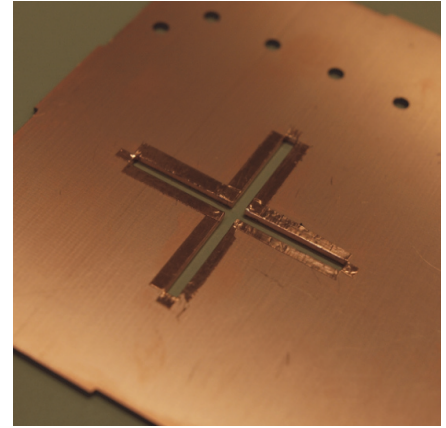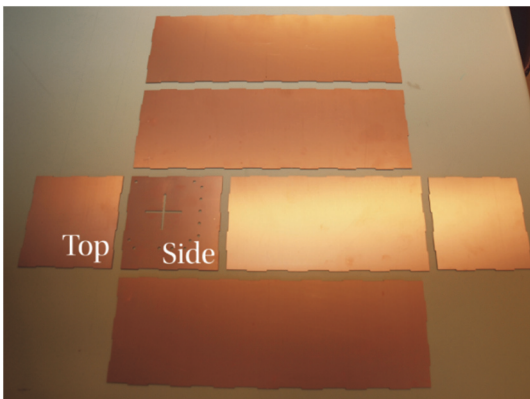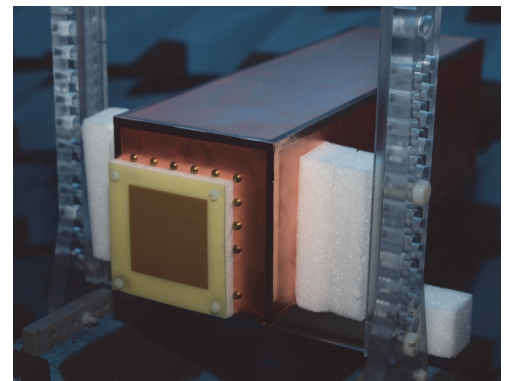
Figure 2.18. TT&C antenna prototype. (a) Individual antenna layers before assembly, bottom view. Numbers indicate the stacking order. (b) Close-up view of the coupling slot covered with conductive tape. (c) Panels of the CubeSat mock-up before assembly. Panels marked with 'top' and 'side' were interchanged during measurements. (d) Assembled patch antenna (back view). (e) Antenna mounted on a large CubeSat face. (f) Antenna mounted on a small CubeSat face.

2.6.3. Antenna Performance

The first set of measurements was performed with the antenna mounted on a large CubeSat face. The antenna was afterwards moved to the small face, and all the measurements were repeated. Figure 2.19 compares the simulation and measurement results of the antenna matching and radiation characteristics. The beam tilt of 5° was observed for the antenna on a large CubeSat face, caused by the ground-plane size increase. The small beam tilt does not pose a problem, since the main lobe is a smooth function of the radiation angle. There was not a significant change in the measurement results when the antenna was moved to the small CubeSat face. Therefore, the presented results correspond to the antenna mounted on the large CubeSat face only.

There is a larger discrepancy between the measured and simulated responses, with respect to the wideband antenna prototype. Most notably, the measured results show a shift of the cavity mode towards the higher frequencies, as it appears at 2.55 GHz. The resonance effect also exhibits a more-wideband character compared to the simulations. Several aspects of the low-cost mock-up construction can be used to explain this difference: the copper tape used to provide the slot conductivity, feed-slot-patch misalignment, material thickness tolerance, etc. Despite this, the radiation patterns are in agreement with the simulations and the gain reduction at the cavity resonance frequency is ~4 dBi, as seen in Figure 2.19. This reduction is not larger since the main driving mechanism of the antenna is not the cavity mode, but the stripline feeding network.

The measured S_{11} parameter, shown in Figure 2.19, is below -15 dB at both ECSS bands. The antenna beamwidth is 74° and 67° at 2 and 2.3 GHz, respectively, and the AR values are below 3 dB across the entire radiation beamwidth, as seen in. If larger gain values are required at the edges of the band, the single patch can be replaced with a stacked-patch structure, similar to the one in the wideband antenna model.

2.7. X-band Antenna

In previous sections, it was shown how an enclosed-stripline feeding network can improve the element matching and the overall performance of limited-profile aperture-coupled patch antennas. This was demonstrated on several designs in S band, with rather complex feeding networks. The purpose of this section is to show how this new technique can be used to boost the performance of other antenna types, such as aperture-coupled antenna geometries with much simpler feeding methods. A patch antenna for data downlink and telemetry in X band, described in this section, represents this principle. The frequencies allocated for the purpose are the Earth Exploration-Satellite service and Space Research frequency bands (8.025 – 8.5 GHz) [38].
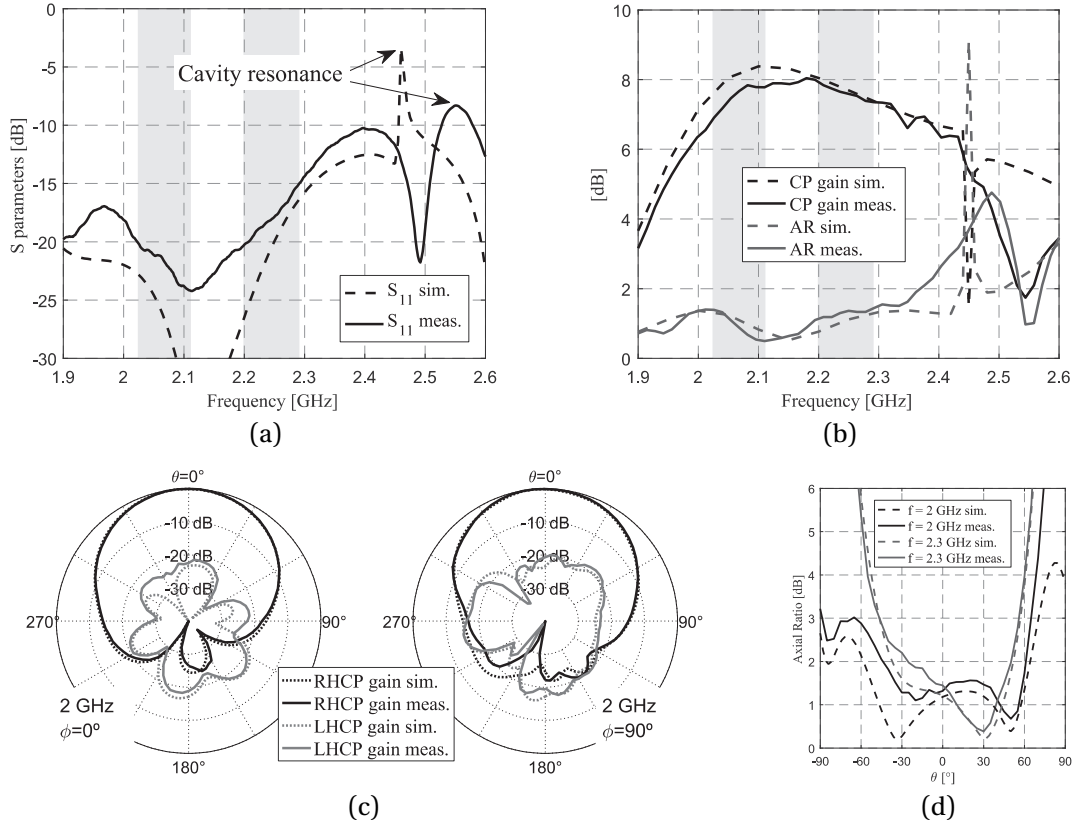
Figure 2.19. Simulation and measurement results for the TT&C antenna mounted on a long face of a 3U CubeSat mock-up. (a) S11 parameter vs. frequency, for φ=0°. Inset: antenna prototype with visible metallic screws that form the cavity. (b) Broadside gain and AR vs. frequency. (c) Radiation patterns in two orthogonal planes, at 2 and 2.3 GHz. (d) AR vs. angle, at 2 and 2.3 GHz.

2.7.1. Antenna Geometry

Since the early development of circularly polarized microstrip patch antennas, it was evident that the bandwidth strongly depends on the antenna thickness and substrate permittivity, but also the feeding technique. There was an effort over time to improve their inherently narrow impedance and AR bandwidths, without compromising the simplicity of the feeding method. One proposed solution was a single-feed CP patch antenna, coupled to a microstrip feeding line through a symmetrical crossed slot in the ground plane [51]. The bandwidth was further optimized by adding a second patch and introducing asymmetries in the coupling slot and the first patch [52]–[55].

This geometry was a starting point for our design, which is shown in Figure 2.20. The antenna is fed with a 50-ohm line realized in asymmetric stripline technology. The feeding structure and materials are identical to ones used in the S-band antenna. The patch has a square shape, and the unequal length of the orthogonal coupling slots introduces the 90° phase shift, required for CP
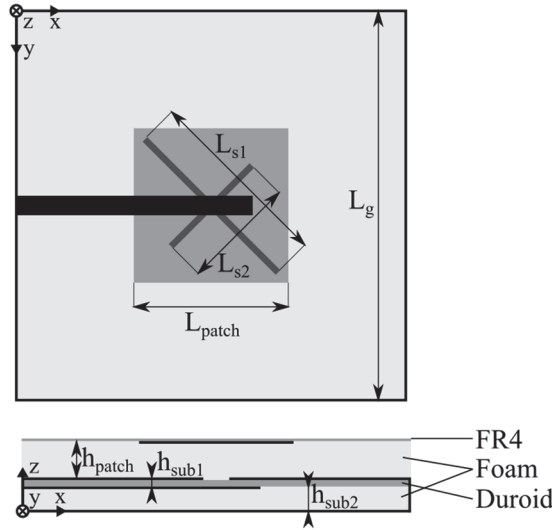
Figure 2.20. X-band aperture-coupled patch antenna geometry.

radiation. As the wavelength in the desired band is ~36 mm, the limitations for the antenna profile are less stringent, and the total thickness of the structure is less than $0.15\,\lambda_0$ at 8 GHz.

The initial antenna designs were performed using an open (unshielded) asymmetrical stripline in the feeding part. A prototype of the design was built and evaluated. The measured impedance bandwidth was larger than 20%, but the cross-polarization levels were higher than specified. A detailed study of the first prototype, including the simulation and measurement results, can be found in [56].

2.7.2. Simulation Results

After the successful performance improvement in S-band antennas by the stripline enclosure, the same technique was applied here. A PEC wall was added around the stripline in the simulation model, and the antenna was slightly retuned. To get a better understanding of how this modification influences the antenna operation, three designs were compared:

- Microstrip feeding
- Open stripline feeding
- Enclosed stripline feeding

Apart from the feeding-network technology, all the design parameters remain identical in the three models. Their performance is compared in Figure 2.21. Microstrip model is matched at the entire frequency band, exhibits low AR values, but has a back lobe due to the radiation of the open slot. Adding a second ground plane in the open-stripline model improves the FTBR, but deteriorates the AR. An enclosed-stripline model takes the best from both worlds, having at the same time a similar polarization to the microstrip model and a unidirectional radiation pattern.
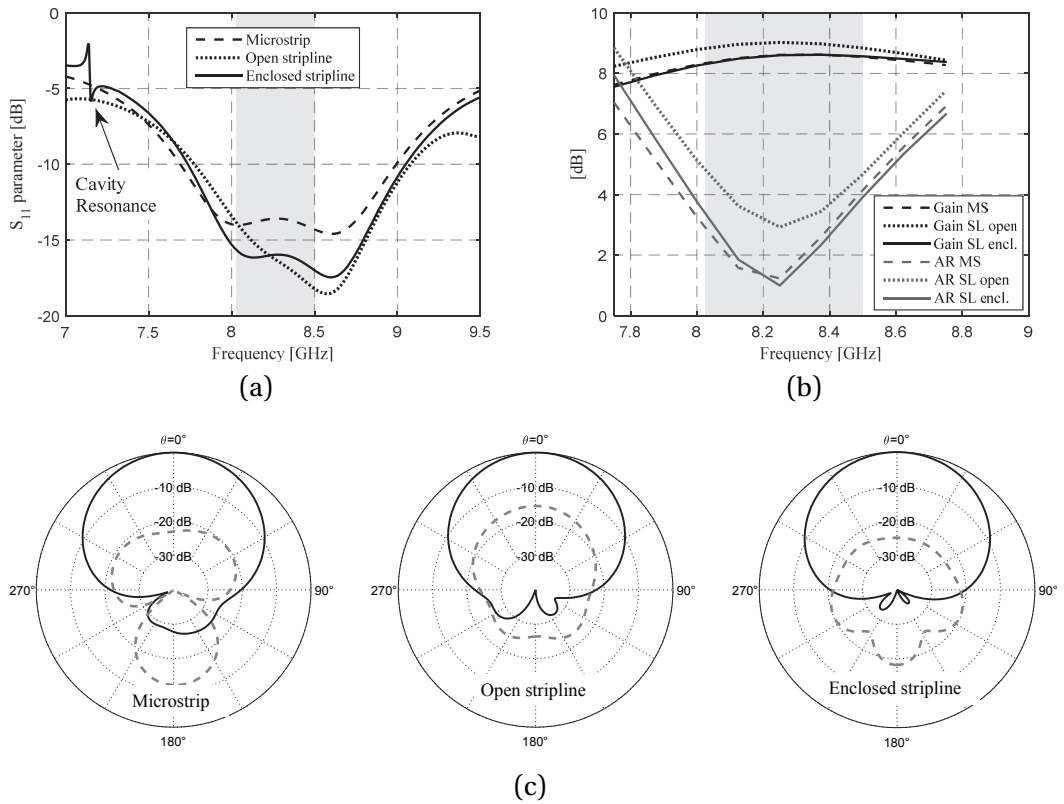
Figure 2.21. X-band patch antenna – the performance of its three variations. (a) S11 parameter. (b) Broadside gain and axial ratio vs. frequency. (c) Radiation patterns.

A cavity resonance is evident in the enclosed-stripline model at 7.2 GHz, indicating that the antenna operates above the first resonance. Following the analysis in Section 2.5, the cavity dimension must be carefully selected in order to have a beneficial field distribution in the stripline, across the entire operating bandwidth. To give an example of an improperly sized cavity, the stripline dimension was increased and the field was calculated inside the stripline in the original and larger models. The plots in Figure 2.22 show the field distribution for the two cases. For the correct cavity size, electric field is focused below the slot. The field distribution of the larger cavity gradually changes over frequency, until the second higher-order resonant mode at 8.8 GHz. The coupling to the radiating patch is consequently inhibited and a full reflection occurs at the resonant frequency. The first resonant mode of the larger cavity is lower than the displayed range of S parameters. It should also be noted that the plotted fields are normalized for clarity and that the maximum field strength at the resonant frequency is an order of magnitude higher.
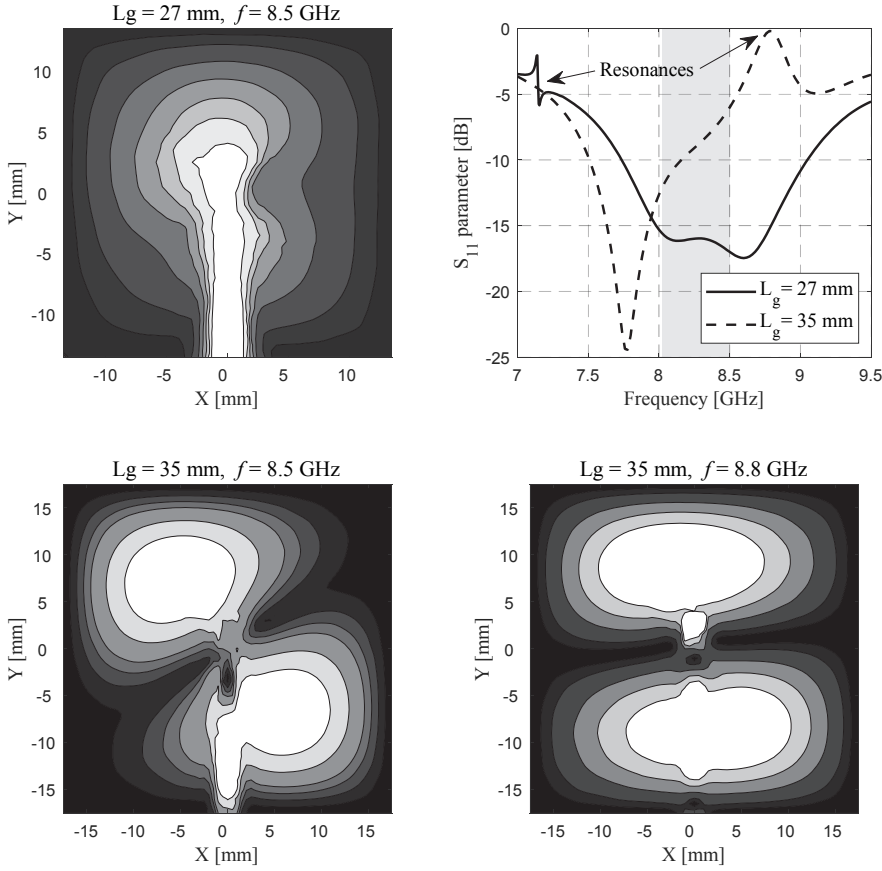
Figure 2.22. (a,c,d) Electric field distribution inside the feeding stripline of the X-band antenna and (b) the corresponding S parameters.

2.7.3. 4-Element Antenna Array

The small antenna dimension allows for an array of X-band patch antennas on a CubeSat, and the designs in the literature usually come in the form of 2×2 arrays. Although the radiation beamwidth is reduced in an array, and consequently the duration of the link with the ground station, shorter high-data-rate bursts are possible due to an increased antenna gain.

A 4-element array was constructed using the previously described element. The sequential rotation technique was used as a means of improving the AR [57]. Various types of corporate and serial feeding networks were designed for the four-element array. Finally, a serial FN with a minimal line length is presented in this chapter. The characteristic impedance of the feeding sections were modified to obtain matching of the entire structure [58], [59]. As there is no unique solution to this problem, the authors of [58] used a global optimization algorithm to solve for characteristic impedances. The result of this optimization process was directly implemented here and the line dimension were tuned for our specific stripline technology. The geometry of the full array is shown in Figure 2.23. The four stripline sections are isolated with vertical PEC walls,

except for a small opening for feeding lines. Similarly as in[60], the openings are small enough not to perturb the field distribution below the slots, and large enough to allow the TEM mode of the stripline to pass through. Instead of PEC walls, the stripline sections/cavities can be built with columns of shorting pins in an antenna prototype, as in the S-band prototype.

The simulation results in Figure 2.24 show that the AR bandwidth of the array easily covers the required frequencies. The results imply that a smaller patch element, with a higher permittivity dielectric, can be used inside such an array, with the performance still satisfying the design specifications.

2.8. Summary and Discussion

Several wideband low-profile antenna designs in S and X bands are presented in this chapter. The antennas perform the TT&C as well as data downlink functions, in the case of the first S-band antenna. A TT&C antenna and the system as a whole are identified as the crucial satellite component, upon which every subsequent operation depends. For this reason, no deployable structure is used for the antenna geometry, with the high reliability in mind. Considering the electrical size of a CubeSat at S-band frequencies, it can be seen that the available space on the spacecraft surface is strictly limited. Having a single-port multi-band antenna efficiently optimizes the usage of the sparse real estate onboard, simplifies the antenna placement, and eliminates the cross coupling between several antenna elements.
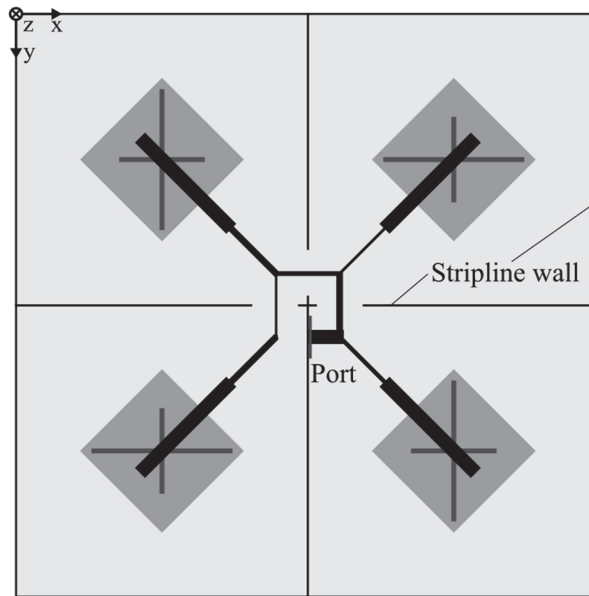
Figure 2.23. X-band series-fed aperture-coupled patch antenna array. The line sections have a 90° phase delay and the characteristic impedance values are taken from [58].
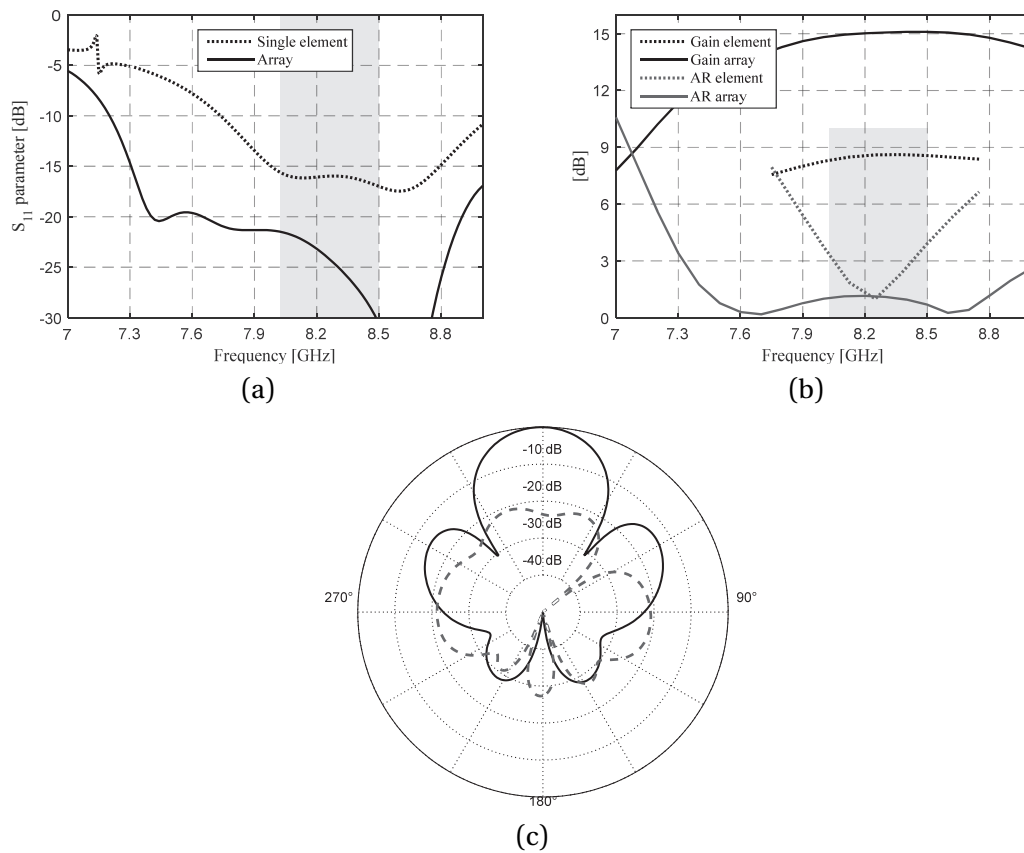
Figure 2.24. X-band antenna array performance. (a) S11 parameter. (b) Broadside gain and axial ratio vs. frequency. (c) Radiation pattern.

Therefore, the S-band antennas are designed to cover several (up to three) frequency bands simultaneously. The CubeSat antennas in S band are traditionally simple, robust, and narrowband, in line with the design complexity of early systems. As new technologies become available regularly, and CubeSat capabilities improve, there will be an increased demand for high-performance wideband antennas.

In the antenna design process, special attention is paid to distinguish the S_{11} parameter of the antenna element and that of the entire antenna, including the feeding network. The difference is otherwise well known in the antenna community, but often not clearly explained in publications on CubeSat antennas. Therefore, it is emphasized in this chapter.

The aperture-coupled patch-antenna geometry maximizes the bandwidth in the allocated volume for the antenna. Beside the bandwidth, another key requirement is the unidirectional radiation pattern, which allows a seamless antenna placement on the CubeSat structure. The initial feeding network was modified from microstrip to stripline, removing the back radiation, but leading to a set of problems related to the field distribution inside the feeding stripline. After

a series of attempts to suppress the electric field inside the stripline with shorting pins, it was observed that the magnitude of the electric field below the coupling slot is the driving mechanism of the antenna. This magnitude is then maximized, by shielding the stripline on all sides, resulting in wideband impedance, gain and AR performance of the antenna.

The stripline shielding forms a resonant cavity. At the cavity resonance, unlike at other frequencies, the field distribution inhibits the coupling to the patch and traps the energy inside the stripline. By properly sizing the cavity, the resonance can be moved outside the operating bandwidth. The antenna preserves its performance for a large range of cavity dimensions, given that the resonance is sufficiently far from the working frequencies. A set of rules is presented for a correct selection of the stripline cavity dimensions that yield a good performance. The harmful resonance effects can further be used to reduce the radiation at the resonant frequency, thus suppressing the interference in an arbitrary adjacent band.

A novel method of integration into the CubeSat is proposed for this type of antennas, where the feeding network is placed at the CubeSat interior, and the patches at the surface are excited through coupling slots, cut in the metallic chassis of a CubeSat. This approach significantly reduces the total antenna thickness on the surface of the CubeSat. Although the profile of the antenna structure is still larger than what the CubeSat standard specifies, it is deemed necessary for the given set of requirements. The problem can be alleviated by a recess of the CubeSat face on which the antenna is mounted.

The stripline-shielding method is applied in the case of the S-band antenna with a rather complex feeding network. In the last section of the chapter, the method is demonstrated in the case of an X-band patch antenna and, having a single feed line and an asymmetric coupling slot. The purpose of this section is to show the potential of the described principle for stripline feeds with simpler geometries. The same effects are observed in the obtained results as in the previous designs, confirming the presented analysis. A four-element array of sequentially rotated patch antennas is designed using the described patch-antenna element. The performance of the patch array makes it suitable for wideband high-speed CubeSat communication.

In the cases of both single elements and antenna arrays, a foam layer in the feeding network complicates the fabrication procedure, since no metallization is possible on the foam material. Instead, this layer can be replaced by a low-permittivity substrate, such as Rogers Duroid 5870. Following the rules outlined in Section 2.5.1, the second substrate of the feeding network must then be also replaced by a higher-permittivity substrate, for efficient focusing of the electric field close to the coupling slots. Such modifications require the complete redesign of the feeding network, which is not performed here.

3. L-band Antenna System for CubeSats

When a CubeSat's initial attitude is determined, the spacecraft is oriented to the flight position by the ADCS. The system afterwards continues to monitor and correct the attitude, allowing the payload (downlink and/or uplink) antennas to be facing the Earth at all times. This capability enables high-performance CubeSat antenna designs with an increased directivity or even shaped beams. Planar antennas or antenna arrays are a good candidate, since their narrower beamwidth is not a limiting factor in this scenario. If, however, a lower communication frequency is selected (L, S bands), a 3U CubeSat offers a very limited surface for antennas, much less arrays. Therefore, various miniaturization techniques must be applied during the antenna design in order to fit the low-frequency antennas on a CubeSat face.

Another alternative is to use the surfaces allocated to the solar cells and integrate the antenna radiating elements with them. The degree of integration depends on the relative position of the antenna and solar cell elements: one above the other, in the same level, or on opposing sides of deployable wings. A larger degree of integration presents an increased difficulty of preserving a good performance of both functions – radiation and power generation.

A combination of the two approaches is used in this chapter to design an antenna system for full-duplex communication in L band [C2]. Miniaturized antenna elements are placed on either the CubeSat body or the Earth-facing side of deployable solar panels. In the first stage, a single patch antenna per frequency band is designed. The high-permittivity substrate reduces the antenna size, but also causes the antenna to couple to the CubeSat chassis, distorting the radiation pattern. The effects of the pattern distortion are considered in detail for an arbitrary antenna placement on a 3U CubeSat body or deployable solar panels.

Antenna arrays are created in the following stages, using the designed patch antennas as array elements. The arrays radiate first two and then four tilted CP beams for an increased capacity of

the communication system. The sequential rotation of dual-band Tx/Rx LP antenna elements is used to generate CP radiation while halving the required number of antennas. Alternatively, the L-band antennas are combined with S-band elements as another way of minimizing the surface required for antennas on a CubeSat [C3].

The chapter opens with a short literature review on the planar antennas for solar cell integration. Although the integration level considered in this thesis is rather low, it was deemed necessary to compare the different approaches here, in order to show the difficulties and efforts associated with this task.

3.1. Review of Solar-Panel-Integrated Antennas

The CubeSat onboard power is limited and most of today's CubeSats have a majority of the surface covered by the solar cells, including the deployable solar-panel wings (see, for example, Figures 1.4 and 2.1). The power requirements lead to a contest for the precious satellite real estate, between the solar cells, antennas, sensors, and other features on the spacecraft surface. To overcome this challenge, several different attempts were made to combine the solar cells and antennas on the same surface, with an aim of maximizing the efficiency of both individual components. There are several ways of how antennas and solar cells can coexist on a common surface, depending on the spacecraft section:

- Satellite body:
    - Antennas below solar cells
    - Antennas and solar cells at the same level
    - Antennas above solar cells
- Deployable wings:
    - Antennas on the back side of solar cells (this thesis)

A detailed comparison of the possible integration configurations versus various antenna types and geometries are given in [61] alongside several demonstrated implementations.

Several examples are shown in Figure 3.1. Three variations of modified patch antennas, placed above and below the solar cells, are presented in [62] for CubeSat communication in UHF and S bands. One of the presented designs is a transparent patch antenna, where both the patch and the ground plane are made of a gridded conductor on a glass substrate. The entire design is to be placed on top of the solar cell with a minimal impact on the cell performance, due to a large antenna transparency. The CP performance was enabled using two sequentially rotated dual-band LP elements. A similar technique was adopted in [63] for the reflectarray elements on top of solar cells. A tradeoff between the metallic conductivity (copper or transparent conductors) and the optical transparency was demonstrated.

The described techniques are useful for scenarios where it is necessary to optimize the usage of the satellite body. Moreover, similarly as in conventional satellites, CubeSats usually have one or several deployable solar panels as a source of additional power supply. In LEO, the solar cells are placed on the panel sides facing away from Earth. This leaves the panel surface facing Earth available – ideal location for Earth-communication antennas. This feature was used in [13] to create a structure that contains a reflectarray on one face of the deployable panel and solar cells on the other, with a metallic ground completely isolating the two components.

Combining the two functionalities does not come free, as the total structure thickness must be minimal for a neat stowage on the CubeSat exterior. The antenna elements suffer the most from this limitation since the bandwidth of resonant element is reduced. The effect of a narrow bandwidth is more critical at low frequencies.

(a)
(b)
(c)
(d)
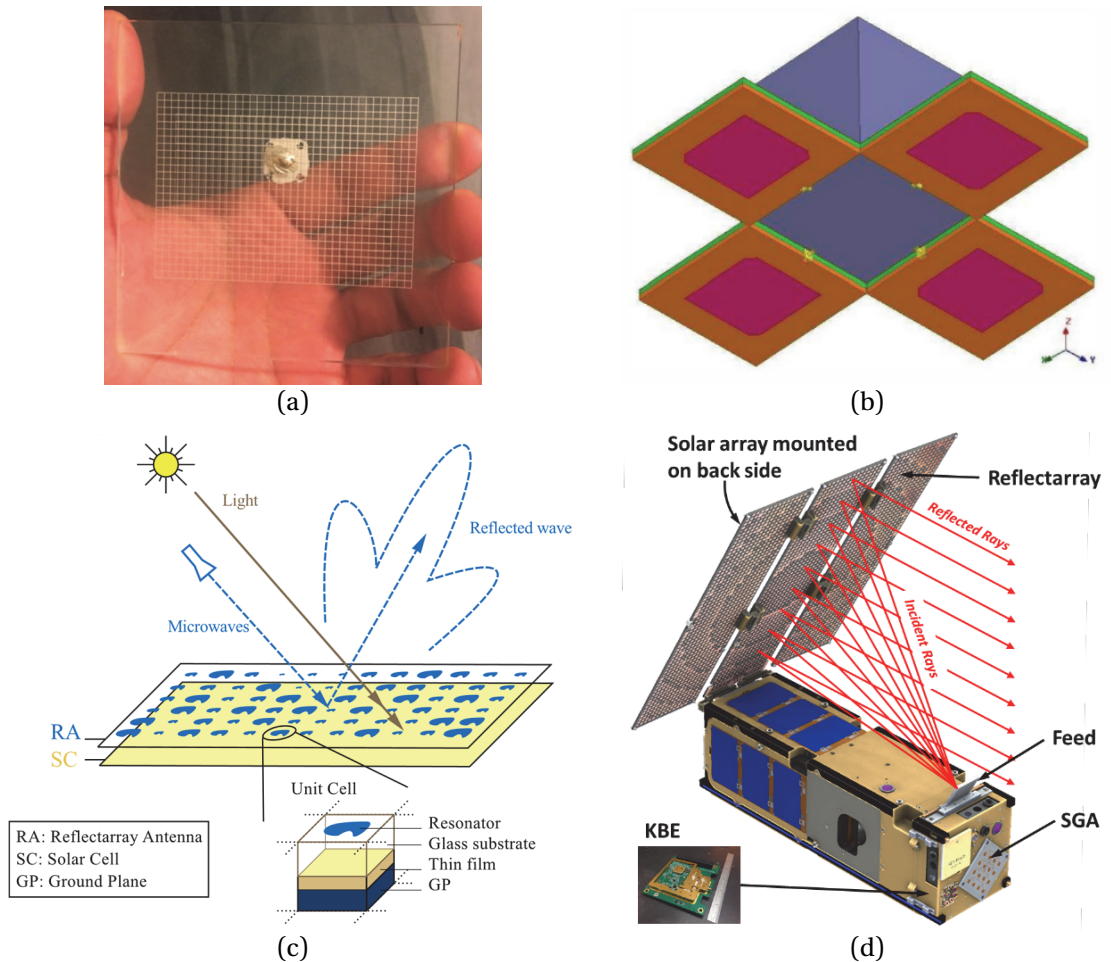
Figure 3.1. Solar-panel-integrated antennas. (a) Transparent-mesh patch antenna on a glass substrate [62]. (b) Deployable patch antenna array [64]. Reflectarray cells on the (c) same [63] and (d) opposite side of the solar cells [13].

3.2. Design Requirements

L band is not often used for CubeSat communication purposes, mostly radiometry [2]. However, the CubeSats can profit from the frequencies allocated for Iridium and other LEO satellite constellations. Such a scenario is considered in this chapter, where a duplex communication is specified, at the downlink (i.e. Tx, 1.525 – 1.555 GHz) and uplink (i.e. Rx, 1.6265 – 1.66 GHz) frequencies of the Mobile Satellite bands, allocated for the by the ITU [24]. The specifications correspond to bandwidths of ~2.2% per frequency band.

The requirements predict the evolution of the antenna system in several stages:

- Stage 1: Single 90° x 90° broadside beam
- Stage 2: Two 45° x 90° beams, tilted away from broadside by ~20°
- Stage 3: Four 45° x 45° beams, tilted away from broadside by ~35°

The purpose of multibeam radiation is to increase the total system capacity by several independent transceivers and an increased antenna gain per beam. Each beam must be served by both Rx and Tx frequencies for full duplex communication. The final operating frequencies of the system within the Tx/Rx bands will be only a subset of the specified range, and can be a subject of change over time. Therefore, the goal is to cover as much of the specified range as possible. The antenna gain should be larger than 5 dBi and the polarization should be circular.

The space allocated for the antennas is the 3U-CubeSat body for Stage 1 and the backsides of solar panels for Stages 2 and 3. Due to the previously outlined reasons, the antenna elements must have a low profile. The number of solar panels for the considered scenario varies from one to three 3U panels on each side of the CubeSat. A visual representation of the radiation-stage evolution is depicted in Figure 3.2. The number of solar panels on each side (two) is arbitrarily selected for this illustration.
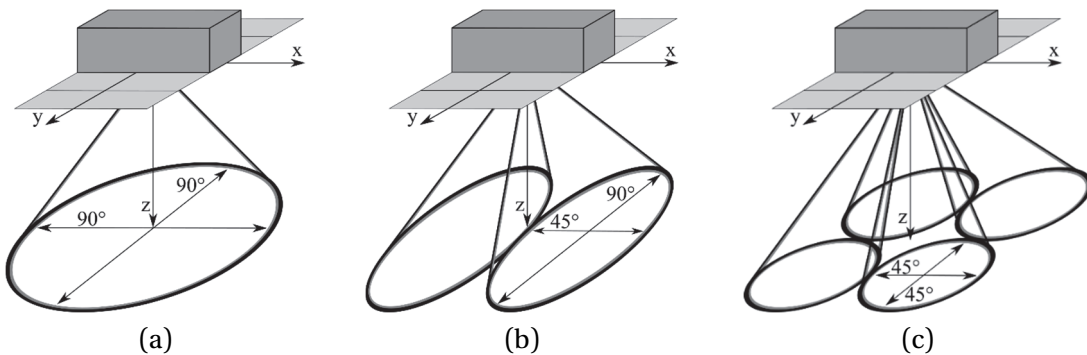
Figure 3.2. Evolution stages of the radiation-pattern configuration, having (a) one, (b) two, and (c) four beams.

3.3. Single Beam (Stage 1)

A broadside beam is easily generated by a single patch antenna element; the real difficulty here is to cover both Tx and Rx frequency bands by that same element. It is difficult to achieve the bandwidth of 8.5% and control the radiation characteristics with a single patch antenna, considering the strict profile limitation at L-band frequencies. Therefore, it was decided to use one patch antenna per frequency band (Tx/Rx). Although this configuration requires more space on the CubeSat exterior, the system design is simplified, as the transmitter and receiver are connected directly to the corresponding antennas and a diplexer is not needed inside the CubeSat.

The antenna size is indeed a key requirement, since two conventional L-band patch antennas require a majority of the 3U CubeSat face, leaving no space for other devices (e.g. S-band antenna). A high-permittivity dielectric material Rogers TMM10i (ε_r=9.9, tan δ=0.002, h=5.08 mm) is used for the antenna substrates, and the antennas are miniaturized through dielectric loading. The substrate has stable properties in a large temperature range – a desirable feature for space applications. The dielectric loading significantly increases the quality factor of the antenna, leading to reduced antenna dimensions, at the cost of a narrow frequency bandwidth. The two miniaturized patches fit comfortably on a 3U CubeSat face. As the radiator size is reduced, the beamwidth also becomes larger, consequently. The associated design tradeoffs are summarized in Table 3.1.

A small electrical size of the antenna causes the radiating element to couple to the satellite structure – an effect commonly seen in small antennas [65]. The effects related to the patch antenna placement on small spacecraft were briefly investigated previously [66]. In the following section, the effects are studied in detail, for the special case of CubeSats.

3.3.1. Chassis Coupling Effects

Throughout this chapter, the ground plane is approximated by a 300×100-mm^2 PEC rectangle, having in mind that the exact dimension of the CubeSat chassis is slightly larger. The ground plane dimensions accurately model both the large CubeSat face and the backsides of solar panels, whichever of the two is chosen for the final antenna location.

Three LP patch antennas, having different substrate permittivities, were placed asymmetrically on the 3U ground plane, and the S_{11} parameters and radiation patterns were calculated. The radiation patterns are also calculated on a 100×100-mm^2 (1U) ground plane, for comparison. The results clearly show a stronger main-lobe degradation for a higher substrate permittivity, indicating that the excited 3U ground plane is also contributing to the total radiation. The degradation can be observed for other antenna locations on the ground plane.

Table 3.1. Design tradeoffs for CubeSat patch antennas, versus the dielectric permittivity of the antenna substrate.

Relative permittivity (ε_r)	High	Low
Dimensions	+ Small	− Medium/Large
Beamwidth	+ Wide	− Medium
Bandwidth	− Narrow	+ Wide
CubeSat structure coupling	− Strong	+ Weak

The effect is predominant for the antenna polarization aligned with the long axis of the ground plane, as in Figure 3.3(a), and it is negligible for the orthogonal antenna orientation (not shown here). Nevertheless, a CP antenna will suffer from the same degradation effects.

In another set of models, a single CP antenna was placed on several locations on an identical ground plane, as in Figure 3.3(c), and the radiation pattern was calculated. It was observed that the main lobe shape strongly depends on the antenna position, and this effect must be carefully considered for a given antenna configuration [C2]. Furthermore, if there is a freedom of selecting the antenna position, it can be selected to exhibit a certain radiation pattern and suit a specific scenario. For example, the antenna offset of 0 mm yields a beamwidth of 110° and its shape resembles an isoflux pattern – a very desirable feature for LEO satellites in general. Note that this pattern shape is generated by nothing else other that a proper antenna placement.

In other words, the antenna coupling to the CubeSat structure is not necessarily a negative effect, and in some cases, it can be used to our advantage. Some researchers even propose to excite the CubeSat chassis itself for radiation, using a set of properly distributed small antenna elements [67]. In any case, the chassis coupling effects should not be neglected when designing CubeSat antennas, especially if the antennas are electrically small.

3.3.2. Antenna Prototype

As a high-permittivity substrate reduces the antenna bandwidth, a large substrate thickness was selected to alleviate this reduction. The antenna geometry is a square patch with chamfered corners for CP operation. Two patch antennas were designed and tuned for Tx and Rx frequencies. First antenna prototypes were fabricated and placed on a metallized 100×300-mm^2 FR4 panel for anechoic chamber measurements [C2]. The antennas are fed using a small MMCX connector with a lock-snap mechanism and connected to a VNA with an MMCX-to-SMA adapter. The antenna simulation model and the Rx antenna prototype are shown in Figure 3.4.

(a)

(b)

(c)

(d)
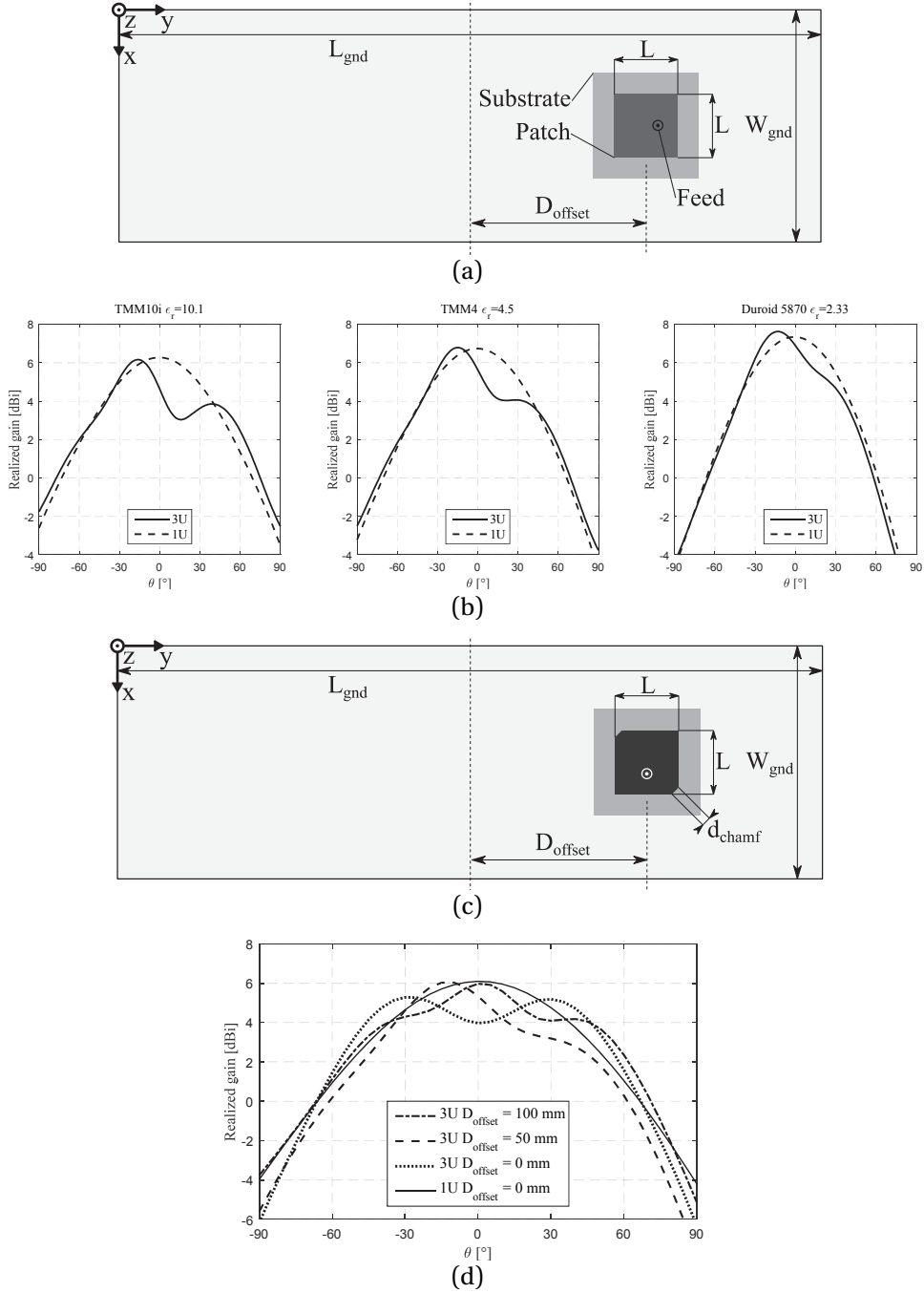
Figure 3.3. (a) LP patch antenna on a 3U CubeSat face. Dimension L changes according to the substrate permittivity, and the antenna is always resonant at the same frequency. (b) LP radiation patterns along the large axis of the ground plane, for various substrate permittivities. (c) CP patch antenna on a 3U CubeSat face. (d) CP radiation patterns along the large axis of the ground plane, versus the offset from the center. Radiation patterns of identical antennas, placed on a 1U CubeSat face, are shown for comparison. Default dimensions (mm): L=27, W_{gnd}=100, L_{gnd}=300, D_{offset}=75, d_{chamf}=4.25.

(a)

(b)   (c)
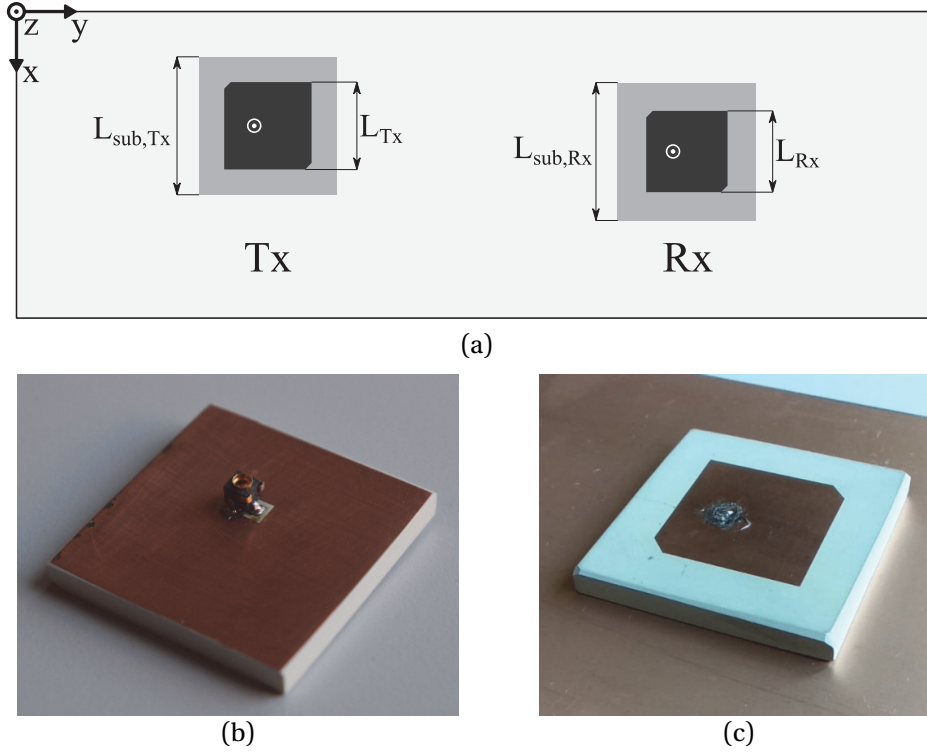
Figure 3.4. (a) Tx and Rx patch antennas on a 3U CubeSat face. (b,c) Rx patch antenna prototype. (b) Bottom, with the MMCX connector visible. (c) Top. Dimensions (mm): L_{Tx}=28.7, L_{Rx}=27, $L_{sub,Tx}$=$L_{sub,Rx}$=45.

After the first set of prototypes was characterized, a frequency shift of ~35 MHz was observed in the measured S parameters, as compared to the simulations (Figure 3.5(a)). The permittivity was tuned in the simulation models, and an estimated final value was found to be ~10.15 in L-band. After the correction, there was still a discrepancy attributed to the used connectors, which were not included in the simulation model.

Realized gain and AR values of both prototypes are presented in Figure 3.5(b). The gain of the Rx antenna is lower due to a mismatch introduced by the used connector, as can be seen in the S-parameter response. The measured and simulated radiation patterns of the Rx antenna only are compared in Figure 3.5(c). The results of the Tx antenna are omitted here, as that antenna exhibits a similar performance. The patches exhibit a wide beamwidth of ~90°, conforming to the design requirements. The radiation results show that the pattern in the φ=0° plane is not influenced by the antenna offset with respect to the long axis of the satellite face, except for a small beam tilt of 5°. However, there is a more significant pattern distortion in the φ=0° plane as a consequence of a large ground.

3.4. Two Tilted Beams (Stage 2)

The next considered scenario is having two 45° x 90° radiating beams, tilted away from broadside. The given configuration can be enabled using 2×1-element patch-antenna arrays. However, since the elements, described in the previous section, are single-band, a separate array must be assigned per beam and per frequency band. The total required number of antenna elements in that case is eight. Without the loss of generality, the scenario can be analyzed considering only the Rx patch antenna.

The patch antenna described in the previous section is used as an array element, and the inter-element spacing is tuned to provide the required beamwidth in the narrow plane. A two-element CP array is shown in Figure 3.6(a). The array center coincides with the ground plane center. The inter-element spacing of 100 mm yields a beamwidth of 45°, and the beam tilt of -20° is enabled by an appropriate relative phase shift.

3.4.1. Sequential Rotation of CP elements

Sequential rotation of the two elements can be used to improve the axial ratio performance in both frequency and angular coverage [57], [68]. The technique was implemented in the array shown in Figure 3.6(a), as the element rotation angles are selected as multiples of 90°. Active-S parameters were calculated at each port, which take into account both the matching and the cross coupling between elements. The individual active-S parameters from Figure 3.6(b,c) strongly depend on the relative rotation angle the cross-coupling value reaches -16 dB for some cases. The element rotation can be selected to simultaneously minimize the coupling and to keep the active-S parameters below -10 dB. The individual antenna elements can be further adapted for each rotation angle, but it was avoided here for simplicity.

Although this technique exhibits its real potential for a larger number of elements in an array, it has demonstrated a significant AR improvement even for only two elements considered here. The results of two representative array configurations are presented in Figure 3.6(d). A two-fold increase in AR bandwidth is obtained by the sequential rotation technique. Maximum gain reaches 7.5 dBi. The total array radiation was plotted in polar coordinates in Figure 3.7. The coverage area is indicated by a dashed line in the polar plots. The gain is larger than 3 dBi and the average AR value is 2.63 dB, along the entire specified angular range. An identical 2-element array is to be used to cover the opposite half of the hemisphere.

It might seem that the array performance is not as good as it could be expected from the single-element results. Several factors prevent further improvement:

- Beam scanning – The main lobe of the array is scanned to 20° from broadside, at which direction the element pattern naturally has a lower gain.

- Element rotation – Different orientation with respect to the ground plane cause the two elements to exhibit a slightly different radiation pattern.
- Element location – It is previously shown that the element position on the asymmetric ground plane is a dominant factor that determines the element radiation pattern. Although the elements' offset from the ground center is identical, the individual gain values are different in the beam-scanning direction.
- Cross-coupling – The radiation pattern of one element further changes in the presence of the other.

(a)

(b)

(c)
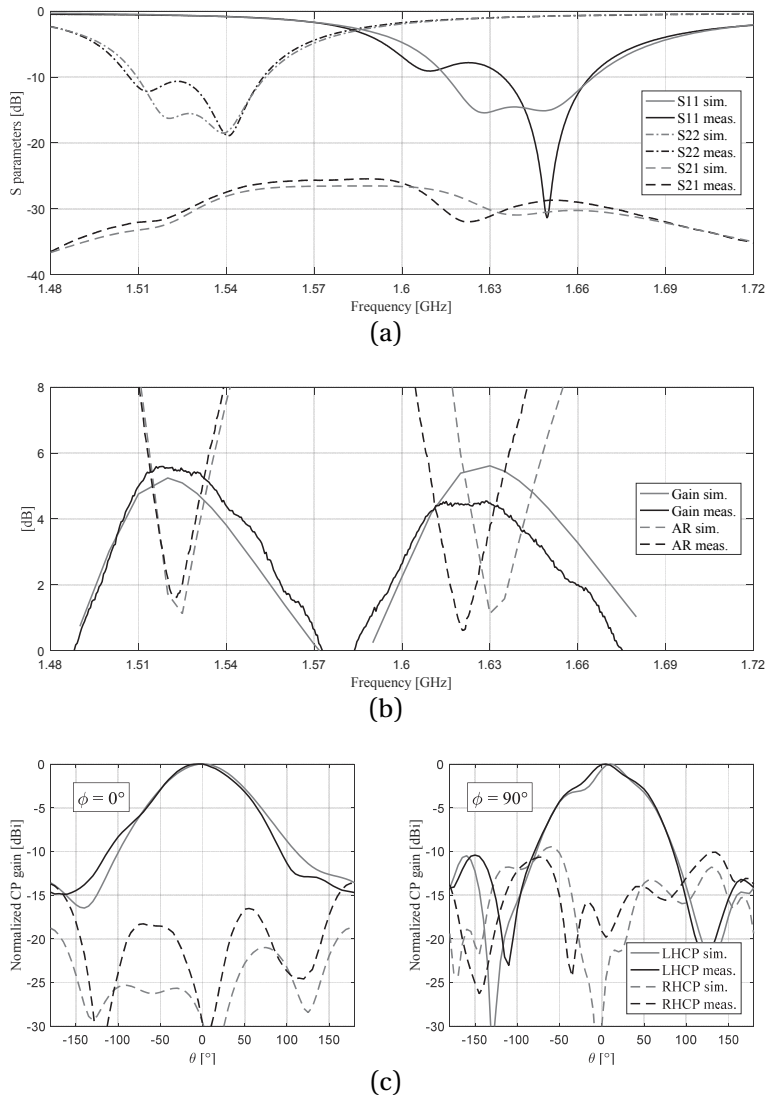
Figure 3.5. Simulation and measurement results of Tx and Rx patch antennas. (a) S parameters. (b) Broadside realized CP gain and AR vs. frequency. (c) Radiation patterns of the Rx antenna, in two principal planes, at 1.63 GHz.

(a)

(b)

(c)

(d)
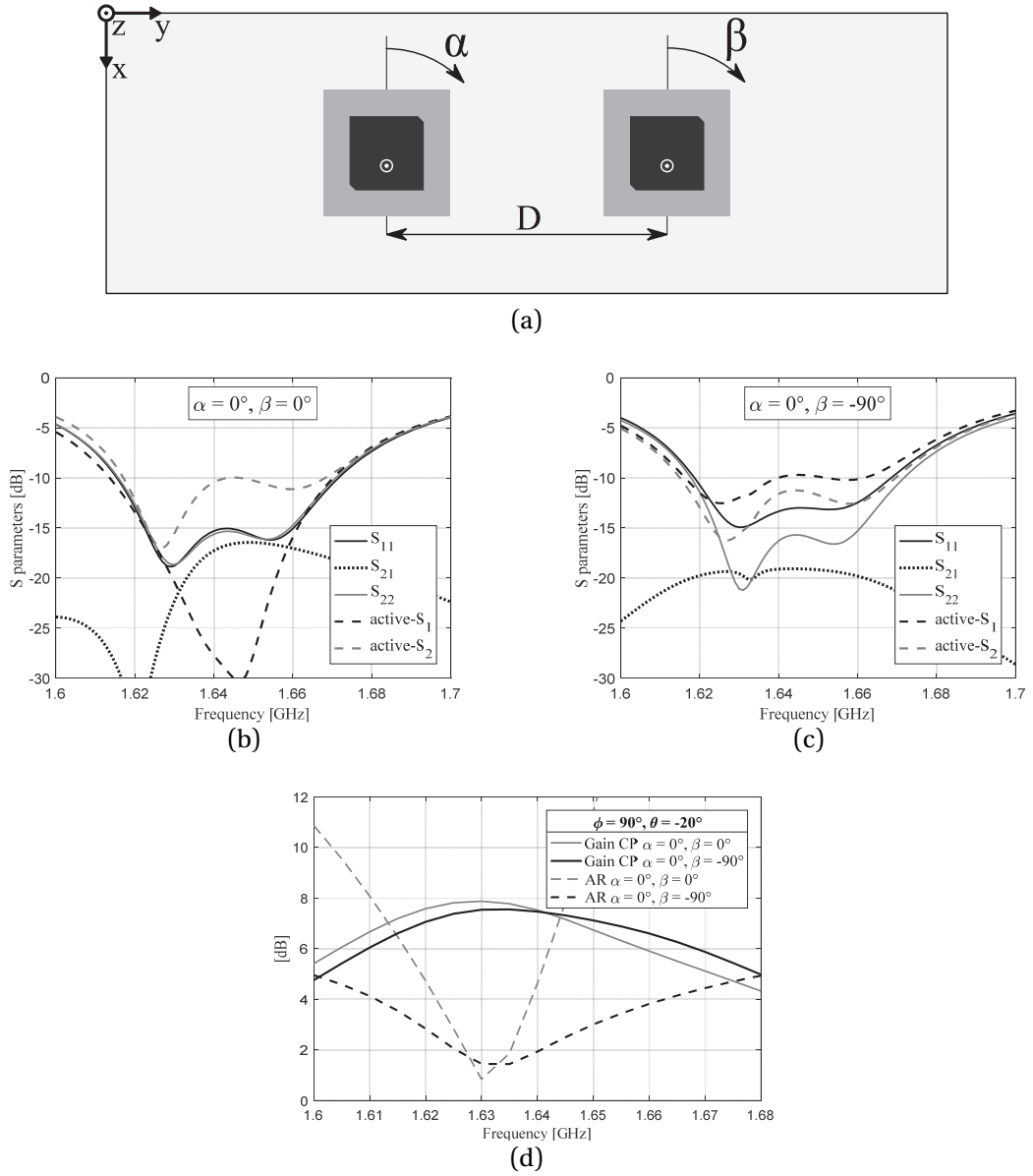
Figure 3.6. (a) A 2-element Rx patch antenna array on a 3U CubeSat face. (b,c) S parameters and active-S parameters, and (d) realized CP gain and AR, for the two rotation configurations, versus frequency. The gain and AR are calculated at $\varphi=90°$, $\theta=-20°$.
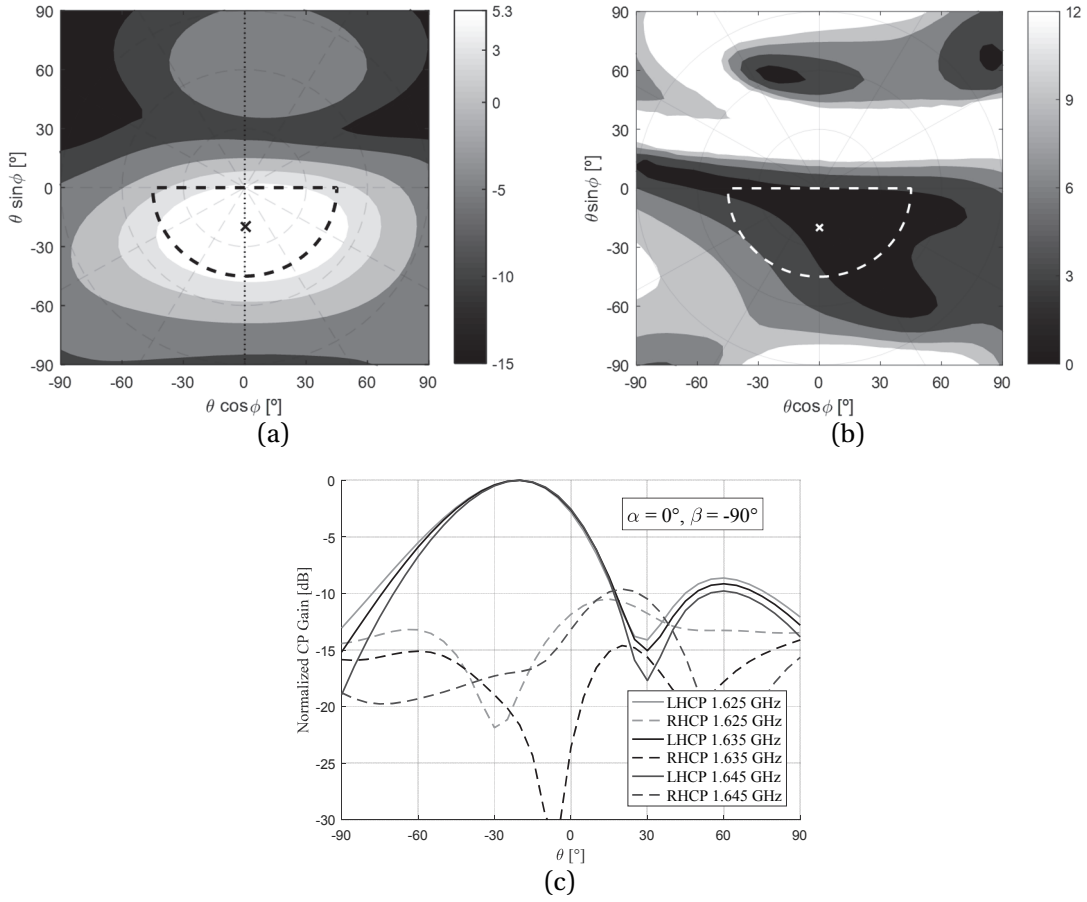
Figure 3.7. The radiation performance of a 2-CP-element patch array. Presented are contour plots in polar coordinates, at 1.63 GHz. (a) Realized CP gain. (b) AR. (c) Realized CP gain in the plane marked by a dotted line in (a). The rotation configuration is α=0°, β=-90°. Dashed lines and the cross indicate the coverage area and the beam scanning direction, respectively.

A MATLAB code was developed to visualize the beam footprint on the Earth's surface. The maximum half-angle of Earth visibility, seen from the CubeSat (θ_{max}), is a function of the orbit altitude, and can be obtained from Figure 3.8(a) using the relation:

$$\theta_{max} = \text{asin}\left(\frac{R}{R + h}\right) \tag{3.1}$$

The radiation pattern of the CubeSat antennas can be projected on the Earth surface by:

$$\theta = \text{atan}\left[\frac{R \sin\beta}{h + R(1 - \cos\beta)}\right] \tag{3.2}$$

where β is the angle between the CubeSat's projection and the observation point on the Earth surface. A contour plot, shown in Figure 3.8(c,d), is obtained using the function `sphere3d.m` [69].
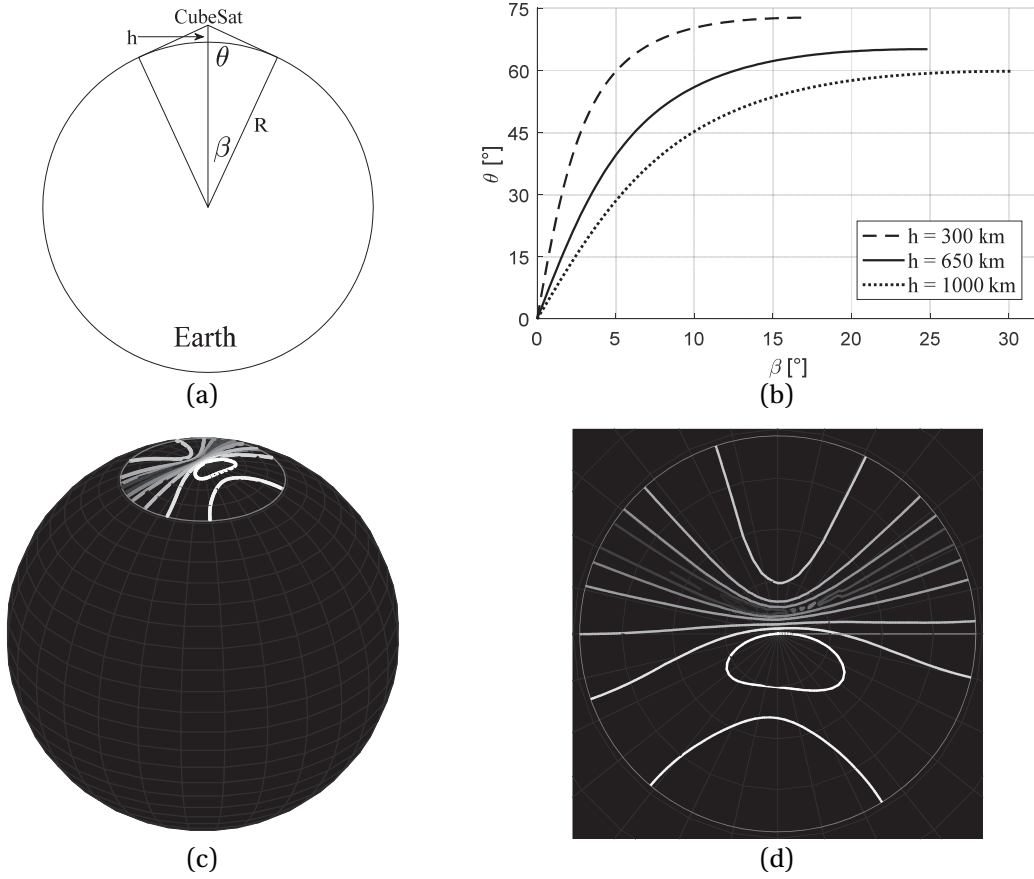
Figure 3.8. (a) The CubeSat's position above the Earth surface, with associated dimensions indicated. h=650 km, R=7378 km. (b) A visual representation of the relation (3.2). (c,d) The radiation pattern of the array from Figure 3.6, projected on the surface of the Earth.

A 650-km orbit was considered for the contour plot. The projection is useful for estimating the antenna coverage for a given radiation pattern. The results can be combined with the antenna transmitting power and the propagation losses to obtain the power density on the surface of the Earth.

3.4.2. Antenna Array Prototype

An array prototype was built using two patch antenna prototypes from the previous measurement campaign. The resonant frequency of both elements is 1.6 GHz. The MMCX connectors were replaced with SMA connectors and the measured S_{11} parameter was below -9 dB for both antennas. Two dedicated power dividers were built for the array radiation measurements. The power dividers consist of Wilkinson dividers and phase-delay lines, where the delay-line lengths are calculated to suit a specific antenna rotation scenario (0° or 90°). The array prototype is shown in Figure 3.9.

(a)

(b)

(c)

(d)
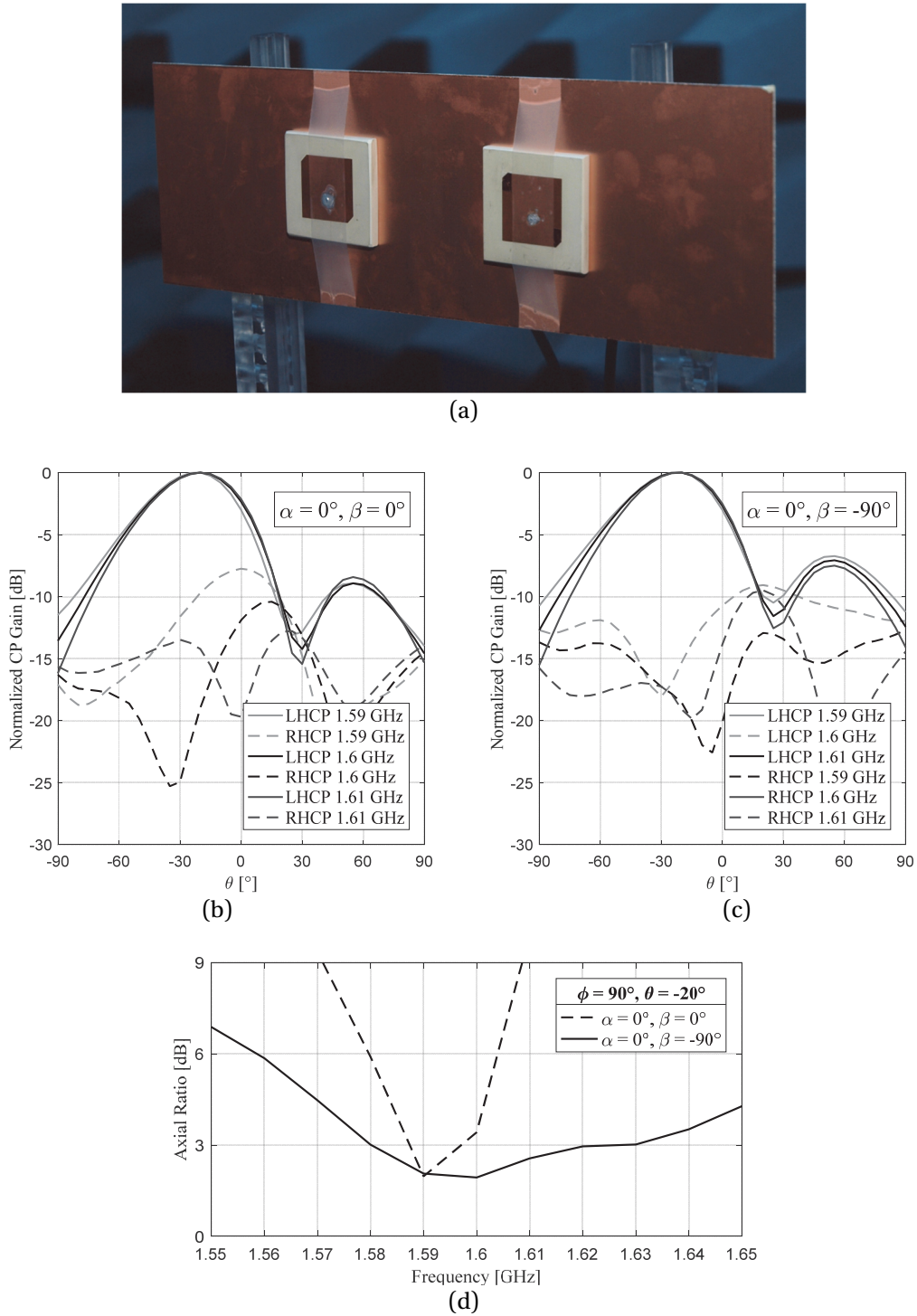
Figure 3.9. (a) Patch-antenna array prototype inside the anechoic chamber. (b,c) Measured radiation patterns, and (d) measured AR at φ=90°, θ=-20°, versus frequency, for the two rotation configurations.

The array was evaluated in an anechoic chamber for the two simulated configurations, and the radiation patterns are presented in Figure 3.9(b,c). The AR improvement of the sequentially rotated array was confirmed through the experiment, tripling the AR bandwidth of a single element, which can be seen in the same figure.

3.5. Four Tilted Beams (Stage 3)

Proceeding in the same fashion as until now, a four-element array is formed to radiate a 45° × 45° tilted beam. If the same technique is applied for the four-element array, as in the previous stage, the required number of elements would be 4 elements x 4 arrays x 2 frequencies = 32 antennas. This configuration is not acceptable for a CubeSat, considering the required surface, associated total weight and feeding-network complexity. Instead, a different approach is adopted.

Sequential rotation technique was initially proposed to generate CP radiation using LP antenna elements [57]. Here, we can simply modify our CP patch element into a dual-band dual-LP element. In that design, the two feeding ports excite two independent orthogonal modes in the patch, at two different frequencies. The mode independence means that it is possible to generate a distinct beam at the two frequencies, with dedicated feeding networks for each of the frequencies. The advantage of this method is the reduction of the total number of antenna elements by a factor of two.

The antenna array is shown in Figure 3.10, indicating the separate feeding locations for the two modes/frequency bands. The array radiation is calculated for three different scanning azimuth angles of -90°, -64° and -45°. The beam tilt is achieved with a varying phase of the excitation signals, on top of the fixed progressive phase in steps of 90°, which follows the physical rotation. The radiation patterns in polar coordinates are presented in Figure 3.11. The array layout, shown next to each set of figures, indicates the scanning direction that corresponds to the results in those figures.

The three beam-scanning scenarios show a comparable performance, with minor differences in AR levels at the ends of the coverage area. The last configuration (45°) shows a slightly lower average AR than the remaining two. The scanning angle will also depend on the CubeSat flying orientation and the network scenario. In any case, the results demonstrate that such array configuration can be used for a multibeam radiation scenario for LEO CubeSats. If a 4-element array of sequentially rotated CP patch antennas were scanned in the same direction, the AR performance would be further improved, at the cost of an increased number of antennas. The proposed configuration of four LP patch elements is the optimal compromise.
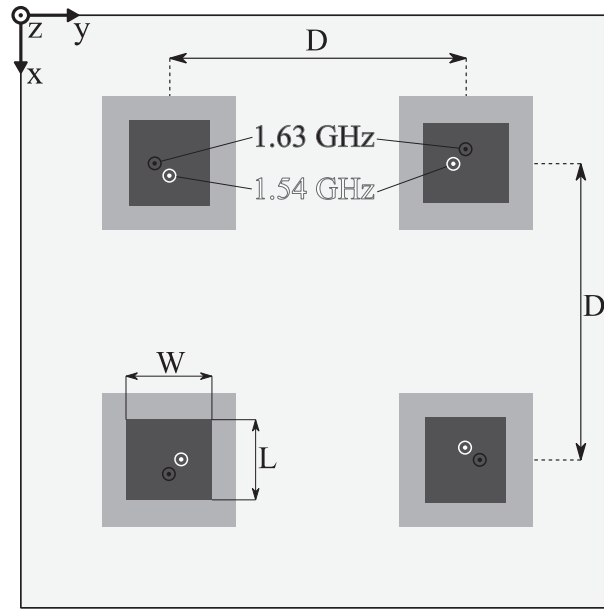
Figure 3.10. The geometry of a 4-LP-element patch array. Black and white circles mark the feeding locations of the 1.63-GHz and 1.54-GHz resonances, respectively. Dimensions (mm): L=27, W=29, D=100.

3.6. Stacked-Patch Antenna in L and S bands

Another way of reducing the surface allocated for the CubeSat antennas is to combine individual patch elements into a dual-band antenna. The approach is demonstrated in this section through a stacked-patch antenna operating in L and S bands. The S-band frequencies are the same as the ones considered in Chapter 2. Each of the two bands contains two uplink/downlink sub-bands and the frequencies considered in this section are arbitrarily selected throughout this section. The presented dual-band stacked patch can also be used as an element of an antenna array in L-band, with the S-band counterpart working as a standalone antenna.

3.6.1. Patch Antenna Elements

Linearly polarized (LP) square patch antennas, shown in Figure 3.12, were initially designed on several space-eligible dielectric substrates to study their size versus the dielectric permittivity. The thickness of the individual substrates was fixed at 3.18 mm, the substrate was 4 mm larger than the patch in each model, and the permittivity was varied from 2.33 to 9.9. The antennas were placed on a 100×100-mm^2 ground plane, which corresponds to a single 1U-CubeSat face. The patches were tuned to 1.54 GHz and 2.05 GHz, and the resulting geometrical parameters of all variations are given in Table 3.2.
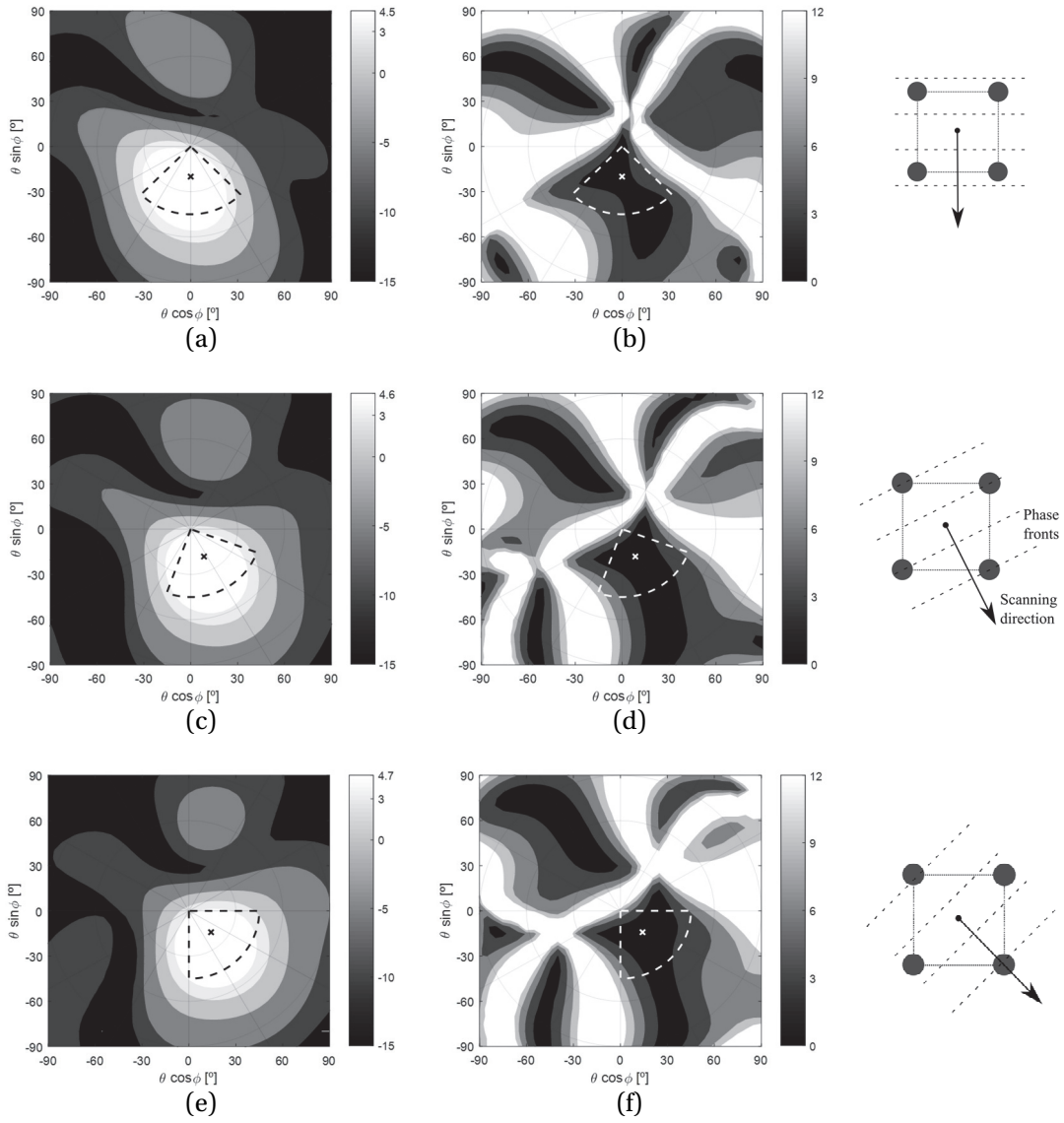
Figure 3.11. The radiation performance of a 4-LP-element patch array. Presented are contour plots in polar coordinates, at 1.54 GHz. (a,c,e) Realized CP gain. (b,d,f) AR. The scanning azimuth angle is (a,b) -90°, (c,d) -64°, and (e,f) -45°. Dashed lines and the cross indicate the coverage area and the beam scanning direction, respectively.

In a stacked-patch configuration, where each radiator is fed independently, the difference in individual patch sizes must be sufficient to increase the isolation. In addition, each of the patches must be exposed to the free space for a proper radiation. With that in mind, a typically chosen configuration is the one with the smaller high-frequency element on top [70]. However, considering the larger required bandwidth in the S band (4.1%), compared to the L band (2.2%), it was advantageous to use a low-permittivity substrate for the S-band antenna, as it would yield a larger bandwidth. For this reason, the geometry that was selected (bold cells in Table 3.2) has a

higher permittivity substrate and a smaller size for the L-band patch. Consequently, it is actually placed above the higher frequency S-band patch, contrary to the more conventional configuration [71].

Two antenna geometries were compared. In the first one, each patch is dual-fed with coaxial probes and a relative phase offset of 90° for the CP excitation. In the second one, the radiating elements are corner-chamfered single-fed patches. The two antenna geometries are shown in Figure 3.13(a,c). Circular holes are removed from the bottom patch in the feeding locations of the top patch. The bottom substrate is Duroid 5870 (S-band patch) and the top substrate is TMM10i (L-band patch). The S-band patch dimension has a large influence on the L-band resonant frequency, and the two patches must be tuned simultaneously.

S parameters of the two antenna geometries are shown in Figure 3.13(b,d). The dual-resonance behavior in the single-fed model is a consequence of the CP excitation method. A rather large coupling between the two elements (S_{13} and S_{12} parameters in the dual- and single-fed models, respectively) come from the fact that these ports excite resonant modes on the two patch elements with parallel current directions. As the radiating edges of the two modes are also parallel and close to each other, the coupling is large. Additional work is required to improve the port isolation, which was not the goal of this study. The radiation patterns show a larger beamwidth in L band, due to a higher permittivity substrate and a smaller patch dimension.

Table 3.2. Geometric parameters and performance LP patch antennas in L and S bands, versus the substrate permittivity.

	Substrate material	TMM10i ε_r=9.9	TMM4 ε_r=4.7	Duroid 5870 ε_r=2.33
L band	Patch [mm]	30	43	60.5
	x_{feed} [mm]	4	6.2	9
	Bandwidth [MHz]	13.7	23	27
	Gain [dBi]	5.8	6.5	7.2
	3-dB Gain BW [MHz]	54	71	82
S band	Patch [mm]	22.3	32.3	45.3
	x_{feed} [mm]	2.5	4.3	7
	Bandwidth [MHz]	22	32	43
	Gain [dBi]	6.3	7	7.8
	3-dB Gain BW [MHz]	68	100	131

Figure 3.12. LP patch antenna geometry.
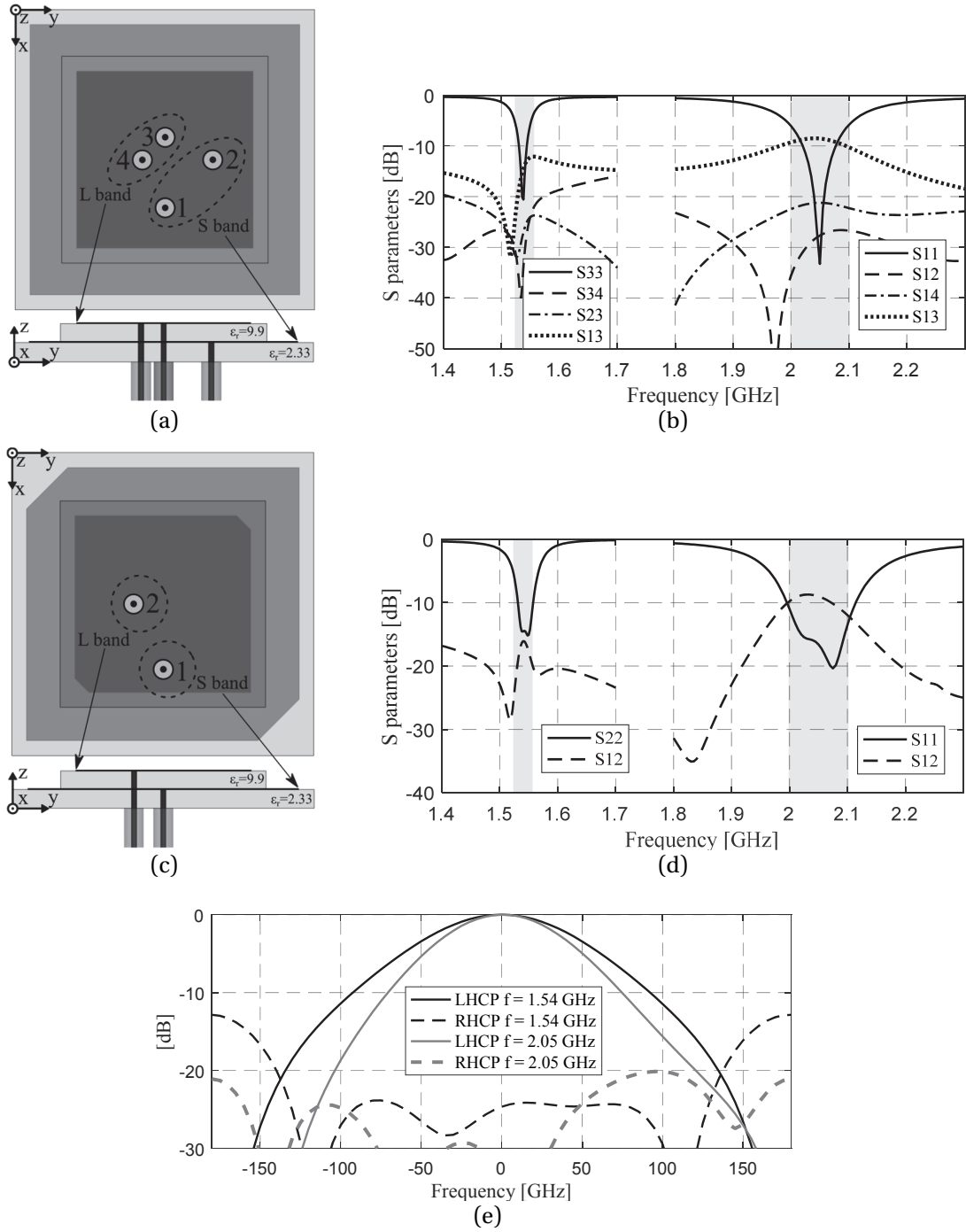
Figure 3.13. (a) Dual-feed stacked-patch antenna geometry and (b) the corresponding S parameters. (c) Single-feed stacked-patch antenna geometry and (d) the corresponding S parameters. (e) Radiation patterns of the dual-feed antenna in (a).

3.6.2. Feeding Networks

Three stripline feeding networks were designed and evaluated for the described stacked-patch dual-fed antenna structure. The networks are based on:

- T-junction power divider
- Wilkinson power divider
- Branchline coupler

The three network layouts are presented in Figure 3.14. In the first two, the phase difference is achieved with 90° phase-delay lines, whereas the branchline coupler has an inherent relative phase difference of the two output ports. However, it is also the largest, and some line meandering was required to reduce its total surface. Rogers RT Duroid 5870 was used for both dielectric layers of the stripline feed, each having a thickness of 0.508 mm. The stripline ground planes were grounded in several locations and shielded along the edges, to avoid the excitation of parallel-plate modes inside the frequency bands of interest. The shielding distribution is performed having in mind the S-band frequencies, where the modes will appear first. Coaxial probes are placed at the locations of the patch feeds.
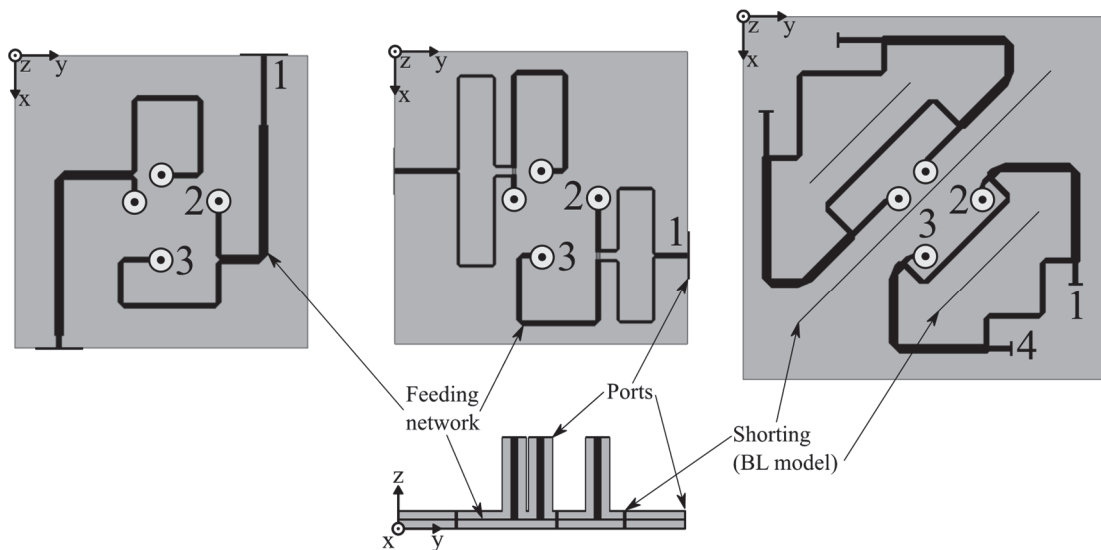
Figure 3.14. Models of the stripline feeding networks used for comparison: (a) T-junction, (b) Wilkinson-divider, and (c) branchline-coupler models. (d) Side view of the feeding networks. The two ground planes are shielded around the edges in all cases. Additional shielding is added in the branchline-coupler model.
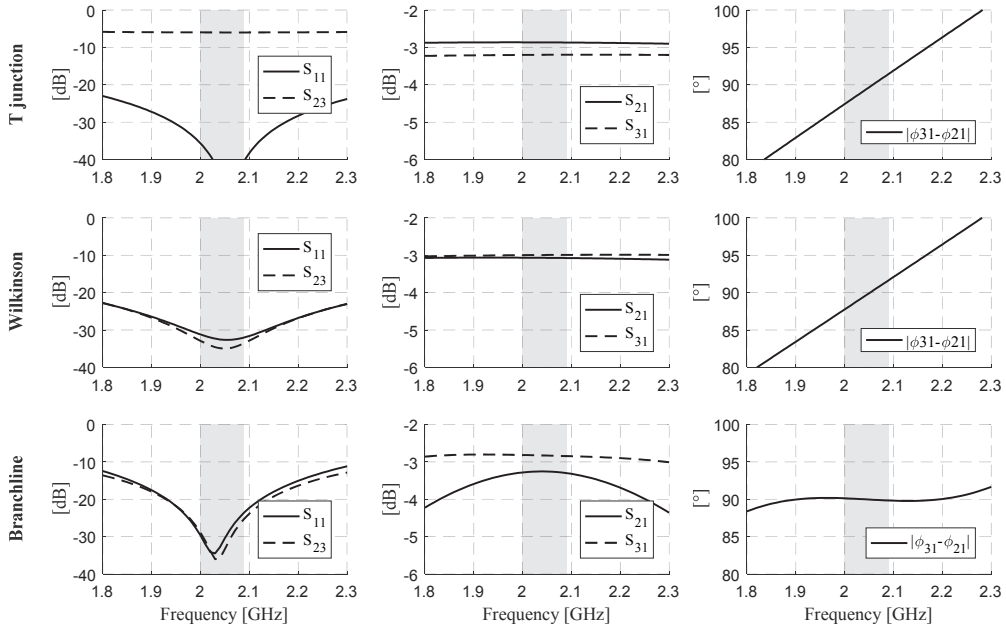
Figure 3.15. S parameters of the three feeding networks in Figure 3.14: (left) input matching and the isolation at the output ports, (center) power distribution at the output ports, and (right) phase difference at the output ports. The presented performance corresponds to the S-band section of each model.

The feeding network performance, without the patch elements, is compared in Figure 3.15. The results are presented for the S band, since the bandwidth requirement is larger in this case, and identical conclusions could be drawn from the L-band results. The delay lines used in the T-junction and Wilkinson-divider models provide a relative phase difference that varies linearly with frequency. However, the difference remains within ±2.5° along the required band. On the other hand, the branchline coupler exhibits a wideband phase difference. The output isolation is higher than 20 dB except in the T-junction model (6 dB). All three networks are matched at the input ports.

3.6.3. Full Antenna Models

Three antenna models in Figure 3.16, composed of the patch elements from Figure 3.13 and the feeding networks from Figure 3.14, were analyzed on a 100×100-mm² ground plane. The simulation results are presented in Figure 3.17.

The dual feed and the sophisticated feeding networks cannot influence the narrowband nature of the patch elements. In all analyzed antenna geometries, the radiating elements only accept the incident power at the close vicinity of their resonant frequency, and the remaining power is reflected in the feeding network. Therefore, the overall gain bandwidth changes only slightly among different models and is mostly limited by the narrowband S_{11} parameter of the dual-fed
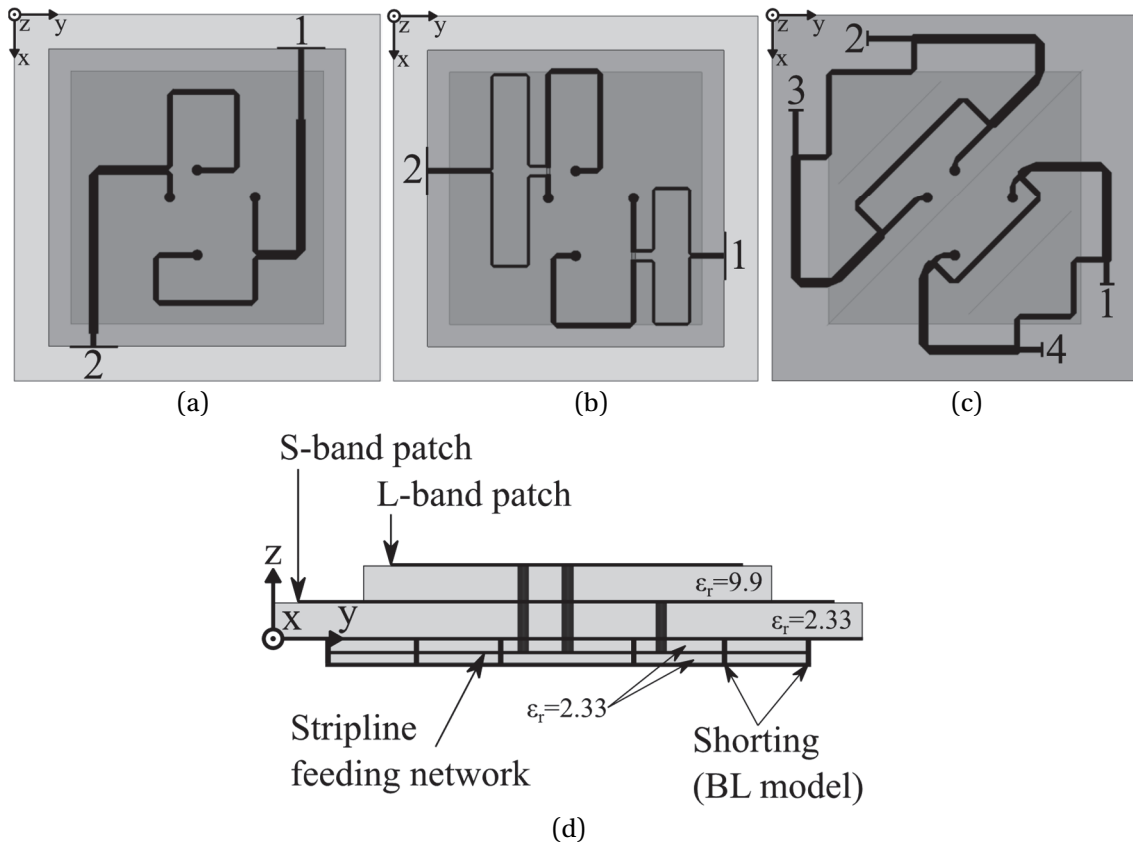
Figure 3.16. Antenna geometry of the three models: (a) T-junction, (b) Wilkinson-divider, and (c) branchline-coupler models. (d) Side view of all models.

patch element. On the other hand, the single-feed antenna elements from Figure 3.13(c) have a wider impedance bandwidth than the dual-feed models. In this case, the main factor limiting the gain bandwidth is the inherently low AR of the single-feed antenna geometry. Consequently, all four versions have comparable realized CP gain bandwidths.

The purpose of a feeding network is to provide a stable relative phase difference at the antenna ports, over a specified frequency range. Thus, only the AR bandwidth improvement can be expected if a sophisticated feeding network is used in combination with a narrowband radiating elements. The three feeding network configurations illustrate the discussed points.

In the case of the T-junction divider, the signals, reflected from the patch element, partially travel to the opposite antenna feed, contributing to the cross-polarization (see Chapter 2 for a detailed explanation). For this reason, the AR of the T-junction model is low only at frequencies where the S_{11} parameter is also low. In the other two scenarios (Wilkinson, branchline) the power reflected from the patch is dissipated in the resistors, which can be seen from the low S_{23} values in Figure 3.17. Consequently, the two models exhibit a wideband AR performance and impedance matching at the input ports. In fact, the S_{14} parameter of the branchline coupler model can be used

to estimate the return losses of the patch element itself. The S_{11} of the T-junction models, with two resonances, resembles the one of the single-feed model. However, this is because the FN (higher resonance) and the patch element (lower resonance) were not tuned to exactly the same frequencies.
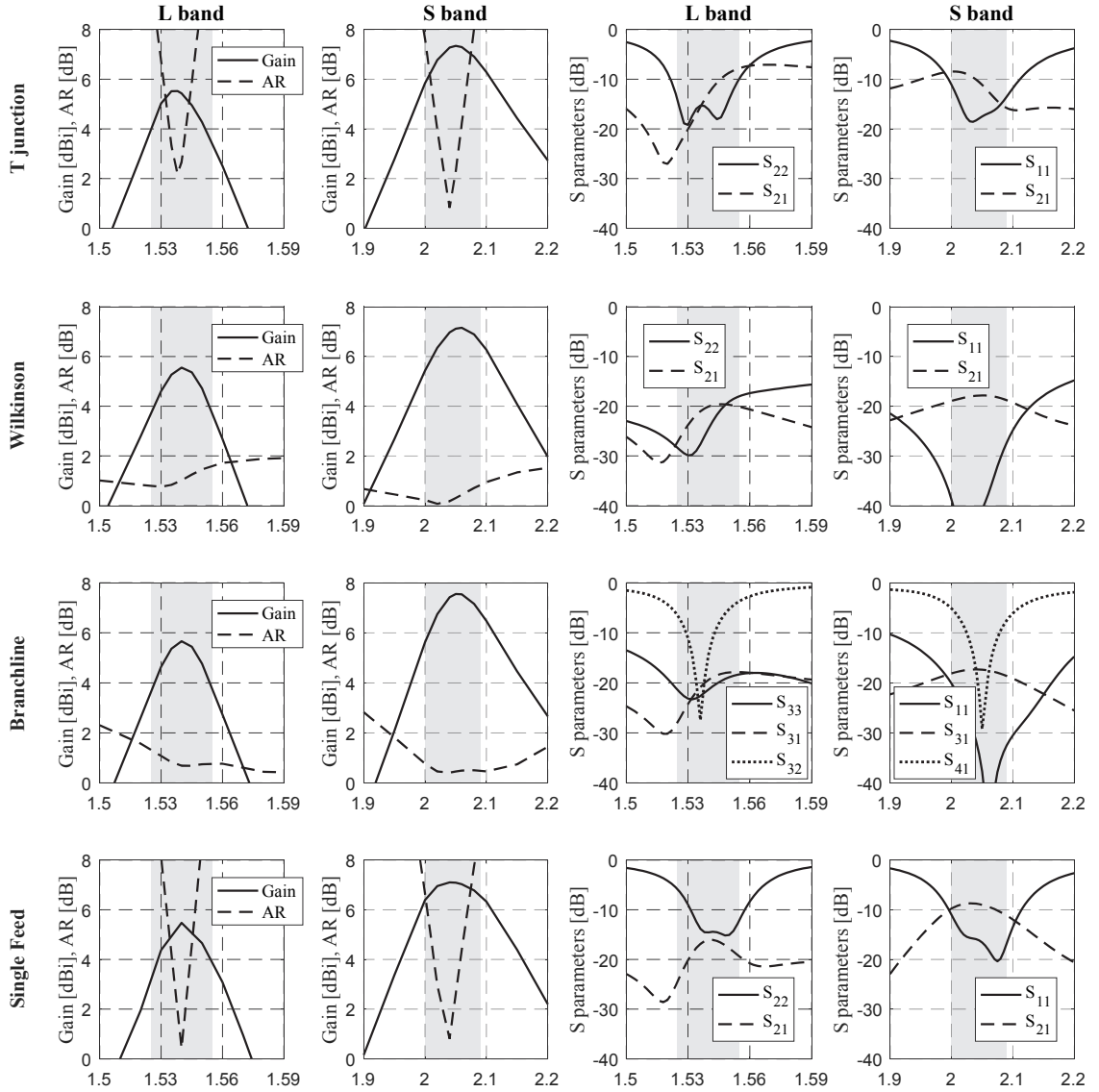
Figure 3.17. Complete antenna performance of (top) T-junction, (center-top) Wilkinson-divider, (center-bottom) branchline-coupler models in Figure 3.16, and (bottom) the single-feed model in Figure 3.13(c).

Of the analyzed models, the branchline-coupler model provides the most stable phase difference over a wide frequency band. However, having in mind the required bandwidths, the phase difference of the Wilkinson-divider model is sufficient here, even in the more limiting case, in the S band (4.9%). Considering all criteria, it was selected as the optimal for this application. A prototype of this antenna was fabricated and the results are presented in the following section.

3.6.4. Antenna Prototype

The antenna prototype was finally tuned to the Tx frequencies of L and S bands. A Wilkinson-based stripline FN was initially fabricated. Some complications were experienced while attaching the two stripline layers together, and this FN prototype was discarded. Another FN was realized in microstrip technology and used during experiments. The ground plane of the inverted microstrip FN acts as a ground plane for the patch elements above. SMA connectors are soldered vertically to the microstrip board. The two FNs were excited individually, one at a time, while the other one was matched with a coaxial 50-Ω load. The antenna prototype is shown in Figure 3.18. The measurement results of the full antenna, presented in Figure 3.19, confirm the predicted antenna performance. The main performance aspects are compared in Table 3.3. The input reflection coefficient corresponds mainly to the S_{11} parameter of the FN and the impedance bandwidth is therefore not specified. The broadside AR values are lower than 2 dB across the 3-dB-gain bandwidth, in all models. The beamwidth difference at two frequency bands is a direct consequence of the substrate permittivity, and thus, the patch size.

(a)   (b)
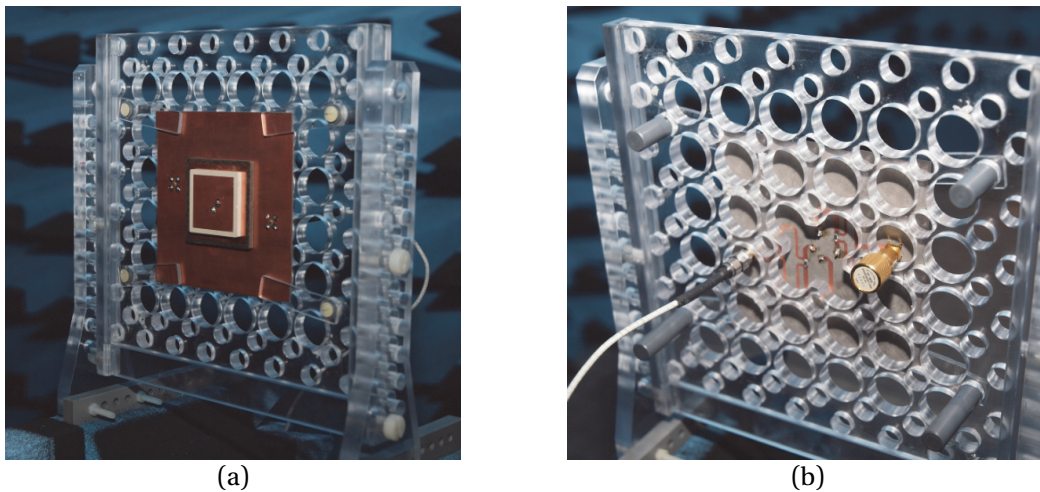
Figure 3.18. Stacked-patch antenna prototype in the anechoic chamber. (a) Front. (b) Back. The coaxial matched load is connected to the opposite FN connector.
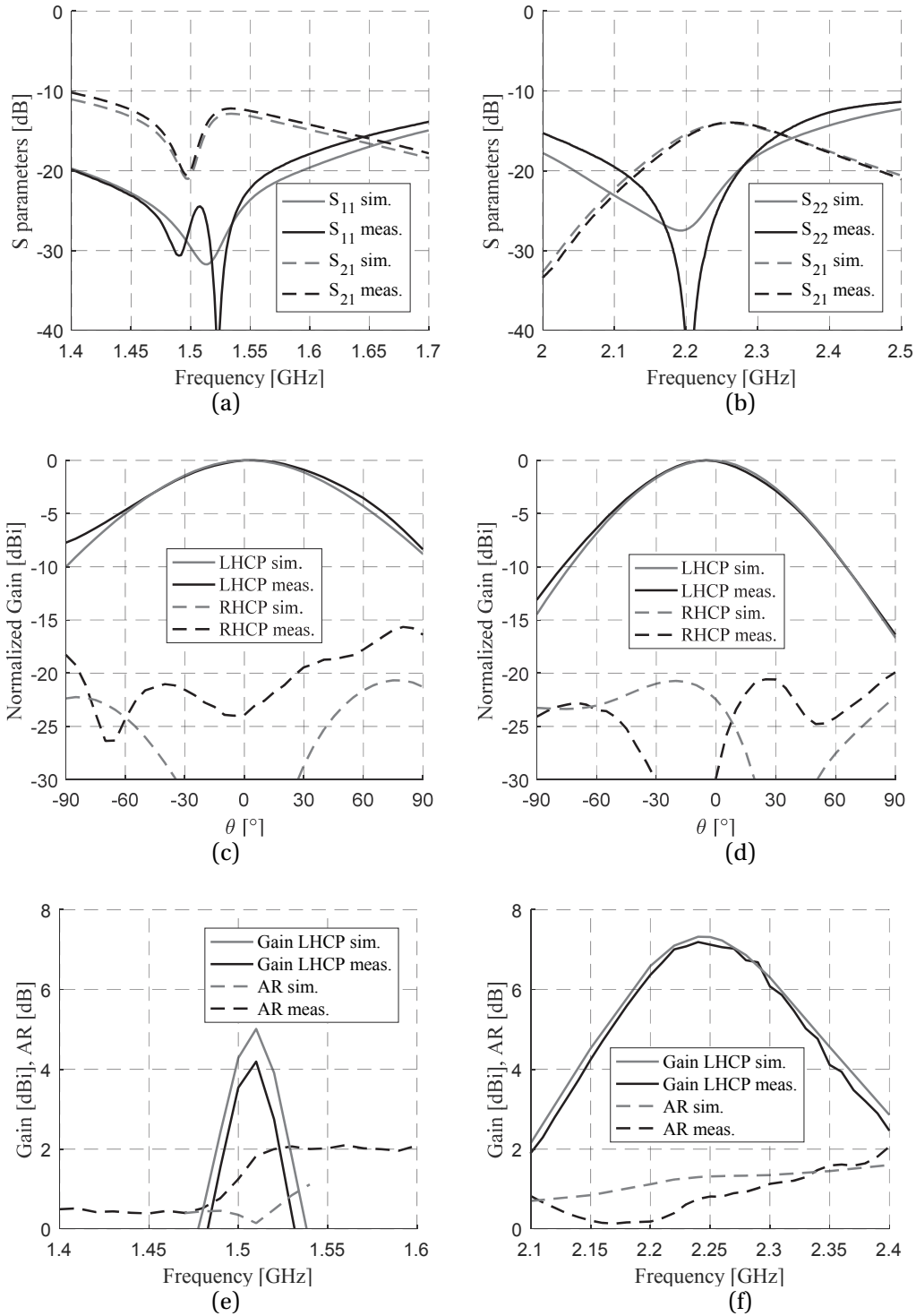
Figure 3.19. Measured and simulated performance of the dual-band stacked-patch antenna. (a,b) S-parameters. (c,d) Radiation patterns. (e,f) Broadside realized gain and AR versus frequency. The second resonance in the measured S_{11} curve of the L-band patch is frequency-shifted patch-antenna resonance.

Table 3.3. A comparison of the simulated and measured dual-band antenna performance.

	L band		S band	
	Simulation	Measurement	Simulation	Measurement
Maximum gain [dBi]	5	4.2	7.3	7.2
3-dB gain bandwidth [MHz]	40	40	200	200
Maximal AR [dB]	0.9	2	1.4	1.6
Beamwidth [°]	93	100	78	75

3.7. Summary and Discussion

A patch-antenna system in L band is proposed in this chapter, with a focus on 3U-CubeSat communication in LEO. The CubeSat's attitude-control system constantly maintains the satellite orientation with respect to the Earth. Therefore, the locations envisioned for the antenna elements include the satellite face and the backsides of deployable solar panels, which are facing the Earth at all times. Both antenna locations are approximated as $300 \times 100\text{-mm}^2$ PEC rectangles throughout this study. The chapter proposes several antenna configurations, which radiate of one, two and four independent beams.

Considering the small electrical size of CubeSats at L-band frequencies, dielectric loading with high-permittivity substrates is used to reduce the patch-antenna dimensions. A small, high-permittivity antenna exhibits a wide beamwidth, narrow bandwidth, and, most of all, strong coupling to the asymmetric ground plane, which causes the radiation pattern of the antenna to be deteriorated. A detailed analysis of the pattern deterioration showed that the antenna placement is critical for its radiation performance, and that it should not be neglected in the antenna design phase.

Two patch elements are tuned to the Rx and Tx frequencies in L band, and analyzed on a large face of a 3U CubeSat. In the next stage, the Rx element is used to create two-element sequentially rotated arrays and provide a beam tilt of 20° from broadside. The sequential rotation technique improves the AR over frequency, although the number of elements is rather small. The individual element pattern, caused by the coupling to the asymmetric ground plane, is shown to be the main limitation of the array performance. Nevertheless, the array satisfies the design requirements, covering the half of the coverage area. Another antenna array, and the two arrays corresponding to the Tx frequencies, yield a total of 8 antenna elements required for this scenario.

Proceeding in the same manner, a total of 32 patch elements would be necessary for 4 independent tilted beams, radiated by 4-element arrays of single-band elements. Instead, a Tx/Rx-dual-band dual-feed LP patch element is designed, which halves the required number of elements. A sequential rotation of LP elements is used to radiate CP beams, and the excitation phase of each feeding port can be tuned to independently scan the beams at Tx and Rx frequencies. At least four LP elements are necessary for satisfactory performance in the sequentially rotated array configuration. Therefore, this method cannot be implemented in the previous design stage. The total number of antenna elements is compared in Table 3.4.

In both the two- and four-element arrays, the patches are rotated in steps of 90°. Other angular steps (45°, for example) were not investigated, and could potentially further improve the array performance.

It can be argued that the described patch elements, in their current form, have a profile that is too large for a convenient stowage of the deployable wings, if the antennas are placed on their backside. All the effects studied in the scope of this chapter will be also valid for patch antennas with a smaller profile, except that the frequency bandwidth will be reduced.

A large number of L-band antennas might occupy a majority of the CubeSat's Earth-facing surface, not leaving enough space for other features, e.g. S-band antennas. For that reason, the L- and S-band elements are integrated in a single dual-band stacked-patch antenna in the last part of the chapter. To improve the AR, three FN, most commonly seen in the literature, were designed for each of the bands, and compared with a simple single-feed CP stacked-patch antenna. The FN based on Wilkinson power dividers is found to be the optimal compromise for CubeSat applications, in terms of its AR performance, size and complexity. Furthermore, the CP gain bandwidth of a narrowband patch element cannot be significantly improved, regardless of the FN selection.

Table 3.4. The total number of elements required for the arrays of the CubeSat antenna system in L band. Each beam is duplex and CP.

Frequencies	Stage	Beams	Elements per array	Element polarization	Feeds/bands per element	Total elements
2 (Tx/Rx)	1.	1	/	CP	1	2
	2.	2	2	CP	1	8
	3.	4	4	CP	1	32
				LP	2	16

3.7.1. Antennas Flying in Orbit

Several evaluated prototypes of individual patch-antenna elements and antenna arrays were fabricated and evaluated. The measurement results of all prototypes confirm the antenna performance, predicted through EM simulations. These are typically first or second prototype iterations. Afterwards, several other antenna designs, based on the ones presented in this thesis, were further optimized, including the tuning to the final operating frequencies. The two Tx and Rx antennas were launched in December 2018 and April 2019, on two of the Astrocast precursor satellites. Based on the communication-system tests, the antennas operate nominally. A modified version of the Rx patch antenna and the dual-band stacked-patch antenna are in the final testing phases, and will be launched on the first batch of commercial satellites in 2020.

4. Inter-Satellite Links for LEO CubeSats

The CubeSat technology offers a cost-efficient alternative to the conventional large-scale satellites, for achieving global coverage. The reason CubeSats became commercially attractive is their low development and deployment cost, which allows them to be efficiently launched to LEO. The advantages of any LEO satellite are low communication latency and propagation loss. On the other hand, the coverage area of a LEO satellite is small and the link duration with the ground is short (10-15 minutes), due to the low altitude and high orbital velocity, respectively. These inherent drawbacks render the global coverage impossible with a small number of satellites.

The solution is to use a large group of CubeSats to achieve global coverage. In that case, each point on the Earth's surface is in contact with at least one CubeSat at all times. A smaller orbit altitude would then mean a larger required number of CubeSats. However, the information that a CubeSat collects, or receives from communication devices, is inaccessible until the first time the CubeSat makes contact with a ground station and downlinks the gathered data. Given the fact that dedicated ground stations are sparsely distributed, the time delay can reach several hours. Such a latency is undesirable for most practical commercial applications, and unacceptable for communication purposes.

One impractical approach is to increase the number of ground stations, which would reduce the latency only by a small factor and virtually undo the low-cost nature of the CubeSat system [72]. Another idea is to interconnect the constellation in a network and allow the nodes (CubeSats) to exchange data among themselves. These connections can be established using inter-satellite links (ISL). The impact a connected space network can have is stunning, as the order of magnitude of the latency can be reduced from hours to seconds. Although the system complexity is unavoidably increased by introducing ISLs, it is the optimal solution to achieve a global coverage.

The design requirements for ISL antennas and the associated design difficulties are outlined in this chapter. An advantage can be taken from the specific CubeSat flying formation to simplify the conventional complex ISL antenna geometries. It is shown that deployable reflectarray and transmitarray antennas are good candidates for the ISL within a CubeSat constellation, when the surface of the CubeSat body is not sufficient for a planar antenna to achieve the specified gain.

4.1. Review of ISL Antennas

The first known ISL was established between *Orbiting Satellite Carrying Amateur Radio (OSCAR) 6* and *7*, two amateur-radio satellites on almost identical circular orbits. When the two spacecraft were 7000 km apart, *OSCAR 6* has received the signal, transmitted from *OSCAR 7*, and re-transmitted it, thus directly connecting two amateur Earth stations. In the following period, two-way communication has been reported between points on Earth as far as Japan and Finland [73]. The later ISL systems were more advanced, being developed for satellite formations with well-defined and maintained relative positions. ISL communication exists in S-band and Ka-band frequencies, as well as in the optical range. An exhaustive study of the past, current and future ISL antennas is presented in [74]. A survey of ISL communication systems for small satellites can be found in [75].

Data relay satellites represent the first and the largest group of satellites that utilize ISLs. The purpose of a relay satellite is to connect two satellites, ground stations, airplanes, etc. that cannot establish a line-of-sight communication. Most famous examples of such systems in GEO are the Tracking and Data Relay Satellite System (*TDRSS*) [76] and the European Data Relay System (*ERDS*) [77], which primarily serve to enable cross-links between other LEO satellites and ground stations. These satellites use ISL frequencies from S to Ka bands to relay data using directional antennas. A notable non-GEO example is the *Iridium* constellation for satellite phone and data, shown in Figure 4.1 [78]. *Iridium* satellites are distributed in several polar orbits and have four K-band phased-array ISL antennas – two for ISLs in the same orbital plane, and one for each of the two adjacent planes. Common feature for all of these satellites is their large size (antenna diameter up to 2 m) and mass (up to several tons).

A second smaller group of satellites using ISL includes small formation flying missions, almost all being technology demonstrations. This group is particularly interesting for CubeSat ISLs, since the described spacecraft is much smaller in mass in volume, compared to the first group. A good example is the Canadian Advanced Nanospace eXperiment (*CanX*), which is a dual-nanosatellite formation-flying demonstration mission [79]. *CanX* 4 and 5 satellites are two identical 8U CubeSats ($200 \times 200 \times 200$ mm^3) which communicate at S-band frequencies. Two ISL patch antennas are placed on opposite sides of the spacecraft, and each antenna provides hemispherical coverage.
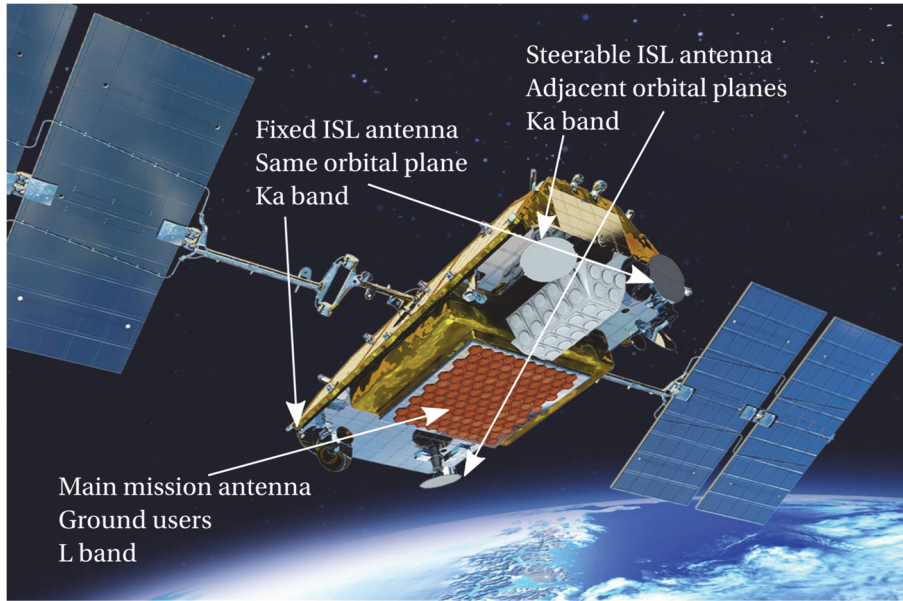
Figure 4.1. Iridium NEXT satellite [80]. Four phased-array ISL antennas are visible, out of which two serve for ISLs in the same orbital plane, and one for each of the two adjacent orbital planes. L-band antenna radiates 48 beams for users on Earth.

Another example is the Network and Operation Demonstration Satellite (*NODES*) mission, whose objective was to test the control of connected small-satellite swarms that make distributed scientific measurements [74]. The two *NODES* are 1.5U CubeSats that achieve the ISL through two UHF monopoles.

Except for the mentioned examples, no ISL systems or antennas for CubeSats have been demonstrated to date. On the other hand, several innovative high-gain CubeSat antennas were designed for different purposes, such as radar, communication, and even deep space. These antenna geometries are very promising candidates for CubeSat ISL applications, in scenarios where the satellite relative orientation and distance are defined. The most interesting geometries were designed in the Jet Propulsion Laboratory (JPL), among which are several deployable reflectarrays and a deployable mesh reflector antenna, shown in Figure 4.2. The LP reflectarray (RA) antennas are composed of square patch elements and operate at X and Ka bands, with a total deployed surface of approximately 18U and 9U, respectively [7], [13]. A very interesting feature for ISL applications is the capability of CubeSat RA antennas to tilt their beams at an arbitrary direction, regardless of the relative position of the deployed panels with respect to the CubeSat body.
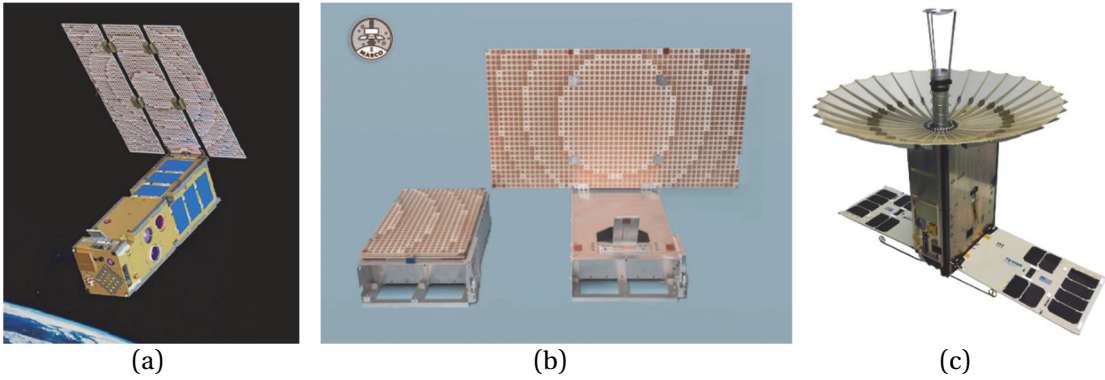
Figure 4.2. High-gain CubeSat antennas designed at JPL. (a) Integrated Solar Array and Reflectarray Antenna (*ISARA*) [13]. (b) Mars Cube One (*MarCO*) reflectarray antenna [7]. (c) Deployable Ka-band mesh reflector antenna [11].

4.2. ISL Communication Scenarios

Depending on the mission design, the configuration of the satellite constellation can vary, from flying in clusters, to well-ordered formations. The most common formation types, depicted in Figure 4.3, are [23]:

- **Trailing** – every satellite of the group flying in the same orbit with an equal relative distance
- **Cluster** – satellites follow individual orbits which allow them to remain with a dense, tightly spaced arrangement
- **Constellation** – a set of satellites organized in several orbital planes, that cover the entire Earth, with sufficient overlap in ground coverage
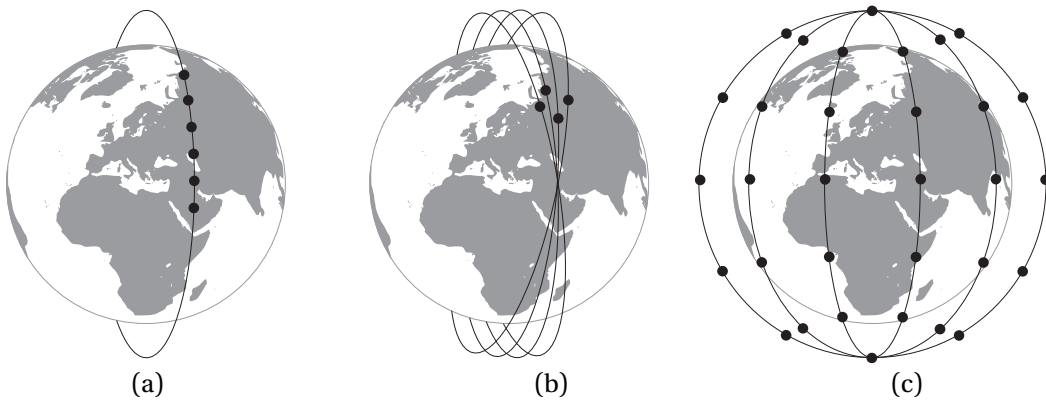
Figure 4.3. Common types of satellite flying formations. (a) Trailing. (b) Cluster. (c) Constellation.

Depending on the selected flying formation, the ISL antenna design requirements can vary drastically. In an ideal case, each spacecraft should have a number of dedicated high-gain scanned-beam antennas for communication with several neighboring satellites. Such solutions have been implemented in large-scale satellites, such as the *Iridium* constellation. This can be afforded since the total mass of every *Iridium* satellite is over 600 kg. The dimension and weight limitations of CubeSats, however, require simpler ISL designs in terms of mechanical requirements and total volume.

In order to conform to the specifications without drastically increasing the complexity and cost, the antenna design must be suited for the specific flying formation. In cluster formations, as the spacecraft relative position and orientation is not defined, omnidirectional antennas are preferred, which are mechanically simpler, at the price of a modest data rate. Trailing and constellation formations do not necessarily require a scanned beam, if the satellite attitude can be maintained with precision higher than the antenna beamwidth. These constellations can consequently profit from cost-efficient high-performance fixed-beam antennas, without the need for a complex scanning scheme (electrical or mechanical).

In this thesis, a constellation formation is considered, where N CubeSats are distributed along a single orbital plane, and the entire system is composed of M such orbital planes, for a total of N x M satellites. It is also considered that at least one CubeSat from each orbital plane is in contact with a ground station, and there is no need for a link between CubeSats from different orbital planes. Therefore, the CubeSats of a single orbital plane communicate in a ring network, where each satellite establishes a link only with two adjacent satellites, as shown in Figure 4.4. The CubeSats are required to communicate in both directions along the ring. Two scenarios are possible:

- Single frequency – All CubeSats communicate at a single ISL frequency. Two-way communication is performed in a form of time-division multiplexing (TDM).
- Dual frequency – Every ISL is two-way and consists of two channels, forward and return, at separate frequencies.
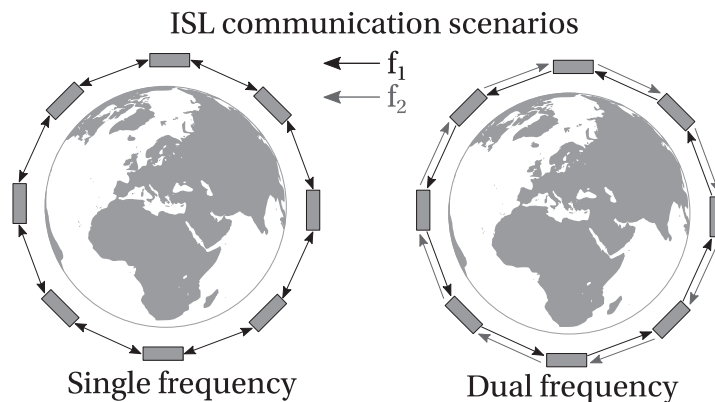
Figure 4.4. ISL communication scenarios.

A single communication channel simplifies the system design of the first scenario, but limits the total system capacity, as the communication can be performed only in one direction at a time. The second scenario offers a continuous two-way communication. However, the dual-band links complicate the ISL system design, primarily its RF part, as it will be shown in the following sections.

4.3. ISL System Requirements

The key-enabling component of an ISL system is the antenna. Being a subject of strict mechanical limitations and EM requirements, the antenna is challenging to design. The antenna geometry mostly depends on the RF specifications, which are determined by the link budget calculations for the ISL system. In the case of the considered CubeSat constellation, the main requirements are a high-gain fixed-beam radiation pattern and the antenna bandwidth that covers the frequency band(s) of interest. The following section discusses different aspects of the ISL requirements.

4.3.1. Frequency

An individual CubeSat, which is a part of a constellation with a global coverage, will require collecting and handling a large amount of data. The data is gathered, for example, by Earth observation, tracking or communicating with a large number of devices, etc. The ISL is the bottleneck of the constellation network, since all the collective data is aggregated and sent through it. Therefore, the capacity requirement of the ISL is several times that of any individual channels for data uplink/downlink. As an excellent example, the satellites of the Iridium constellation in Figure 4.1 (not CubeSats, but a valid example) provide voice and data services in L band and ISL in Ka band [78]. The millimeter-wave ISL naturally provides a high-capacity connection for the aggregated user data, in real time.

The ISL frequency bands are sparsely allocated below 40 GHz, only in S, K and Ka bands [24]. The bands above 40 GHz require sophisticated RF technology that is not mature enough for commercial CubeSat applications. The choice of ISL frequencies is therefore limited to either S or K/Ka bands. The tradeoff between these two bands is presented in Table 4.1. Although the propagation loss is lower at S band and the antenna-gain requirement is not as stringent as for the Ka band, the antenna dimensions (for instance, a deployable helix) would still have to be significantly larger than the Ka-band counterpart. Furthermore, the S-band link capacity could be insufficient to support the ISL data rate. Thus, K/Ka bands are selected as optimal for the high-data-rate ISL communications in a CubeSat constellation.

Table 4.1. Tradeoff between available frequency bands for ISL.

	S band	K/Ka band
Propagation loss	+ Small	– Large
Antenna size	– Very large	– Large
Data rate	– Low/Medium	+ High
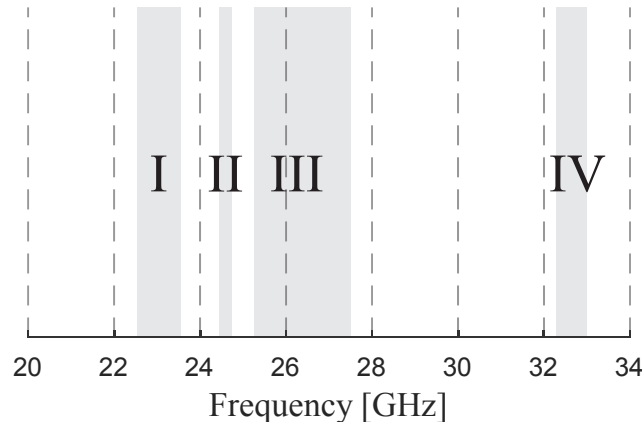
Figure 4.5. A visual representation of the frequencies allocated for ISL applications in K/Ka bands.

Several individual ISL bands are allocated at K/Ka-band frequencies, and visually represented in Figure 4.5 [24]. A large variation of the frequency bandwidths (from 1.2% to 8.5%) may require different antenna solutions, depending on the selected band. Some of the wider bands are composed of narrower segments, and it is expected that only a subset of frequency segments will be eventually used. However, the exact center frequency within a band may vary over time, and the goal is to cover as many frequencies of a given band as possible.

4.3.2. Antenna Radiation

The radiation requirements for the ISL antenna are derived from the CubeSat mission parameters. The CubeSat configuration related to the described process is depicted in Figure 4.6.

1. After the orbital altitude is specified, low-frequency user antennas (L band in this case) are designed with sufficient beamwidth for the required coverage of a single CubeSat.
2. The total number of CubeSats per orbital plane N is determined from the full-coverage condition in a single plane. The number of orbital planes is found in a similar manner.
3. For a given number of CubeSats, the ISL beam tilt, away from the orbit tangent, is fixed and is calculated simply by:

$$\theta_0 = \frac{\pi}{2} - \frac{1}{2}\left(\pi - \frac{2\pi}{N}\right) = \frac{\pi}{N}. \tag{4.1}$$

For practical LEO applications, the beam-tilt angle is always smaller than 30° and the associated scanning loss smaller than ~0.6 dB.

4. The inter-satellite distance is obtained by:

$$d_{ISL} = (R_E + h)\sqrt{2\left(1 - \cos\frac{2\pi}{N}\right)} \tag{4.2}$$

where R_E and h are the Earth radius and the orbit altitude, respectively. The path loss is calculated at the ISL frequency.

5. The antenna-gain requirement is found using the link budget calculations (path loss, data rate, modulation, coding, etc.). The preliminary value of 30 dBi was obtained for eight satellites per orbit, with a minimum bit rate of 0.5 Mb/s using the QPSK modulation.

6. The ISL antenna beamwidth is estimated from the antenna gain and compared against the angular stability of the CubeSat's ADCS.

The satellite attitude must be maintain by the ADCS, so that the high-gain ISL antennas accurately point towards the adjacent CubeSats. If the angular precision of this system is smaller than the ISL antenna beamwidth, the link cannot be constantly maintained and one of the design decisions must be revisited. Shaped-beam radiation patterns (for example, a flattop beam) are an interesting option to tackle a poor-performing ADCS, at the cost of a reduced maximum gain. This antenna functionality is not considered in the scope of this thesis.

4.3.3. Antenna Size

The small wavelength at K/Ka-band frequencies provides a large freedom in the antenna design. The design process, in this and following chapters, focuses on the case of LEO CubeSats, and, more specifically, 3U CubeSats having their long axis aligned with the orbital velocity vector. In other words, the small CubeSat face (1U) is facing the adjacent satellites within the same orbital plane. This orbital attitude allows several TT&C and payload antennas to be accommodated on the large CubeSat face and oriented towards the Earth.

A natural approach in this case is to allocate the two small faces for two low-profile ISL antennas. However, by calculating the achievable directivity with an aperture of that area, having a realistic antenna efficiency, it can quickly be seen that an antenna, with a total area equal to that of a 1U face, cannot provide the specified antenna gain.

An ideal, uniformly illuminated antenna aperture provides a maximal antenna directivity. In practice, the electric field across the aperture is non-uniform, and the loss related to this effect is described by the aperture efficiency η_a, with typical values between 0.4 and 0.7. A theoretical antenna directivity, versus the aperture efficiency, is calculated by:

$$D = 10 \log_{10}\left(\eta_a \frac{4\pi A}{\lambda_0^2}\right) \tag{4.3}$$

where A is the total aperture area. The aperture efficiency η_a in the previous expression does not include the dielectric and ohmic losses of the antenna (the antenna efficiency is described in detail in Chapter 6). The directivity is calculated for different efficiency and area values, and represented graphically in Figure 4.7. Two points should be noted when inspecting this figure. Firstly, it only shows theoretical values of directivity, not including any losses related to antenna mismatch, polarization, dielectric or ohmic losses, etc. Secondly, the directivity is calculated at broadside, and the results should be multiplied by a cosine factor for a tilted beam. In other words, the final antenna size must be selected with an additional margin, to account for the mentioned losses.
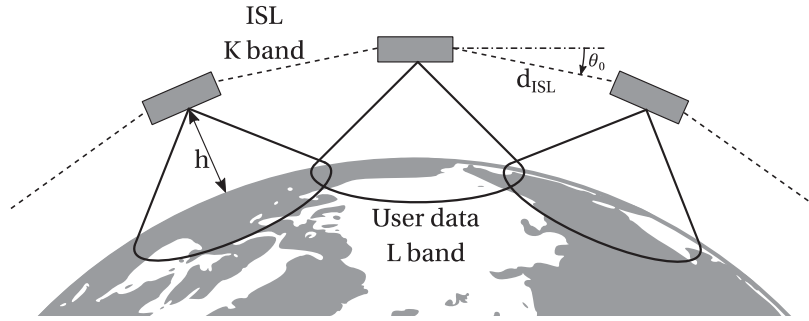
Figure 4.6. The geometry of a single orbital plane in a constellation, used to determine the design requirements of the ISL antenna system.
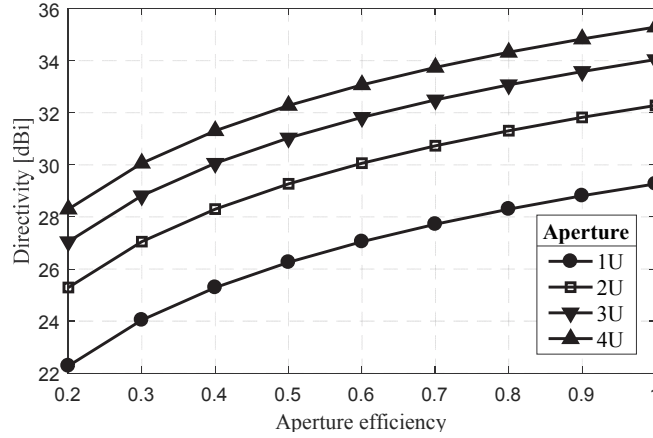
Figure 4.7. Theoretical antenna directivity at broadside versus the aperture efficiency, for different antenna apertures in terms of CubeSat Units (U), at 24.6 GHz.

4.4. Reflectarray and Transmitarray Antennas

It can be seen that an antenna surface larger than 3U is required to achieve the specified gain. This area is not available on the small CubeSat face, and therefore, the antenna will have to incorporate some sort of a deployable mechanism to increase its effective area. Regardless of the geometry, the entire antenna must be stowed within the 3U CubeSat volume during launch in orbit.

Having any microwave components (amplifiers, feeding networks) on the deployed part of the antenna would require a microwave transmission line between it and the satellite body, such as an RF hinge or a flexible coaxial cable. These solutions were discarded early on, due to associated risks. Therefore, the deployable sections should preferably contain only non-connected components. Two well-known high-gain candidates are reflector and lens antennas. Both geometries require a feeding antenna in the focal point of the reflector/lens, which can be placed on the CubeSat body, while the focusing mechanism is deployed.

The conventional reflector and lens antennas come in various forms, usually being bulky and/or heavy (dielectric lenses). Several techniques exist for the reduction of their total profile. The most efficient approach is the design of reflectarray (RA) [81] and transmitarray (TA) antennas [82], which are essentially planar reflector and lens antennas, respectively. The operating principle of RA and TA antennas is illustrated in Figure 4.8. A RA antenna creates a reflection phase gradient over the flat antenna surface, modeling the curvature of the conventional parabolic reflector surface. A TA antenna uses a similar approach to model the refraction in dielectric lenses. The phase gradient is created with an array of resonant elements, typically by changing one or several geometrical parameters of the array element, and using a gradual change in the reflection/transmission phase around the resonant frequency.

RA and TA antennas have a focal point, at which the feeding antenna is placed. The feed has a low gain, and it is typically a patch antenna (array) or a small horn antenna. The RA and TA antennas can be designed for an arbitrary position of the feed and the main-beam direction, which is, besides their low profile, their biggest advantage.

The individual array elements of RA and TA antennas are standalone – not connected through a feeding network, as in corporate-fed arrays, for instance. Therefore, the number and distribution of elements are also arbitrary, as long as they follow a specified distribution lattice. Consequently, the RA and TA antennas can have any shape and size, necessary to achieve the required antenna gain. This fact enables an interesting mechanical advantage – the antenna can be made of several separate panels, over which the array elements are distributed. During the launch, the panels can be stowed on the CubeSat's surface, similarly as the solar panels, and deployed once the CubeSat is in orbit. Some examples are the RA antennas in Figure 4.2.
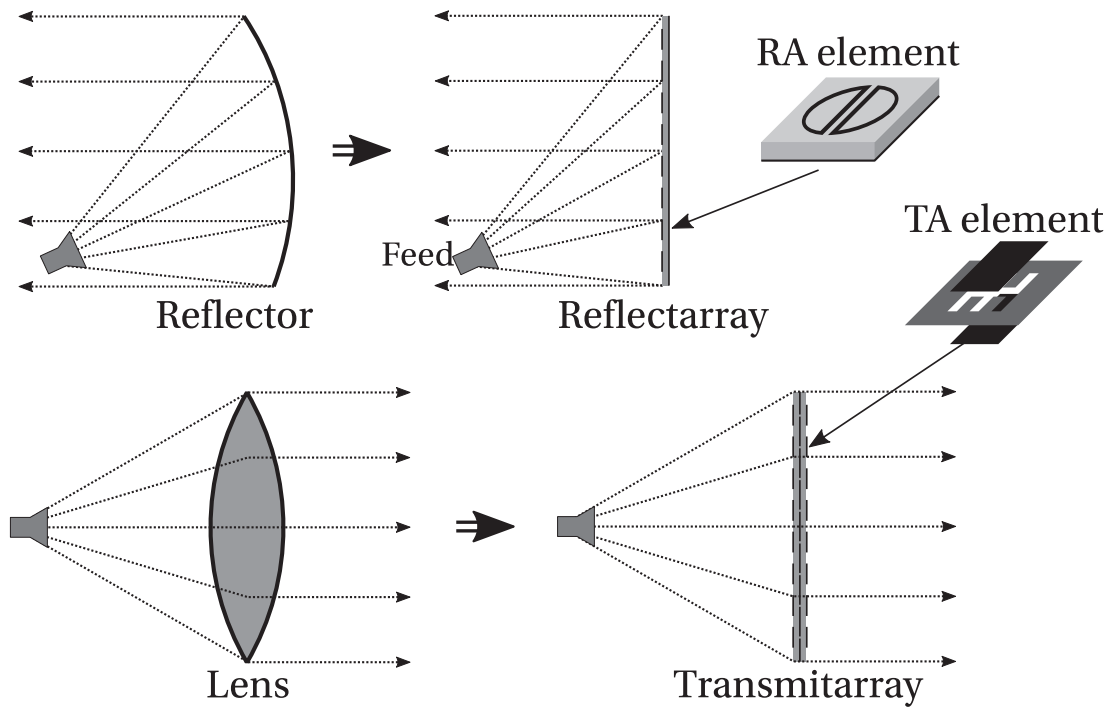
Figure 4.8. Operation principle of reflectarray (RA) and transmitarray (TA) antennas. Reflection and transmission phase gradient of RA and TA flat panels models the focusing effect of the parabolic reflector and dielectric lens, respectively. Feed position and main beam direction of RA and TA antennas are arbitrary. (Upper-right) Examples of RA and TA elements presented in Chapter 5.

4.4.1. Antenna Configurations for CubeSat ISL

Two ISL antennas are required on every CubeSat inside the constellation, for a communication with the two adjacent satellites in the orbital plane, as illustrated in Figure 4.6. If the antennas are in the form of a RA and/or TA, there are various scenarios how the arrays and feeds can be arranged on a 3U CubeSat. Several configurations are conceptualized here, and presented in Figure 4.9, both for single- and dual-band ISL communication scenarios from Figure 4.4. The presented configurations are drawn in the plane of the orbit, although other options are possible. Beside the CubeSat orientation, the choice of the final scenario also depends on the location of other deployable CubeSat features, primarily solar-panel wings.

It is straightforward to obtain single-frequency configurations from Figure 4.9(a-d) simply by removing the second frequency in the sketches. If a dual-band performance is required, the RA and TA panels (and their array elements) must operate independently at two frequencies. The dual-band element design depends greatly on the frequency spacing and bandwidth of the individual forward and return ISL channels. This can be achieved with either a single dual-band or wideband element, or by interleaving two lattices of single-band elements.

It is equally important that the feeding antenna operate at both frequencies. Interleaved single-band elements provide a benefit of having independent operation at the two frequencies. In this case, two single-band feeding antennas, simpler to design and construct than a dual-band feed, can be placed in different locations on the CubeSat body. Each of the two sub-arrays is then designed for focal point at the location of the corresponding feeder, and the two beams are radiated in the same direction. Otherwise, a single wideband feeder can be used for a wideband-element scenario.

Any panel, deployed towards the Earth, will partially obstruct the Earth-facing low-frequency antennas. An RA antenna can be made transparent at low frequencies for this purpose, if the ground plane is replaced with a frequency-selective surface (FSS) [83]. This scenario is depicted in Figure 4.9(c). The FSS behind the RA elements acts as a ground plane for the frequency of RA operation, and transmits other frequencies, including the L and S frequency bands.

4.4.2. A Unified TA/RA Antenna

The last example of Figure 4.9 is a unified transmitarray/reflectarray antenna, shown in Figure 4.9(d). This exotic configuration consists of a single panel, which performs the functions of both the RA and TA at two separate frequencies. The FSS layer provides reflection at the RA frequency and transmission at the TA frequency. It could potentially be omitted if the properly designed TA element had the ability to provide a reflection at RA frequencies.

The main difficulty in this configuration is the proper handling of the mutual coupling between RA, FSS and TA elements. The standalone performance of individual layers is drastically deteriorated when the layers are placed together. In order to reduce the coupling, the total thickness of the structure would have to be increased to the point where the antenna is not suitable for the stowage on a CubeSat exterior. The only solution is to account for the coupling in the design phase, performing a co-design of the three layers simultaneously and thus significantly complicating the design process.

One example of this structure, with a significant profile and only for LP operation, is previously proposed in [84]. A design based on a TA/FSS combination provides the desired function, again, with a large panel thickness. In the scope of this thesis, many attempts were made to design an array element, without arriving to a solution that satisfied the design requirements. The most promising geometry, shown in Figure 4.10, is based on the dual-band TA design from [85].

The proposed TARA concept enables independent scanning of the transmitted and reflected beams. However, if the satellites are uniformly distributed within a single orbital plane (as is the case here), and if the array aperture is perpendicular to the orbit, the angles for both scanning directions are the same. Under these conditions, a newly proposed class of antennas, called transmit-reflect-array (TRA) antennas, is appealing for ISL applications. The TRA is designed as a single metallic layer, and it provides a bidirectional CP high gain at the same frequency [86].

A reconfigurable version of the same antenna incorporates PIN diodes for active beam steering, simultaneously in the two directions [87].
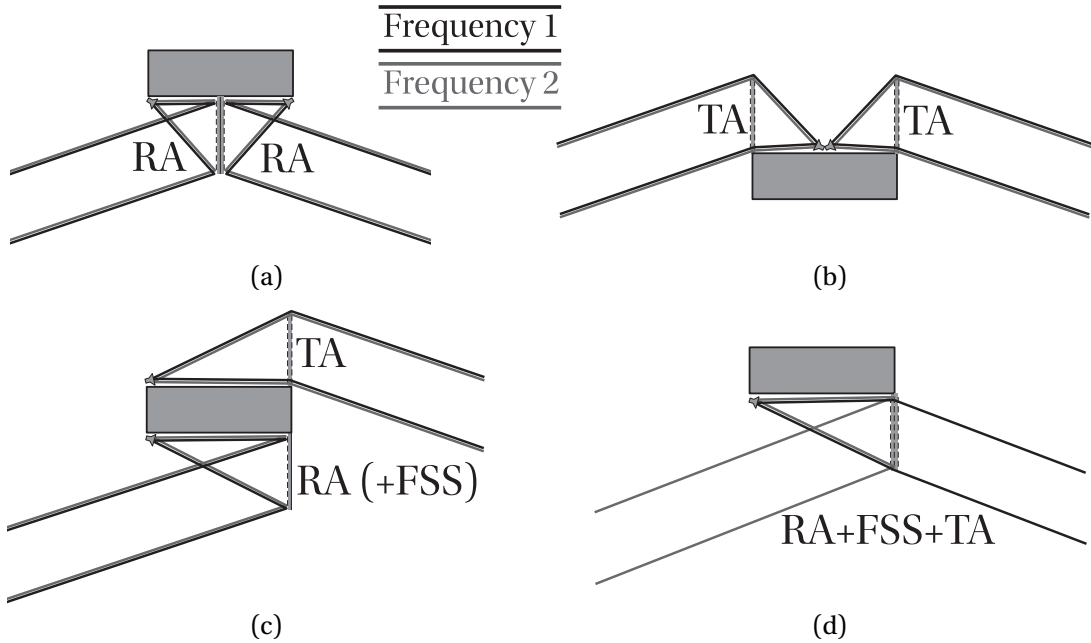
Figure 4.9. Reflectarray and transmitarray configurations for ISL between 3U CubeSats. (a) Two RA antennas. (b) Two TA antennas. (c) TA and RA antenna. The RA antenna is potentially backed with a FSS. (d) The TARA concept: unified TA and RA antennas, separated by a FSS.
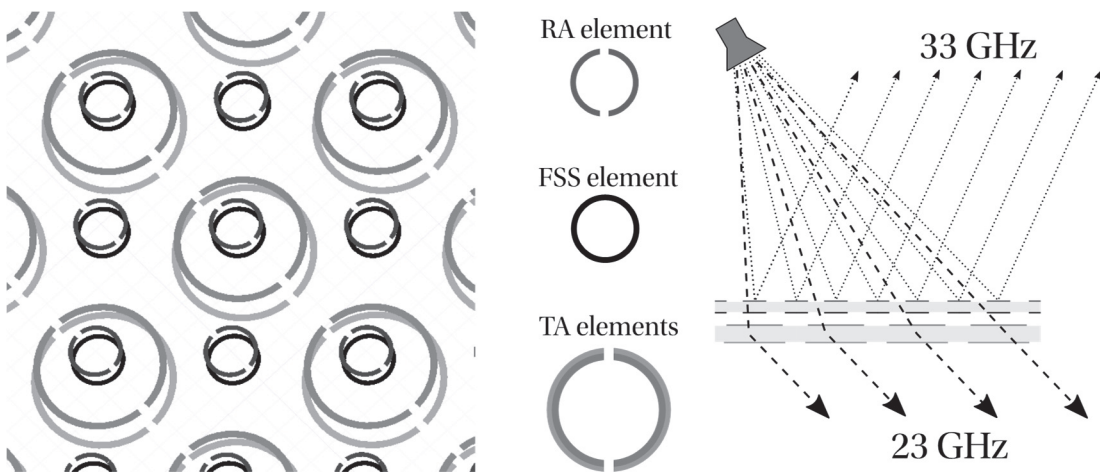
Figure 4.10. Transmitarray/reflectarray (TARA) antenna concept. (left) Array layout. (center) Individual elements. (right) Principle of operation.

4.5. ISL Antenna Design Requirements

It was seen that an antenna aperture larger than 3U is necessary at 24.6 GHz to obtain a gain larger than 30 dBi with a sufficient margin. RA and TA antennas are selected as excellent candidates due to their ability to provide the required antenna aperture through several non-connected passive panels. A design of one RA and one TA antenna is presented in this thesis, for the frequency band II from Figure 4.5. However, the geometry should be scalable and the antenna geometries should ideally be able to provide a satisfactory CP performance over any of the other ISL bands, with more demanding bandwidth requirements.

The design requirements for both RA and TA ISL antennas are presented in The main design goal of the RA element in the following chapters is to improve the CP bandwidth of the RA element, without compromising the complexity. The element should be designed on a single dielectric layer, without metallized vias or SMD components. Among several presented geometries in Chapter 5, one novel RA element satisfies these requirements.

Table 4.2. Beside the given requirements, the antennas should also have a profile low enough, so that the combined thickness of all stowed panels does not violate the CubeSat limitation of 6.5 mm for features on the chassis exterior. Ideally, the thickness should not exceed 70-80% of the limitation.

If the array panel is deployed perpendicularly to the CubeSat's long axis (and the orbit tangent), the angle between the main beam and the tangent is at the same time the antenna beam-scanning angle away from broadside. For practical applications, this angle is smaller than 30° and the associated scanning loss smaller than ~0.6 dB, as seen in Figure 4.11. Depending on the selected ISL antenna configuration and the relative position of the feed, the deployment angle with respect to the CubeSat body can differ from 90° to alleviate the scanning loss.

4.5.1. RA Antenna

Conventional reflector and lens antennas have a theoretically infinite bandwidth, as they rely on the principles of geometrical optics. The resonant nature of RA and TA antenna elements limits their bandwidth [81]. Furthermore, maintaining good CP performance over the entire reflection or transmission bandwidth is even more challenging.

The bandwidth limitation is more severe in RA antennas, compared to TA antennas. Since the introduction of the RA antennas, many techniques, having different levels of complexity, have been developed to tackle this limitation [81], [88]. The key step in the RA antenna design is the design of the RA element itself. In the literature, the RA element bandwidth is often improved at a cost of an increased structural complexity, typically by introducing several metallic and/or dielectric layers. Such approaches violate the CubeSat requirements, where a simple, low profile and robust solution is preferred.

The main design goal of the RA element in the following chapters is to improve the CP bandwidth of the RA element, without compromising the complexity. The element should be designed on a single dielectric layer, without metallized vias or SMD components. Among several presented geometries in Chapter 5, one novel RA element satisfies these requirements.

Table 4.2. ISL antenna design requirements.

Parameter	Value
Frequency [GHz]	24.45 – 24.75
Polarization	CP
Gain [dBi]	> 30
S_{11} [dB]	< -15
AR [dB]	< 3
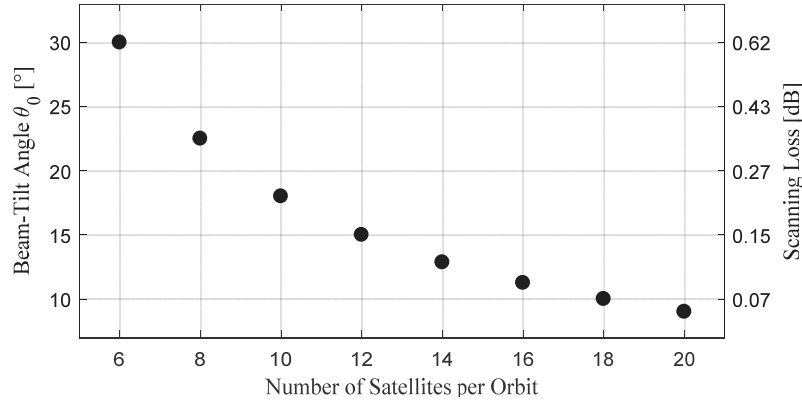
Figure 4.11. ISL antenna beam-tilt angle θ_0 with respect to the orbital tangent (see Figure 4.6) and the associated scanning loss, versus the number of CubeSats in a single orbital plane.

4.5.2. TA Antenna

The bandwidth limitation is not as critical in conventional TA elements, compared to the RA antennas. A wideband performance of TA antennas typically comes from their large overall thickness, which can reach a full wavelength [89]. Needless to say, the resulting panel thickness would be incompatible with the CubeSat standard. The goal in this case is to minimize the overall thickness of a TA element (and the antenna) while preserving the CP bandwidth.

Among the TA-element geometries, previously presented in the literature, one proposed configuration is based on two patch elements on opposite sides of the ground plane, connected with a metallized via [90]. Although the total element thickness is very low, this geometry yields

a wide CP bandwidth. Promising results are also achieved using two pairs of stacked patches and EM coupling through a slot in the ground plane [91]. In Chapter 5, a novel TA element is proposed, which combines the best aspects of both previous designs – an aperture-coupled geometry (without metallized vias) with a low profile and only two patch elements.

4.6. Summary

Inter-satellite links (ISL) are a key feature for CubeSat constellations that aim to provide global coverage and a very low communication latency. Conventional ISL antennas for small satellites are not suitable for CubeSats, due to the size and weight limitations. A general approach of simplifying the antenna geometry is to adapt the design to a specific CubeSat flying formation.

Among several flying formations, a satellite constellation is considered in this thesis. In a constellation formation, CubeSats are uniformly distributed over multiple orbital planes, having identical relative distance and orientation within a single plane. High-gain fixed-beam antennas are a good cost-efficient candidate for ISLs in this configuration, since the two adjacent satellites see each other at a same angle, at all times. The CubeSat's attitude control system must have an accuracy higher than that of an ISL antenna beamwidth, for the link to be maintained without interruptions.

An ISL in K/Ka band was selected, among the sparse bands allocated for ISL applications below 40 GHz, due to the large capacity at those frequencies. Each 3U CubeSat of the constellation is flying with its long axis tangential to the orbit and facing the adjacent CubeSats with the smallest face. Based on the link-budget calculations, the 1U surface cannot provide sufficient gain for a required data rate. Therefore, a deployable antenna is necessary, and deployable reflectarray and transmitarray antennas are found to be optimal for this application. The nature of the RA and TA antennas allows the reflector/lens to be constructed out of several separate panels. The panels can then be neatly stowed or wrapped at the CubeSat exterior and no electrical or RF connection is required with the main satellite body.

Several RA and TA configurations for ISL applications are envisioned and depicted in this chapter. The configurations differ in the relative position of deployable panel and the feeding antenna, with respect to the chassis. Although they are adapted to the specific CubeSat attitude described in this thesis, they can also be suitable for CubeSats having different form factors or in-orbit attitudes.

The RA and TA antennas consist of an array of resonant elements, and one or several geometrical parameters are tuned to vary the phase of the reflected/transmitted signal. Different techniques were previously proposed to improve the bandwidth of the inherently resonant RA elements, usually compromising the overall simplicity. On the other hand, the existing TA elements have a good bandwidth performance, but a large total thickness. Chapter 5

proposes one novel element for each of the RA and TA CubeSat antennas: a single-layer wideband RA element, and a low-profile TA element. The chapter also presents the design and measurement results of an axially corrugated horn antenna used as the feeding element for both arrays. The presented RA and TA element geometries, designed for the CubeSat ISL applications, can be equally interesting for other applications and different frequency bands.

Although the RA and TA antennas seem to serve completely opposite purposes, the essence of their design process is identical, safe for the design of the array element itself. Chapter 6 describes the RA and TA antenna design process in detail, based on the simulation results of individual array elements and the feeding antenna from Chapter 5. The simulation and measurement results of several manufactured prototypes are finally presented in Chapter 6.

5. Reflectarray and Transmitarray Components

Both RA and TA antennas belong to a group of phase-shifting surfaces (PSS). Although many different PSS design techniques and geometries exist, the focus of this thesis is on PSS arrays of discrete elements. A detailed design process of such geometries was previously presented, for example, in [81], [82], [88]. Individual array elements within most PSS arrays have a similar topology, and the phase-shifting property is achieved by changing one or several design parameters of the array element.

A CP radiation is used in space communications to eliminate the losses related to LP misalignment. For the same reason, it will be used for the design of RA and TA antennas for CubeSat ISLs. In the CP case, both RA and TA elements can benefit from a design technique known as the element-rotation technique [92]. The geometry of elements, designed with this technique, is identical in the entire array, and the phase shifting is done by a simple rotation around the element's vertical axis. The rotation angle of individual elements is then proportional to the phase of the reflected/transmitted waves, depending on the antenna type (RA or TA). A set of conditions that an array element and the feeding antenna must satisfy and a detailed theoretical analysis are presented in Section 5.1.2.

The antenna arrays are intended for operation in one of the ISL frequency bands allocated in K/Ka-band. The antenna design requirements are given in Table 4.2. Both the array elements, whether RA or TA, and the feeding antenna should have an excellent CP performance across the entire frequency band. Ideally, the array elements and the feed should also be scalable to the ISL K/Ka-bands other than the specified one, where the bandwidth requirement is more stringent.

The simulation environment of an array unit-cell and the associated assumptions are presented in the beginning of this chapter. Following a theoretical description of the element-rotation technique, two novel RA and TA elements are proposed for CubeSat ISL applications in K band, based on coupled microstrip loops and aperture-coupled microstrip patches. As discussed in Chapter 5, the design goal of the RA antenna element is the improvement of the CP bandwidth of

existing geometries without compromising the array thickness or complexity. In the case of TA elements, the goal is opposite – a thickness reduction with a preserved aperture efficiency.

Finally, a 3D-printed all-metal corrugated-horn feed chain is designed, as a feed for RA and TA antennas. The CP operation of the feed, required for the element-rotation technique, is achieved with a septum polarizer in a square WG. Simulation and measurement results of the horn feed demonstrate its suitability for CubeSat ISL applications.

5.1. Element Design Approach

The fundamental part of the general design process is the design of the array element itself. The elements of the array are distributed over a square lattice. A common approach is to assume local periodicity of elements and analyze the element in an infinite-array environment [81]. In other words, each element of the array is surrounded by elements typically having only slight differences in geometry. The approximation is less applicable for elements close to the edge of the array. However, the amplitudes of the waves, incident at these elements, are also smaller, so that the introduced error is also reduced. This approximation was shown to give excellent results in RA and TA antenna design for many different element geometries[81], [82]. The approach is equally suitable for full-3D and quasi-3D EM solvers. It is favorable to use the quasi-3D solver for the planar geometries presented here, as it requires significantly less computing resources.

5.1.1. Infinite-Array Approximation

In an infinite-array approximation, the simulation relies on the application of Floquet's theorem on infinite periodic structures [81], [93]. It states that the field in the infinite periodic structure can be expressed as a superposition of travelling waves, called Floquet's spatial harmonics. In the case of a 2D periodic structure, the total field in two adjacent cells of the periodic structure differs only by a propagation factor of a plane wave. The theorem then becomes:

$$E(\mathbf{r} + \mathbf{R}) = E(\mathbf{r})e^{-j\mathbf{k}\mathbf{R}} \tag{5.1}$$

where E is the electric field component, $\mathbf{r}$ is the element position vector, $\mathbf{R}$ is the lattice vector, and $\mathbf{k}$ is the propagation vector of a plane wave. It is shown that, if the element spacing is chosen to prevent the appearance of grating lobes in the visible space, only one pair of harmonics is supported. The two harmonics have identical propagation constants and orthogonal polarizations, and they can be used for a full characterization of the periodic structure, including the phase response, losses and cross-polarization.

It directly follows from the previous analysis, that it is sufficient to analyze a single element of the periodic structure (in this case, the array), called the unit cell. The simulation environment of RA

and TA unit cells is shown in Figure 5.1. The element is surrounded on lateral sides by periodic symmetry planes. The field amplitudes on opposing symmetry planes within each pair are imposed by the solver to be equal, allowing for a phase shift. The two independent phase shifts of the cell determine the propagation vector of a supported plane wave, given by:

$$k_x = k_0 \cos\phi \sin\theta$$
$$k_y = k_0 \sin\phi \sin\theta \qquad\qquad (5.2)$$
$$k_z = k_0 \cos\theta$$

where θ and ϕ are angles in the spherical coordinate system, and $k_0 = 2\pi/\lambda_0$. Boundary conditions at the remaining cell faces, defined as Floquet ports, are used for excitation of the unit cell. A modal decomposition of the fields at Floquet ports is performed, where the two fundamental supported modes correspond to incoming LP plane waves with orthogonal polarizations, referred to as TE and TM modes. The relations between all supported (incident and scattered) modes is presented in the form of S parameters. Therefore, the order of the resulting S matrix is four and two in the TA and RA case, respectively. Two Floquet ports are defined for TA cells in order to calculate the transmission as well as reflection coefficients of the cell. In the case of a RA, the bottom port is usually replaced with a PEC plane. If the RA is used in a combination with a FSS, a setup similar to the TA cell should be used.

5.1.2. Variable Rotation Technique

The reflection phase shift of most RA elements is obtained by modifying one or several element's geometrical parameters. This way, the resonant frequency of the element is shifted around the central operating frequency of the RA, simultaneously controlling the phase of the reflected signal. The phase range that can be achieved with simple, single-resonance elements, such as a microstrip patch, is smaller than 360°, meaning that some of the required phase values will be impossible to achieve. Moreover, the size variations between adjacent elements can invalidate the local periodicity assumption in the RA locations where the phase wrapping occurs [88].

A special technique is applicable for CP RA and TA antennas, referred to as the variable rotation technique. The following conditions must be satisfied [91], [92]:

- The feeding antenna must radiate CP
- RA case:
  - The CP sense must be the same for the incoming and scattered waves
- TA case:
  - The CP sense must change while passing through the TA surface
  - The reflection is minimal
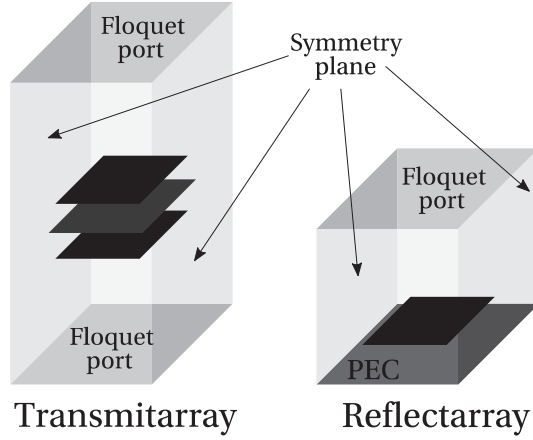
Figure 5.1. The simulation environment of TA and RA antennas in a full-wave 3D EM solver.

If these conditions are fulfilled, the phase can be changed simply by rotating the elements around the vertical axis. The range of attainable phase values is continuous from 0° to 360°, while the amplitude of reflection/transmission coefficients and the coupling to adjacent elements remains nearly constant across this range.

An excellent comparison between two types of TA elements – phase-delay and phase-rotation elements – is presented in [94]. The theoretical development of the element-rotation technique, for RA and TA antennas, is presented in [91], [92], [94], [95], and the main points are outlined in this chapter for the more general case of CP TA antennas. The equations for the RA are derived afterwards from the TA case.

The S-parameter matrix $\mathbf{S}^{LP}$ of the unit cell from Figure 5.1 is defined as:

$$\mathbf{b}^{LP} = \mathbf{S}^{LP}\mathbf{a}^{LP} \tag{5.3}$$

where $\mathbf{b}^{LP}$ and $\mathbf{a}^{LP}$ and the matrices of scattered and incident TE/TM modes. Its expanded form is:

$$
\begin{bmatrix} b_1^{TE} \\ b_1^{TM} \\ b_2^{TE} \\ b_2^{TM} \end{bmatrix} = \begin{bmatrix} S_{11}^{TETE} & S_{11}^{TETM} & S_{12}^{TETE} & S_{12}^{TETM} \\ S_{11}^{TMTE} & S_{11}^{TMTM} & S_{12}^{TMTE} & S_{12}^{TMTM} \\ S_{21}^{TETE} & S_{21}^{TETM} & S_{22}^{TETE} & S_{22}^{TETM} \\ S_{21}^{TMTE} & S_{21}^{TMTM} & S_{22}^{TMTE} & S_{22}^{TMTM} \end{bmatrix} \begin{bmatrix} a_1^{TE} \\ a_1^{TM} \\ a_2^{TE} \\ a_2^{TM} \end{bmatrix} \tag{5.4}
$$

If the element is rotated by an angle α, the new matrix $\mathbf{S}_{rot}^{LP}$ can be written as:

$$\mathbf{S}_{rot}^{LP} = (\mathbf{R}^{LP})^{-1}\mathbf{S}^{LP}\,\mathbf{R}^{LP}, \qquad \mathbf{R}^{LP} = \begin{bmatrix} \cos\alpha & \sin\alpha & 0 & 0 \\ -\sin\alpha & \cos\alpha & 0 & 0 \\ 0 & 0 & \cos\alpha & \sin\alpha \\ 0 & 0 & -\sin\alpha & \cos\alpha \end{bmatrix}, \tag{5.5}$$

where $\mathbf{R}^{LP}$ is the rotation matrix. As the incident and scattered radiation is always CP, it is convenient to work with circular unit vectors and define the matrix $\mathbf{S}_{rot}^{CP}$ as:

$$\mathbf{b}^{\text{CP}} = \mathbf{S}^{\text{CP}}_{\text{rot}} \mathbf{a}^{\text{CP}}. \tag{5.6}$$

The matrix $\mathbf{S}^{\text{CP}}_{\text{rot}}$ relates incident and scattered CP waves, while also taking into account the variable rotation angle. It can be obtained by:

$$\mathbf{S}^{\text{CP}}_{\text{rot}} = \mathbf{T}^{\text{L2C}} \, \mathbf{S}^{\text{LP}}_{\text{rot}} (\mathbf{T}^{\text{L2C}})^{-1}, \qquad \mathbf{T}^{\text{L2C}} = \begin{bmatrix} 1 & -j & 0 & 0 \\ 1 & j & 0 & 0 \\ 0 & 0 & 1 & -j \\ 0 & 0 & 1 & j \end{bmatrix}, \tag{5.7}$$

where $\mathbf{T}^{\text{L2C}}$ is the transformation matrix from Cartesian (x, y) to circular (RHCP, LHCP) unit vectors. Expression (5.6) can also be written as:

$$\begin{bmatrix} b_1^L \\ b_1^R \\ b_2^R \\ b_2^L \end{bmatrix} = \begin{bmatrix} S_{11}^{LR} & S_{11}^{LL} & S_{12}^{LL} & S_{12}^{LR} \\ S_{11}^{RR} & S_{11}^{RL} & S_{12}^{RL} & S_{12}^{RR} \\ S_{21}^{RR} & S_{21}^{RL} & S_{22}^{RL} & S_{22}^{RR} \\ S_{21}^{LR} & S_{21}^{LL} & S_{22}^{LL} & S_{22}^{LR} \end{bmatrix} \begin{bmatrix} a_1^R \\ a_1^L \\ a_2^L \\ a_2^R \end{bmatrix} \tag{5.8}$$

where, for example, a_2^L is the incident LHCP wave at port 2, b_1^R is the scattered RHCP wave at port 1, and S_{12}^{RL} is the matrix entry that relates the two mentioned waves. Since the feed antenna is always placed on the top of the array, all signals that are incident at port 2 are of no importance. The relevant matrix entries are obtained by substituting (5.5) in (5.7) and comparing with (5.8):

$$S_{11}^{RR} = \frac{1}{2}\big[S_{11}^{\text{TETE}} - S_{11}^{\text{TMTM}} + j\big(S_{11}^{\text{TETM}} + S_{11}^{\text{TMTE}}\big)\big]e^{+j2\alpha}$$

$$S_{11}^{LL} = \frac{1}{2}\big[S_{11}^{\text{TETE}} - S_{11}^{\text{TMTM}} - j\big(S_{11}^{\text{TETM}} + S_{11}^{\text{TMTE}}\big)\big]e^{-j2\alpha}$$

$$S_{21}^{LR} = \frac{1}{2}\big[S_{21}^{\text{TETE}} - S_{21}^{\text{TMTM}} + j\big(S_{21}^{\text{TETM}} + S_{21}^{\text{TMTE}}\big)\big]e^{+j2\alpha}$$

$$S_{21}^{RL} = \frac{1}{2}\big[S_{21}^{\text{TETE}} - S_{21}^{\text{TMTM}} - j\big(S_{21}^{\text{TETM}} + S_{21}^{\text{TMTE}}\big)\big]e^{-j2\alpha} \tag{5.9}$$

$$S_{11}^{LR} = S_{11}^{RL} = \frac{1}{2}\big(S_{11}^{\text{TETE}} + S_{11}^{\text{TMTM}}\big)$$

$$S_{21}^{RR} = S_{21}^{LL} = \frac{1}{2}\big(S_{21}^{\text{TETE}} + S_{21}^{\text{TMTM}}\big).$$

It directly follows that, if the element satisfies the previously outlined conditions for the TA case, the phase shift is then equal to twice the value of the rotation angle and the CP sense of the scattered wave is of the opposite hand compared to the incident wave [92]. The CP-sense change is achieved if the phase difference between the two co-polarized LP components is 180°, or equivalently:

$$\arg\big(S_{21}^{\text{TETE}}\big) - \arg\big(S_{21}^{\text{TMTM}}\big) = 180°, \qquad S_{21}^{\text{TETE}} = -S_{21}^{\text{TMTM}} \tag{5.10}$$

By properly selecting the rotation angles across the TA surface, the resulting phase distribution can collimate the radiated beam and scan it in an arbitrary direction.

The response of a RA cell is obtained simply by using the expressions of (5.9) with a subscript '11', which take into account exclusively port 1. Similar conclusions apply as in the TA case, except that the reflection of the same CP sense is the desired effect in CP RA antennas.

A notable example in the group of RA elements, which satisfies the described conditions, is the microstrip split loop [96], [97]. Different stacked and coplanar configurations of split loops were reported for dual band performance, sometimes in a combination with FSS if transparency was required at lower frequencies [83], [98]. On the other hand, TA examples of CP elements include an aperture-coupled stacked patches [91], stacked split loops [85], and various other, not listed here [99]. The existing elements served as a starting point for the RA and TA element design. The following sections present novel elements, developed from the existing ones, which significantly improve the bandwidth or panel thickness of the RA and TA structures, respectively.

5.2. TA Element: CP Aperture-Coupled Patches

The general approach in one group of TA elements is to have two resonant elements at opposite sides of a ground plane. Several element geometries are illustrated in Figure 5.2. The element facing the feed accepts the incoming radiation, resonates and transfers the energy to its counterpart, which in turn resonates and radiates the waves on the opposite side of the TA.

The first TA lens based on this concept is shown in Figure 5.2(a) [100]. Two parallel arrays of rectangular patches are connected with delay lines and metallized vias, where the variable line length provides the required phase shift. The design from Figure 5.2(b) eliminates the delay lines and uses only a metallic pin to connect the receiving LP patch to a transmitting CP patch, in combination with the element-rotation technique [90].

Another work presented a design shown in Figure 5.2(c) where the patches are aperture-coupled to stripline delay lines, removing the need for unreliable metallized vias [101]. The geometry was later improved further, by eliminating the stripline delay lines and directly coupling the patches through a crossed slot in the common ground plane.
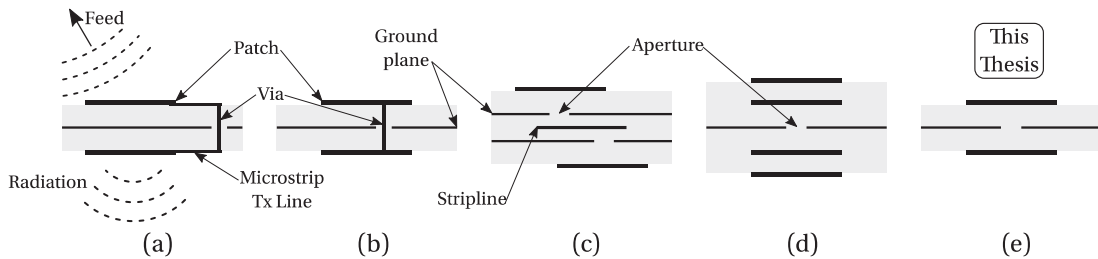

Figure 5.2. A comparison of different methods to achieve phase shifting in TA elements based on microstrip patches. (a) Delay line and via connection. (b) Via connection, variable rotation. (c) Stripline delay line and aperture coupling. (d) Aperture coupling of stacked patches, variable rotation. (e) Aperture coupling of single patches, variable rotation (this thesis).

This structure is proposed for dual-LP [102]and CP operation [91] and the element geometry is shown in Figure 5.2(d). The transmission phase is varied by changing the patch physical dimensions in the dual-LP case, and by using the element-rotation technique in the CP case. A stacked-patch structure is used in both designs, due to difficulties to obtain satisfactory transmission parameters with only a single patch element.

As discussed in Section 5.1.2, the element-rotation technique requires the phase difference between the transmitted LP components to be 180°. This difference is achieved in [91] with a rectangular patch shape. A large aspect ratio of the rectangle separates the two orthogonal resonances in frequency and increases the phase difference of transmitted components. The authors stated that it was difficult to obtain the required difference of 180° with a single patch, and that the stacked patches were used for this purpose. The resulting structure has a wide CP transmission bandwidth, but also a large profile, as it is composed of four dielectric and five metallic layers.

The remaining part of this section presents a TA element shown in Figure 5.2(e) having only two dielectric layers, which achieves the 180° phase difference using a modified shape of the coupling aperture.

5.2.1. Geometry Evolution

Introducing asymmetries in conventional patch antennas is commonly used to excite CP by creating a phase difference of 90° between orthogonal resonances. This was done in Section 2.7 by introducing a small asymmetry in the coupling slot of an aperture coupled patch antenna. The same idea is used here for the described TA element. Since the required phase difference is twice that of the patch antenna, the slot asymmetry must be larger, in combination with rectangular instead of square patches. The evolution of the TA-element geometry is shown in Figure 5.3. One slot in the pair of crossed slots is drastically elongated at first, and then loaded at the ends in the form of a dog-bone slot [103]. It is shown that a single patch on each side is sufficient to achieve a phase difference of 180° with this geometry.

Indeed, the transmission polarization-sense change and minimal reflection are found to be conflicting criteria in the design of the aperture-coupled element. In other words, if the reflection is minimized at the same frequency for both LP components, the difference in transmission phase tends to be smaller than the required 180°. A phase difference close to 180° is achieved with a significant slot and patch asymmetries, while maintaining low values of reflected LP components. After the initial manual tuning, the element was optimized to minimize both reflected and cross-polarized transmitted CP components at the design frequency. The dimensions of the optimized element given in Figure 5.4 present the best compromise.

Design evolution
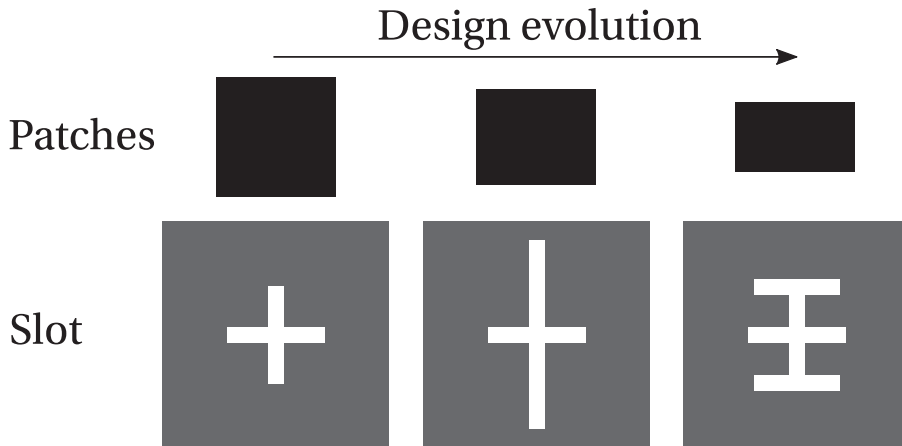
Patches

Slot

Figure 5.3. Design evolution of aperture-coupled patches as TA antenna elements. Two identical patch elements are placed symmetrically on the two opposite sides of a ground plane with a slot. The slots are shown in white on the gray ground plane.
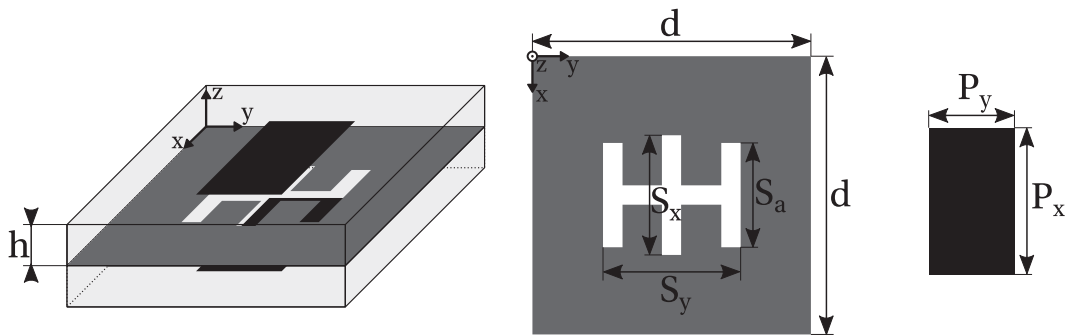
Figure 5.4. The geometry of the TA element based on aperture-coupled patches. Dimensions (in mm): d=6, h=0.76, P_x=3.19, P_y=1.87, S_x=2.63, S_y=2.99, S_a=2.28.

5.2.2. Simulation Results

The simulated performance of the optimized element is shown in Figure 5.5. Although the maxima of the LP transmission components do not appear at the same frequency and the phase difference is not exactly equal to 180°, the unwanted CP components are all below -17 dB at 24.6 GHz.

When used as a part of an array, the incoming radiation arrives at individual elements at a range of different incidence angles. This range is increased for TA antennas with a low F/D ratio (TA focal distance over the total array dimension, as explained in the next section) and offset-fed TA antennas. For a good array performance, the element must show stable characteristics over the given angular range. The CP performance is calculated for three elevation incidence angles: 0°, 20°, and 40°, and the simulation results are presented in Figure 5.6. The response shifts to lower

frequencies with the increase of the incidence angle. As a compromise, the element is designed at a slightly higher frequency to account for this effect. Nevertheless, the CP cross-polarized and reflected components remain below -15 dB at 24.6 GHz in all cases.

The TA element is designed on two Rogers RO6002 laminates (ε_r=2.94, tanδ=0.0012, h=0.76 mm). The total thickness of the structure is ~0.13 λ_0 at 24.6 GHz. The initial design was done on Rogers RT/Duroid 5870 boards, yielding a total thickness of ~0.09 λ_0 , but the substrate material was changed due to material availability. By comparing the two models, a better performance-stability versus the incident angle was observed in the Duroid 5870 element due to a lower profile. The same conclusion can be made by comparing this element's performance at large incidence angles versus the stacked-patch element from [91].
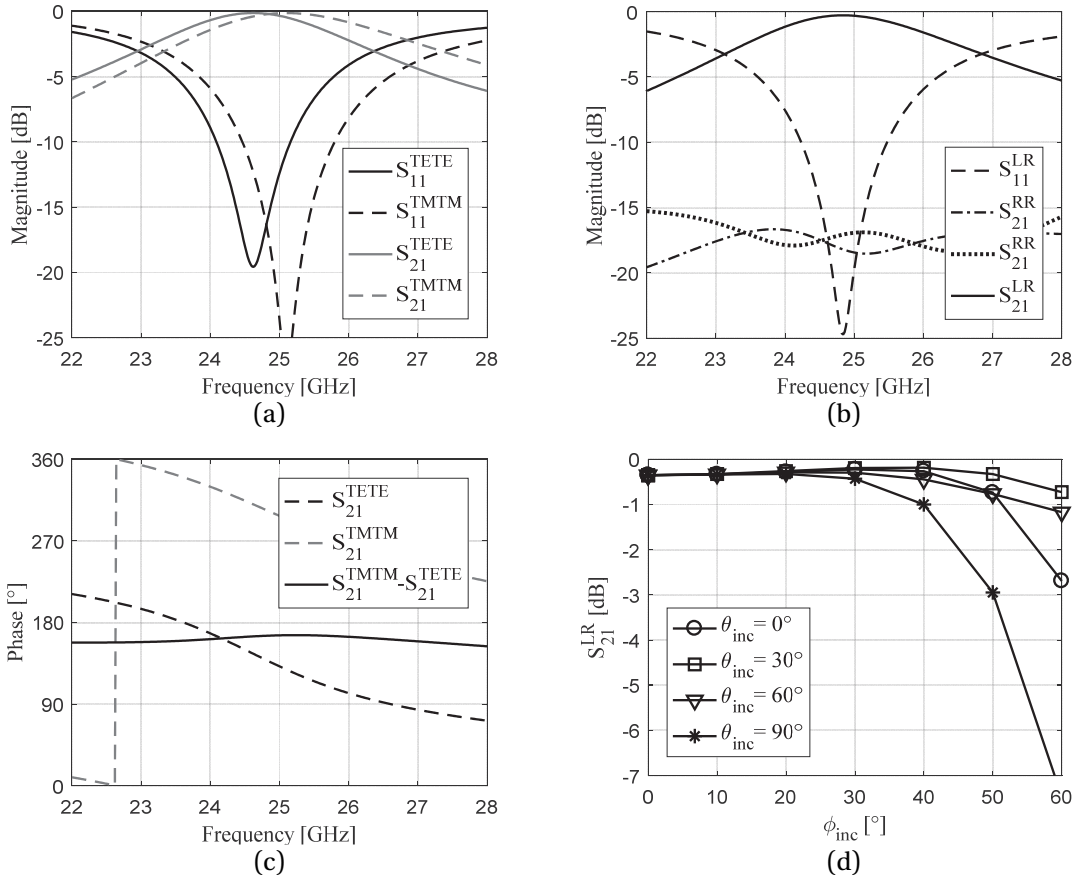
Figure 5.5. Simulation results of the aperture-coupled-patch TA element. (a) Transmission and reflection S parameters for the two orthogonal LP components – TE and TM. (b) Transmission and reflection S parameters for the two CP components – LHCP and RHCP. (c) Phase and phase difference of the LP transmission S parameters. (d) The co-polar transmission magnitude versus the elevation incidence angle, for different azimuth incidence angles.
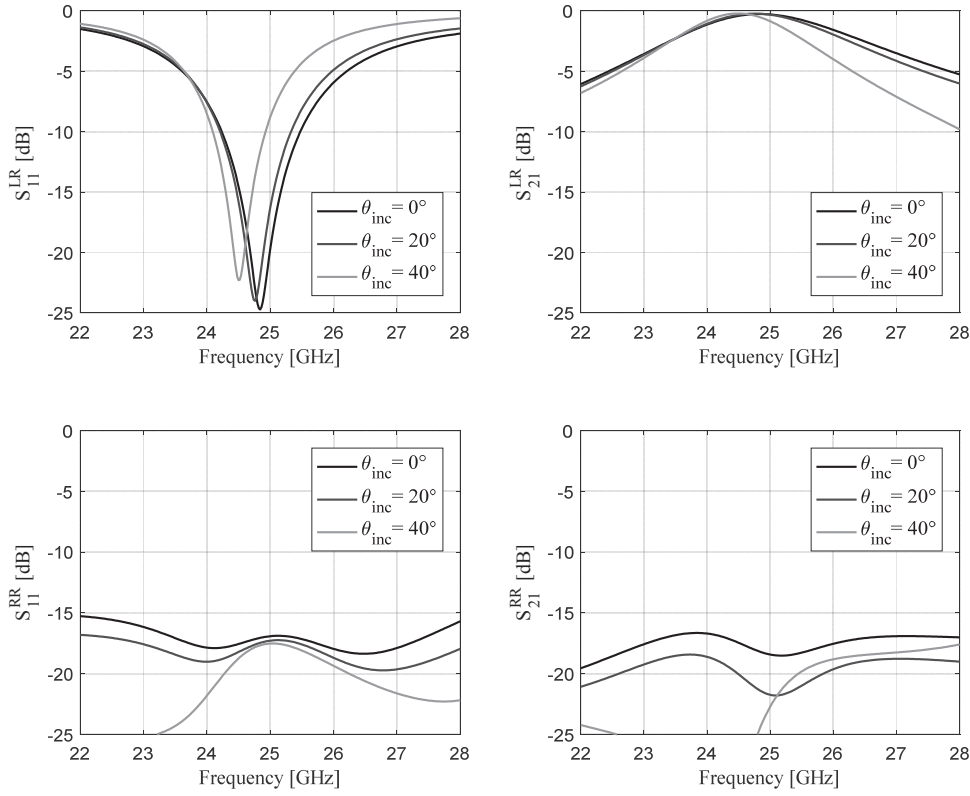
Figure 5.6. The dominant S parameters of the aperture-coupled-patches TA element versus the elevation incidence angle.

5.3. RA Element: Coupled Loops

RA antennas with elements having variable rotation angles were first designed with square microstrip patch element and attached delay lines [92], followed by the split-loop element [96]. Split loop remains the most attractive CP RA element to date. Its small conductive surface makes it convenient to stack or interleave elements with different dimensions, for multiband RA operation [98], [104]. Furthermore, the circular shape of the element minimizes the variations of the mutual coupling for various rotation angles of adjacent elements. The split loop is used in combination with a backing FSS structure to make the RA panel transparent to low frequencies [83]. This configuration is especially appealing for the RA CubeSat configuration previously illustrated in Figure 4.9(c).

The design goal of this section is to improve the split-loop element bandwidth, starting from the existing geometries, for it to be able to cover any ISL frequency band in K/Ka bands. The simulation setup for the RA unit cell is shown in Figure 5.1(b).

5.3.1. Geometry Evolution

RA element geometries and the corresponding simulated S parameters are shown in Figure 5.7 – 5.9. The starting design for the wideband RA element is the known split-loop from Figure 5.7(a) [96]. It is a metallic ring above a ground plane, cut in two positions on opposite sides. In this structure, the phase of the reflection coefficient for vertically polarized waves is 180° larger compared to the horizontally polarized, which is the key condition for the element-rotation technique. The CP sense of the incident and scattered waves is thus the same. The underlying principles of its narrowband CP performance will be explained in the following section.

The bottom-left element in Figure 5.7(a) is presented in [97], where it is claimed that the vertical line is added to reduce the cross-polarization. The bottom-right element in Figure 5.7(a) is the result of an attempt to increase the capacitive coupling at the edges of the two circular arcs. Consequently, the element has a smaller dimension compared to the conventional split loop, for a given resonant frequency, and a slightly smaller bandwidth. However, elements of this type can be distributed with a smaller separation, potentially improving the bandwidth of the full array. This element is novel and it can be considered as an intermediate design step that led to the development of the final wideband geometry. The performance of both split-loop modifications is found in the simulations to be very similar to a conventional split loop.

The RA element shown in Figure 5.8 is an evolution from the bottom-left element in Figure 5.7(a), where the vertical line is extended to an I-shaped line. An interesting property of the element is its dual-band performance. The angular positions of the gaps determine the ratio of the two central frequencies. Unfortunately, the element cannot be used simultaneously for both bands, since the required rotation angles will be different in the two frequencies, even if the main beam is scanned in the same direction. The same conclusion can be made for the dual-band TA element from [99]. While trying to bring the two frequencies together, an anti-resonance was observed between the two bands, preventing the two resonances to collapse into a single, wide band. This element geometry could be of interest for a future study.

Although the attempts to generate a wideband geometry were unsuccessful for the element in Figure 5.8, the final design yields two collapsed resonances with a potential for a significant bandwidth increase. The RA element in Figure 5.9 is obtained by continuing the process, used to generate the capacitive-coupled loop in Figure 5.7(a), until the two pairs of arc edges are connected. The obtained geometry is composed of two coupled loops. When the element is re-sized to the design frequency, it is larger than the original split loop. However, the total diameter is equal to only $0.33\lambda_0$ at the design frequency. The element-spacing condition that prevents the excitation of grating lobes in a RA is given by:

$$\frac{d}{\lambda_0} < \frac{1}{1 + |\sin\theta|} \tag{5.11}$$

where d is the element separation and θ is either the incidence angle from the feed or the beam-

tilt angle, whichever is larger [93]. Therefore, the excitation of grating lobes is eliminated by using the described element in any feeding or scanning configuration, since the element-separation limit is larger than $0.5\lambda_0$ for all incidence angles.

The full-wave simulation results of the coupled loops are presented in Figure 5.9(b,c). A dual-resonant behavior is evident from both the CP and LP S parameters. Consequently, the CP-reflection bandwidth of the coupled loops is significantly improved compared to the traditional split-loop element. The following Sections 5.3.2 and 5.3.3 provide a detailed modal analysis and the full-wave simulation results of the coupled-loops element, for a deeper insight into the wideband CP nature.
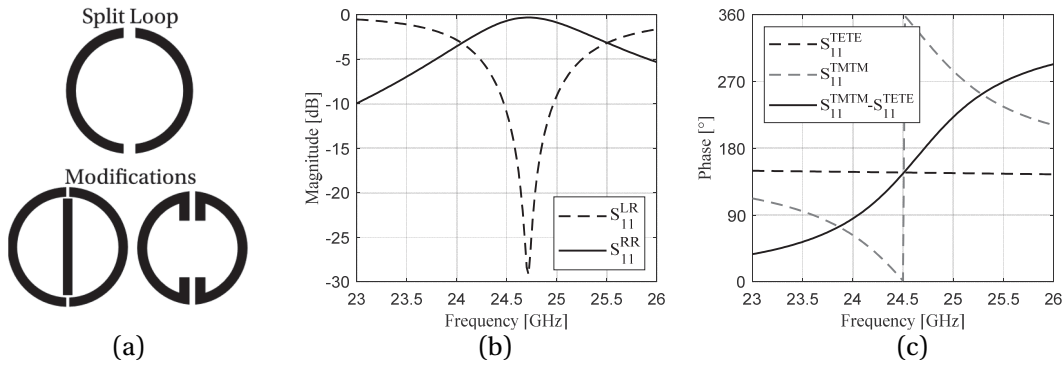
Figure 5.7. Geometry of split-loop RA elements and the full-wave simulated performance. (a) The original element geometry and two modifications. The three geometries have a similar single-resonant performance. (b) Magnitude of the CP S parameters. (c) Phase of the LP S parameters.
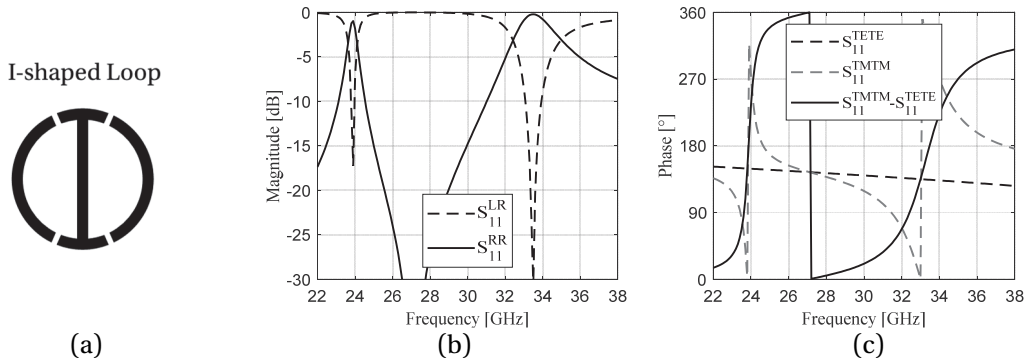
Figure 5.8. Geometry of the I-shaped-loop RA element and the full-wave simulated performance. (a) The element geometry. (b) Magnitude of the CP S parameters. (c) Phase of the LP S parameters. Note the expanded frequency axis.
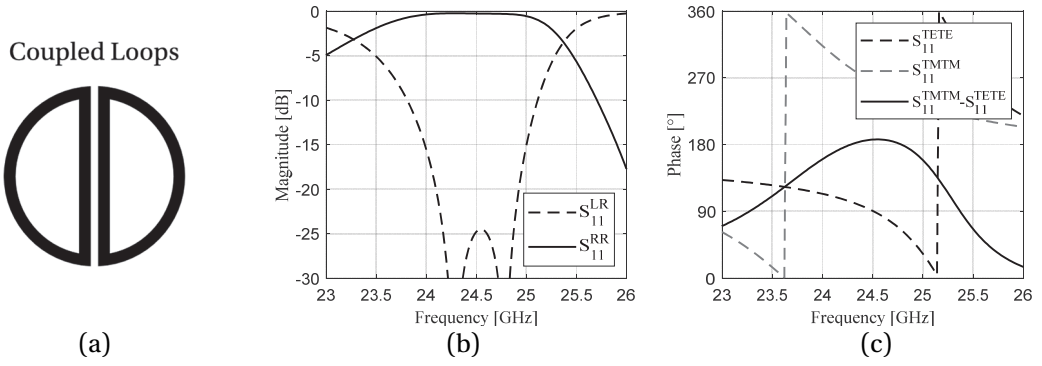
Figure 5.9. Geometry of the coupled-loops RA element and the full-wave simulated performance. (a) The element geometry. (b) Magnitude of the CP S parameters. (c) Phase of the LP S parameters.

5.3.2. Modal Analysis

The performance of different elements can be explained by examining the structural resonances of the geometry, as well as the electric currents on the element when it is illuminated by LP and CP plane waves. Different solvers are used for the two tasks – the eigenmode solver for the structural resonances in the absence of any excitation and the modal-driven solver for the full-wave simulation with plane-wave excitations. The periodic boundary conditions are used in both cases. The only setup difference is that, in the eigenmode simulations, the Floquet port is replaced with an open (radiation) boundary. The split loop and the coupled loops are used for comparison.

The first two resonant modes of the two geometries are calculated and the characteristic electric-current distributions are shown in Figure 5.10. The two split-loop modes can be seen as the even and odd modes and their eigen-frequencies are the same. On the contrary, the first two modes of the coupled loops have different eigen-frequencies, with a spacing of ~7.6%. When the two RA elements are excited by LP plane waves at the central frequency in the full-wave simulations, the currents on the coupled loops correspond exactly to the two mode distributions. However, only the first mode is excited on the split loop for both vertical and horizontal polarizations, as the second mode is not supported. CP plane waves excite the same (first) mode, explaining the narrowband character of the split-loop element.

The current distribution of the coupled loops in the case of a CP plane-wave excitation is a combination of the two eigen-mode distributions. Individual modes are dominant at different frequencies within the operating band, in agreement with the relationship of the mode eigen-frequencies. The current distribution of the coupled loops is presented in Figure 5.11 at several frequency points. The distribution is mainly determined by the first mode at lower frequencies, and vice versa.
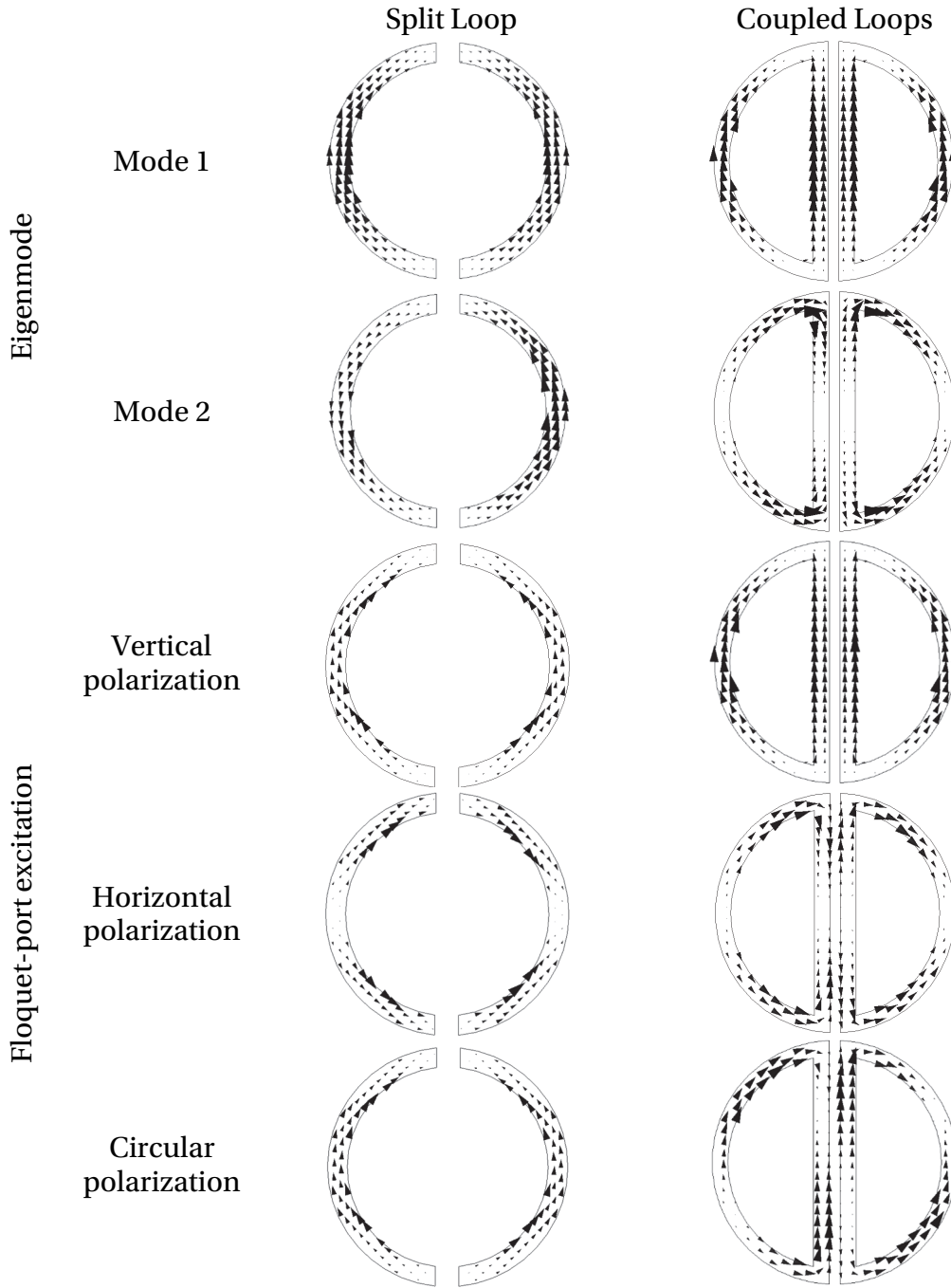
Figure 5.10. Electric currents on the split-loop and coupled-loops RA elements. The top two rows show the results of the eigenmode analysis, and the bottom three rows show the results of a full-wave 3D simulation with a Floquet-port excitation. Periodic boundary conditions are used in both sets of simulations.

5.3.3. Full-Wave Simulation Results

The simulated S parameters of the RA coupled-loops element, with a Floquet-port excitation in the infinite-array environment, are shown in Figure 5.12. It is observed that the two resonances separate in frequency, as the incidence angle of the incoming wave increases. Therefore, it is essential for the element to be designed with closely spaced resonances in the case of broadside incidence, in order to preserve a low cross polarization at the center of the band for large incidence angles. On the other hand, if the resonances are designed too closely together, the overall element bandwidth is reduced. The main parameter that influences the resonance separation is the gap between the two loops. As seen in Figure 5.12(b), the S parameters are very sensitive to the gap distance.

The coupled-loops element is modeled using zero-thickness conductor layers during the simulations, including the conductive and dielectric losses in the materials. This approximation significantly accelerates the quasi-3D simulation process. However, through prototype measurements in Chapter 6, it will be shown that the effect of the finite conductor thickness is important, since it also affects the sensitive coupling between the two loops. Therefore, it is advised to include the finite conductor thickness in the simulation models, for maximum accuracy.

The effect of resonance separation is also evident from Figure 5.13, where the co-polar reflection S parameter is presented for different incidence angles. The magnitude of the co-polar reflection drops most rapidly in the center of the band, at 24.6 GHz, which is in line with the results from Figure 5.12(a). Nevertheless, a wideband performance of the coupled loops is preserved across a wide range of incidence angles, with a low cross polarization across the entire band.
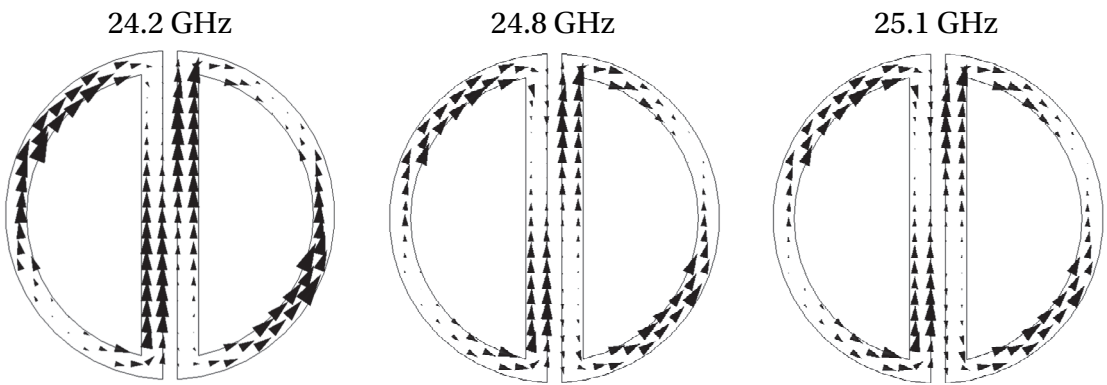
Figure 5.11. Electric-current distributions on the coupled-loop element at different frequencies. The results are obtained using a full-wave 3D simulation and a Floquet-port excitation.
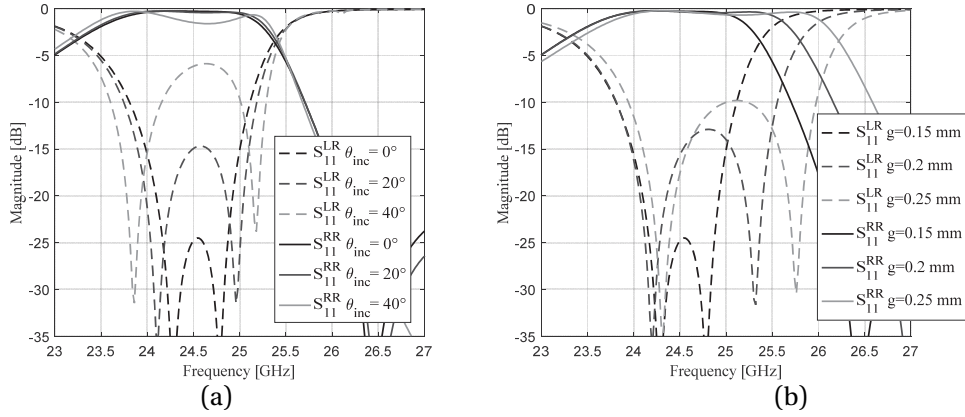
Figure 5.12. Simulated S parameters of the coupled-loops RA element (Element 5 from Figure 5.7). (a) Variation of the elevation incidence angle. (b) Variation of the gap between the two D-shaped loops.
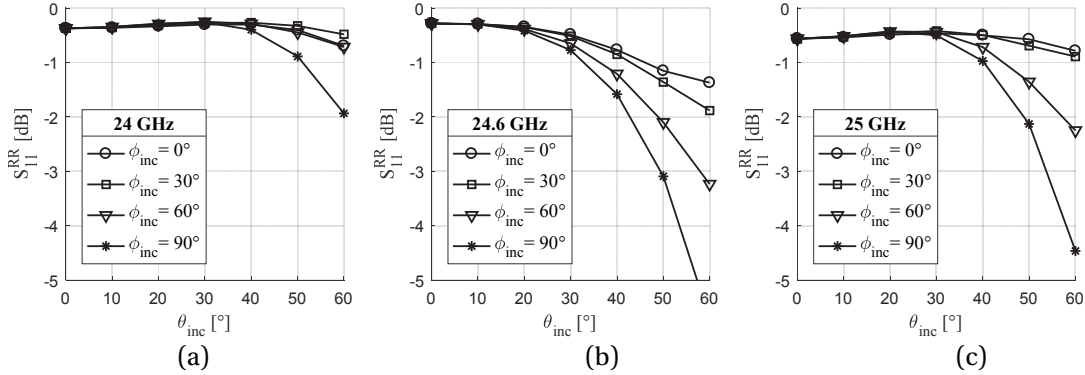
Figure 5.13. The co-polar reflection magnitude S_{11}^{RR} versus the elevation incidence angle, for different azimuth incidence angles. (a) 24 GHz. (b) 24.6 GHz. (c) 25 GHz.

5.4. 3D-Printed Corrugated-Horn Feed Chain

A feeding antenna is an equally important part of the RA or TA system as the array element. Its properties must be carefully chosen for the given array geometry. In the case of arrays that use the element-rotation technique, the feeding antenna must be circularly polarized. Moreover, the CP quality should be preserved along the entire range of angles, under which the array is visible. A circular horn antenna is selected for this application, although other geometries can be equally suitable (a patch antenna array, to name one). The choice was driven by a high operating frequency and the fact that the horn antenna is an all-metal geometry – an attractive feature for space applications.

5.4.1. Array Focal Distance

The F/D ratio is the main parameter that determines the properties of the feeding antenna. Some antenna aspects are outlined in Table 5.1 and illustrated in Figure 5.14, versus the F/D value. The beamwidth of the feed is inversely proportional to the F/D ratio, meaning that a more directive antenna should be selected for a larger feed distance [81]. The incidence-angle estimate in the table is given for center-fed antennas or the antennas where the feed projection is at the array center. This issue becomes more important for offset-fed arrays (and especially for large offset values) since the maximum incidence angle is increased and the central area of the array is illuminated at a larger angle as well. The central array area is also the one with the strongest illumination, and which plays the largest part in the total RA performance. A larger F/D will reduce the maximum incidence angle in any case, but will require a more directive feed, which will also be larger.

For the antenna geometries depicted in Figure 4.9, the array is deployed from the CubeSat surface, and the feed is located on the large face of the CubeSat, with a distance F from the array base. Therefore, an offset value of $0.5D$ is adopted in this thesis, as the worst-case scenario, while having in mind that the actual offset in the practical antenna model will be slightly smaller. Offset-fed arrays are more prone to exciting grating lobes for element-spacing values larger than $0.5\lambda_0$. The maximum allowed element spacing is calculated using (5.11) for different array sizes and F/D values, and the results are presented in Table 5.2. The elements used in this thesis are designed with an element spacing of approximately $0.5\lambda_0$ and thus never excite grating lobes.

Table 5.1. Design tradeoffs of RA and TA antennas, for different values of the F/D ratio.

F/D ratio	Small	Large
Feed beamwidth	Wide	Narrow
Maximum element incidence angle	Large	Medium
Feed size	Small	Large
Total RA antenna size	Medium	Large
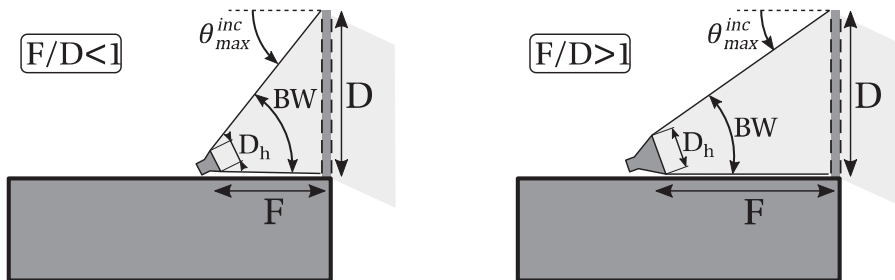
Figure 5.14. The impact of the F/D value on the design parameters of the feed and the array: feed beamwidth BW, maximum/average incidence angle θ_{max}^{inc}, and feed horn diameter D_h.

Table 5.2. The maximum element separation (in λ_0) that does not generate grating lobes, versus the focal distance and the array dimension.

F [mm] D [mm]	100	150	200	250
100	0.59	0.64	0.69	0.73
150	0.54	0.59	0.62	0.66
200	0.53	0.56	0.59	0.62
250	0.52	0.54	0.56	0.59

Table 5.3. The angle (in °) at which the deployed RA or TA aperture is visible from the feed position on the surface of the CubeSat.

F [mm] D [mm]	100	150	200	250
100	45	34	27	22
150	56	45	37	31
200	63	53	45	39
250	68	59	51	45

In the given array configuration on a CubeSat, the angle at which the array is visible from the feed, given in Table 5.3, is calculated by:

$$\theta_{feed} = \text{atan}\frac{D}{F}. \tag{5.12}$$

This angle gives an initial estimate of the feed's 10-dB beamwidth. In the literature, maximum aperture efficiency of the array is typically obtained if the illumination in the array edge is approximately 10 dB below the center illumination [81]. A similar rule is adopted for the designed feed, as explained later on.

5.4.2. Axially Corrugated Horn

A horn antenna is the most common choice for the feeding element of a reflector. An all-metal horn geometry is an attractive feature for space applications. CP radiation of a horn antenna is excited with two orthogonal modes in the input waveguide, which should be either circular or square. The radiation performance then depends on the horn geometry. In general, a larger horn will have a higher directivity and a lower beamwidth. As described in the previous chapter, one of the main requirements for the RA and TA feeders is a good off-axis CP performance. The cross polarization of an ordinary horn (circular or square) deteriorates quickly when moving off axis, making it unsuitable for this scenario. Several known techniques are used for the improvement of the cross polarization: corrugated horn (axial or radial corrugations), scalar horn, spline horn, etc [105].

Starting from an ordinary circular horn, designed at 25 GHz, two variations were implemented.

- **Scrimp horn** – a multimode horn element, consists of a flared section, a single axial corrugation and the cylindrical section
- **Axially-corrugated horn** – the same geometry, only with three axial corrugations

The geometry and radiation characteristics of the two horn geometries are compared with a regular circular horn in Figure 5.15. The diameter of the feeding circular WG is chosen to be 7.8 mm to prevent excitation of higher-order modes in the waveguide. Two orthogonal WG modes, with the same cutoff frequency, are supported in the specified frequency band. In the simulations, the waveguide is fed with a wave port, and the two modes are excited with a phase delay of 90° for CP radiation. The corrugated horn has the largest aperture area, and therefore the highest directivity. Several corrugations yield a significant improvement in the broadside cross-polarization, over the other two models. The corrugated horn, with its increased directivity and a narrower beamwidth, will require a larger F/D value to achieve an optimal aperture efficiency, as it will be explained in the next chapter. The cross-section of the axially corrugated horn with optimized dimensions is shown in Figure 5.16.

5.4.3. Septum Polarizer

The practical excitation of CP in horn antennas can be done in a number of ways, including external feeding networks, meander-line polarizers, etc. One of the simplest methods is to use a so-called septum polarizer, shown in Figure 5.17 [106]–[108]. The septum polarizer consists of a thin, ridged, metallic wall, placed in the middle of a square waveguide.
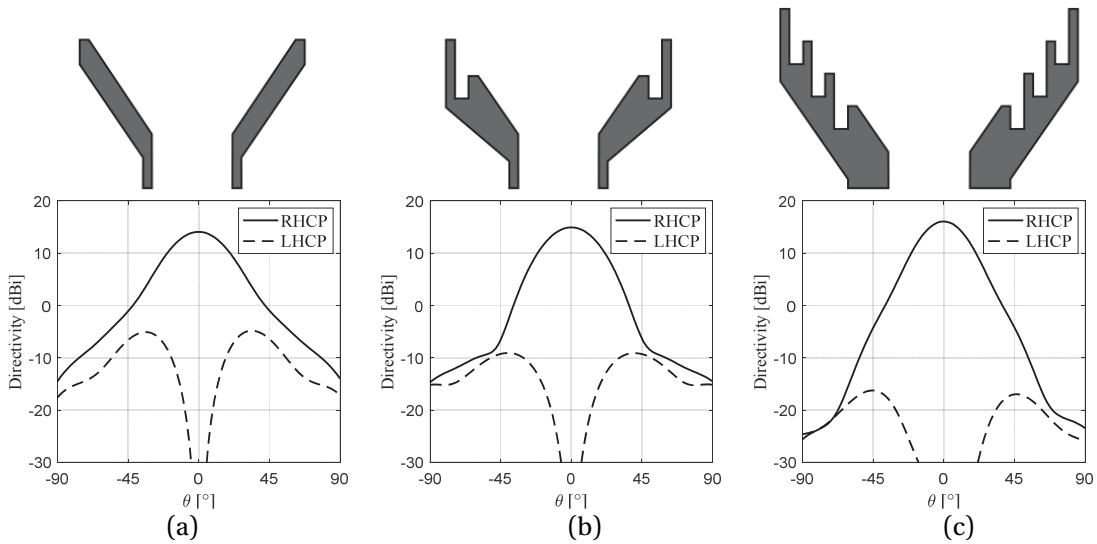
Figure 5.15. Simulated CP radiation patterns of the three horn antennas. (a) Regular circular horn. (b) Scrimp horn. (c) Axially corrugated horn. Cross-sections of horn-antenna geometries are shown above the corresponding radiation patterns.
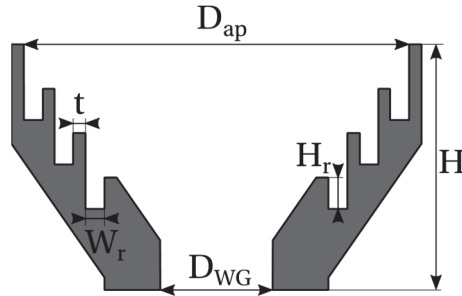
Figure 5.16. Cross-section of the axially corrugated horn antenna. Dimensions (in mm): D_{WG}=9, D_{ap}=31, t=1, W_r=1.5, H_r=2.5, H=18.7.
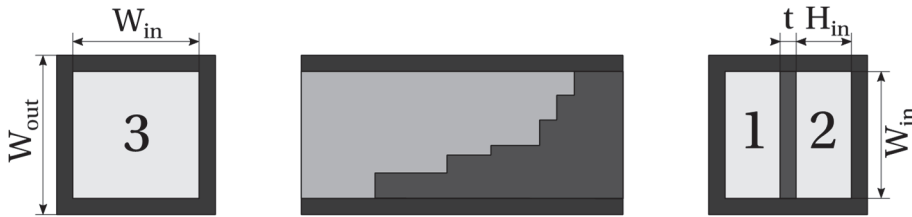
Figure 5.17. Septum polarizer in a square WG. Numbers denote the rectangular ports (1,2) and the common square port (3). Dimensions (in mm): W_{out}=9.8, W_{in}=7.8, H_{in}=3.4, t=1.
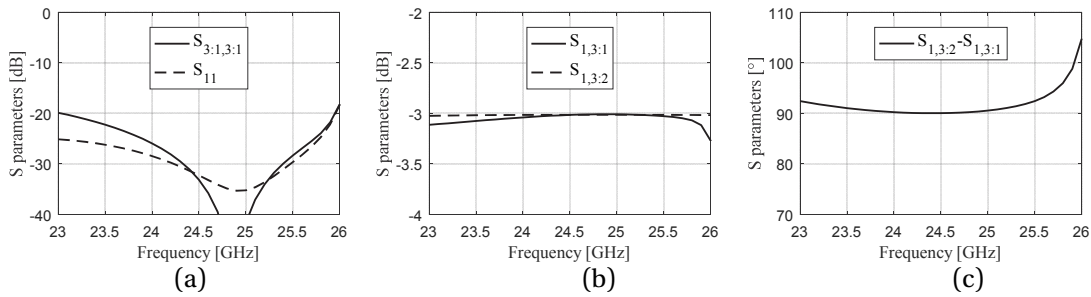
Figure 5.18. Septum-polarizer S parameters. '3:1' in the subscript stands for port 3, mode 1. (a) Matching at ports 1 and 3. (b) Transmission magnitude from port 1 to the two orthogonal modes of port 3. (c) Transmission phase difference from port 1 to the two orthogonal modes of port 3.

The polarizer consists of three ports: a square port that leads to the horn antenna, and two rectangular ports. If one of the rectangular ports is excited, the resulting wave scattered on the square port is CP. The excitation of the other port results in the CP of an opposite sense.

During the simulations, the fundamental TE10 modes are excited in the rectangular wave ports 1 and 2, and two fundamental modes, TE10 and TE01, in the square wave port 3. The heights and lengths of the individual ridged sections of the septum are optimized to give the best CP performance with a minimum total length. The optimized polarizer performance is presented in Figure 5.18. The return loss at all ports and rectangular-port isolation are better than 30 dB in the

frequency band of interest. The equal power division to the two orthogonal modes in the square WG and the transmission-phase difference of 90° ensure the excitation of a high-quality CP radiation. The polarizers of this kind can be optimized further for a wideband or dual-band performance.

5.4.4. Full Feed Chain

The 3D simulation model of the full feed-chain geometry is shown in Figure 5.19. The composing parts of the antenna are:

1. **Corrugated Horn** – described in Section 5.4.2.
2. **Circular to square WG transition** – a simple linear taper from a 9-mm circular WG to a 7.8-mm square WG
3. **Septum polarizer** – described in Section 5.4.3.
4. **WR42 transition** – an S-shaped WG twist, with a gradual linear taper from a 7.8 x 3.4-mm^2 WG to a standard-sized WR42 (10.668 x 4.318 mm^2)
5. **WR42 flange** – a standard flange for mating with the adapters of the measurement system

The fabrication method, selected for the prototyping of the feeding system, is the additive manufacturing in aluminum, or more precisely Direct Metal Laser Sintering (DMLS) [109]. It allows the entire feed chain to be built as a single metallic piece. During this procedure, an aluminum-alloy powder is selectively melted, layer by layer, with a high power-density laser. The structure is therefore gradually 'grown' along one axis. In the case of this antenna, the printing direction is along the Z-axis. The WR42 transition has a characteristic smooth shape since the DMLS process cannot handle interior walls perpendicular to the printing direction (these would appear if right-angle bends were used). The standard WR42 is designed as the input WG since the WR42-to-coaxial (3.5 mm connector) adapters are available in the measurement facilities.

The pictures of the fabricated prototype are shown in Figure 5.20. During the anechoic-chamber measurements, two WG-to-coaxial adapters were connected to both ports of the feed chain, and a 50 Ω termination was additionally connected to the port that is not used for measurements. The measured radiation pattern and AR of the antenna are compared with simulations in Figure 5.21. The measured co-polarized pattern is in agreement with the simulated one. There is a larger discrepancy in the cross-polarized pattern, which is attributed to the fabrication accuracy of the DMLS method. The most critical part of the feed chain, in terms of fabrication, is the polarizer, since it is difficult to accurately 3D-print the small geometrical details of the septum. However, the measured AR is smaller than 2 dB within a beamwidth of ±20°, and the broadside AR is smaller than 0.5 dB across the specified frequency bandwidth. Moreover, the radiation patterns retain the shape and levels in this frequency range.
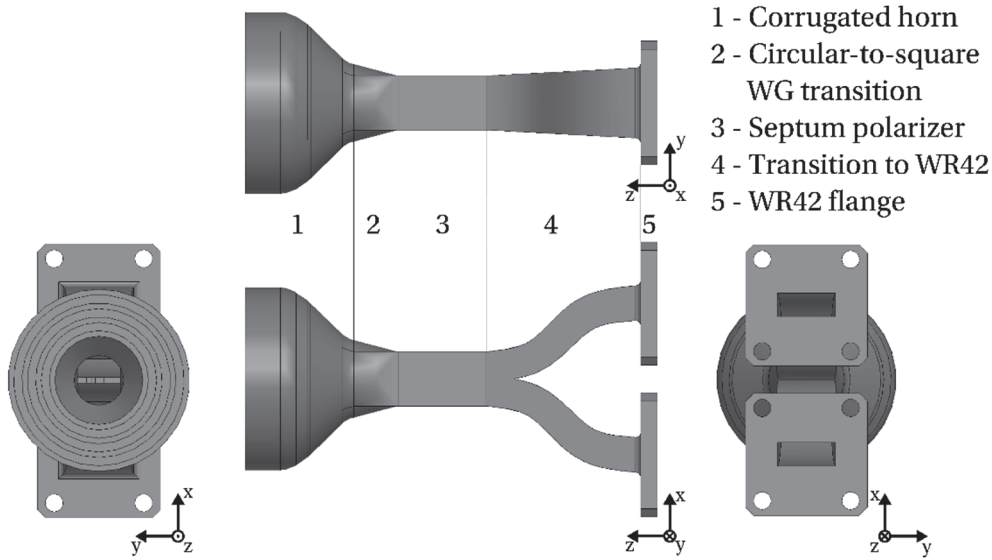
Figure 5.19. Simulation 3D model of the feed chain, with denoted individual components.

5.4.5. Future Integration with a CubeSat

The measured performance of the horn antenna prototype makes it suitable for RA and TA feed applications. A stable AR over frequency is especially important for the operation with the wideband RA antenna element, described in Section 5.3.

The presented feed-chain geometry is primarily developed for the laboratory evaluation of RA and TA prototypes. The final antenna prototype will have to be redesigned for an efficient integration with the CubeSat structure. The main aspects that could be modified are:

- **Coaxial-to-WG transition** – Instead of the bulky adapters, the coaxial probe can be directly integrated into the feeding WG immediately before the septum polarizer. Depending on the polarization used in the system, it could be possible to match one of the two polarizer's ports.
- **Horn aperture** – If the total horn antenna diameter (33 mm) is too large, the size can be reduced by using only two corrugations. The increased horn beamwidth would then require a smaller F/D of the antenna system, for an optimal illumination of the array aperture.
- **Septum polarizer in a circular WG** – The square-to-circular WG transition can be omitted by designing the septum polarizer in the circular WG, and gradually changing the cross-section to the two rectangular output ports of the polarizer.
- **Total length optimization** – Once one or several of the mentioned modifications are implemented and individually optimized, the entire structure should be optimized as a whole with the main goal of minimizing the total length.
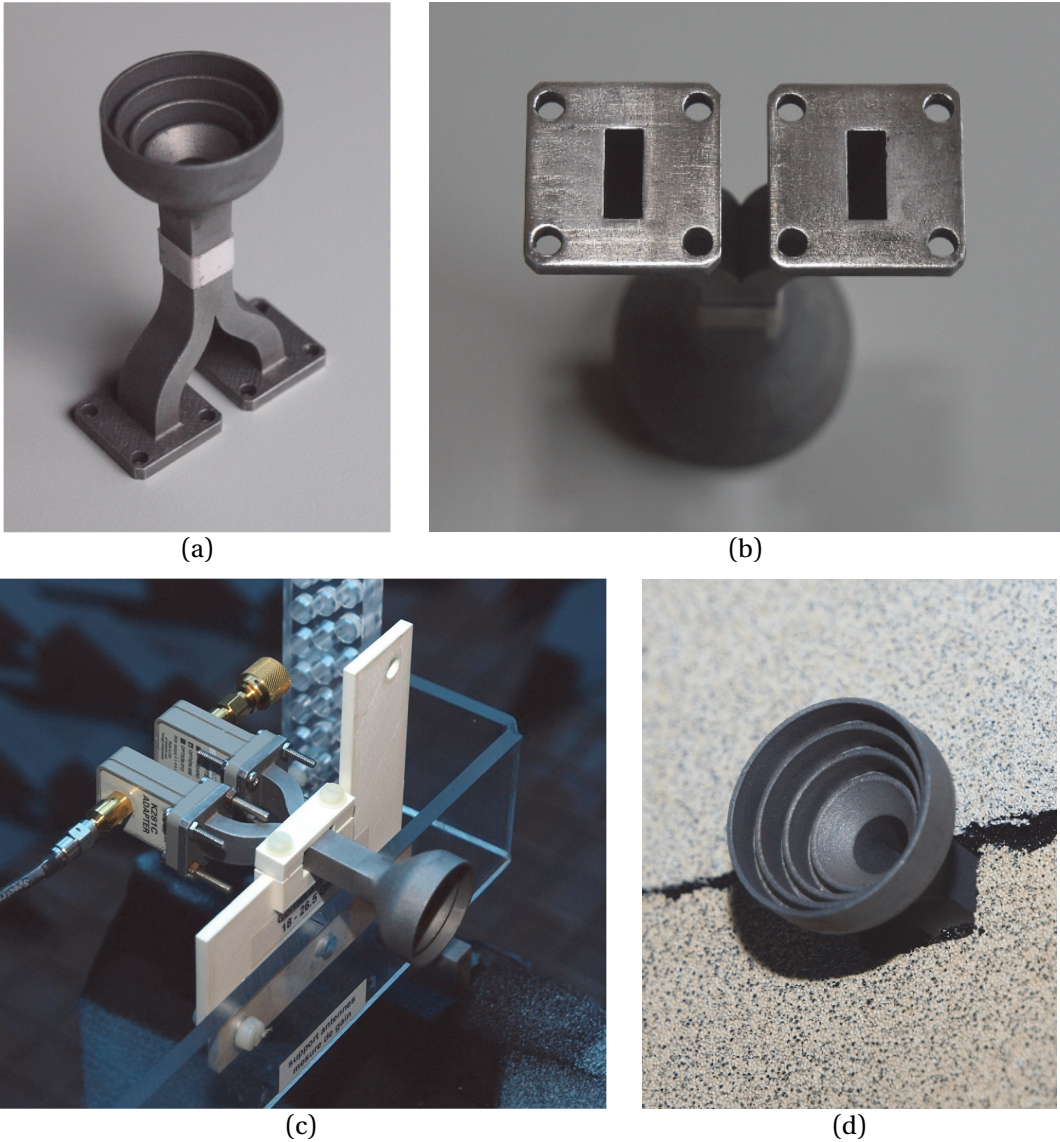
Figure 5.20. (a) Prototype of the 3D-printed feed chain. (b) Polished mating surfaces of the WR42 flanges, for ensuring a good contact. (c) Feed chain mounted on a plastic support inside the anechoic chamber, before adding the absorbers. The WG-to-coaxial adapters and the 50-Ω load are visible in the picture. (d) Horn antenna detail, after the absorbers were placed.
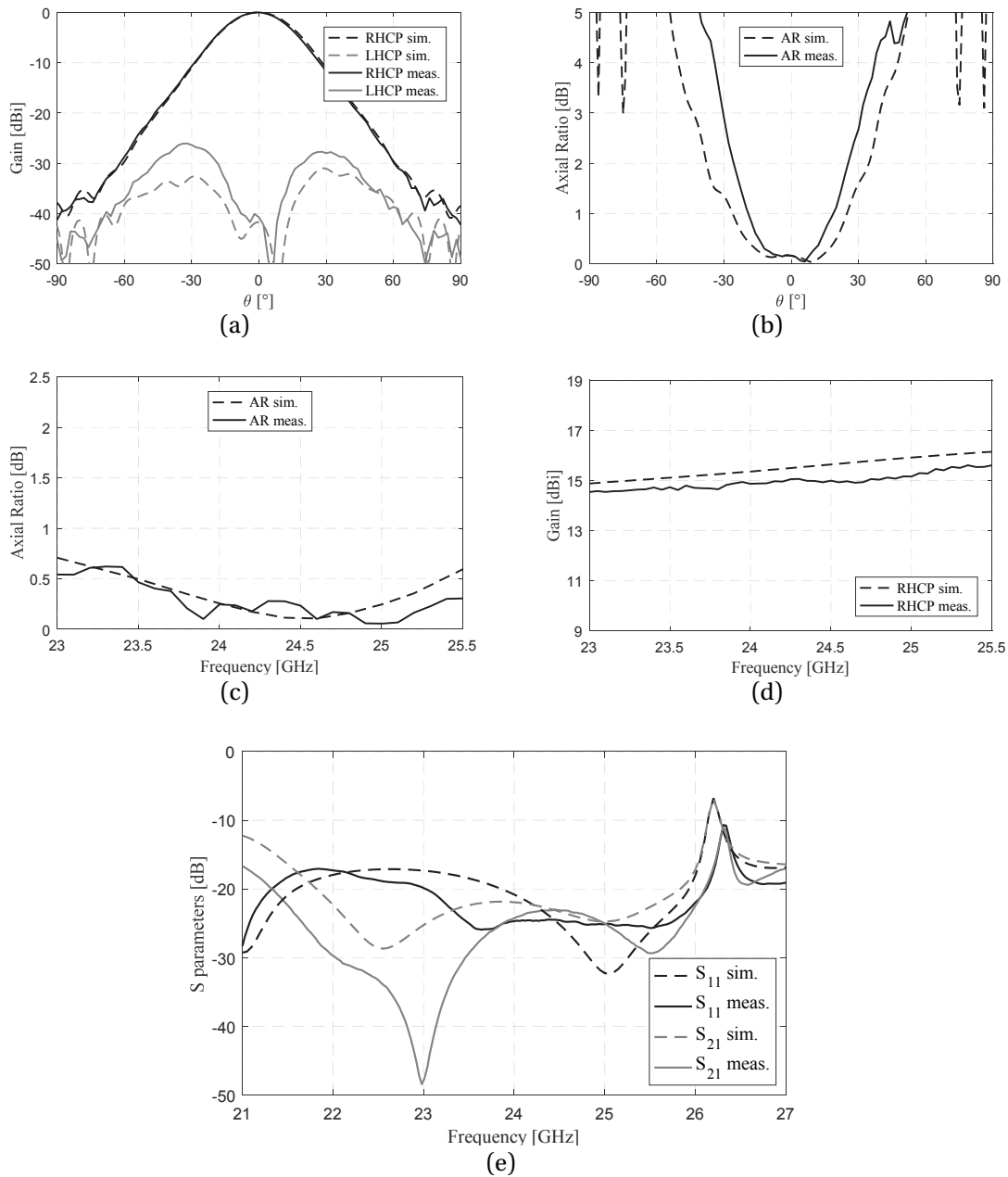
Figure 5.21. Simulation and measurement results of the feed chain. (a) CP radiation patterns. (b) AR versus angle. (c) AR versus frequency. (d) Realized gain vs. frequency. (e) S parameters.

A drastic size reduction could be achieved with these modifications, without a significant loss in performance. However, the horn aperture remains the bulkiest part of the feed chain. During the CubeSat launch, it would have to be stowed in a dedicated compartment inside the satellite body. One envisioned configuration is shown in Figure 5.22. The feed chain is stowed inside the CubeSat

and covered with the array panel(s). Following the panel deployment in orbit, the horn simply moves up to the required position by a spring mechanism. The rotation is done around the axis of the feeding coaxial probe. The feeding structure can be integrated into the rotating hinges.

This type of feed occupies a significant volume compared to planar feeds (patch arrays) that are stowed on the CubeSat exterior. As such, it is not compatible with most standard CubeSat chassis and internal components directly below the feeding mechanism. However, the ISL functionality is, in itself, an exotic feature for CubeSats in today's standards. Therefore, the feed and array designs are primarily intended for high-performance CubeSats, for which a custom-built chassis is typical.
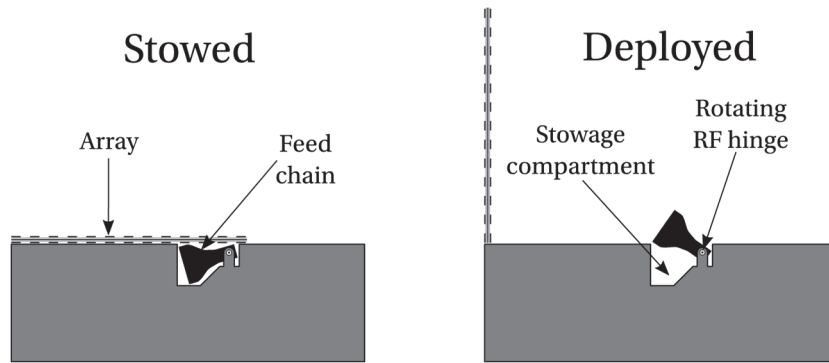
Figure 5.22. The stowage and the deployment mechanism of the proposed feed chain. The side view shows the cross section along the CubeSat center.

5.5. Summary and Discussion

RA and TA antennas offer an excellent compromise in terms of mechanical complexity and electrical performance. They are an attractive choice for CubeSat CP ISL communications in K/Ka bands, when a required antenna aperture is not available on the satellite surface. These antenna types consist of a planar array of discrete elements and a feeding element, placed in the array focal point. Different methods are used to achieve the phase shifting of the incident radiation from the feed, in order to scan the beam radiated by the antenna aperture, in the desired direction. This chapter focused on the study of individual elements of RA and TA antenna systems.

Most of the elements in the considered arrays are similar in geometry and they can be efficiently analyzed using the infinite-array approximations. Simulation setups for RA and TA elements, using periodic boundary conditions and Floquet-harmonic excitations, are presented in Section 5.1.1.

If the array radiation is CP, a special technique of variable element rotation can be used for the phase-shifting purpose. A detailed theoretical analysis of the technique is given in Section 5.1.2. The RA elements that qualify for the element-rotation technique must have the same CP sense of

the scattered and incident waves, whereas the CP sense of the wave should change while passing through an eligible TA element. The CP-sense change is achieved with a phase difference of 180° between the two LP wave components. The phase shifting is then done with a simple element rotation around the vertical axis. Two novel elements that satisfy described conditions, one each for RA and TA antennas, are presented in this chapter for CubeSat ISL applications.

Conventional TA elements achieve the required phase difference with either a significant profile or unreliable metallized vias. The TA element proposed in Section 5.2 introduces a simple modification to the slot shape, thus reducing the number of required metallic layers from five to three. The associated profile reduction and the manufacturing simplicity can be the enabling factors for CubeSat applications. The element is incorporated in two final TA antenna designs. The full array performance is simulated using the approach described in Chapter 6, where the prototype measurements of the TA antenna are also presented.

The novel coupled-loops RA element, presented in Section 5.3, is an evolution from a well-known microstrip split-loop. By coupling two microstrip loops, a significant bandwidth improvement is obtained. The frequency spacing of the two resulting resonant modes is a key factor for enabling a wideband performance. The increase in complexity is minimal, compared to the original element, as the final geometry remains single-layer without any metallized vias or SMD components. The simple geometry and a wideband CP performance make the coupled-loops element a very promising candidate for CubeSat communications, as well as other RA applications.

The feed antenna should radiate CP across the entire frequency band that the RA and TA elements cover. An axially corrugated horn antenna is designed for this purpose. The axial corrugations provide a lower off-axis cross polarization, compared to the conventional circular horn. A septum polarizer in the common square WG provides the required CP radiation at the horn aperture. The feed-chain prototype is fabricated for laboratory testing, using the additive manufacturing in aluminum. The measured standalone performance of the all-metal feed-chain prototype confirms its eligibility for CubeSat ISL applications as the RA and TA feeding element. The presented horn antenna is used during the design and measurement phases of several RA and TA antennas in the Chapter 6.

6. RA/TA Design Process

Once the individual components (array elements and the feeding antenna from Chapter 5) have been designed and characterized, the simulation results are combined to predict the performance of the entire RA or TA antenna system. The array synthesis and radiation analysis processes are presented in the beginning of this chapter. Both functions are performed with a custom MATLAB code, which imports the simulated results from the EM software, generates the array geometry, and performs the necessary far-field calculations.

Both the arrays and the feeding antenna exhibit CP radiation, which is a main requirement for ISL communications. The AR of individual array elements and the feed horn, described in the previous chapter, is low across the entire specified frequency band. Consequently, the variable rotation technique can be used to generate the required phase shift across the array, for collimating the array radiation and tilting the main beam.

The variable rotation technique for RA and TA antennas in its standard form uses an analytical formula to calculate the rotation angles that provide the necessary phase shift across the array aperture. Depending on the element geometry and the elevation angles of incidence, a phase error is introduced with this approach. A different, and yet simple, process is used here to eliminate the phase errors and consequently increase the array gain.

One RA and one TA antenna, with 900 elements each, are designed and analyzed using the described code. The aperture efficiency of the arrays is calculated as a combination of individual efficiency factors. The designed array yield a gain of at least 32 dBi, with the aperture efficiency larger than 60%. The 1-dB CP bandwidths of the two array are comparable, at ~6%.

Two prototype sets of the designed arrays are fabricated for measurements at two different facilities. The prototype measurements are compared with the simulations at the end of the chapter. The agreement between the conducted measurements and simulations verifies the antenna performance and the RA and TA design process.

6.1. Design Process Overview

The entire design process is summarized with a flowchart in Figure 6.1. The program is separated into two main parts:

- **Synthesis and analysis** – calculates the element rotation angles and the array radiation at the central frequency
- **Frequency analysis** – calculates the radiation parameters over a frequency band for the obtained element rotations

The first part uses the array unit-cell and the feed simulation results at the center frequency as the input. The simulation results are then interpolated and sampled, and the scattered fields are calculated using the procedure described in Section 5.1.2. The results are then used to obtain the array geometry in the form of the element-rotation matrix. The total array radiation and aperture efficiency are calculated at the center frequency with the approach described in Sections 6.4 and 6.5, starting from the scattered fields on individual array elements.
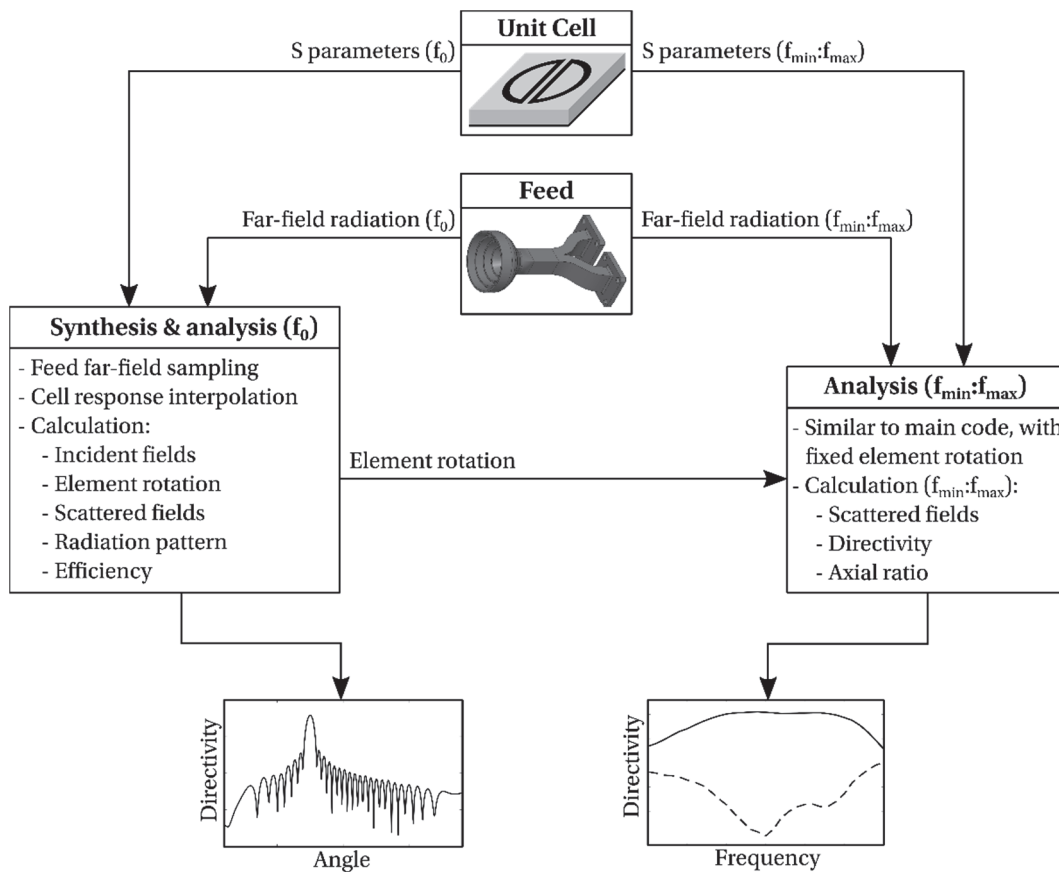
Figure 6.1. A flowchart of the RA and TA antenna design and analysis process. Frequency f_0 represents the central (design) frequency of the array, and f_{min}:f_{max} the analyzed frequency range.

The inputs for the second part of the code are the unit-cell results in the entire frequency range of interest and the element-rotation matrix, obtained in the first part. The same analysis procedure is then repeated at every frequency point, for which the unit-cell and the feed responses are available.

The unit-cell simulations can become time consuming over a frequency band, having in mind the large number of incidence angles that must be considered. The use of a quasi-3D EM solver for this part accelerates the process and obtains the wideband unit-cell performance in a shorter time.

The antenna geometry and coordinate systems used for the arrays considered in this thesis are presented in Figure 6.2. The focal point is located above one edge of the array, to model the feed antenna placed on the CubeSat surface and the array deployed perpendicularly to that surface. The following sections (6.2 – 6.5) describe the individual steps of the array-design process, and discuss the main points from the CubeSat perspective.

6.2. Feeding-Antenna Radiation

6.2.1. Methodology

The radiated fields from the feeding antenna illuminate the individual array elements with a different incidence angle, magnitude and relative phase. Determining the incident fields accurately is necessary for a good array synthesis and the estimation of the array far field. Two methods, commonly used to evaluate the array illumination, are depicted in Figure 6.3.

The first method involves sampling the far field of the feeding antenna, calculating the distance from the feed to the individual elements and combining the far field with the path loss to obtain the magnitude and phase of the incident fields. The method assumes that the array is located far enough from the feed, so that it is not influenced by the near fields of the feed. Since an FEM code is used for the 3D simulation, the model of the feeding antenna needs to be enclosed with an 'airbox' – a 3D object with radiation/PMC boundaries at the object faces.

The second method calculates the near fields in the exact locations of the individual elements. The method implies either having a large airbox or using a hybrid FEM-MoM setup (FEM inside the two regions and MoM at the exterior). The Poynting vector is calculated at the element locations and adopted as the incidence angle for each element. The electric fields transversal to this vector are adopted as the incidence fields, from which the magnitude and phase are obtained. Alternatively, (6.1) can be used for the same purpose.

The second method can be considered more accurate, as it calculates exact fields at element locations. However, if the feed position changes, the entire model must be re-simulated, since the relative position of the array elements has changed. For the first method, it is only required to re-sample the existing far-field results, which requires significantly less resources.

The first method is adopted in this thesis. It is found more convenient in the case where several arrays with different F/D values are used. It gives the freedom to optimize the F/D for a given feeding antenna, with just one 3D simulation. The array elements considered in this chapter are located in the far-field zone of the feeding antenna, and thus satisfy the conditions to use this method.
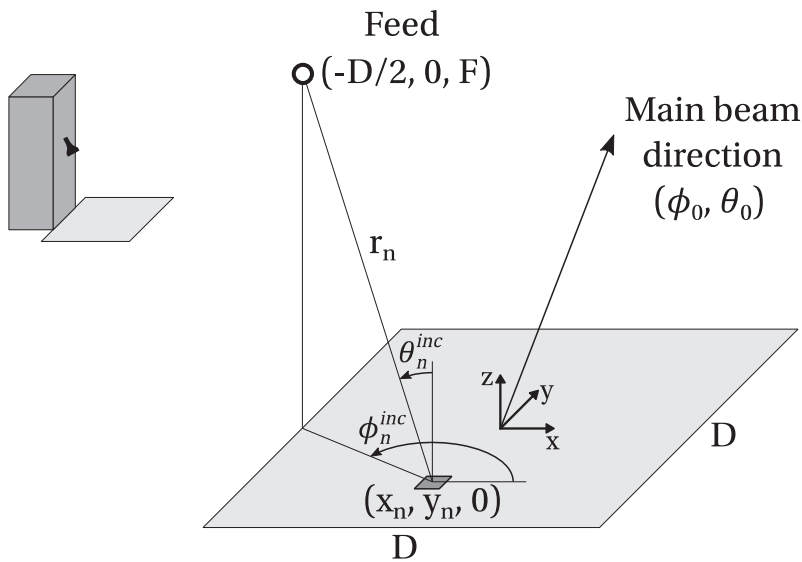
Figure 6.2. The array geometry and nomenclature used throughout the chapter, with respect to the deployed-array configuration on a 3U CubeSat (top-left).
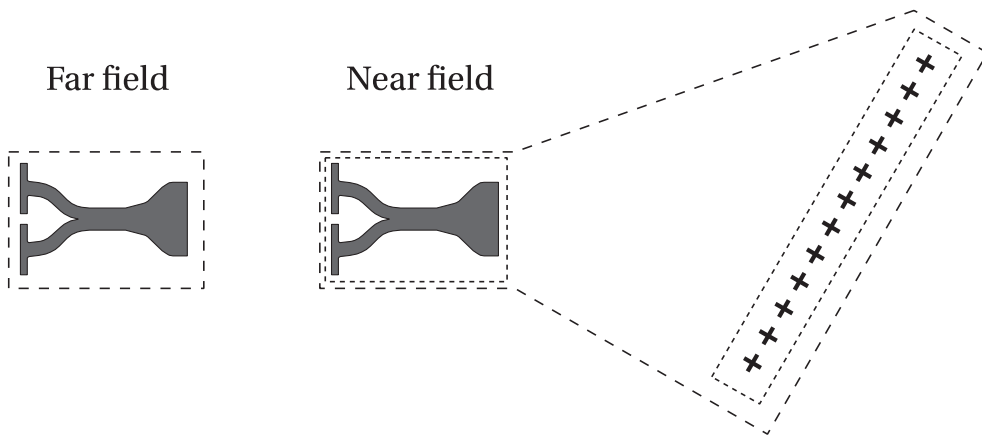
Figure 6.3. Two common EM simulation setups for the calculation of the feeding-antenna radiation. The dashed lines represent the airbox boundaries for the FEM model and the dotted lines represent the boundaries for the hybrid FEM-MoM regions.

6.2.2. Calculation of Incident Fields

Two Cartesian coordinate systems are defined for the feed and the array elements. The systems are aligned at first, and then the elements are moved to their final position using geometrical manipulations (rotation and translation matrices). The element positions are determined in the feed's coordinate system and converted to the spherical coordinates. The far field is sampled at coordinates θ and ϕ (in the feed's system) and the element distance can be obtained from the coordinate r. Finally, the path loss is calculated from the distance to the individual elements and combined with the radiation pattern of the feed to obtain the incident fields on the array.

Examples of the normalized magnitude of the incident electric field is presented in Figure 6.4 for three values of F/D, in the case of an offset-fed array from Figure 6.2. The axially corrugated horn from Chapter 5 is used as the feeding element in all cases, pointing towards the array center. As often suggested in the literature, the goal is to have the array edges illuminated by a field magnitude approximately 10 dB lower compared to the center illumination, for optimal aperture efficiency. This condition is fulfilled in Figure 6.4(b). The two sub-optimal scenarios are illustrated in Figure 6.4(a,c). Having a lower F/D results in a poor utilization of the array aperture, as the feed radiation is focused in the array center. On the other hand, a large F/D value yields a large power spillover. The loss mechanisms are further discussed in Section 6.5.

6.3. Array Synthesis

6.3.1. Unit-Cell Incidence Angle

The element-rotation technique states that the phase of the co-polarized reflected or transmitted signal is equal to twice the element rotation angle. This is, however, strictly valid only for the broadside wave incidence. The actual phase of the considered RA and TA elements (and many other) deviates from this rule for large elevation angles, as seen in Figure 6.5.
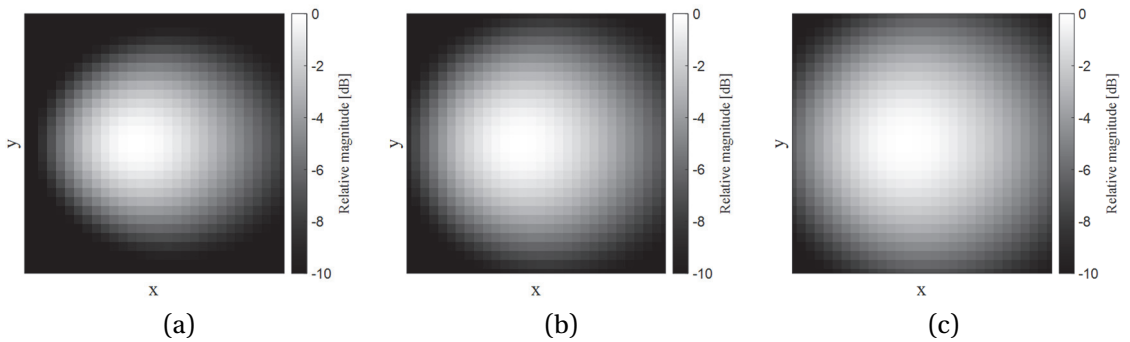
Figure 6.4. The normalized magnitude of the electric field incident on the offset-fed array, for different values of F/D. (a) F/D=0.7. (b) F/D=0.9. (c) F/D=1.1.
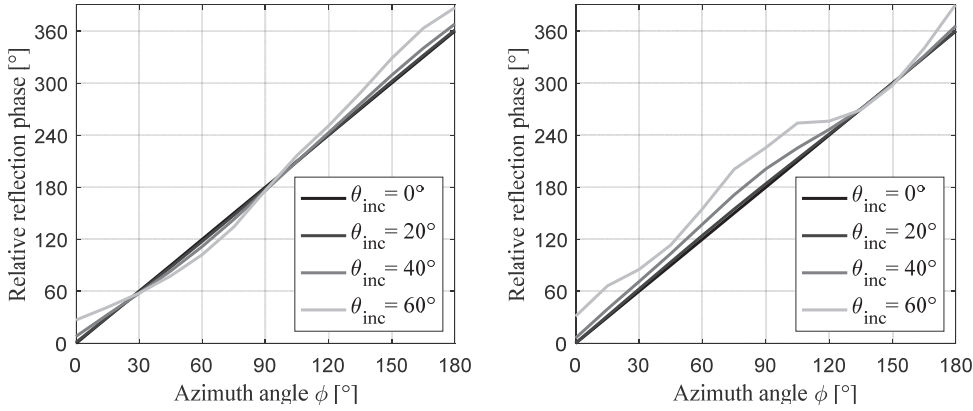
Figure 6.5. Phase response of the (a) RA and (b) TA elements, versus the azimuth incidence angle, for different elevation incidence angles.

The effect is more severe for offset-fed RA and TA antennas, as the average elevation angle of incidence is larger in that case. For an accurate array synthesis, the element rotation and the resulting phase of every element must be determined for the given elevation angle of incidence.

6.3.2. Assumptions

The RA and TA are typically composed of hundreds of elements, and the angle of incidence is different for most of the elements. Ideally, the unit cell should be simulated for every combination of azimuth/elevation angles of incidence and rotation angles. This would not only be a tedious task, it would also have to be repeated every time a different position of the feed is desired. Instead, a given unit cell is simulated for a set of uniformly distributed azimuth/elevation angles, and the results are interpolated. The phase of a certain incidence angle is then obtained by a simple table lookup in the interpolated results. During this process, an assumption is made that the negative change of the element-rotation angle is equal to an identical positive change of the azimuth angle of incidence [91]. The unit cell is then simulated only with the element rotation set to zero. Although this arrangement is not representative for the majority of the array elements, the assumption is valid if the inter-element coupling is low, as is the case in this thesis.

6.3.3. Element Rotations

For the array configuration of Figure 6.2, the incidence angles of element n, located at coordinates (x_n, y_n), can be found by:

$$\theta_n^{inc} = \mathrm{acos}\left(\frac{F}{r_n}\right), \qquad \phi_n^{inc} = \mathrm{atan}\left(\frac{y_n}{x_n + \dfrac{D}{2}}\right) - \pi \tag{6.1}$$

$$r_n = \sqrt{\left(\frac{D}{2} + x\right)^2 + y^2 + F^2} \, ,$$

where angles θ and ϕ are defined starting from z and x axes, respectively. To scan the beam in the (θ_0, ϕ_0) direction, the phase distribution across the array is given by:

$$\psi_n = k_0(r_n - x_n \sin\theta_0 \cos\phi_0 - y_n \sin\theta_0 \sin\phi_0) + \psi_0 \qquad (6.2)$$

where ψ_0 is an arbitrary constant. Expressions (5.9) suggest that the element rotation should be set to:

$$\alpha_n = \frac{\psi_n}{2} \qquad (6.3)$$

since the phase shift is equal to twice the value of the rotation angle. However, this rule is valid only for broadside incidence, although it yields more accurate results for center-fed arrays, or arrays having a large F/D value.

A different approach of element-rotation calculation is adopted here to eliminate the phase errors that arise for large elevation angles of incidence. The arrays considered in this thesis are offset-fed, meaning that the angles θ^{inc} have a large value on average. As an illustration, if F/D equals 0.8 for the configuration in Figure 6.2, approximately 66% of elements will have the θ^{inc} angle larger than 30°.

The array synthesis is described here for RA antennas. The procedure for the n-th element of the array is as follows:

1. Calculate the azimuth angle of incidence ϕ_n^{inc} using (6.1).
2. Determine the current phase of S_{11}^{RR} for the given azimuth angle ϕ_n^{inc}.
3. Determine the required phase ψ_n in that array location with (6.2) and the associated required azimuth angle.
4. The element rotation angle is the difference between the required and initial azimuth angles.

The procedure is graphically represented in Figure 6.6. An equivalent procedure is used for TA antennas, except that the parameter S_{21}^{LR} is used in step 2. The proposed approach does not notably increase the execution time, compared to the closed-form expression (6.3), even for several thousand elements within the array. The procedure is repeated for every array element, to obtain the element-rotation matrix for a given F/D and beam-steering direction.

The element rotations are calculated for three F/D values as an example, similarly as in Figure 6.4, and shown in Figure 6.7. A lower F/D yields more phase wraps. Unlike the conventional RA elements, which cannot achieve a full 360° reflection-phase range, the phase wrapping is not an issue here, and it is hardly visible in the final antenna prototypes.
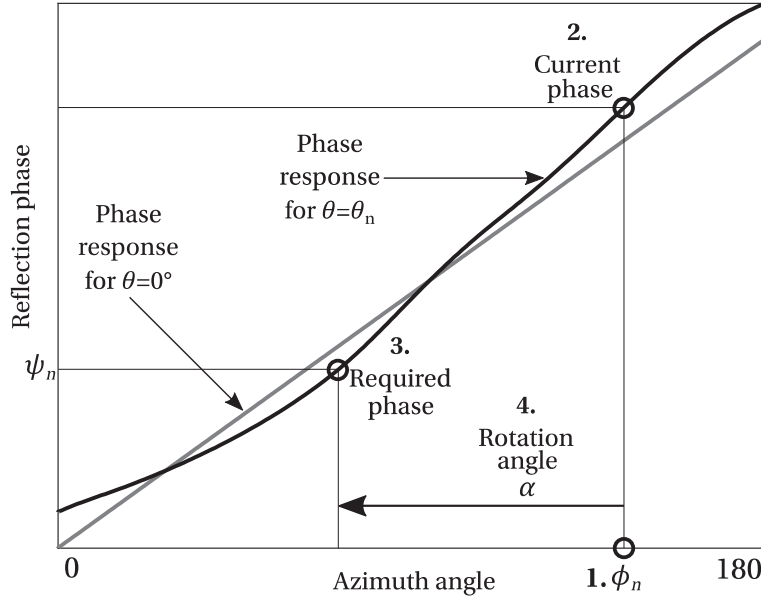
Figure 6.6. A graphical representation of the array-synthesis procedure on the element level. Numbers in bold mark the order of steps.
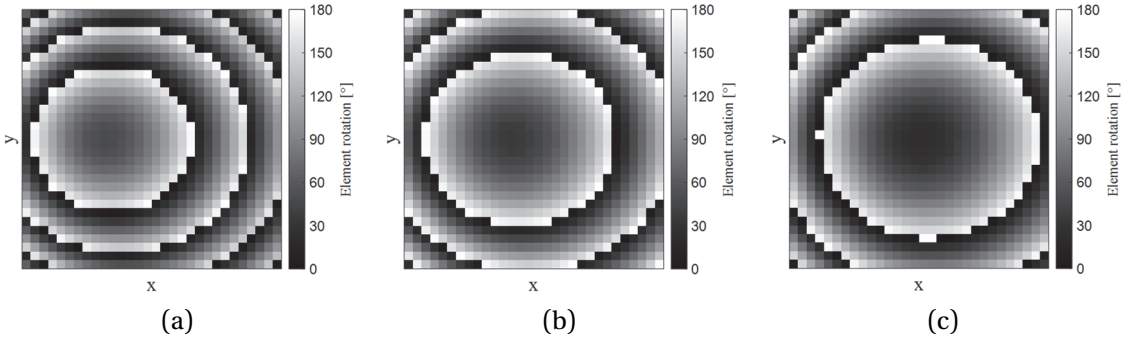
Figure 6.7. Characteristic element-rotation angles across the RA surface, for different values of F/D. (a) F/D=0.7. (b) F/D=0.9. (c) F/D=1.1.

6.4. Array Analysis

The analysis in Chapter 5 is used to calculate the fields, scattered from the array of rotated elements. The described procedure is performed for every array element, summing the individual far-field contributions afterwards.

The unit-cell simulations are done with LP excitations (TE, TM) in the quasi-3D EM software and the S parameters are converted directly in the software to $\mathbf{S}_{\text{rot}}^{\text{CP}}$ using expressions (5.9). This is convenient since the field radiated by the feeding antenna is also CP, and the CP performance of the unit cells can be quickly inspected within the software. The incident fields on the array ($\mathbf{a}^{\text{CP}}$)

are obtained by adding the propagation loss to the horn-antenna gain, sampled in the direction of every element. The incident fields are then combined with CP S parameters to obtain the scattered fields ($\mathbf{b}^{CP}$) using (5.6), taking into account the exact incidence and rotation angles for every element. The rotation angles are calculated using the procedure in Section 6.3.2.

The far-field radiation of the array is calculated using the special case of the Field Equivalence Principle applied to radiation of rectangular apertures. A RA scenario is considered here for simplicity, although an identical procedure is applied for the TA case. Every array element is treated as a uniformly illuminated rectangular aperture in an infinite PEC plane and the element is replaced by the equivalent magnetic currents, from which the radiation is calculated. The scattered fields $\mathbf{b}^{CP}$ are represented in the form of two LP orthogonal components. For an arbitrary oblique incidence, the scattered fields are first converted to TE and TM components:

$$\begin{bmatrix} b^{TE} \\ b^{TM} \end{bmatrix} = \frac{1}{\sqrt{2}} \begin{bmatrix} 1 & 1 \\ j & -j \end{bmatrix} \begin{bmatrix} b^R \\ b^L \end{bmatrix} \tag{6.4}$$

and then to Cartesian components:

$$\begin{bmatrix} b^X \\ b^Y \end{bmatrix} = \frac{1}{k_c} \begin{bmatrix} -k_y^{inc} & k_x^{inc} \\ k_x^{inc} & k_y^{inc} \end{bmatrix} \begin{bmatrix} b^R \\ b^L \end{bmatrix} \tag{6.5}$$

where k_x^{inc} and k_y^{inc} can be obtained by replacing (ϕ, θ) with $\left(\phi^{inc}, \theta^{inc}\right)$ in (5.2), and:

$$k_c = \sqrt{\left(k_x^{inc}\right)^2 + \left(k_y^{inc}\right)^2} = k_0 \sin \theta^{inc} . \tag{6.6}$$

Index n is omitted in (6.4)-(6.6) for clarity, and it is implied that the expressions are calculated for every array element. The spherical components of the radiated fields are then obtained by:

$$E_n^{\theta}(\theta, \phi) = jk_0 F \frac{e^{-jk_0 r}}{2\pi r} \left(b_n^X \cos \phi + b_n^Y \sin \phi\right) \tag{6.7}$$

$$E_n^{\phi}(\theta, \phi) = jk_0 F \frac{e^{-jk_0 r}}{2\pi r} \cos \theta \left(-b_n^X \sin \phi + b_n^Y \cos \phi\right) . \tag{6.8}$$

$$F = d^2 \operatorname{sinc}\left(\frac{k_x d}{2}\right) \operatorname{sinc}\left(\frac{k_y d}{2}\right) e^{j(x_n k_x + y_n k_y)} \tag{6.9}$$

where k_x and k_y are obtained from (5.2) and a is the square unit-cell dimension. Expressions (6.7) and (6.8) give the radiated electric-field components for a single cell n, and the total far field of the entire array is obtained by summing the contributions from N individual cells:

$$E_\theta(\theta, \phi) = \sum_n E_n^{\theta}(\theta, \phi), \qquad E_\phi(\theta, \phi) = \sum_n E_n^{\phi}(\theta, \phi) . \tag{6.10}$$

Finally, the RHCP and LHCP radiated components, directivity and AR are:

$$E_{R|L} = \frac{1}{\sqrt{2}} \left(E_\phi \mp j E_\theta\right) \tag{6.11}$$

$$D_{R|L} = 10 \log_{10}\left(\frac{2\pi}{\eta}\left|rE_{R|L}\right|^2\right) \tag{6.12}$$

$$AR = 20 \log_{10}\left(\frac{|E_R| + |E_L|}{|E_R| - |E_L|}\right) \tag{6.13}$$

all being functions of spherical angles θ and ϕ, where η is the free-space wave impedance. The power radiated by the feed is set to 1 W.

The described analysis procedure is performed at the central frequency, for which the element rotation angles are calculated. After the element-rotation matrix is obtained, the far-field calculation procedure is repeated for every frequency point, for which the cell and feed performance is available, as illustrated in Figure 6.1. During the frequency analysis, a fixed element-rotation matrix is used. The radiation pattern is calculated at the central frequency, and the directivity and AR are calculated at the beam-steering direction over the frequency band.

6.4.1. Alternative Approach

As an alternative to the method described in this section, the total array radiation can be calculated using the phased-array theory. With this approach, the element's radiation pattern is evaluated in the 3D EM software, and the far field is obtained using the scattered field of every element as the array excitation vector. The approach simplifies the far-field calculations, but requires the calculation of the active element pattern across a hemisphere. The active element pattern is obtained in the infinite-array approximation by illuminating the unit cell from a set of directions and recording the realized gain in the wave-incidence direction. This is a lengthy procedure, as it requires simulating the unit cell many times. However, the simulations for the magnitude/phase response of the cell can be re-used for this purpose, and the angular range can be reduced if the element possesses symmetry planes. The method has not been implemented in this thesis.

6.5. Aperture Efficiency

A uniformly illuminated aperture with a linear phase gradient would have an ideal efficiency of 100% and a maximal theoretical directivity. In a realistic antenna, several factors decrease this ideal directivity, and their combined contributions are quantified by the total efficiency:

$$\eta_{total} = \eta_{feed}\eta_{taper}\eta_{spill}\eta_{phase}\eta_{trans}\eta_{pol} \tag{6.14}$$

The total efficiency value consists of several terms:

- η_{feed} – the mismatch and ohmic losses associated with the feeding antenna

- η_{taper} – taper efficiency; quantifies the effects of the electric-field magnitude across the aperture deviating from the ideal, uniform distribution:

$$\eta_{taper} = \frac{(\sum_n |b_n|)^2}{N \sum_n |b_n|^2} \qquad (6.15)$$

- η_{spill} – spillover efficiency; the ratio between the power incident on the array and the total radiated power by the feed:

$$\eta_{spill} = \sum_n \frac{(|a_n^R|^2 + |a_n^L|^2)}{2\eta} d^2 \cos \theta^{inc} \qquad (6.16)$$

- η_{phase} – quantifies effects of the electric-field phase across the aperture deviating from the ideal, linear gradient, required for beam steering to $(\phi_0 = 0°, \theta_0)$:

$$\eta_{phase} = \frac{(1 + \cos \theta_0)^2}{4d^4} \frac{\left| \sum_n b_n e^{jk_0 d^2 x_n \sin \theta_0} \right|^2}{(\sum_n |b_n|)^2} \qquad (6.17)$$

- η_{trans} – the ratio between the total power scattered from the array to the total power incident on the array:

$$\eta_{trans} = \frac{\sum_n (|b_n^R|^2 + |b_n^L|^2)}{\sum_n (|a_n^R|^2 + |a_n^L|^2)} \qquad (6.18)$$

- η_{pol} – the ratio between the power scattered from the array in the desired polarization to the total power scattered from the array

$$\eta_{pol} = \frac{\sum_n (|b_n^R|^2)}{\sum_n (|b_n^R|^2 + |b_n^L|^2)} \qquad (6.19)$$

The expressions (6.16) – (6.19) are obtained by combining the analysis in [82], [91], [105] and writing the main results in the terminology used here. Depending on the specific RA or TA scenario and the feed/array polarizations, the waves a and b should be replaced by the proper polarization components (RHCP or LHCP) and port indices.

6.5.1. Discussion

The taper and spillover efficiencies are combined into a single parameter called the aperture efficiency:

$$\eta_{aperture} = \eta_{taper} \eta_{spill} \qquad (6.20)$$

This component is the dominant contributor to the total antenna efficiency, and it is imperative to maximize it by a proper selection of the system geometry and the feeding antenna parameters. In the literature, the aperture efficiency is typically maximized by using a center-fed circular array. A circular array aperture is the most suitable due to the circular symmetry of the feed's radiation pattern. A center-fed array results in a good taper efficiency and a relatively low average value of incidence angles, especially in the strongly illuminated array center, which is preferable for many

RA or TA elements with poor angular performance. Closed-form expressions for the aperture efficiency are available for this specific scenario [81].

The array geometry for antennas described in this thesis is constrained by the CubeSat structure, the deployment mechanism of the RA/TA panels, and the beam-steering direction. Therefore, the feeding element is always positioned with an offset from the array center. On the other hand, a rectangular (or square) array aperture is more suitable for the stowage on the CubeSat surface. From a clearly engineering standpoint, a rectangular aperture that maximizes the available surface is more advantageous due to an increased gain, although its aperture efficiency is lower. A detailed study on the efficiency of square reflectarray antennas showed how the aperture efficiency drops as the function of the feed offset-angle [110].

In our case, it would not be justified to use a circular aperture, simply to artificially boost the array performance (efficiency). Therefore, the values of aperture efficiencies for the square RA and TA antenna prototypes, presented in Chapter 7, are lower than what the proposed array elements can reach. To alleviate the effect, a larger F/D value is selected and the feeding antenna is designed to have a higher directivity than the conventional feed horns. In this way, the average value of incidence elevation angles is reduced.

The phase efficiency is calculated by (6.17) having in mind that the considered beam scanning is only within the plane ($\phi_0 = 0°, \theta_0$) (in other words, in the plane containing the focal point and the CubeSat's long axis). The ohmic and dielectric losses of the unit cell are described by η_{trans}, and the element's polarization performance by η_{pol}. All EM simulations are performed including realistic substrate materials. Other factors that contribute to the total efficiency (feed blockage, specular reflection) can only be quantified by 3D simulations of the entire array [82], which is not performed due to limited available computational resources.

6.6. Array Simulations

The total array size, for either RA or TA antennas, should be larger than a surface equivalent to three CubeSat units (3U) to achieve a gain larger than 30 dBi with a realistic efficiency and a small margin (see Figure 4.4). The arrays composed of 30 x 30 elements (a total of 900) are selected. As the unit-cell dimension is 6 mm, the total array dimensions are 180 x 180 mm^2 ($\sim$218 λ_0^2 @ 24.6 GHz) or 3.24 U in CubeSat units.

If the (quasi-)3D simulation results are available, the complete array synthesis and analysis procedures are efficiently executed on an ordinary PC, for 900-element RA and TA antennas. This, combined with the re-sampling of the feed radiation, allows us to vary the F/D of the arrays is in several sequential program runs. An optimal F/D value, in terms of the aperture efficiency (6.20), is found to be 0.9. The design procedure is again repeated several times for various phase

constants ψ_0. Changing ψ_0 moves the elements having a poor reflection/transmission efficiency away from the strongly illuminated array center and increases the total gain.

The simulation results of the RA and TA antennas are presented in Figure 6.9 – 6.12, and their performance is summarized in Tables 6.1 and 6.2. Both considered arrays have an F/D value of 0.9. According to Figure 4.11, the required beam-scanning angle for ISLs is in the range from 10 to 30°. Here, this angle is arbitrarily set to 25° and 20° for the RA and TA antennas, respectively. Figure 6.8 shows the same result as presented in Figure 6.9, only along one dimension of the RA aperture.
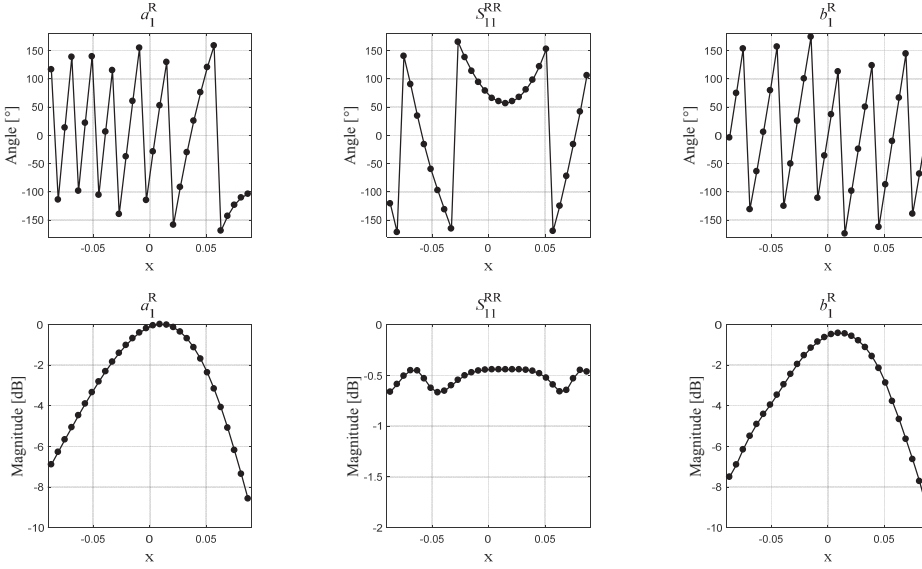
Figure 6.8. Simulated incident and scattered electric fields, and the S parameters, of a 900-element RA antenna at 24.6 GHz, for one row of elements along the x axis. The field components are the same as in Figure 6.9.

Table 6.1. Simulated-performance summary of the RA and TA antennas. Gain and AR values are calculated at 24.6 GHz in the main-beam direction.

Parameter	Limit	RA antenna	TA antenna
Gain @ (ϕ_0, θ_0)		32 dBi	32.6 dBi
AR @ (ϕ_0, θ_0)		1.4 dB	0.7 dB
SLL		-19 dB	-19.2 dB
Beam-Steering Angle		-25°	-20°
Beamwidth	1-dB	2.5°	2.5°
Gain bandwidth	1-dB	6.5%	5.7%
	3-dB	8.2%	> 8%
AR bandwidth	3-dB	7.4%	> 8%
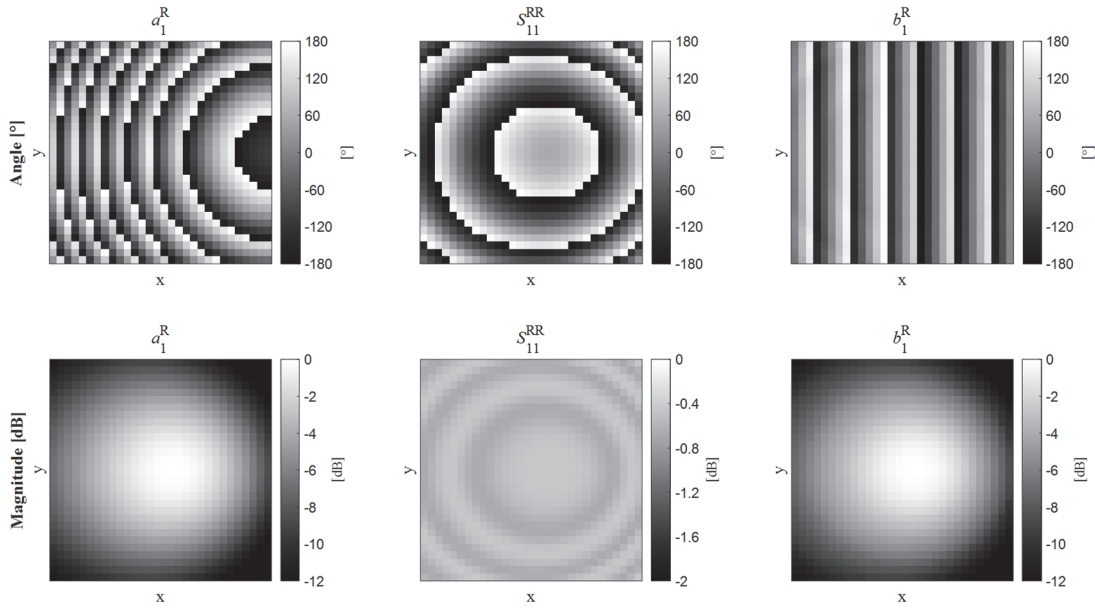
Figure 6.9. Simulated incident and scattered electric fields, and the S parameters, of a 900-element RA antenna at 24.6 GHz. (Top) The angle and (bottom) magnitude of the (left) incident electric field, (center) the S parameters, and (right) the scattered electric field.
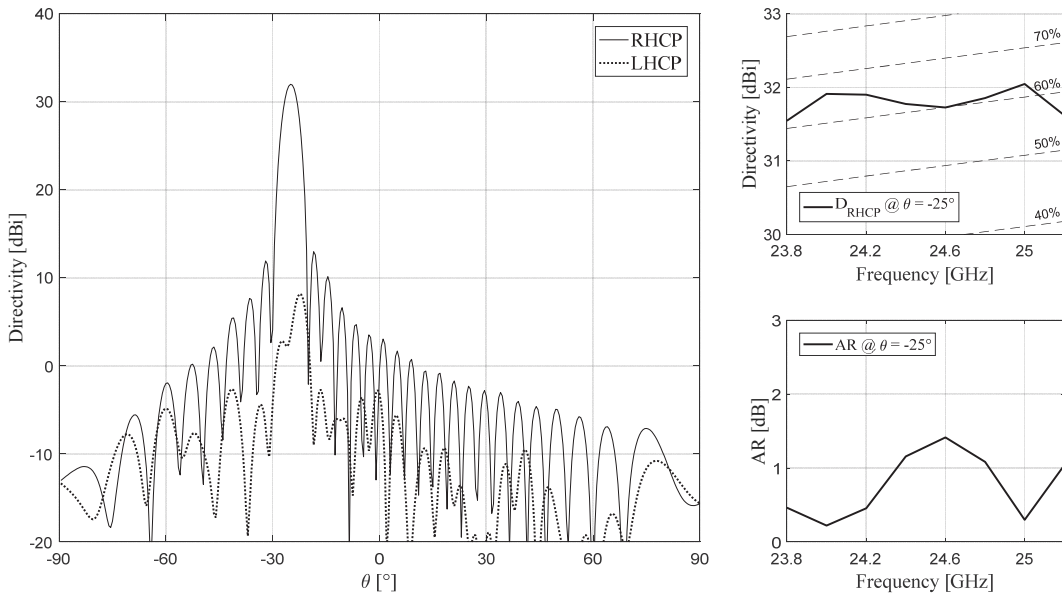
Figure 6.10. Simulated far-field performance of a 900-element RA antenna. (left) CP gain versus angle, at 24.6 GHz. (top-right) CP gain versus frequency, at the maximum-gain angle. Dashed lines represent the aperture-efficiency values, in percent. (bottom-right) AR versus frequency, at the maximum-gain angle.
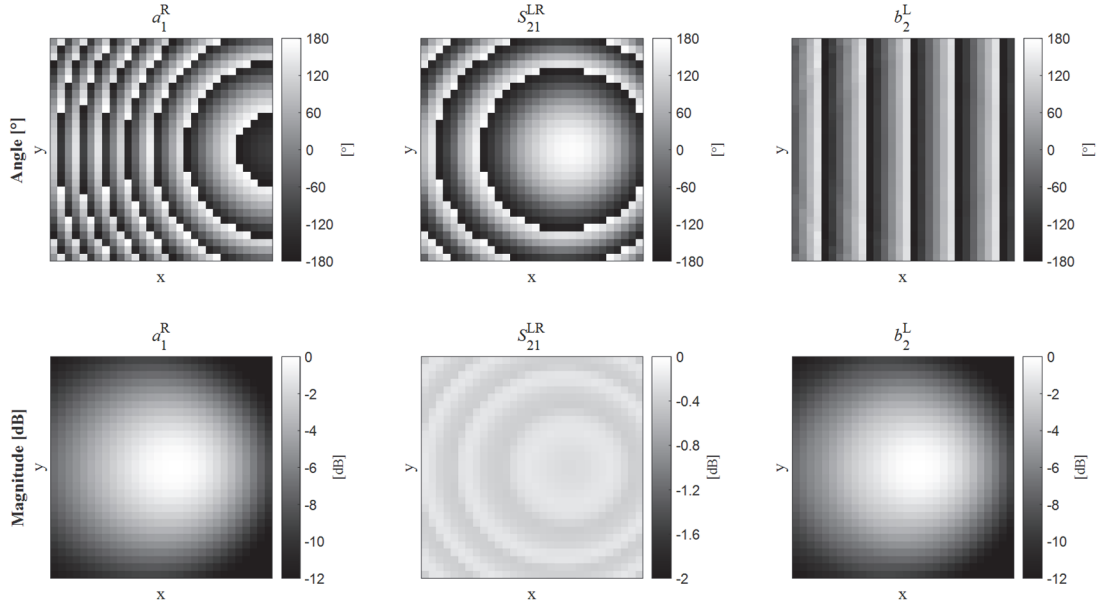
Figure 6.11. Simulated incident and scattered electric fields, and the S parameters, of a 900-element TA antenna at 24.6 GHz. (Top) The angle and (bottom) magnitude of (left) the incident electric field, (center) the S parameters, and (right) the scattered electric field.
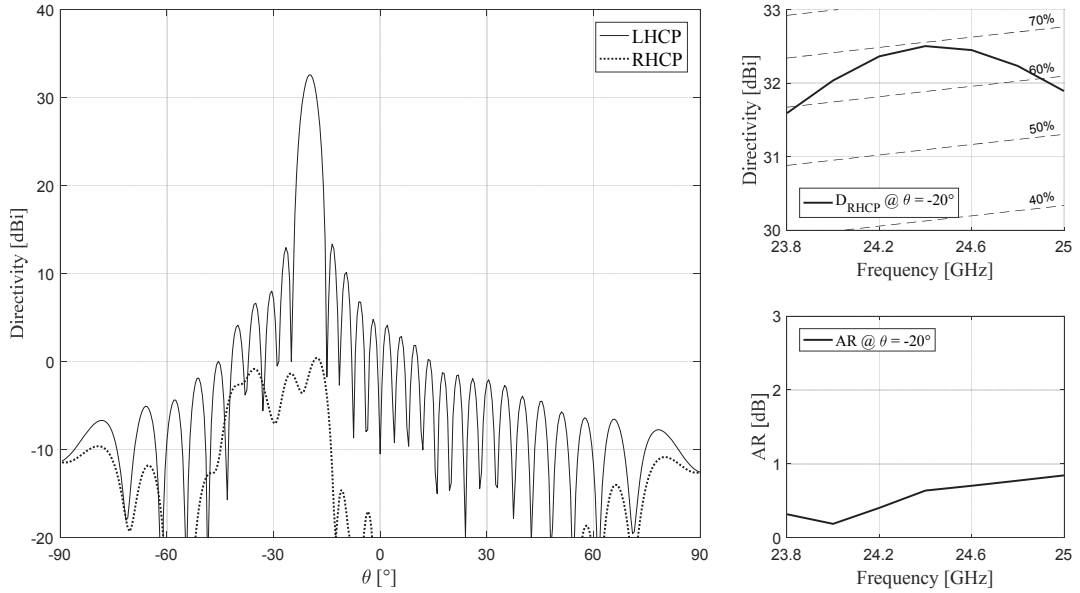
Figure 6.12. Simulated far-field performance of a 900-element TA antenna. (left) CP gain versus angle, at 24.6 GHz. (top-right) CP gain versus frequency, at the maximum-gain angle. Dashed lines represent the aperture-efficiency values, in percent. (bottom-right) AR versus frequency, at the maximum-gain angle.

Table 6.2. A breakdown of RA and TA antenna efficiencies at 24.6 GHz. The factor η_{feed} is set to 100%.

Efficiency	RA antenna		TA antenna	
	%	dB	%	dB
Taper	87	-0.58	87	-0.59
Spillover	81	-0.91	81	-0.91
Aperture	71	-1.49	71	-1.5
Phase	100	0	99	-0.03
Transmission	–	–	95	-0.21
Polarization	85	-0.71	98	-0.09
Total	**60**	**-2.21**	**69**	**-1.62**

In the case of the RA antenna, the phase distribution of the incident field a_1^R in Figure 6.9 is a consequence of a spherical wave propagation form the feeding antenna. In combination with the phase of the reflection coefficient S_{11}^{RR}, it yields a linear phase across the antenna aperture, required to scan the beam in the desired direction. The average magnitude of the parameter S_{11}^{RR} is -0.55 dB, and therefore, the magnitude of the scattered field has a very similar distribution to the incident one. Concentric circles, visible in the S_{11}^{RR} magnitude plot, correspond to the elements that have a lower reflection efficiency for the combinations of azimuth/elevation incidence angles at those element locations. As previously discussed, the positions of these lower-efficiency circles can be varied by changing ψ_0 in the array-synthesis design phase.

It should be noted that the presented S-parameter is calculated at the design frequency of 24.6 GHz, which is between the two resonances of the coupled-loops RA element, as previously presented in Figure 5.10. This frequency corresponds to the minimum value of the S_{11}^{RR} parameter across the element bandwidth and consequently, a minimum efficiency value of the RA antenna across the operating bandwidth. Therefore, the RA efficiency is further improved above and below the design frequency, resulting in a wideband performance. Both the gain and the AR over frequency follow a similar trend, with slightly better values above and below the design frequency.

For the TA antenna, the according transmission parameter S_{21}^{LR} and the transmitted scattered component b_2^L are presented in a similar fashion. The average magnitude of the parameter S_{21}^{LR} is - 0.29 dB, and the aperture efficiency reaches a value of 69% with an AR lower than 0.8 dB. Although the aperture-coupled-patch element has a single-resonance response and a low profile, a 1-dB CP bandwidth of 5.7% is achieved.

Overall, the simulated performance of the RA and TA arrays is significantly improved over the similar designs in the literature. The reported 1-dB and 3-dB gain bandwidths are typically 2 – 3% and 5 – 7% respectively, for the conventional single-layer split-loop RA geometries and other CP

single-layer RA elements. In contrast, the calculated values for the proposed coupled-loop RA element are 6.5% and 8.2%. Note especially the improvement of the 1-dB gain bandwidth by a factor of two. The proposed TA antenna reaches an aperture efficiency of 69% with only three metallic and two dielectric layers, as compared to a previously reported simulated efficiency of 56%, for a similar array having five metallic layers [91]. The CP aperture efficiency is among the highest reported for this type of antennas, with the total thickness of only $0.13 \lambda_0$ (1.6 mm). Despite the low electrical profile, a good gain bandwidth of the array is a consequence of the wideband performance of the aperture-coupled patch element.

As an additional illustration, the TA antenna, having a circular array geometry, is simulated with a simple CP square horn as the feeding element, centered on top of the circular array. A total efficiency of 0.73 (-1.4 dB) is achieved with an F/D value of 0.8 and a beam scanned to broadside, showing that the efficiency of both arrays can be increased further if a different system geometry and the feeding antenna parameters are selected.

Most importantly, the total efficiency of the proposed arrays is mainly determined by the aperture efficiency, which does not take into account the element performance. The efficiency degradation by the elements themselves is minimal. In other words, the reflection/transmission and polarization performance of the presented RA and TA element geometries maximizes the achievable capability of this antenna type, under the constraints of the given feeding scenario.

6.7. Prototype Measurements

6.7.1. Array Prototypes

Several antenna prototypes are fabricated to evaluate the antenna performance. The laminate Rogers Duroid 5870 ($\epsilon_r = 2.33, \tan \delta = 0.0012, h = 0.508$ mm) is used for the RA substrate, and Rogers RO6002 ($\epsilon_r = 2.94, \tan \delta = 0.0012, h = 0.76$ mm) for the two TA substrates. The two TA boards are bonded together using the Rogers 2929 BondPly ($\epsilon_r = 2.94, \tan \delta = 0.003, h = 51$ μm) adhesive film. The selected bonding layer has the same permittivity as the two substrates, to eliminate the potential reflections at the dielectric interfaces.

The 30 x 30-element arrays (180 x 180 mm^2) are printed on a 200 x 200 mm^2 PCBs. A PVC plastic support seen in Figure 6.13 is designed and fabricated specifically for these arrays, to place the feed and the array in the correct position during the measurements. Both RA and TA antennas are measured using this support. The support also allows to translate the feed along the axis perpendicular to the array aperture, and to rotate the feed around its phase center. Arrays of different F/D can be measured using this support and the position can be finely tuned during the measurements.

The far-field anechoic chamber, available at the MAG premises, offers a maximum measurement distance of 2.3 m. The 900-element antennas have the boundary between the radiating near field and the far field zones at:

$$d_{FF} = \frac{2\left(\sqrt{2}D\right)^2}{\lambda_0} = 10.63 \text{ m} . \qquad (6.21)$$

Measuring full-sized arrays in the said anechoic chamber is not adequate. Therefore, a smaller version of each array is designed and fabricated for the initial measurement campaign. The elements inside the smaller arrays are arranged in a circle with a diameter of 120 mm and the far-field zone exactly at 2.3 m. The total number of elements is 316.

The same plastic support, designed for the 900-element arrays is also used for the measurements of the 316-element array. Due to the support constraints, the projection of the feed's phase center is outside of the circular array, putting it in a disadvantageous position for achieving a high aperture efficiency. Therefore, the overall performance for this set of prototypes are lower than in the case of full-sized arrays.

After the initial far-field measurements in the anechoic chamber, the 900-element square arrays are measured using the near-field scanner at Viasat premises, located in the EPFL Innovation Park. The plastic support is modified for a proper mating to the standard flange inside the scanner.

6.7.2. RA Measurement Results

The 316-element prototype of the circular RA antenna, and the corresponding simulation and measurement results, are shown in Figure 6.14. The horn-antenna rotating mechanism, the sliding rail and the plastic frame around the array are not considered in the numerical analysis of the array. The sliding rail presents an obstacle for the RA radiation, and it is the cause of a large discrepancy between the simulations and measurements for positive θ angles.

The measured RA radiation agrees with the numerical analysis in the remaining angular range. The measured SLL in the RHCP radiation pattern are within 2 dB of the predicted values. The maximum-gain direction is shifted by 0.5°, which is explained by the incorrect estimation of the substrate permittivity in the unit-cell simulation model. The resulting frequency shift is also visible in the gain-vs-frequency plot in Figure 6.14(e).

Both the gain and AR measurement results show an improvement in the central part of the band, between the two coupled-loop resonances, compared to the calculations. The effect stems from an increased coupling between the two D-shaped loops in the RA prototype, with respect to the simulation model. As analyzed in Figure 5.10(b), a smaller gap between the loops, and a higher coupling at the same time, correspond to a smaller separation between the two resonances. The RA element is simulated with zero-thickness conductors throughout the study, to accelerate the analysis with the quasi-3D solver. On the other hand, the actual prototype has finite-thickness

conductors (~17 μm), as it can be noticed in Figure 6.14(a). In the prototype, the coupling is increased due to the increased lateral surface between the two loops, most importantly in the gap region. As the element resonances are less spaced in frequency, the gain over frequency is consequently flatter than predicted, and the AR values lower. For a more accurate prediction of the RA antenna radiation based on this type of elements, finite-thickness conductors must be included in the simulation models.

In spite of all the unaccounted factors, the circular RA prototype, although of suboptimal system geometry, achieved a maximum gain of 26.2 GHz (52% efficiency), 1-dB gain bandwidth of 7.5% and 3-dB AR bandwidth of 8.1%, validating the results predicted through simulations.

Similar conclusions apply for the 900-element square RA antenna prototype, as for the smaller-scale circular antenna. The large prototype is shown in Figure 6.15 alongside simulation and measurement results. As expected, the aperture efficiency and radiation-pattern agreement are significantly improved. The improvement is due to a more advantageous feeding location, as well as an increased array size. The antennas of this type are known to perform better as their size increases, since the infinite-array assumption is valid for a larger number of elements inside the array. The maximum gain of this antenna at -25° reaches 31.7 dBi for a total efficiency of 60%. The measured 1-dB CP-gain bandwidth is 6.8% for an array profile of only $0.08\,\lambda_0$ at 24.6 GHz. The measured 3-dB AR bandwidth is 10%.

(a)   (b)
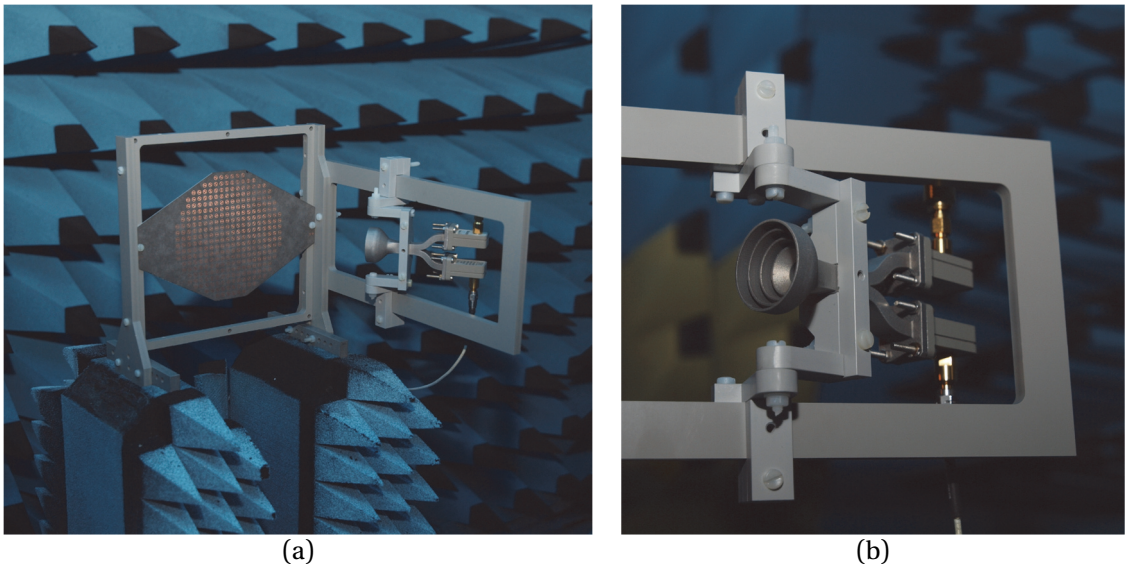
Figure 6.13. RA measurement setup inside the anechoic chamber. (a) The array and the feed horn mounted on the plastic support. (b) Feed horn detail.

(a)

(b)

(c)

(d)

(e)

(f)

Figure 6.14. The 316-element circular RA antenna prototype. (a) Array detail. (b) Antenna prototype in the anechoic chamber. (c) Radiation patterns in the plane $\phi = 0°$, at 24.6 GHz. (d) AR versus angle, in the vicinity of the main lobe. (e) CP gain versus frequency, at $\theta = -30°$. Gray lines represent the aperture-efficiency values. (f) AR versus frequency, at $\theta = -30°$.

Figure 6.15. The 900-element square RA antenna prototype. (a) Antenna prototype in the near-field scanner. (b) Radiation patterns in the plane $\phi = 0°$, at 24.6 GHz. (c) AR versus angle, in the vicinity of the main lobe. (d) CP gain versus frequency, at $\theta = -25°$. Gray lines represent the aperture-efficiency values. (e) AR versus frequency, at $\theta = -25°$.

6.7.3. TA Measurement Results

The prototype of the circular TA antenna and the corresponding simulation and measurement results are shown in Figure 6.17. Unlike the RA case, the effect of the plastic support is minimal in the radiating hemisphere, as the feed and the sliding rails are located in the opposite side of the array. In this setup, the feeding horn antenna is oriented towards the test antenna in the anechoic-chamber setup. Therefore, the spillover RHCP radiation from the horn becomes dominant when it appears behind the TA aperture, as seen from the test antenna. The effect is visible in the radiation patterns (especially at $\theta = -40°$), where the cross-polarized RHCP radiation is significantly increased, with respect to the numerical analysis.

Nevertheless, the calculations accurately predict the TA antenna radiation, as the measured and simulated main lobes practically overlap, as well as the AR value at that angle. The measured maximum gain shows a larger discrepancy, compared to the RA case. The measured 1-dB gain bandwidth is 6.5% and the 3-dB AR bandwidth is larger than the measured frequency range (12%).

The plastic support had to be significantly modified for measurements of the 900-element TA antenna in the near-field scanner. The differences between two measurement setups are shown in Figure 6.16. The measurement results of the 900-element prototype are shown in Figure 6.18.

The maximum measured gain of the large square TA antenna reaches 31.7 dBi for an efficiency of 56%. The measured 1-dB gain bandwidth of this prototype is 5.7%, as predicted through calculations. The AR values are below 0.6 dB throughout the gain bandwidth, and below 1 dB in the entire measurement range. The maximum-gain difference between the calculations and measurements is larger than in the RA antenna case. This discrepancy is potentially related to the assumption made in Section 6.3.2, and the fact that the RA element has a more compact shape, which reduces the inter-element coupling inside the array. This effect will be further investigated in the future.

(a) (b)
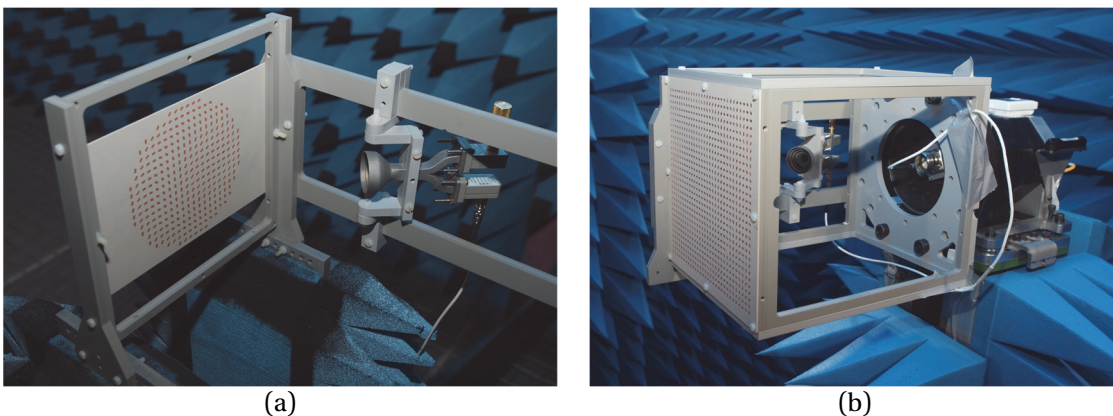
Figure 6.16. The measurement setups of the TA antenna. (a) Anechoic chamber, 316-element array. (b) Near-field scanner, 900-element array.
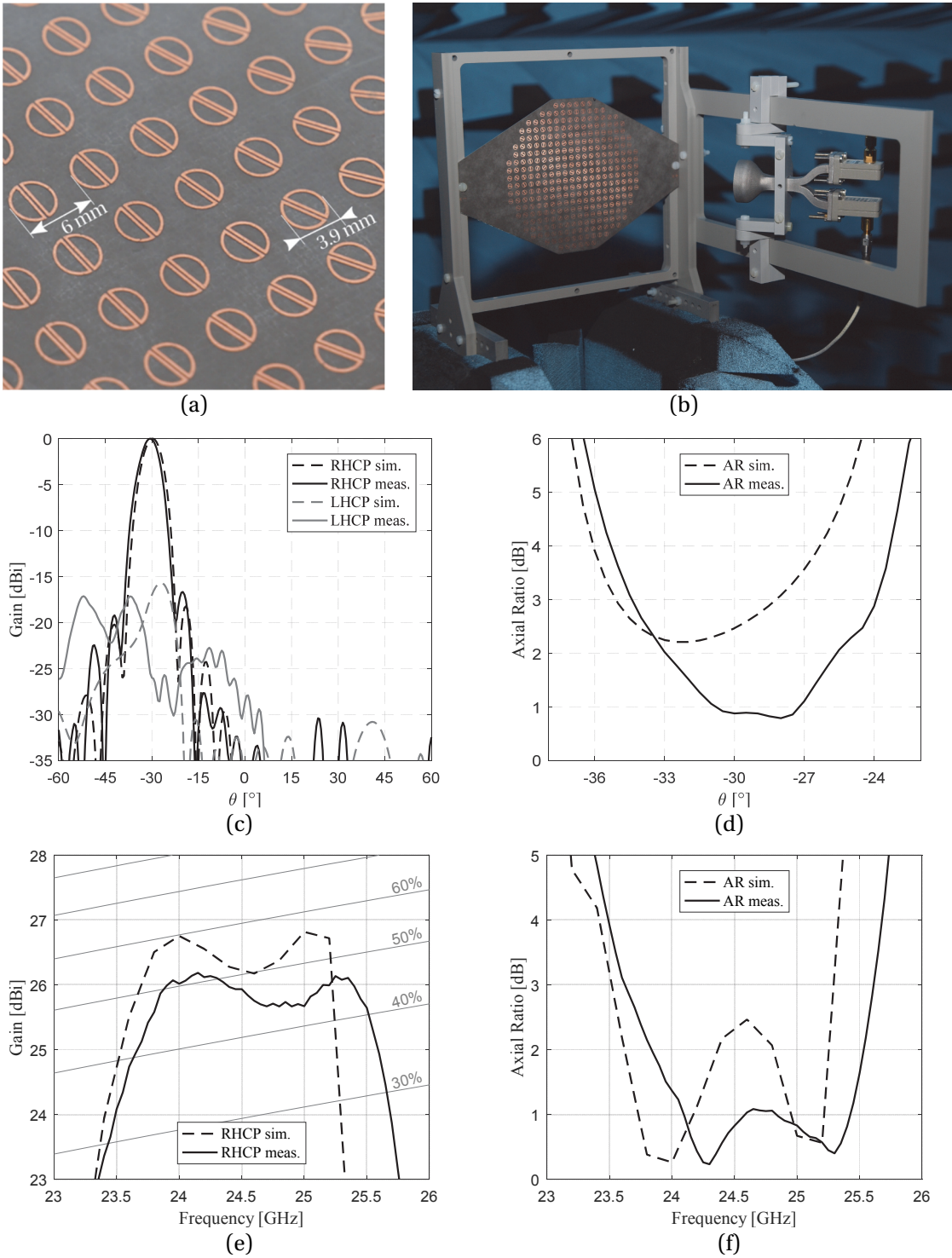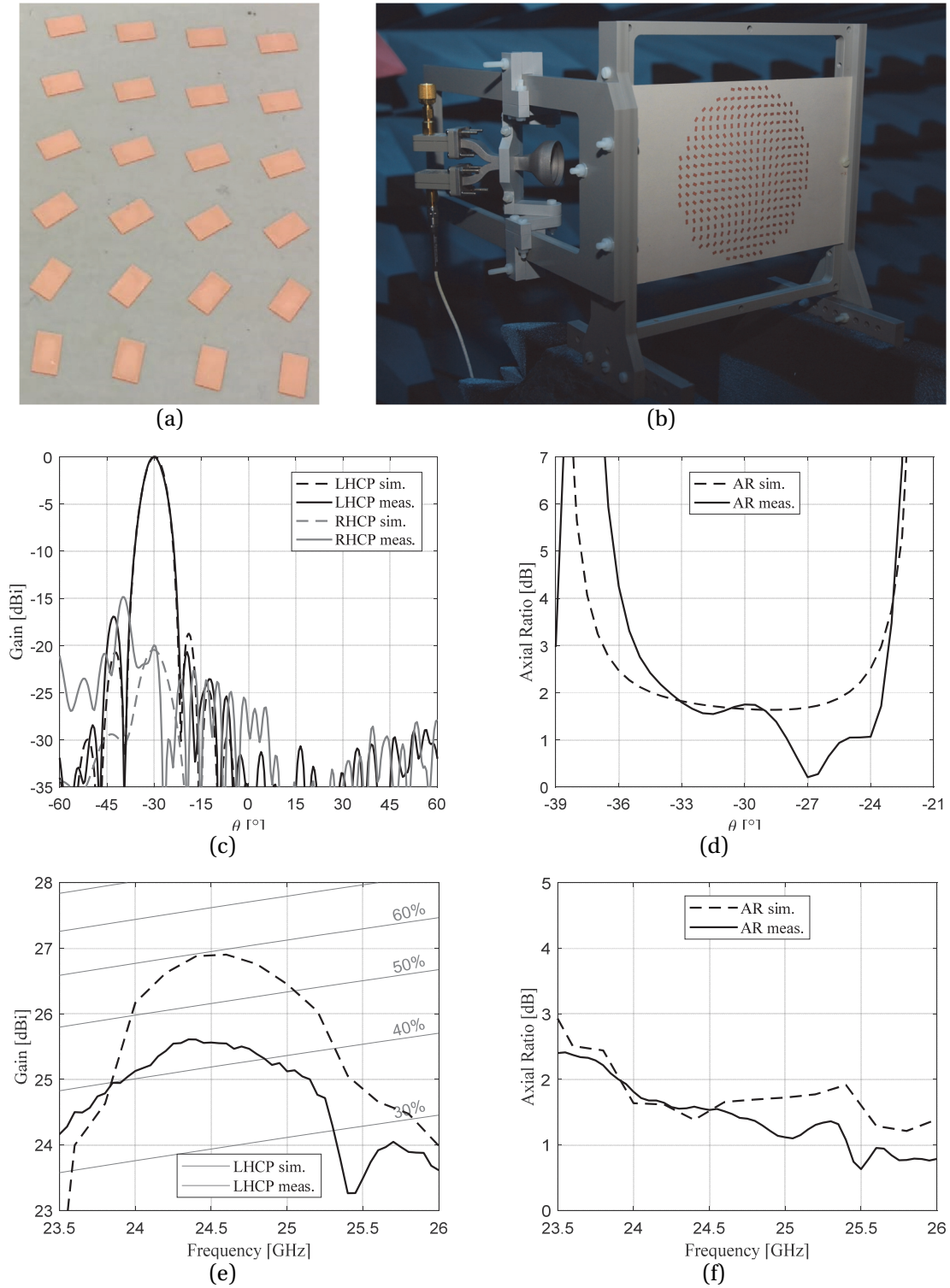
Figure 6.17. The 316-element circular TA antenna prototype. (a) Array detail. (b) Antenna prototype in the anechoic chamber. (c) Radiation pattern in the plane $\phi = 0°$, at 24.6 GHz. (d) AR versus angle, in the vicinity of the main lobe. (e) CP gain versus frequency, at $\theta = -30°$. Gray lines represent the aperture-efficiency values. (f) AR versus frequency, at $\theta = -30°$.
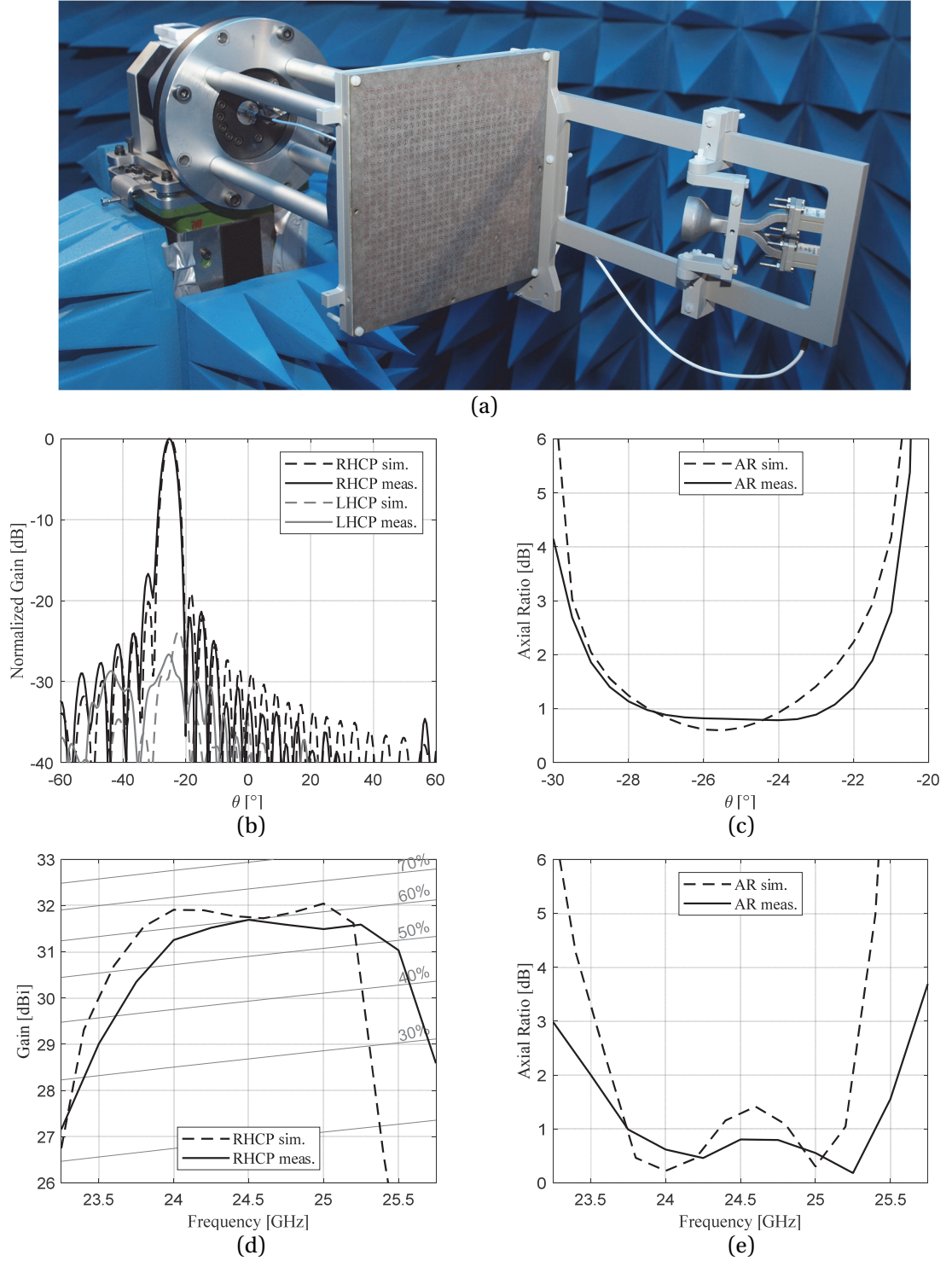
135

(a)

(b)

(c)

(d)

(e)
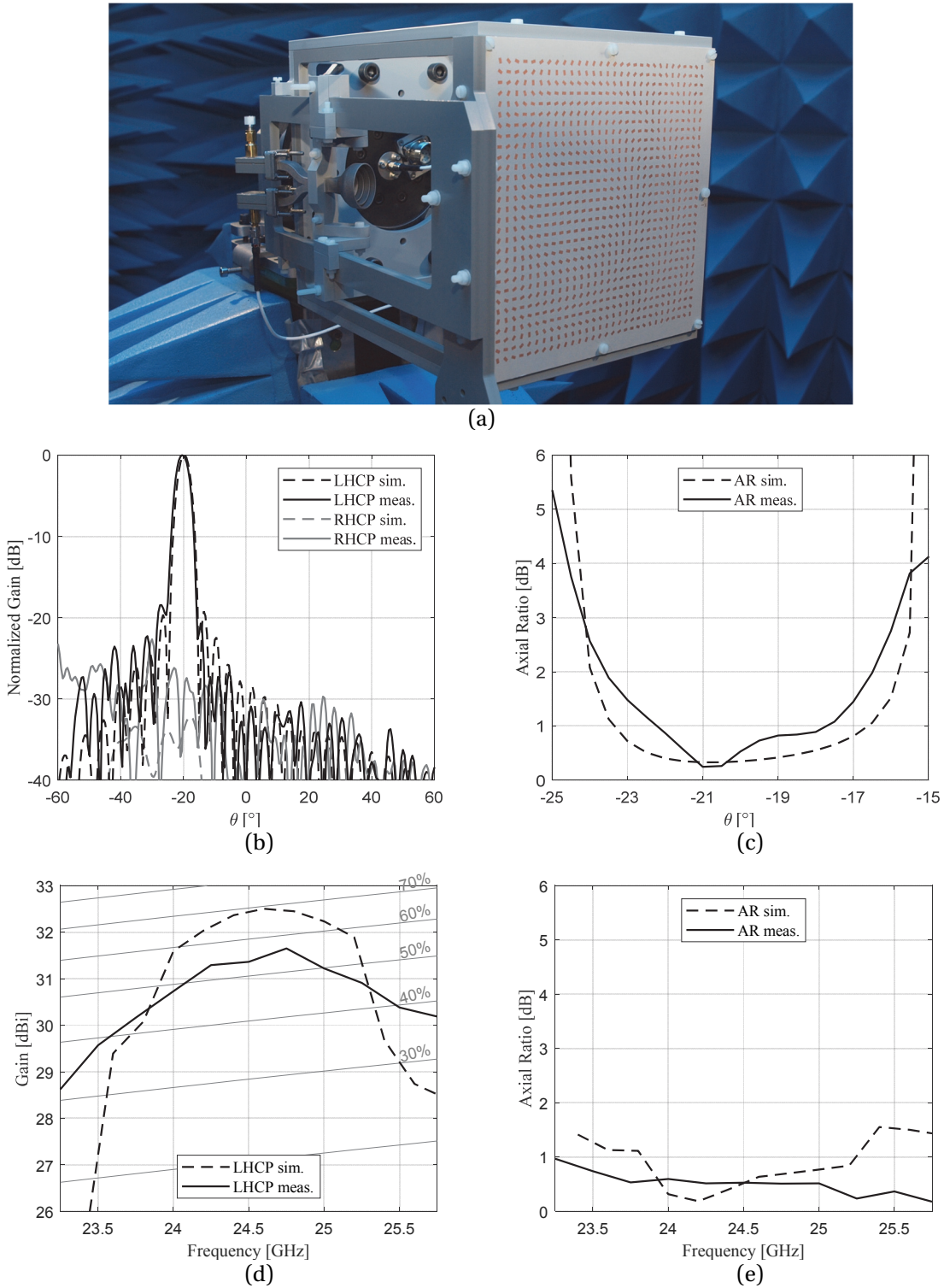
Figure 6.18. The 900-element square TA antenna prototype. (a) Antenna prototype in the near-field scanner. (b) Radiation patterns in the plane $\phi = 0°$, at 24.6 GHz. (c) AR versus angle, in the vicinity of the main lobe. (d) CP gain versus frequency, at $\theta = -20°$. Gray lines represent the aperture-efficiency values. (e) AR versus frequency, at $\theta = -20°$.

6.8. Summary and Discussion

Following the design of RA and TA elements and the feeding antenna in Chapter 5, this chapter presents the synthesis and analysis procedures for the complete RA and TA antennas, based on the designs in Chapter 5.

A custom code is developed for the generation of the array geometry, starting from the interpolated results of the quasi-3D EM unit-cell simulations and the corrugated-horn feed. The arrays in this chapter use the variable rotation technique (Section 5.1.2) to convert the incident spherical phase-fronts to a linear phase of the scattered field across the array aperture, required for beam steering. Instead of a well-known formula (6.3), a different procedure was implemented here to obtain the element-rotation matrix, which eliminates the phase errors for any angle of incidence on the individual elements. The electric field, incident on the individual elements, is obtained by sampling the interpolated far-field radiation of the feeding antenna and combining it with the path loss. The method allows for a fast re-calculation of the incident fields, if the array focal point changes.

The analysis portion of the code calculates the scattered fields at each array element, using the incident fields and the element S parameters, for a specific incidence angle and the element rotation obtained in the previous step. Different S parameters are used, depending on the considered case (RA or TA). The far-field array radiation is calculated using the Field Equivalence Principle applied on the radiation of rectangular apertures. The scattered fields on each element are decomposed into two orthogonal components, and the individual contributions are combined to find the CP performance of the full array.

As a final analysis step, the simulated array efficiency is evaluated as a combination of individual factors, and the aperture efficiency is found to be the dominant factor. It does not depend on the array elements, but solely on the feed and the antenna-system parameters. In the case of deployable CubeSat arrays, these parameters are constrained by the mechanical requirements – an offset feeding and a rectangular aperture. Under these conditions, the arrays do not reach their maximum potential, but their performance is maximized from an engineering standpoint. Nevertheless, the elements themselves introduce minimal losses in terms of phase, polarization and reflection/transmission.

The calculated 1-dB gain bandwidth of the 900-element RA antenna, based on the coupled-loop element from Chapter 5, reaches 6.5%. This result is a significant improvement over the reported bandwidths of simple split-loop elements, originally proposed for RA CP applications. A literature review reveals that it is somewhat easier to achieve a wideband-gain performance of single-layer microstrip LP elements, compared to the CP elements, as the microstrip resonators can be coupled with a larger freedom. Some CP elements report the CP bandwidths reaching 20%. These elements are either composed of several dielectric and metallic layers, or a use a thick air layer

between the RA substrate and the ground plane. The novel RA element proposed in this thesis yields a unique wide bandwidth while having a profile of only 0.042 λ_0 at 24.6 GHz.

The presented aperture-coupled-patch TA element is a modification of the element from [91]. The number of dielectric layers is reduced from five to three by modifying the slot shape in the ground plane, thus improving the element performance versus the incidence angle. Although the total profile is reduced to 0.13 λ_0 at 24.6 GHz, the calculated 1-dB gain bandwidth of the TA antenna is 5.7%, while the efficiency reaches a value of 69%. This value is constrained by the offset feeding and the rectangular aperture. Efficiencies of up to 73% are obtained in the calculations for a circular array geometry.

The performance of RA and TA antennas is verified through measurements of several prototypes. Smaller-scale array prototypes are built for compatibility with the available far-field anechoic chamber. The plastic support, originally developed for the 900-element antennas, is used for the measurements of all arrays. Although this configuration is suboptimal in terms of aperture efficiency, the agreement between the measurement and calculation results confirms the wideband performance of the novel array elements. The large 900-element square arrays are measured in the near-field scanner. The measurement results show an improvement with respect to small-scale prototypes, due to a larger array size and a more advantageous feed position. The RA and TA antennas exhibit 1-dB CP-gain bandwidth of 6.8% and 5.7% and AR values smaller than 1 dB and 0.6 dB, respectively, across the entire gain bandwidth.

A combination of an extremely low profile and wideband performance is highly desired for CubeSat applications, due to the limited antenna-stowage volume and the simplicity of the fabrication process. Both presented designs are fabricated with a simple PCB etching process (and bonding for the TA antenna) and require no metallized vias, SMD component soldering, or a complicated multi-layer assembly. The array aperture can be constructed of several panels folded at the satellite exterior, while the total thickness does not violate the CubeSat constraints.

7. Conclusions and Perspectives

7.1. Summary

The CubeSat has established itself as the dominant nanosatellite standard, since its conception in 1999. CubeSats have since proven their capabilities for Earth observation, RADAR, and even inter-planetary missions, in spite of their small size. Their low development and orbital deployment cost are the main features that attracted satellite developers. In recent years, this increased interest has caused the fast-growing number of CubeSats for commercial applications to surpass the number of CubeSats developed for academic purposes, for which the standard was initially developed.

The volume constraints specified by the standard have encouraged scientists and engineers to redesign and miniaturize conventional satellite components, for them to fit into the tiny CubeSat chassis. Among different on-board components, CubeSat antennas are one of the most constrained, since their physical size is directly proportional to the wavelength at the operating frequency. This was especially important for early CubeSats, which communicated in the VHF and UHF frequency bands, where the 1U CubeSat dimension is only $\lambda_0/20$ and $\lambda_0/7$, respectively.

The domain of CubeSat antennas has since seen a large and still growing number of innovative antenna solutions in a wide frequency spectrum, spanning from VHF to V band. Depending on the application and the design specifications, different methods were used to adapt the conventional antenna geometries to the CubeSat environment. The main novelty for a majority of the proposed geometries (primarily the exotic deployable antenna geometries) is actually in their mechanical design, as their electrical performance is well known.

The research for this thesis is conducted with a final goal to enable different communication aspects of an IoT constellation of CubeSats in LEO. The thesis presents several new antenna designs, innovative in terms of both their CubeSat integration, and most importantly, their EM performance. The proposed antennas operate in frequency bands ranging from L to K bands, and exhibit a different performance depending on their intended application. The common design requirement of all presented antennas is to increase or preserve the operating bandwidth under

a constrained or reduced available volume, respectively, while the critical limiting factor is the total antenna thickness. The main achievements per thesis chapter are summarized in the following paragraphs.

Chapter 2 – Wideband CP stripline-fed aperture-coupled patch antennas in S and X bands are presented in this chapter. The primary function of the S-band antennas is the satellite TT&C, for which a highly reliable antenna is necessary. Therefore, a low-profile solution is preferred here over the deployable geometries. An asymmetric-stripline feeding network enables a unidirectional radiation and isolates the antenna from the CubeSat structure, but introduces difficulties with the antenna matching over a wide band, considering the profile limitation. Adding a metallic shielding around the stripline structure drastically improves the antenna impedance bandwidth. After a detailed investigation of the electric fields inside the formed stripline cavity, it was discovered that the strong electric field magnitude below the coupling slot boosts the coupling to the radiating patches. Design rules for this antenna type are outlined based on this study. The wideband antenna covers up to three adjacent frequency bands simultaneously. A unidirectional radiation pattern, a 3-dB gain bandwidth of 27% and an AR bandwidth of 32% were obtained with a total antenna prototype profile of $0.08\,\lambda_0$ at 2 GHz. In a modified version of the antenna, the resonances of the stripline cavity are used to reduce the gain and suppress the interference from an adjacent band. A novel method of integrating this type of antennas in the CubeSat structure is proposed.

The chapter also emphasizes the importance of evaluating the radiating-element matching in the case of multi-fed antennas of antenna arrays, and distinguishing it from the matching at the feeding network input. The S-band antennas incorporate a rather complex feeding network to enable high-quality CP over the operating bandwidth. As a means of demonstrating that the shielded stripline technique is equally powerful with antennas having simpler feeding networks, a CP stripline-fed patch antenna is designed in X band with a single feed line and an asymmetric coupling slot. The same improvements over the microstrip-fed model are observed as with the S-band antenna. An array of four sequentially rotated elements is designed with the described patch element that achieves a gain of 15 dBi a wideband AR.

Chapter 3 – A patch-antenna system in L band is presented in this chapter for IoT 3U-CubeSat duplex communications in LEO. Several antenna array configurations are proposed, with antenna elements placed on the backsides of deployed solar panels, facing the Earth. A high-permittivity dielectric substrate is used to miniaturize the size of CP patch elements until they are suitable for placement on a CubeSat. A separate antenna element is designed for each of the communication directions (uplink/downlink) due to a reduced impedance bandwidth. The small electrical size of the antennas resulted in a large coupling to the asymmetric 3U ground plane, causing a distortion of the radiation pattern. It is shown that the placement on the 3U CubeSat is critical for the radiation performance of this type of antennas. Several independent radiating beams, scanned away from broadside, are envisioned to increase the capacity of the IoT system. Four two-element

sequentially rotated arrays are required to provide two duplex beams using the described CP patch antenna elements. Similarly, 32 CP antennas would be necessary for four independent beams. Instead, arrays of four sequentially rotated dual-band LP patch antennas are used for the same purpose, reducing the number of antennas to 16.

As another method of optimizing the available real estate on a CubeSat, an L-band patch antenna is combined with an S-band element in a stacked-patch configuration to obtain a dual-band dual-fed CP antenna. The L-band element is actually smaller than the higher-frequency S-band element, due to the heavy dielectric loading, and consequently located on top of the stacked structure. Three feeding configurations are compared, and the network based on a Wilkinson divider is found to be optimal for CubeSats in terms of size, complexity and AR. It is further demonstrated that the choice of a feeding network does not significantly influence the CP gain bandwidth of the antenna, even compared with a simple single-fed CP antenna.

Chapter 4 – This chapter proposes several configurations for high-gain inter-satellite-link (ISL) antennas in K band, which enable a low-latency high-data-rate global coverage with a CubeSat constellation. The ISL for small satellites was previously reported in literature only in low frequencies, such as S band, and this thesis discusses the K-band CubeSat ISL for the first time. The conventional K-band ISL antennas are either too large, heavy and/or too complex for CubeSats. Therefore, advantage is taken from the specific flying scenario to design simpler and robust fixed-beam antennas. In the considered constellation, the CubeSats are uniformly distributed over distinct orbital planes and the individual satellites are connected with ISLs to adjacent neighbors within one plane. Based on the number of satellites per orbit, the antenna requirements in terms of CP gain and beam-steering angle are calculated and presented in this chapter. The antenna gain is calculated versus the aperture efficiency for different aperture areas, and it is found that the smaller face of a 3U CubeSat does not provide sufficient gain for a required ISL data rate at K-band frequencies. Among the candidates for deployable antennas, reflectarray (RA) and transmitarray (TA) antennas offer an excellent tradeoff between the performance, complexity and the stowage volume. Several RA and TA ISL configurations are envisioned and illustrated for 3U CubeSats in LEO.

Chapter 5 – This chapter presents the individual elements of the CubeSat ISL antenna system described in Chapter 4 – one novel CP array element for each of the RA and TA antennas, and a 3D-printed CP axially-corrugated horn antenna. The CP specification allows the phase shifting across the RA and TA antennas to be achieved using the element-rotation technique, where the phase shift of the reflected or transmitted waves is proportional to the element rotation angle. A unit-cell infinite-array simulation environment and the theoretical developments are presented for the element-rotation technique. From the results, a set of conditions is obtained, which an element must satisfy in order to qualify for this technique. Two new TA and RA elements, based on the conventional CP elements, are designed to satisfy these conditions. The shape of the coupling slot is modified for a TA element based on aperture-coupled patches, reducing the

required number of metallic layers from five to three and preserving a high-quality CP performance. A novel coupled-loops RA element is designed as a modification of a known split-loop. The dual-resonant nature of the proposed element doubles the CP bandwidth, while preserving the simplicity and the low profile of a single-layer design. The presented modal analysis of the element provides a deeper insight into the mechanisms behind the wideband CP operation. An axially corrugated CP horn is designed as the feeding element for RA and TA antennas. The axial corrugations improve the off-axis AR of the horn, and a septum polarizer generates two CP radiation modes of the horn, depending which input port is excited. A feed-chain prototype is fabricated for laboratory testing using additive manufacturing in aluminum (DLMS). The presented prototype measurement results validate the simulations and confirm the feed eligibility for ISL CubeSat applications.

Chapter 6 – The synthesis and analysis, as well as prototype measurements of RA and TA antenna geometries is presented in this chapter. The simulated performance of the RA, TA elements, and the feeding horn from Chapter 5 is first used to generate the array geometry. The radiation pattern of the feed is combined with the path loss to obtain the incident fields on the array – a process that allows a fast re-calculation of incident fields for different feed positions. Instead of a known analytical formula suggested by the analysis in Chapter 5, the element rotation angles are determined with a simple and fast procedure, which eliminates the phase errors for large elevation incidence angles. The array geometry is first generated at the design frequency, and the array far-field radiation is then calculated at several frequency points. To achieve this, the scattered field on all elements is obtained by combining the incident fields and the unit-cell responses for different incidence angles. The CP far field of entire arrays is finally obtained using the Field Equivalence Principle applied on the radiation of rectangular apertures.

The achievable aperture efficiency for this type of antennas is limited by the specific CubeSat ISL scenario. The offset rectangular RA and TA antennas conform to the CubeSat structure during stowage and maximize the performance from an engineering standpoint, although their aperture efficiency is reduced. A study of the overall antenna efficiency shows that the main factor for both antennas is indeed the aperture efficiency, which only takes into account the array geometry. In other words, the proposed RA and TA elements introduce minimal losses in terms of phase, polarization and reflection/transmission and maximize the antenna capabilities under the given constraints. The calculations for two 900-element RA and TA antennas show a 1-dB CP gain bandwidth of 6.5% and 5.7% with total efficiency of 60% and 69%, respectively. This achievement is especially important in the case of RA antennas, since the bandwidth is significantly improved with respect to the conventional elements, without any loss of simplicity. Two smaller-scale prototypes are fabricated for anechoic chamber measurements, whereas the prototypes of 900-element arrays were measured in a near-field scanner. The presented measurement results confirm the high-quality CP performance of the designed elements, in spite of a sub-optimal

aperture efficiency. The CP performance, along with the low profile and simplicity of the proposed antennas, are the main enabling factors for ISL CubeSat applications.

7.2. Discussion

A shielded asymmetric stripline is used in Chapter 2 to generate a unidirectional radiation pattern while preserving a good impedance matching under a low profile. The stripline cavity formed by the shielding exhibits resonant modes and it is essential to keep the modes outside of the operating bandwidth. The narrowband nature of these modes, and the fact that the field distribution inside the cavity is similar below and above the resonance, allow for a certain freedom in selecting a suitable cavity dimension. Electric-field analysis helps to understand the causes of mismatch in case of an improperly sized stripline cavity. Very often, the required dimension will be different from the CubeSat face, and a row of metallic screws can be used to create a cavity of arbitrary dimensions or shape. In addition, the feeding network can be placed inside the metallic CubeSat chassis, reducing the antenna protrusion on the surface. This integration method requires a custom-made CubeSat chassis with slots cut for the coupling aperture between the feeding network and the radiating patches.

The S-band low-permittivity patch antenna in Chapter 2 and the L-band high-permittivity patch antenna in Chapter 3 are studied on a large face of a 3U CubeSat (modeled as a 300 x 100 mm² PEC). The effect of the substrate permittivity is seen by comparing their radiation performance. The miniaturized high-permittivity antennas couple strongly to the asymmetric ground plane and their radiation pattern is consequently deteriorated. The pattern distortion is negligible in the S-band case due to a low substrate permittivity, despite the extreme offset on the 3U CubeSat face. In conclusion, the antenna placement on a CubeSat is critical in case of small antennas, and the satellite structure, or at least parts of it, must be considered in the design phase. Furthermore, the proper antenna placement can also be used to generate isoflux-like patterns, which is demonstrated in Chapter 3.

Distinguishing the matching of the multi-fed antenna elements from the matching at the feeding-network input is crucial for an accurate antenna design. This fact is well known in the antenna domain, but often omitted in the CubeSat literature. Therefore, it is emphasized in Chapters 2 and 3. In the beginning of the design phase, it is recommended to create several intermediate antenna models in the absence of the feeding network, and evaluate the active S parameters. Afterwards, a suitable feeding network can be selected. The comparison of three feeding-network geometries in Chapter 3, with varying performance and complexity, can be of assistance in this step.

RA and TA antennas for CubeSat ISL in LEO, as well as the IoT arrays in L band, are proposed specifically for the 3U CubeSats, flying with their long axis aligned with the orbit. In the considered scenario, the deployable flat reflectors and lenses offer an excellent compromise between the

complexity and the performance. However, this might not be the case for similar CubeSat constellations, with satellites having different form factors (6U and more) or flight attitudes. As an example, a patch antenna array, covering a large face of a 3U CubeSat, could achieve a gain comparable to the presented deployable antennas. Such scenarios are not considered here, but should definitely be taken into account if the design specifications allow.

TA antennas are for the first time proposed for CubeSats in this thesis, to the best knowledge of the thesis author. TA antennas are less sensitive to the array flatness, compared to RA antennas [81]. The symmetrical dielectric and metallic structure of the proposed TA element can help to minimize the bending of the array panel with drastic changes in temperature in LEO.

The presented RA and TA elements – the coupled loops and the aperture-coupled patches – have demonstrated their excellent CP performance, taking into account their simplicity and low profile. These elements are equally suitable for other applications (terrestrial, GEO, etc.) in different frequency bands.

7.3. Future Work

Both the feeding network and the patch elements of wideband antennas in S band can be redesigned on substrates with a higher permittivity. This would reduce the total antenna dimensions and improve the beamwidth required for TT&C applications. Although the impedance bandwidth will be reduced by this approach, a stacked-patch configuration should be sufficient to cover the two TT&C frequency bands.

The L-band patch antennas are too thick in their present form, for an efficient stowage of one or several solar panels, on which the antennas are placed. Furthermore, a feeding-network substrate required for arrays will additionally increase the total stowed profile. The antennas should be redesigned on a thinner substrate. In combination with the sequential rotation, the arrays should still be able to cover the entire Tx or Rx band, in terms of both impedance matching and AR.

The combined TA/RA antenna panel is a promising concept that could result in a single deployable panel for an independent two-way dual-band ISL communication. The initial study showed that the response of the RA, FSS and TA layers changes when they are assembled, due to a large coupling between individual elements. The approach to this problem would be either to analyze the entire structure simultaneously or to design individual elements that exhibit less cross-coupling.

The measurements of the 900-element arrays showed a larger difference between the calculated and measured maximum gain of the TA antenna, with respect to the RA antenna. The reasons for this difference will be investigated in the future.

7.4. Perspectives

A very low substrate permittivity (1.08) in Chapter 2 is used to achieve a CP bandwidth larger than 20% in the wideband patch antenna. However, the TT&C antenna bandwidth criteria are less demanding (~12%). A higher feeding network and patch substrates can be selected in this case, in order to reduce the antenna size (primarily profile), increase the beamwidth and simplify the fabrication and assembly processes. This would require a complete redesign of the feeding network and the radiating element. Therefore, it is not performed in this thesis, but should be used if demanded by the volume constraints.

The presented patch antennas in Chapter 3 cover the entire allocated downlink and uplink bandwidths. The antenna thickness is increased to alleviate the narrowband matching, caused by a high substrate permittivity. The antennas are not immediately suitable for placement on the backsides of solar panels, as the total thickness of stowed panels would violate the CubeSat constraints. Once the final operating frequency is known within the bands, a thinner patch having a narrower bandwidth can be tuned to that frequency. The conclusions of Chapter 3 would then also apply for such patches, although these are not studied in this thesis. Otherwise, a different substrate/thickness combination can achieve the same bandwidth performance, if the allocated space allows.

It has been over one year since the first Astrocast CubeSat is launched with several L-band antennas on-board. During this time, the satellite communication systems are tested and the hardware, including the antennas, performs as predicted. This result has encouraged the use of more complex dual-fed L-band and L/S-dual-band stacked-patch antennas for the first batch of commercial satellites, which is to be launched during 2020. The high-gain deployable arrays in K band are currently being evaluated by the mechanical engineers, for use in the future satellite versions.

The total count of launched CubeSats in Figure 7.1 shows a growth explosion in the past several years [2]. This rapid increase is driven by the increased interest of the commercial sector for CubeSat platforms. One reason for this is that the CubeSats' cost-efficient nature opens many new opportunities in the space industry, which would otherwise be inaccessible with conventional satellite technologies. Several companies have either deployed or announced LEO constellations incorporating tens or hundreds of CubeSats, with indications that the progress will continue in the future. The trends show that recent CubeSats have a larger form factor (6U and more) to accommodate specialized components and modules that provide new communication functions. The future developments in this field will likely include a higher level of component integration and customization, which will also include the antennas.
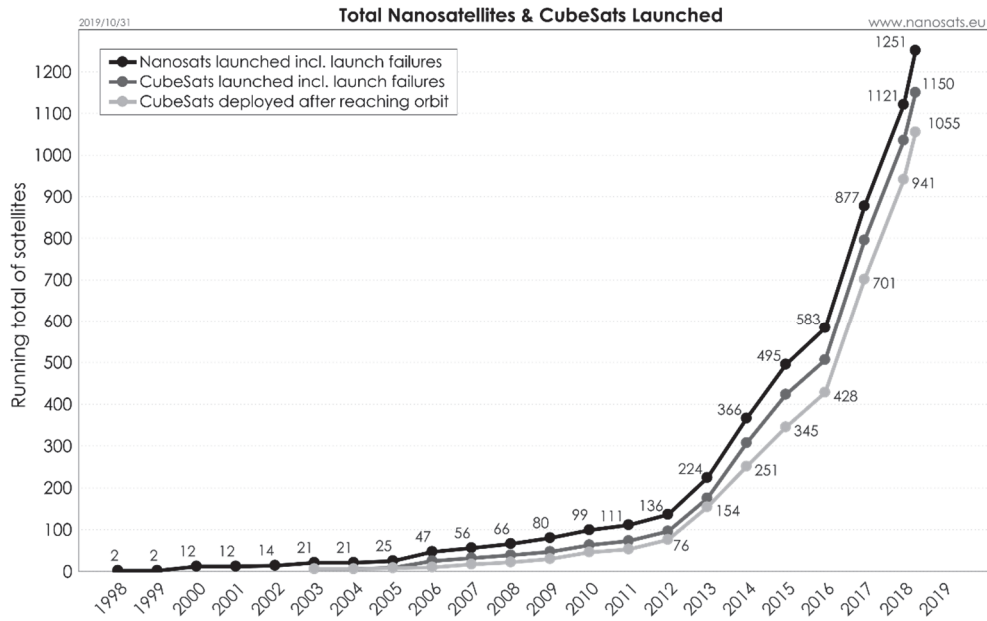
Figure 7.1. The total number of nanosatellites and CubeSats over time [2].

Besides CubeSats, there is an even more drastic increase in the number of planned satellites in the small-satellite class (<500 kg). Several companies have announced and started the deployment of LEO constellations spanning from hundreds to even tens of thousands of small satellites (SpaceX, OneWeb, Kepler). Some questions were recently raised regarding the sustainability of such mega-constellations, considering the long lifetime of space debris (non-operational satellites), especially at high LEO altitudes above 1000 km. Therefore, it is imperative to incorporate a deorbiting functionality on every LEO satellite, to preserve a clean and safe space environment in orbit. There is also an effort to use dedicated spacecraft that track and deorbit non-responsive satellites from orbit.

The growth of the CubeSat and small-satellite industry will provide new exciting challenges and opportunities for antenna design. As the CubeSats continue to expand their communication functions, there will be an increased demand for innovative, performant antenna designs that conform to the nanosatellite paradigm. Modern CubeSat antennas will most likely achieve this by revisiting conventional antenna geometries and adapting them to the CubeSat environment, in combination with new fabrication and integration techniques.

References

[1]   CalPoly, "Cubesat design specification," 2009.

[2]   E. Kulu, "Nanosats Database," 2019. [Online]. Available: https://www.nanosats.eu/database. [Accessed: 24-Jul-2019].

[3]   C. Kakoyiannis and P. Constantinou, "Electrically Small Microstrip Antennas Targeting Miniaturized Satellites: the CubeSat Paradigm," *Vienna, Austria: InTech*, pp. 273–316, 2011, doi: 10.5772/14947.

[4]   S. Clark, "A chat with Bob Twiggs, father of the CubeSat," 2014. .

[5]   S. Gao *et al.*, "Antennas for small satellites," *2008 Loughbrgh. Antennas Propag. Conf. LAPC*, pp. 66–69, 2008, doi: 10.1109/LAPC.2008.4516867.

[6]   NASA, "Mission Overview: GeneSat-1," 2007. [Online]. Available: https://www.nasa.gov/centers/ames/missions/2007/genesat1.html. [Accessed: 21-Dec-2019].

[7]   R. E. Hodges, N. Chahat, D. J. Hoppe, and J. D. Vacchione, "A Deployable High-Gain Antenna Bound for Mars: Developing a new folded-panel reflectarray for the first CubeSat mission to Mars," *IEEE Antennas Propag. Mag.*, vol. 59, no. 2, pp. 39–49, 2017, doi: 10.1109/MAP.2017.2655561.

[8]   S. Gao, Y. Rahmat-Samii, R. E. Hodges, and X. X. Yang, "Advanced Antennas for Small Satellites," *Proc. IEEE*, vol. 106, no. 3, pp. 391–403, 2018, doi: 10.1109/JPROC.2018.2804664.

[9]   ISIS, "CubeSat Antenna System for 1U/3U." [Online]. Available: https://www.isispace.nl/product/cubesat-antenna-system-1u-3u/. [Accessed: 21-Dec-2019].

[10]   E. Pittella *et al.*, "Feature article: Reconfigurable S-band patch antenna system for cubesat satellites," *IEEE Aerosp. Electron. Syst. Mag.*, vol. 31, no. 5, pp. 6–13, 2016, doi: 10.1109/MAES.2016.150153.

[11]   N. Chahat, R. Hodges, J. Sauder, M. Thomson, and Y. Rahmat-Samii, "CubeSat Deployable Ka-Band Mesh Reflector Antenna Development for Earth Science Missions," *2016 IEEE Antennas Propag. Soc. Int. Symp. APSURSI 2016 - Proc.*, vol. 64, no. 6, pp. 1531–1532, 2016, doi: 10.1109/APS.2016.7696472.

[12]   N. Chahat, G. Agnes, J. Sauder, and T. Cwik, "One meter deployable reflectarray antenna for earth science radars," *2017 IEEE Antennas Propag. Soc. Int. Symp. Proc.*, vol. 2017-Janua, pp. 245–246, 2017, doi: 10.1109/APUSNCURSINRSM.2017.8072165.

[13]   R. E. Hodges, M. J. Radway, A. Toorian, D. J. Hoppe, B. Shah, and A. E. Kalman, "ISARA - Integrated Solar Array and Reflectarray CubeSat deployable Ka-band antenna," *IEEE Antennas Propag. Soc. AP-S Int. Symp.*, vol. 2015-Octob, pp. 2141–2142, 2015, doi: 10.1109/APS.2015.7305460.

[14]   A. Tatomirescu, G. F. Pedersen, J. Christiansen, and D. Gerhardt, "Antenna system for nano-satellite mission GOMX-3," *Proc. 2016 6th IEEE-APS Top. Conf. Antennas Propag. Wirel. Commun. IEEE APWC 2016*, pp. 282–285, 2016, doi: 10.1109/APWC.2016.7738178.

[15]   EnduroSat, "S-band Antenna ISM." [Online]. Available: https://www.endurosat.com/cubesat-store/all-cubesat-modules/s-band-patch-antenna/. [Accessed: 21-Dec-2019].

[16]   J. Fouany *et al.*, "New Concept of Telemetry X-Band Circularly Polarized Antenna Payload for CubeSat," *IEEE Antennas Wirel. Propag. Lett.*, vol. 16, pp. 2987–2991, 2017, doi: 10.1109/LAWP.2017.2756565.

[17]   EnduroSat, "X-band Patch Antenna Array." [Online]. Available: https://www.endurosat.com/cubesat-store/all-cubesat-modules/x-band-4x4-patch-array/. [Accessed: 21-Dec-2019].

[18]   C. J. Vourch and T. D. Drysdale, "V-band 'bull's eye' antenna for cubeSat applications," *IEEE Antennas*

Wirel. Propag. Lett., vol. 13, pp. 1092–1095, 2014, doi: 10.1109/LAWP.2014.2327852.

[19]   X. Xia *et al.*, "NanoSats/CubeSats ADCS survey," *Proc. 29th Chinese Control Decis. Conf. CCDC 2017*, pp. 5151–5158, 2017, doi: 10.1109/CCDC.2017.7979410.

[20]   R. Lehmensiek, "Using the physical structure of a passive aerodynamic attitude- stabilization system as a multi-frequency antenna on nano-satellites," *IEEE Antennas Propag. Mag.*, vol. 54, no. 3, pp. 39–49, 2012, doi: 10.1109/MAP.2012.6293948.

[21]   "Astrocast: The first Swiss CubeSat IoT Constellation." .

[22]   Y. Voumard, L. Etienne, and F. George, "Space Center EPFL: SwissCube Live Tracking," 2019. .

[23]   R. Radhakrishnan, W. W. Edmonson, F. Afghah, R. M. Rodriguez-Osorio, F. Pinto, and S. C. Burleigh, "Survey of Inter-Satellite Communication for Small Satellite Systems: Physical Layer to Network Layer View," *IEEE Commun. Surv. Tutorials*, vol. 18, no. 4, pp. 2442–2473, 2016, doi: 10.1109/COMST.2016.2564990.

[24]   International Telecommunication Union, "Radio Regulations Articles," *ITU Radio Regul.*, vol. IV, no. Radio stations and systems, p. 435, 2012, doi: 10.1016/B978-0-12-394583-9.00020-X.

[25]   W. Lan, R. Munakata, R. Nugent, and D. Pignatelli, "Poly Picosatellite Orbital Deployer Mk III Rev. E User Guide," 2014.

[26]   S. Gao, "Antennas for Modern Small Satellites," *IEEE Antennas Propag. Mag.*, vol. 51, no. 4, 2009.

[27]   *Handbook of Frequency Allocations and Spectrum Protection for Scientific Uses: Second Edition.* Washington, DC: The National Academies Press., 2015.

[28]   Y. Tsuda *et al.*, "University of Tokyo's CubeSat Project - It's Educaitonal and Technological Significance," in *15th Annual AIAA/USU Conference on Small Satellites*, 2001.

[29]   A. Guillen *et al.*, "PhoneSat in-flight experience results," 2014.

[30]   E. S. Moghaddam, N. Aboutorablad, S. Amiri, S. Nikmehr, and P. Rezaei, "Design and Analysis of a Dualband Antenna for Small LEO Satellite Applications," in *3rd International Conference on Computational Electromagnetics and Its Applications*, 2004, pp. 228–231.

[31]   M. Samsuzzaman, M. T. Islam, S. Kibria, and M. Cho, "BIRDS-1 CubeSat Constellation Using Compact UHF Patch Antenna," *IEEE Access*, vol. 6, pp. 54282–54294, 2018, doi: 10.1109/ACCESS.2018.2871209.

[32]   A. Awaludin, J. Tetuko, S. Sumantyo, S. Gao, C. E. Santosa, and M. Z. Baharuddin, "Wideband Circularly Polarized Triangular – Ring Slot Antenna for GAIA – I Microsatellite," *Eur. Conf. Antennas Propag.*, pp. 2283–2286, 2017.

[33]   F. E. Tubbal, R. Raad, K.-W. Chin, and B. Butters, "S-band shorted patch antenna for inter pico satellite communications," *Telecommun. Syst. Serv. Appl. (TSSA), 2014 8th Int. Conf.*, pp. 1–4, 2014, doi: 10.1109/TSSA.2014.7065938.

[34]   A. Nascetti, E. Pittella, P. Teo, and S. Pisa, "High-Gain S-band Patch Antenna System for Earth-Observation CubeSat Satellites," *IEEE Antennas Wirel. Propag. Lett.*, vol. 14, pp. 434–437, 2015, doi: 10.1109/LAWP.2014.2366791.

[35]   A. Tatomirescu and G. Pedersen, "Compact S Band Antenna for CubeSat," *2018 12th Int. Conf. Commun. COMM 2018 - Proc.*, pp. 231–234, 2018, doi: 10.1109/ICComm.2018.8430138.

[36]   A. Bellion, K. Elis, and S. De Gaetano, "New compact S-band antenna for Nanosatellite TeleMetry and TeleCommand applications - EyeSat program," *2016 10th Eur. Conf. Antennas Propagation, EuCAP 2016*, pp. 6–10, 2016, doi: 10.1109/EuCAP.2016.7481875.

[37]   J. Padilla, G. Rosati, A. Ivanov, F. Bongard, S. Vaccaro, and J. Mosig, "Multi-functional miniaturized slot

antenna system for small satellites," *Antennas Propag. (EuCAP), 2011 Proc. Fifth Eur. Conf.*, no. 1, pp. 2170–2174, 2011.

[38]   ESA Requirements and Standards Division, "Standard ECSS-E-ST-50-05C Rev. 2," 2004.

[39]   R. Manrique, G. Le Fur, N. Adnet, L. Duchesne, J. M. Baracco, and K. Elis, "Telemetry X-band antenna payload for nano-satellites," *2017 11th Eur. Conf. Antennas Propagation, EUCAP 2017*, vol. 1, pp. 549–552, 2017, doi: 10.23919/EuCAP.2017.7928249.

[40]   R. Lehmensiek, "Design of a wideband circularly polarized 2 x 2 array with shorted annular patches at X-band on a CubeSat," in *ISAP2017*, 2017, pp. 6–7.

[41]   K. Elis, T. Maleszka, and A. Bellion, "TT & C and Payload Telemetry Antennas for Nanosatellite – Eye-Sat Nanosatellite Program," in *European Conference on Antennas and Propagation (EUCAP)*, 2017, pp. 537–541.

[42]   E. Arnaud, L. Duchesne, K. Elis, J. Fouany, T. Monediere, and M. Thevenot, "X-band compact choke horn antenna with circular polarization and isoflux pattern for nanosatellite applications," *Int. J. Microw. Wirel. Technol.*, vol. 8, no. 3, pp. 651–659, 2019, doi: 10.1017/S1759078715000677.

[43]   J. F. Zurcher, "The ssfip: a global concept for high-performance broadband planar antennas," *Electron. Lett.*, vol. 24, no. 23, pp. 1433–1435, 1988, doi: 10.1049/el:19880979.

[44]   D. M. Pozar, "Microstrip antenna aperture-coupled to a microstripline," *Electron. Lett.*, vol. 21, no. 2, p. 49, 1985, doi: 10.1049/el:19850034.

[45]   S. D. Targonski, R. B. Waterhouse, and D. M. Pozar, "Design of wide-band aperture-stacked patch microstrip antennas," *IEEE Trans. Antennas Propag.*, vol. 46, no. 9, pp. 1245–1251, 1998, doi: 10.1109/8.719966.

[46]   J.-F. Zürcher and F. E. Gardiol, *Broadband Patch Antennas*. Artech House, 1995.

[47]   A. Bhattacharyya, O. Fordham, and Y. Liu, "Analysis of stripline-fed slot-coupled patch antennas with vias for parallel-plate mode suppression," *IEEE Trans. Antennas Propag.*, vol. 46, no. 4, pp. 538–545, 1998, doi: 10.1109/8.664118.

[48]   P. Brachat and J. M. Baracco, "Dual-polarization slot-coupled printed antennas fed by stripline," *IEEE Trans. Antennas Propag.*, vol. 43, no. 7, pp. 738–742, 1995, doi: 10.1109/8.391150.

[49]   J. Y. Lee and S. N. Hwang, "Parallel-plate mode suppression technique for stripline-fed microstrip antennas," *Trans. Korean Inst. Electr. Eng.*, vol. 57, no. 6, pp. 982–984, 2008, doi: 10.1049/el.

[50]   D. Sievenpiper, H. Hsu, and R. M. Riley, "Low-Profile Cavity-Backed Crossed-Slot Antenna With a Single-Probe Feed Designed for 2.34-GHz Satellite Radio Applications," *IEEE Trans. Antennas Propag.*, vol. 52, no. 3, pp. 873–879, 2004.

[51]   T. Vlasits, E. Korolkiewicz, A. Sambell, and B. Robinson, "Performance of a cross-aperture coupled single feed circularly polarised patch antenna," *Electron. Lett.*, vol. 32, no. 7, pp. 3–4, 1996.

[52]   C. B. Ravipati and L. Shafai, "A Wide Bandwidth Circularly Polarized Microstrip Antenna Using a Single Feed," in *IEEE Antennas and Propagation Society International Symposium*, 1999, pp. 244–247.

[53]   B. Lee and T. Yang, "A Novel Wide Bandwidth CP Stacked Microstip Patch Antenna," in *IEEE Antennas and Propagation Society International Symposium. Transmitting Waves of Progress to the Next Millennium*, 2000, pp. 1004–1007.

[54]   K. Chung and A. M. Sanagavarapu, "Gain and bandwidth enhancement of a 2.4 GHz singly-fed cross-aperture coupled patch antenna," in *IEEE Antennas and Propagation Society International Symposium*, 2002, no. June 2014, doi: 10.1109/APS.2002.1016334.

[55]   R. Glogowski, "Planar Antennas for Ka-Band Space Applications," vol. 6098, 2013.

[56] J. M. Ll. Coll, "X-Band Antenna for Cubesat Satellite," EPFL, 2017.

[57] T. Teshirogi, M. Tanaka, and W. Chujo, "Wideband Circularly Polarized Array Antenna with Sequential Rotations and Phase Shift of Elements," in *Proceedings of ISAP*, 1985, pp. 117–120.

[58] H. Evans, P. Gale, B. Aljibouri, E. Korolkciwicz, and A. Sambell, "Application of simulated annealing to design of serial feed sequentially rotated 2 2 antenna array," *IET Electron. Lett.*, vol. 36, no. 24, pp. 1987–1988, 2000, doi: 10.1049/el:20001407.

[59] H. Evans and A. Sambell, "ROTATED PATCH ANTENNA ARRAY WITH A SERIES FEED," vol. 40, no. 4, pp. 292–294, 2004, doi: 10.1002/mop.11356.

[60] P. Park and R. Elliott, "Design of collinear longitudinal slot arrays fed by boxed stripline," *1980 Antennas Propag. Soc. Int. Symp.*, vol. 18, no. 1, pp. 135–140, 1980, doi: 10.1109/APS.1980.1148243.

[61] S. Vaccaro, "SOLANT: Study and Development of Planar Antennas Integrating Solar Cells," EPFL, 2003.

[62] X. Liu *et al.*, "Transparent and Nontransparent Microstrip Antennas on a CubeSat: Novel low-profile antennas for CubeSats improve mission reliability," *IEEE Antennas Propag. Mag.*, vol. 59, no. 2, pp. 59–68, 2017, doi: 10.1109/MAP.2017.2655529.

[63] P. Dreyer, M. Morales-Masis, S. Nicolay, C. Ballif, and J. Perruisseau-Carrier, "Copper and transparent-conductor reflectarray elements on thin-film solar cell panels," *IEEE Trans. Antennas Propag.*, vol. 62, no. 7, pp. 3813–3818, 2014, doi: 10.1109/TAP.2014.2316539.

[64] M. P. Magalhaes, M. V. T. Heckler, J. C. M. Mota, A. S. B. Sombra, and E. C. Moreira, "Design and analysis of microstrip antenna arrays for meteorological nano-satellites for UHF uplink," *2014 Int. Telecommun. Symp. ITS 2014 - Proc.*, 2014, doi: 10.1109/ITS.2014.6947985.

[65] A. K. Skrivervik, "Design Strategies and basic antenna structures," in *Handbook on small antennas*, Universitat Politecnica de Catalunya, 2012, pp. 61–152.

[66] K. Muchalski *et al.*, "Optimizing TT&C antenna placement on minisatellites," *15th Int. Conf. Microwaves, Radar Wirel. Commun. (IEEE Cat. No.04EX824)*, vol. 2, 2004, doi: 10.1109/MIKON.2004.1357073.

[67] G. Marrocco, L. Mattioni, A. Potenza, F. Milani, A. Giacomini, and M. Sabbadini, "Distributed multi-function antenna system for micro- and nano-satellites," *Antennas Propag. (EuCAP), 2010 Proc. Fourth Eur. Conf.*, pp. 1–4, 2010.

[68] P. S. Hall, "Application of sequential feeding to wide bandwidth, circularly polarised microstrip patch arrays," *IEE Proc. H Microwaves, Antennas Propag.*, vol. 136, no. 5, p. 390, 1989, doi: 10.1049/ip-h-2.1989.0070.

[69] J. M. de Freitas, "SPHERE3D: A Matlab Function to Plot 3-Dimensional Data on a Spherical Surface," 2005. [Online]. Available: https://ch.mathworks.com/matlabcentral/fileexchange/8585-3d-plot-on-a-spherical-surface.

[70] D. M. Pozar and D. H. Schaubert, Eds., *Microstrip Antennas: The Analysis and Design of Microstrip Antennas and Arrays*. New York, NY, United States: IEEE Press, 1995.

[71] Y. Yao, S. Liao, J. Wang, and K. Xue, "A New Patch Antenna Designed for CubeSat: Dual feed, L/S dual-band stacked, and circularly polarized," *IEEE Antennas Propag. Mag.*, vol. 58, no. 3, pp. 16–21, 2016.

[72] F. J. Dietrich, "Globalstar satellite cellular communication system: Design and status," *Wescon Conf. Rec.*, pp. 180–186, 1997, doi: 10.1109/wescon.1997.632335.

[73] R. SOIFER and P. I. KLEIN, "Intersatellite Communication Using the AMSAT-OSCAR 6 and AMSAT-OSCAR 7 Radio Amateur Satellite," no. October, pp. 1974–1975, 1975.

[74] A. Tiainen, "Inter-Satellite Link Antennas," 2017.

[75] P. Muri and J. McNair, "A survey of communication sub-systems for intersatellite linked systems and cubesat missions," *J. Commun.*, vol. 7, no. 4, pp. 290–308, 2012, doi: 10.4304/jcm.7.4.290-308.

[76] H. B. Poza, "TDRSS Telecommunications Payload: An Overview," *IEEE Trans. Aerosp. Electron. Syst.*, vol. AES-15, no. 3, pp. 414–429, 1979, doi: 10.1109/TAES.1979.308836.

[77] H. Hauschildt, S. Mezzasoma, H. L. Moeller, M. Witting, and J. Herrmann, "European data relay system goes global," *2017 IEEE Int. Conf. Sp. Opt. Syst. Appl. ICSOS 2017*, pp. 15–18, 2017, doi: 10.1109/ICSOS.2017.8357204.

[78] O. P. Gupta, "Iridium: A Global Communication Network," p. 7, 2007.

[79] G. Bonin, N. H. Roth, S. Armitage, J. Newman, B. Risi, and R. E. Zee, "CanX–4 and CanX–5 Precision Formation Flight: Mission Accomplished!," in *29th Annual AIAA/USU Conference on Small Satellites*, 2015, doi: 10.1016/j.jcrysgro.2014.02.053.

[80] "Iridium NEXT Overview," 2018. [Online]. Available: https://aerospacedefenseforum.org/wp-content/uploads/2018/04/Iridium-18-03-23-Slides.pdf.

[81] J. Huang and J. A. Encinar, *Reflectarray Antennas*. Wiley Interscience, 2008.

[82] L. Dussopt, "Transmitarray Antennas," in *Aperture Antennas for Millimeter and Sub-Millimeter Wave Applications*, A. Boriskin and R. Sauleau, Eds. Springer, 2018, pp. 191–220.

[83] T. Smith, U. Gothelf, O. S. Kim, and O. Breinbjerg, "An FSS-backed 20/30 GHz circularly polarized reflectarray for a shared aperture L- and Ka-band satellite communication antenna," *IEEE Trans. Antennas Propag.*, vol. 62, no. 2, pp. 661–668, 2014, doi: 10.1109/TAP.2013.2292692.

[84] F. Xue and H. Wang, "Design of a Novel Ku / X-Band Reflectarray / Transmit-Array Antenna with Frequency Selective Surface," *Prog. Electromagn. Res. C*, vol. 73, no. March, pp. 17–25, 2017.

[85] H. Hasani, J. S. Silva, J. R. Mosig, and M. Garcia-Vigueras, "Dual-band 20/30 GHz circularly polarized transmitarray for SOTM applications," *2016 10th Eur. Conf. Antennas Propagation, EuCAP 2016*, pp. 5–7, 2016, doi: 10.1109/EuCAP.2016.7481869.

[86] F. Yang, R. Deng, S. Xu, and M. Li, "Design and Experiment of a Near-Zero-Thickness High-Gain Transmit-Reflect-Array Antenna Using Anisotropic Metasurface," *IEEE Trans. Antennas Propag.*, vol. 66, no. 6, pp. 2853–2861, 2018, doi: 10.1109/TAP.2018.2820320.

[87] M. Wang, S. Xu, F. Yang, and M. Li, "A 1-Bit Bidirectional Reconfigurable Transmit-Reflect-Array Using a Single-Layer Slot Element With PIN Diodes," *IEEE Trans. Antennas Propag.*, vol. 67, no. 9, pp. 6205–6210, 2019, doi: 10.1109/tap.2019.2925925.

[88] D. M. Pozar, S. D. Targonski, and H. D. Syrigos, "Design of millimeter wave microstrip reflectarrays," *IEEE Trans. Antennas Propag.*, vol. 45, no. 2, pp. 287–296, 1997, doi: 10.1109/8.560348.

[89] A. H. Abdelrahman, A. Z. Elsherbeni, and F. Yang, "Transmission phase limit of multilayer frequency-selective surfaces for transmitarray designs," *IEEE Trans. Antennas Propag.*, vol. 62, no. 2, pp. 690–697, 2014, doi: 10.1109/TAP.2013.2289313.

[90] L. Di Palma, A. Clemente, L. Dussopt, R. Sauleau, P. Potier, and P. Pouliguen, "Circularly Polarized Transmitarray With Sequential Rotation in Ka-Band," *IEEE Trans. Antennas Propag.*, vol. 63, no. 11, pp. 5118–5124, 2015.

[91] R. H. Phillion and M. Okoniewski, "Lenses for circular polarization using planar arrays of rotated passive elements," *IEEE Trans. Antennas Propag.*, vol. 59, no. 4, pp. 1217–1227, 2011, doi: 10.1109/TAP.2011.2109694.

[92] J. Huang and R. J. Pogorzelski, "A ka-band microstrip reflectarray with elements having variable rotation angles," *IEEE Trans. Antennas Propag.*, vol. 46, no. 5, pp. 650–656, 1998, doi: 10.1109/8.668907.

[93]   J.   Perruisseau-Carrier,   "MICROWAVE   PERIODIC   STRUCTURES   BASED   ON
         MICROELECTROMECHANICAL SYSTEMS (MEMS) AND MICROMACHINING TECHNIQUES," vol.
         3969, 2007.

[94]   P. Naseri, S. A. Matos, J. R. Costa, and C. A. Fernandes, "Phase-Delay Versus Phase-Rotation Cells for
         Circular Polarization Transmit Arrays-Application to Satellite Ka-Band Beam Steering," *IEEE Trans.
         Antennas Propag.*, vol. 66, no. 3, pp. 1236–1247, 2018, doi: 10.1109/TAP.2017.2787540.

[95]   S. V. Hum, "Reflectarrays," in *Aperture Antennas for Millimeter and Sub-Millimeter Wave Applications*, A.
         Boriskin and R. Sauleau, Eds. Springer, 2018, pp. 143–190.

[96]   C. Han and K. Chang, "Ka-band reflectarray using ring elements," *Electron. Lett.*, vol. 39, no. March, pp.
         491–493, 2003.

[97]   B. Strassner, C. Han, and K. Chang, "Circularly polarized reflectarray with microstrip ring elements having
         variable rotation angles," *IEEE Trans. Antennas Propag.*, vol. 52, no. 4, pp. 1122–1125, 2004, doi:
         10.1109/TAP.2004.825635.

[98]   C. Han, C. Rodenbeck, J. Huang, and K. Chang, "A C/Ka dual frequency dual layer circularly polarized
         reflectarray antenna with microstrip ring elements," *IEEE Trans. Antennas Propag.*, vol. 52, no. 11, pp.
         2871–2876, 2004, doi: 10.1109/TAP.2004.835144.

[99]   P. Naseri, R. Mirzavand, and P. Mousavi, "Dual-Band Circularly Polarized Transmit-Array Unit- Cell At X
         and K Bands," *2016 10th Eur. Conf. Antennas Propag.*, pp. 1–4, doi: 10.1109/EuCAP.2016.7481440.

[100]   D. T. McGrath, "Planar Three-Dimensional Constrained Lenses," *IEEE Trans. Antennas Propag.*, vol. 34,
         no. 1, pp. 46–50, 1986, doi: 10.1109/TAP.1986.1143726.

[101]   D. M. Pozar, "Flat lens antenna concept using aperture coupled microstrip lpatches," *Electron. Lett.*, vol.
         32, no. 23, pp. 2109–2111, 1996.

[102]   E. G. Plaza, G. León, S. Loredo, and F. Las-Heras, "Dual polarized transmitarray lens," *8th Eur. Conf.
         Antennas Propagation, EuCAP 2014*, no. EuCAP, pp. 2305–2308, 2014, doi: 10.1109/EuCAP.2014.6902276.

[103]   V. Rathi, G. Kumar, and K. P. Ray, "Improved coupling for aperture coupled microstrip antennas," *IEEE
         Trans. Antennas Propag.*, vol. 44, no. 8, pp. 1196–1198, 1996, doi: 10.1109/8.511831.

[104]   T. G. Smith, N. Vesterdal, U. Gothelf, O. S. Kim, and O. Breinbjerg, "An Offset-Fed 20 / 30 GHz Dual-Band
         Circularly Polarized Reflectarray Antenna," *2013 7th Eur. Conf. Antennas Propag.*, pp. 2959–2962, 2013.

[105]   T. A. Milligan, *Modern Antenna Design*. John Wiley & Sons, Inc., 2005.

[106]   M. H. Cheng and G. N. Tsandoulas, "A Wide-Band Square-Waveguide Array Polarizer," *IEEE Trans.
         Antennas Propag.*, pp. 389–391, 1973.

[107]   J. Esteban and J. M. Rebollar, "Field Theory C.A.D. of Septum OMT-Polarizers," in *IEEE Antennas and
         Propagation Society International Symposium 1992 Digest*, 1992, pp. 2146–2149.

[108]   A. A. Kirilenko, D. Y. Kulik, L. A. Rud, V. I. Tkachenko, and N. Herscovici, "Electromagnetic modeling and
         design of dual-band septum polarizers," *Appl. Comput. Electromagn. Soc. J.*, vol. 21, no. 2, pp. 155–162,
         2006.

[109]   T.-H. Chio, G.-L. Huang, and S.-G. Zhou, "Application of Direct Metal Laser Sintering to Waveguide-
         Based Passive Microwave Components, Antennas, and Antenna Arrays," *Proc. IEEE*, vol. 105, no. 4, pp.
         632–644, 2016, doi: 10.1109/jproc.2016.2617870.

[110]   J. Nourinia, C. Ghobadi, B. Mohammadi, and F. Alizadeh, "Aperture Efficiency Study of Square Reflect
         Array Antennas," *Wirel. Eng. Technol.*, no. 9, pp. 66–78, 2018, doi: 10.4236/wet.2018.93006.

Publications

[J1]   M. J. Veljovic and A. K. Skrivervik, "Aperture-Coupled Low-Profile Wideband Patch Antennas for CubeSat," IEEE Transactions on Antennas and Propagation, vol. 67, no. 5, pp. 3439–3444, 2019.

[J2]   M. J. Veljovic and A. K. Skrivervik, "Wideband Single-Layer Circularly Polarized Reflectarray Antenna for CubeSat Inter-Satellite Links," submitted to IEEE Antennas and Wireless Propagation Letters.

[J3]   M. J. Veljovic and A. K. Skrivervik, "Low-Profile Aperture-Coupled-Patch Transmitarray Antenna for CubeSat Inter-Satellite Links," submitted to IEEE Antennas and Wireless Propagation Letters.

[C1]   M. J. Veljovic and A. K. Skrivervik, "Wideband cavity-backed CubeSat antenna in S band," 12th Eur. Conf. Antennas Propagation, EuCAP 2018, London, UK, 2018.

[C2]   M. J. Veljovic and A. K. Skrivervik, "Patch Antenna System for CubeSats in L band," 13th Eur. Conf. Antennas Propagation, EuCAP 2019, Krakow, Poland, 2019.

[C3]   M. J. Veljovic and A. K. Skrivervik, "A Comparison of Three Feeding Networks for CubeSat L/S-dual-band Stacked-Patch Antennas," 13th Eur. Conf. Antennas Propagation, EuCAP 2019, Krakow, Poland, 2019.

[C4]   F. Qaderi, A. Muller, A. Krammer, M. J. Veljovic, Z. Ollmann, M. Hayati, A. Skrivervik, A. Schueler, T. Feurer, A. Ionescu,, "Millimeter-wave-triggering of insulator-to-metal transition in Vanadium dioxide," 2019 44th Int. Conf. Infrared, Millimeter, Terahertz Waves, Paris, France, 2019.

[C5]   M. J. Veljovic and A. K. Skrivervik, "Circularly Polarized Axially Corrugated Feed Horn for CubeSat Reflectarray Applications," in 14th European Conference on Antennas and Propagation, EuCAP 2020, Copenhagen, Denmark, 2020.

[C6]   A. J. M. Montes, I. V. Triviño, M. Bosiljevac, M. J. Veljovic, Z. Sipus, and A. K. Skrivervik, "Antenna for a Cranial Implant: Simulation Issues and Design Strategies," 14th European Conference on Antennas and Propagation, EuCAP 2020, Copenhagen, Denmark, 2020.

[C7]   A. K. Skrivervik, A. J. M. Montes, I. V. Triviño, M. Bosiljevac, M. J. Veljovic, and Z. Sipus, "Antenna design for a cranial implant," in 2020 International Workshop on Antenna Technology (iWAT), Bucharest, Romania, 2020.

[W1]   A. K. Skrivervik, M. J. Veljovic, "CubeSat Antennas," a tutorial given at the ICECOM Satellite Workshop, 23rd International Conference on Applied Electromagnetics and Communications, ICECOM 2019, Dubrovnik, Croatia, 2019.

Curriculum Vitae

EDUCATION

| 2015 – present | **PhD** | **EPFL, Lausanne** |

Microwave and Antenna Group (former LEMA)

- PhD thesis: "Antennas for CubeSat Communication"
  Thesis advisor: Prof. Anja Skrivervik
- Research on cost-efficient antennas for satellite communications:
  CubeSat antennas, SATCOM waveguide arrays
- Antenna design for Astrocast: the first Swiss nanosatellite network
- Low-profile, multi-layer antenna design, frequencies from L to Ka band
- PCB antenna manufacturing and assembly, nanosatellite antenna
  integration, VNA and anechoic chamber measurements

| 2010 – 2015 | **Master & Bachelor** | **School of Electrical Engineering, Belgrade** |

Department of Telecommunications and Information Technology
Module Microwave Engineering

- Master thesis: "Electromagnetic wave propagation in the vicinity of
  humans"
- Average grade: 10/10 (master), 9.41/10 (bachelor)
- Undergraduate laboratory assistant (2011-2014): Conducting student
  laboratory exercises in electrical engineering fundamentals
- Student project: Microwave amplifier design, fabrication and testing at
  2.45 GHz

EXPERIENCE

| 2015 – present | **Doctoral assistant** | **EPFL, Lausanne** |

Teaching: antennas and radiation course

Conducting laboratory experiments: laboratory on microwaves

Supervision of five semester and bachelor student projects

| Mar – Sep 2015 | **Internship** | **Institute for Microwaves and Electronics, Belgrade** |

3-D design and prototype measurements of microwave couplers and baluns

| Sep – Oct 2013 | **Internship** | **WIPL-D, Belgrade** |

Software design company for 3-D electromagnetic simulation

- Modeling of car shells
- Optimization of waveguide filters

PROFESSIONAL COURSES

Sep 11-15, 2017	**Frequency Domain Techniques**	**University of Florence, Italy**

- Methodology and limitations of computational techniques for scattering and antenna problems

Jul 4-8, 2016	**Millimeter-Wave Antennas**	**IETR, Rennes, France**

- Antenna structures and specific technologies for industrial applications at millimeter-wave frequencies

Mar 14-18, 2016	**Antennas for Space Applications**	**European Space Agency**

- Design requirements and solutions for space applications

- An overview of space antennas – ground and space segment

SELECTED SCHOLARSHIPS

2015 – 2016	**Doctoral Fellowship**

EPFL Electrical Engineering Doctoral School

- First-year fellowship given to a single PhD student per year

2015	**Undergraduate/Pre-graduate Scholarship**

IEEE Microwave Theory and Techniques Society (MTT-S)

- A scholarship for the master thesis research project

SKILLS

Software	Ansys HFSS and Designer, CST, WIPL-D
	AWR Microwave Office, Altium Designer
	MATLAB
Language	English: Proficient
	French: Basic
	Russian: Basic
	Serbian: Native

PERSONAL ACTIVITIES

2011 – present	**Rowing**

Belgrade University Rowing Club, Rowing Club Lausanne

- Competing at regional and international regattas in an 8-seat boat

- Assistant of the coach

2003 – present	**Clarinet**

Music School in Belgrade, Folklore Ensemble Orchestra

- Performing with the orchestra at local concerts

- Touring at international music festivals